

# **Modular DNA Constructs for Oligovalent Bio-Enhancement and Functional Screening**

---

**Christin Möser**

**Univ.-Diss.**

**zur Erlangung des akademischen Grades  
"doctor rerum naturalium"  
(Dr. rer. nat.)  
in der Wissenschaftsdisziplin "Biochemie"**

**angefertigt am  
Fraunhofer-Institut für Zelltherapie und Immunologie IZI, Leipzig**

**eingereicht an der  
Mathematisch-Naturwissenschaftlichen Fakultät  
Institut für Biochemie und Biologie  
der Universität Potsdam**

Ort und Tag der Disputation: Potsdam-Golm, 17.03.2021

Unless otherwise indicated, this work is licensed under a Creative Commons License Attribution 4.0 International.

This does not apply to quoted content and works based on other permissions.

To view a copy of this license visit:

<https://creativecommons.org/licenses/by/4.0>

Hauptbetreuer: Prof. Dr. Frank F. Bier  
Mentor: Dr. David M Smith  
Gutachter: Prof. Dr. Ilko Bald  
apl. Prof. Dr. Wolfgang Fritzsche

Published online on the  
Publication Server of the University of Potsdam:  
<https://doi.org/10.25932/publishup-50728>  
<https://nbn-resolving.org/urn:nbn:de:kobv:517-opus4-507289>

Für meine Eltern



---

## Table of contents

<b>Table of contents</b> .....	<b>I</b>
<b>Abstract</b> .....	<b>V</b>
<b>Zusammenfassung</b> .....	<b>VII</b>
<b>List of abbreviations</b> .....	<b>IX</b>
<b>Preface</b> .....	<b>XIII</b>
<b>1 Introduction</b> .....	<b>1</b>
<b>2 Theoretical background</b> .....	<b>3</b>
2.1 Multivalent interactions .....	3
2.2 The structure of DNA .....	5
2.3 DNA nanotechnology .....	6
2.3.1 DNA origami .....	7
2.3.2 Small DNA structures .....	9
2.3.3 Functionalization of DNA nanostructures with peptides .....	10
2.4 Characterization of therapeutic antibodies .....	11
2.4.1 $\alpha$ -Synuclein antibodies .....	12
2.4.2 Anti-Human c-Myc antibody .....	13
2.4.3 Anti-Actin antibody.....	13
2.5 Pathogen interactions with host cells.....	13
2.5.1 Influenza A viruses.....	15
2.5.2 Respiratory syncytial viruses.....	17
2.5.3 <i>Escherichia coli</i> .....	18
2.6 Binding and activation of EphA2 receptors.....	20
2.6.1 Peptide SWL.....	20
<b>3 Materials and methods</b> .....	<b>21</b>
3.1 Equipment and consumables .....	21
3.2 Software.....	23
3.3 Chemicals .....	23
3.4 Buffers .....	25
3.5 Media .....	26
3.6 Antibodies, beads, enzymes, kits, matrices and standards .....	27
3.7 DNA, peptides and sugars .....	27

3.8	Organisms.....	31
3.8.1	Cell lines .....	31
3.8.2	Viruses .....	31
3.8.3	Bacteria .....	31
3.9	Cultivation of cell lines .....	32
3.9.1	Subcultivation .....	32
3.9.2	Cryopreservation .....	32
3.9.3	Counting.....	33
3.10	Quantification of DNA .....	33
3.11	Synthesis of DOhex structures.....	33
3.11.1	Preparation of scaffold DNA .....	33
3.11.2	Production of DOhex structures.....	34
3.12	Synthesis of small DNA nanostructures .....	35
3.13	Modification of DNA.....	36
3.13.1	NHS ester chemistry .....	36
3.13.2	SPAAC.....	37
3.14	Verification of DNA structure folding and functionalization.....	38
3.14.1	Agarose gel electrophoresis .....	38
3.14.2	Native PAGE.....	39
3.14.3	AFM imaging.....	39
3.15	Purification and concentration of DNA .....	40
3.15.1	Ethanol precipitation .....	40
3.15.2	Spin filtration .....	40
3.16	MALDI-TOF .....	41
3.17	ELISA .....	41
3.17.1	Binding of antibodies to peptides on DOhex structures.....	41
3.17.2	Binding of viruses to peptide-functionalized dsDNA constructs.....	42
3.17.3	EphA2 phosphorylation assay.....	43
3.18	MST .....	45
3.19	Hemagglutination inhibition assay .....	46
3.20	Flow cytometry.....	47
3.20.1	Influenza A infection inhibition assay .....	47
3.20.2	Bacteria binding assay.....	48

---

3.20.3	EphA2 expression assay .....	49
3.20.4	EphA2 binding assay .....	49
3.21	Microscopic observation of cells .....	50
3.21.1	Detection of CPE in MDCK cells .....	50
3.21.2	PC-3 cell rounding assay .....	50
<b>4</b>	<b>Evaluating the binding of antibodies to epitopes separated by specific distances.....</b>	<b>51</b>
4.1	Importance and aim .....	51
4.2	Design of DOhex structures.....	54
4.3	$\alpha$ -synuclein antibodies .....	56
4.4	Anti c-Myc antibody.....	57
4.5	Anti-Actin antibody .....	59
4.6	Discussion.....	60
<b>5</b>	<b>Capturing pathogens via peptide- or sugar-coupled DNA nanostructures .....</b>	<b>65</b>
5.1	Global burden of pathogenic infections.....	66
5.1.1	Influenza A virus .....	66
5.1.2	RSV .....	67
5.1.3	<i>E. coli</i> .....	68
5.2	Binding and blocking influenza A via peptide-DNA constructs .....	69
5.2.1	Aim.....	69
5.2.2	Construction of PeB-DNA nanostructures .....	70
5.2.3	Binding of PeB-DNA trimers to IAV X31 .....	71
5.2.4	Blocking IAV X31 .....	73
5.2.5	Discussion .....	78
5.3	Binding and inhibiting RSV via peptide-DNA constructs .....	81
5.3.1	Aim.....	81
5.3.2	Construction of RSV-Peptide-6-DNA nanostructures .....	81
5.3.3	Binding of dsDNA modified with RSV-Peptide-6 to RSV .....	83
5.3.4	RSV infection inhibition assay.....	84
5.3.5	Discussion .....	86
5.4	Evaluating the binding of different sugar-DNA constructs to <i>E. coli</i> .....	87
5.4.1	Aim.....	87
5.4.2	Construction of sugar-modified DNA 4arm structures .....	88
5.4.3	Bacteria binding assay.....	89

5.4.4	Discussion .....	90
<b>6</b>	<b>Pinpointed stimulation of EphA2 receptors via DNA-templated oligovalence .....</b>	<b>93</b>
6.1	Importance and aim .....	93
6.2	Construction of SWL-DNA trimers .....	94
6.3	Binding of SWL-DNA trimers to PC-3 cells .....	97
6.4	Confirmation of EphA2 pathway activation via receptor phosphorylation.....	98
6.5	PC-3 cell rounding caused by EphA2 activation.....	100
6.6	Discussion .....	102
<b>7</b>	<b>Conclusion and outlook .....</b>	<b>105</b>
<b>8</b>	<b>References .....</b>	<b>109</b>
<b>Appendix</b> .....		<b>127</b>
I.	Lists of figures and tables .....	127
II.	DNA Sequences and design for DNA origami hexagonal structure .....	130
III.	Additional and raw data .....	138
<b>Acknowledgements</b> .....		<b>142</b>
<b>Declaration of authorship</b> .....		<b>144</b>
<b>Patents and publications</b> .....		<b>145</b>
<b>Curriculum vitae</b> .....		<b>148</b>



## Abstract

Deoxyribonucleic acid (DNA) nanostructures enable the attachment of functional molecules to nearly any unique location on their underlying structure. Due to their single-base-pair structural resolution, several ligands can be spatially arranged and closely controlled according to the geometry of their desired target, resulting in optimized binding and/or signaling interactions. This dissertation covers three main projects. All of them use variations of functionalized DNA nanostructures that act as platform for oligovalent presentation of ligands. The purpose of this work was to evaluate the ability of DNA nanostructures to precisely display different types of functional molecules (peptides and sugars) and to consequently enhance their efficacy according to the concept of multivalency. Moreover, functionalized DNA structures were examined for their suitability in functional screening assays. The developed DNA-based compound ligands were used to target structures in different biological systems, namely antibodies, viruses, bacteria and cell surface receptors.

In the first part of this work, two antibody-binding peptide epitopes were conjugated to large DNA origami structures. Each variant of DNA origami structures displayed pairs of those epitopes at different locations, thus creating different distances between them. The binding of three monoclonal antibodies to their corresponding epitopes was examined via enzyme-linked immunosorbent assays (ELISAs). Only when the epitopes were positioned in distances that were within reach of the antibody's Fab fragments, could stable binding be proven. The experiments revealed spatial configurations of the antibody's Fab fragments which mainly match literature findings. Interestingly, a different signature for non-canonical antibody binding could also be detected.

The second part of this dissertation attempted to bind pathogens with small modified DNA nanostructures. Pathogens like viruses and bacteria are known for their multivalent attachment to host cells membranes. By blocking their receptors for recognition and/or fusion with their targeted host in an oligovalent manner, the objective was to impede their ability to adhere to and invade cells. For influenza A, only enhanced binding of oligovalent peptide-DNA constructs compared to the monovalent peptide could be observed, whereas in the case of respiratory syncytial virus (RSV), binding as well as blocking of the target receptors led to an increased inhibition of infection *in vitro*. *E. coli* bacteria adhere to glycosylated cell surfaces through the

multivalent binding of many type 1 fimbriae to ligands such as mannose. In order to determine which sugars are preferentially bound, a high-throughput flow cytometry assay, employing DNA structures that present different sugars, was established.

In the final part, the ability of chimeric DNA-peptide constructs to bind to and activate signaling receptors on the surface of cells was investigated. Specific binding of DNA trimers, conjugated with up to three peptides, to EphA2 receptor expressing cells was evaluated in flow cytometry experiments. Subsequently, their ability to activate these receptors via phosphorylation was assessed. EphA2 phosphorylation was significantly increased by DNA trimers carrying three peptides compared to monovalent peptide. As a result of activation, cells underwent characteristic morphological changes, where they "round up" and retract their periphery.

The results obtained in this work comprehensively prove the capability of DNA nanostructures to serve as stable, biocompatible, controllable platforms for the oligovalent presentation of functional ligands. Functionalized DNA nanostructures were used to enhance biological effects and as tool for functional screening of bio-activity. This work demonstrates that modified DNA structures have the potential to improve drug development and to unravel the activation of signaling pathways.

## Zusammenfassung

Desoxyribonukleinsäure (DNS, engl. DNA) - Nanostrukturen ermöglichen die Anbringung funktioneller Moleküle an nahezu jede einzigartige Stelle der zugrunde liegenden Struktur. Aufgrund der Basenpaar-Strukturauflösung von DNA können mehrere Moleküle (z.B. Liganden) entsprechend der Geometrie ihres gewünschten Ziels räumlich angeordnet und genau kontrolliert werden, was zu optimierten Bindungs- und/oder Signalwechselwirkungen führt.

Diese Dissertation umfasst drei Hauptprojekte. Alle Projekte verwenden Varianten von funktionalisierten DNA-Nanostrukturen, die als Plattform für die oligovalente Präsentation von Liganden dienen. Ziel der vorliegenden Arbeit war es, die Fähigkeit von DNA-Nanostrukturen zur präzisen Positionierung verschiedener Arten von funktionellen Molekülen (bioaktive Peptide und Zuckermoleküle) zu evaluieren und folglich die Wirksamkeit der Moleküle gemäß dem Konzept der Multivalenz zu erhöhen. Außerdem wurde untersucht, wie funktionalisierte DNA-Strukturen in verschiedenen Verfahren zur Erforschung von biologischen Interaktionen eingesetzt werden können. Die entwickelten DNA-basierten Liganden wurden verwendet, um Strukturen auf verschiedenen biologischen Systemen (Antikörper, Viren, Bakterien und Zelloberflächenrezeptoren) gezielt zu binden.

Im ersten Teil dieser Arbeit wurden zwei antikörperbindende Epitope an große DNA-Origami-Strukturen konjugiert. Jede Variante der DNA-Origami-Strukturen präsentierte Paare dieser Epitope an verschiedenen Stellen, wodurch unterschiedliche Abstände zwischen den Epitopen geschaffen wurden. Die Bindung von drei monoklonalen Antikörpern an ihre entsprechenden Epitope wurde mittels *Enzyme-linked Immunosorbent Assays* (ELISAs) untersucht. Nur wenn die Epitope in Entfernungen positioniert wurden, die für die Fab-Fragmente des Antikörpers erreichbar waren, konnte eine stabile Bindung nachgewiesen werden. Die Experimente ergaben räumliche Konfigurationen der Fab-Fragmente des Antikörpers, die überwiegend mit der Fachliteratur übereinstimmen. Interessanterweise konnte auch eine nicht-kanonische Antikörperbindung nachgewiesen werden.

Im zweiten Teil dieser Dissertation wurde versucht, Krankheitserreger mit kleinen modifizierten DNA-Nanostrukturen zu binden. Pathogene, wie Viren und Bakterien, sind für ihre multivalente Anheftung an Wirtszellmembranen bekannt. Durch die oligovalente Blockierung ihrer Rezeptoren für die Erkennung und/oder Fusion mit ihrem Wirt sollte ihre Fähigkeit, sich an

Zielzellen anzuheften und in diese einzudringen, beeinträchtigt werden. Bei Influenza A Viren konnte nur eine verstärkte Bindung von oligovalenten Peptid-DNA-Konstrukten im Vergleich zu monovalenten Peptiden beobachtet werden, wohingegen bei Respiratorischen Synzytial-Viren (RSV) sowohl die Bindung als auch die Blockierung der Zielrezeptoren zu einer verstärkten Hemmung der Infektion *in vitro* führte. *Escherichia coli* (*E. coli*) - Bakterien haften an glykosylierten Zelloberflächen durch die multivalente Bindung ihrer Typ-1-Fimbrien an Liganden, wie z.B. Mannose. Um zu bestimmen, welche Zucker bevorzugt gebunden werden, wurde ein Hochdurchsatz-Durchflusszytometrie-Assay etabliert, bei dem verschiedene Zucker-präsentierende DNA-Strukturen eingesetzt wurden.

Im letzten Teil wurden chimäre DNA-Peptidkonstrukte auf ihre Fähigkeit, an Signalrezeptoren auf der Oberfläche von Zellen zu binden und diese zu aktivieren, getestet. Die spezifische Bindung von mit bis zu drei Peptiden konjugierten DNA-Trimeren an EphA2-Rezeptor-exprimierende Zellen wurde in Durchflusszytometrie-Experimenten untersucht. Anschließend wurde ihre Fähigkeit, diese Rezeptoren durch Phosphorylierung zu aktivieren, beurteilt. Die Phosphorylierung von EphA2 war durch DNA-Trimere, die drei Peptide trugen, im Vergleich zu monovalenten Peptiden signifikant erhöht. Infolge der Aktivierung kommt es zu charakteristischen morphologischen Veränderungen der Zellen, bei denen diese ihre Peripherie "abrunden" und zurückziehen.

Die in dieser Arbeit erzielten Ergebnisse beweisen umfassend die Fähigkeit von DNA-Nanostrukturen, als stabile, biokompatible, kontrollierbare Plattformen für die oligovalente Präsentation funktioneller Liganden zu fungieren. Funktionalisierte DNA-Nanostrukturen wurden zur Verstärkung biologischer Effekte und als Werkzeug für das funktionelle Screening von biologischen Interaktionen verwendet. Diese Arbeit zeigt, dass modifizierte DNA-Strukturen das Potenzial haben, die Medikamentenentwicklung zu verbessern und die Aktivierung von Signalwegen zu entschlüsseln.

## List of abbreviations

Apart from standard short forms for metric units (e.g.  $\mu\text{l}$ ), time units (e.g. min) and chemical symbols and formulas (e.g. KCl); the abbreviations listed below are used in this thesis.

2D	two-dimensional
3D	three-dimensional
3-HPA	3-hydroxypicolinic acid
AFM	atomic force microscopy
AN	actin naïve peptide
AP	actin phage peptide
APS	ammonium persulfate
bp	base pair
BSA	bovine serum albumin
CDR	complementarity determining regions
CN	c-Myc naïve peptide
CP	c-Myc phage peptide
CPE	cytopathic effect
Cy3	cyanine 3
Da	Dalton
DBCO	dibenzylcyclooctyne
ddH <sub>2</sub> O	double-distilled water
DMSO	dimethyl sulfoxide
DNA	deoxyribonucleic acid
DOhex	helical-based DNA origami structure
DPBS	Dulbecco's phosphate buffered saline
dsDNA	double-stranded DNA
<i>E. coli</i>	<i>Escherichia coli</i>
EC50	half-maximal effective concentration
EDTA	ethylenediaminetetraacetic acid
ELISA	enzyme-linked immunosorbent assay
Eph receptor	erythropoietin-producing hepatocellular carcinoma receptor

## List of abbreviations

---

ephrin	Eph family receptor interacting protein
FBS	fetal bovine serum
FSC	forward-scattered light
FU	fluorescent units
fw	forward
GFP	green fluorescent protein
HA	hemagglutinin
HAI	hemagglutination inhibition
HAU	hemagglutination units
HEPES	4-(2-hydroxyethyl)-1-piperazineethanesulfonic acid
HIV	human immunodeficiency viruses
HPLC	high-performance liquid chromatography
HRP	horseradish peroxidase
IAV	influenza A virus
IC50	half-maximal inhibitory concentration
Ig	immunoglobulin
K <sub>i</sub> HAI	hemagglutination inhibition constant
LBD	ligand-binding domain
M2 protein	matrix 2 protein
mAb	monoclonal antibody
MALDI-TOF	matrix-assisted laser desorption/ionization – time-of-flight
MDCK	Madin-Darby canine kidney
MST	microscale thermophoresis
MWCO	molecular weight cut-off
NA	neuraminidase
NHS ester	<i>N</i> -hydroxysuccinimide ester
NP-40	Nonidet® P40
OD	optical density
PAGE	polyacrylamide gel electrophoresis
PBS	phosphate buffered saline
PE	phycoerythrin
PEG	polyethylene glycol
PFU	plaque-forming units

PNA	peptide nucleic acid
rev	reverse
RNA	ribonucleic acid
rpm	revolutions per minute
RSV	respiratory syncytial virus
RTK	receptor tyrosine kinase
SPAAC	strain-promoted alkyne-azide cycloaddition
SSC	side-scattered light
ssDNA	single-stranded DNA
TEMED	<i>N,N,N',N'</i> -Tetramethylethylenediamine
TMB	3,3',5,5'-Tetramethylbenzidine
TPCK	tosyl phenylalanyl chloromethyl ketone
UV	Ultraviolet
v/v	volume per volume
w/	with
w/o	without
w/v	weight per volume





## Preface

This work consists of a number of different projects which are unified by the simple principle that DNA nanostructures are investigated for their application as oligovalent carriers for presenting biologically relevant molecules such as peptides or carbohydrates. The results of this work are presented in chapters 4, 5 and 6.

The content of chapter 4 is currently in preparation as manuscript that will be submitted for peer-reviewed publication.

The data presented in chapter 5 results from collaborations with several project partners. Their contributions are clearly indicated.

The results of HAI assays in section 5.2.4 were also published in the patent: D. M. Smith, J. S. Lorenz, C. Möser, J. Fertey, W. Stöcklein, A. Herrmann, and D. Lauster, “Nanostructure with a nucleic acid scaffold and virus-binding peptide moieties,” WO2018215660A1, 2018.

The results of RSV infection inhibition assays in section 5.3.4 were published in October 2020 in the patent: D. M. Smith, C. Möser, T. Grunwald, L. Issmail, C. Jäger, M. Kleinschmidt, D. Ramsbeck, M. Buchholz, “Biological and synthetic molecules inhibiting respiratory syncytial virus infection,” WO2020212576A1, 2020.

Modified versions of the sections 2.6, 3.16, 3.17.3, 3.20.3, 3.20.4, 3.21.2, and part of the abstract as well as the entire chapter 6 were published in a manuscript in the International Journal of Molecular Sciences:

C. Möser, J. S. Lorenz, M. Sajfutdinow, and D. M. Smith, “Pinpointed Stimulation of EphA2 Receptors via DNA-Templated Oligovalence,” *Int. J. Mol. Sci.*, vol. 19, no. 11, p. 3482, Nov. 2018.

Author Contributions: Conceptualization, C.M. and D.M.S.; Data curation, C.M.; Formal analysis, C.M. and M.S.; Funding acquisition, D.M.S. and C.M.; Methodology, C.M., J.S.L. and D.M.S.; Project administration, D.M.S.; Supervision, D.M.S.; Validation, C.M., M.S. and D.M.S.; Visualization, C.M. and M.S.; Writing-original draft, C.M.; Writing-review & editing, J.S.L. and D.M.S.

Parts of the text were rewritten and images were reformatted.



## 1 Introduction

Multivalent interactions can be described as simultaneous and cooperative binding between multiple ligands on one entity to multiple receptors on another entity. Such interactions are orders of magnitudes stronger than the corresponding monovalent binding between one ligand and one receptor. The reason for this enhancement is an increased functional affinity, so-called avidity. In addition to this, multivalency can equip ligands with higher specificity and new properties like receptor clustering that can initiate different signaling processes. Thus, multivalent interactions play pivotal roles in biological systems and processes, such as cell surface adhesion, recognition and cellular migration as well as host-pathogen interactions.

In this work, self-assembled DNA nanostructures were explored as backbone material for engineering oligovalent presentation of bioactive ligands. DNA is a biocompatible molecule that has been extensively exploited as a construction material for all sorts of DNA nanoarchitectures since first proposed in 1982. Nowadays, those structures are increasingly exploited for their applications in nanomedicine. DNA nanostructures can be modified with various molecules and thus enable the precise and controlled positioning of ligands on the (sub)nanometer scale. Hence, modified DNA structures function as geometrically precise linkers that tether multiple ligands together, and thereby constitute a multivalent binding partner with a defined and controllable valency, flexibility and length. Another aspect that benefits from using DNA nanostructures for biological applications, is their enhanced biostability compared to linear DNA and oligonucleotides. Furthermore, the overall size of many DNA nanostructures is much smaller (e.g. the DNA trimer ~30-40 kDa) than the average size of an antibody (~150 kDa), particularly when looking at structures that interact on the size scale of individual cell or viral receptors. Due to their large size, the use of antibodies is mostly restricted to extracellular targets, since molecules of that size are difficult to be taken up by cells <sup>1</sup>. In contrast, small DNA nanostructures as well as bigger DNA origami are reported to have the potential to be taken up by cells and hence can serve as drug-delivery vehicles <sup>2</sup>.

The first subproject of this work aimed to use this concept of DNA-templated oligovalence to characterize the distance and flexibility of bivalent monoclonal antibodies. Most antibodies bind their antigens in a multivalent manner. To give an example, the most common type of antibody, immunoglobulin G (IgG), typically interacts with its antigens in a bivalent fashion due to its Y-

shaped structure. Antibodies are nowadays used to treat diseases like cancer, cardiovascular or autoimmune diseases. Characterization of fluctuation and heterogeneity of such therapeutic antibodies is critical for obtaining a deeper insight into their structural characteristics and for improvement of drug development<sup>3</sup>. Current techniques lack the ability to reproducibly characterize the spatial structure of antibodies in biological conditions. In this work, a DNA origami-based approach integrated into an ELISA was used to assess the spatial configuration of antibody Fab fragments in solution. Therefore, three monoclonal antibodies were examined and the results are presented in chapter 4.

In the last few years, a growing interest has been devoted to target the surface structure of pathogens via multivalent inhibitors<sup>4</sup>. Viruses are of particular interest here since their outer surfaces are usually covered with a very geometrically precise arrangement of proteins enabling binding and fusion. As viruses and bacteria adhere to host cells via multivalent interactions of their surface proteins with host cell structures (mostly carbohydrates), multivalent drugs that inhibit viruses by blocking the function of these surface proteins are presumed to act more efficiently than their monovalent counterparts. With the goal of studying pathogenic multivalent interactions, small DNA nanostructures consisting of up to four short oligonucleotides were functionalized with up to three peptides to tackle influenza A and RSV, and also with sugar molecules to bind to *Escherichia coli* (*E. coli*) bacteria. This subproject explored whether oligovalent ligands bind and/or block viral and bacterial surface receptors better than their monovalent counterpart. The results are shown in chapter 5.

In the course of the last subproject presented in chapter 6, receptor clustering and the subsequent activation of intracellular signaling pathways in mammalian cells due to the oligovalent presentation of functional peptides on trimeric DNA structures was addressed. Receptor clustering is a typical phenomenon for receptor tyrosine kinases to initiate signaling cascades. Erythropoietin-producing hepatocellular carcinoma receptors (Eph receptors) comprise the largest subfamily of receptor tyrosine kinases and control several developmental processes and adult tissue homeostasis<sup>5</sup>. Eph receptors and their ligands are frequently overexpressed in cancer cells. However, a ligand-dependent activation of Eph receptors induces tumor-suppressive signaling pathways. In this work, DNA nanostructures decorated with specific peptides were utilized to bind EphA2 receptors. Subsequent processes such as receptor phosphorylation and cellular morphological changes were investigated.

## 2 Theoretical background

### 2.1 Multivalent interactions

The principle of multivalent presentation and binding is found ubiquitously in nature, being, among others, the basis of specific cell-cell interactions and pathogen-host recognition <sup>6</sup>. Multivalency means the simultaneous and cooperative occurrence of many interactions that collectively are stronger than one single interaction would be. They are present on both macroscopic (e.g. burr or velcro fastener) and microscopic levels (e.g. virus-cell interactions). Multivalent interactions are reversible and important for adhesion, recognition and signal processing. Structurally, they require a multimeric ligand that holds a number of individual binding units together on a common backbone or scaffold material, and a complementary oligomeric receptor with which they interact (Figure 2-1). According to Krishnamurthy *et al.*, multivalency can be roughly divided into categories based on the number of non-covalent receptor-ligand interactions  $i$ . Whereas polyvalency denotes interactions with  $i > 10$ , oligovalency precisely defines a specific number of interactions, usually with  $i \leq 10$ . As the simplest case, bivalency describes  $i = 2$  <sup>7</sup>.

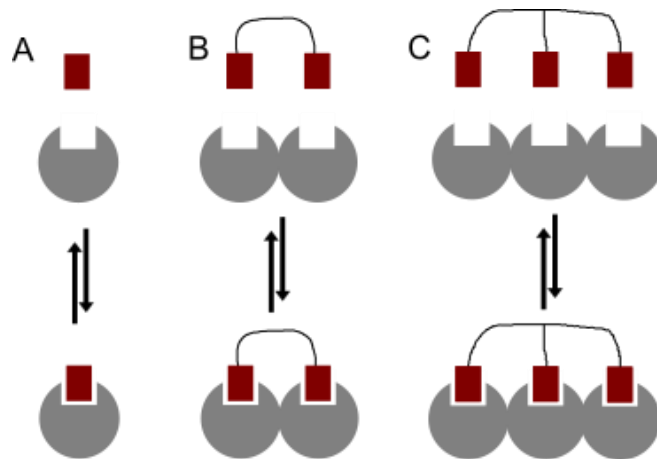


**Figure 2-1. Multivalent interactions.**

**A)** A monovalent ligand (red) binds a monovalent receptor. **B)** An oligovalent (bivalent) ligand with two binding units that are connected via a linker binds two receptors. **C)** An oligovalent (trivalent) ligand binds three receptors.

Multivalent interactions are not only orders of magnitudes stronger but also qualitatively different from monovalent interactions. In general, the strength of monovalent interactions (between a single biomolecule and its binding partner) can be simply described in terms of a binding *affinity*. It is typically reported by the equilibrium dissociation constant  $K_D$ , defined as

the ratio of  $k_d$  (dissociation rate constant for this interaction) /  $k_a$  (association rate constant of a receptor-ligand interaction). In case of more than one linked interaction, i.e. multivalent interactions, the measure of overall strength of those interaction is termed *avidity*. Avidity is dependent on three major parameters: the affinity of one biomolecule to its binding partner, the number of binding units (valency) of both and the structural arrangement of both. The enhancement factor  $\beta$  describes the ratio of avidity to affinity and increases with valency. In case of many biological interactions, multivalency can reduce the dissociation constant of a ligand from the micromolar to the nanomolar range. Thermodynamic principles proposed in the paper by Krishnamurthy *et al.* aim to explain why multivalent systems have enhanced strengths over monovalent arrangements<sup>7</sup>. In an ideal case, the binding enthalpy for multivalent interactions is advantageous and is accompanied by little or no rise in translational or rotational binding entropy. Whereas the enthalpy adds up depending on the valency, entropy remains unchanged, as is explained more deeply in the context of the chelate effect in the last paragraph. Practically, it becomes more complicated, if the geometry of biomolecule and binding partner is not fitting and if the linker engages in interactions with the other binding partner. Another major issue is the thermodynamically disfavored loss in entropy due to constraining the linker into the interaction, effectively eliminating all other possible entropic degrees of freedom.

Prior research<sup>8,9</sup> suggests that the linker for oligovalent ligands should be rigid to keep the loss in conformational entropy to a minimum. In compliance with that, Nangreave *et al.* found that entropic cost of association is lowest, and overall thermal stability is highest when both biomolecule and binding partner are rigid. On the other hand, flexibility led to a more favorable enthalpy of binding. For their study, DNA nanostructures, specifically simple motifs called double-crossover (DX) tiles, were applied as model systems for polyvalent interactions<sup>10</sup>. The backbone material for multivalent presentation of binding units used in this work is also DNA. Using DNA as a backbone material for presenting multivalent interactions allows for adjustments in length, valency and flexibility, in order to optimally address the desired target molecule. Several studies on multivalency achieved through DNA have been reported in the literature<sup>11-18</sup> and have shown, for example, that synthetically produced DNA-based multivalent ligands are able to interfere with biological processes.

Kiessling and Lamanna described several multivalent binding modes<sup>19</sup>. One of them is the “chelate effect,” which implies that the entropic cost for the formation of the first interaction

between a ligand and an oligomeric receptor is sufficient to also establish binding on a second receptor site because the molecules are already close together. This increased binding affinity i.e. avidity was examined in chapters 4 and 5 of the work presented here. Since many transmembrane proteins can move laterally in the cell membrane, multivalent ligands can trigger cell receptor cluster formation. This binding mode is termed receptor clustering and was investigated in chapter 6 of this thesis.

## **2.2 The structure of DNA**

The accepted, central dogma of molecular biology is that the genetic information of all living cells is encoded in their DNA. From there, the information is transferred to ribonucleic acid (RNA) in a process called transcription and subsequently translated into a polypeptide sequence that comprises a protein. In this work, DNA is not used for the genetic information it carries but instead serves as a material for the fabrication of nanometer-sized objects with specific functions.

DNA is a macromolecule composed of repeating units called nucleotides that are made up of a nitrogenous base, a phosphate group and a monosaccharide which connects both. Those nitrogen-containing bases are either purines consisting of two carbon-nitrogen rings (adenine, abbr. as A and guanine, abbr. as G) or pyrimidines consisting of one carbon-nitrogen ring (cytosine, abbr. as C and thymine, abbr. as T). The monosaccharide in DNA is D-2'-deoxyribose. Nucleotides are connected via phosphodiester bonds that covalently link the 5'-carbon of one deoxyribose to the 3'-carbon of an adjacent deoxyribose and thus create directionality. As a result, single-stranded DNA (ssDNA) possesses distinct ends: a 5'-end with phosphate group and a 3'-end with free hydroxyl group (see Figure 2-2).

Base-pairing describes the hybridization of one ssDNA strand to a second, complementary ssDNA strand in an anti-parallel manner by formation of hydrogen bonds between the nitrogenous bases. In the resultant double-stranded DNA (dsDNA), thymine and adenine pair via two hydrogen bonds while cytosine and guanine establish three hydrogen bonds between each other. Consequently, G-C bonds are more stable. The sequence of bases and their hydrogen bonds account for the high specificity of complementary base-pairing.

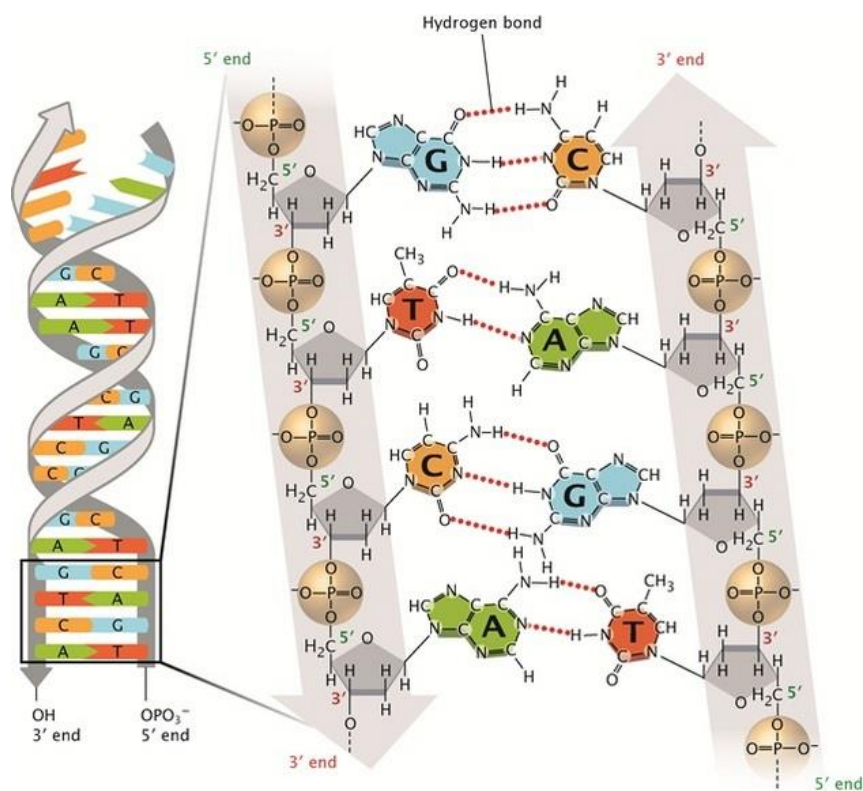


**Figure 2-2. The molecular structure of dsDNA.**

Two complementary ssDNA strands are hybridized via hydrogen bonds (red dotted line): Adenines (A) bind to thymines (T) and cytosines (C) bind to guanines (G). Shown is B-DNA. Image reproduced from Pray <sup>20</sup>.

Because of these hydrogen bonds, hydrophobic interactions and additional van der Waals forces between the stacked bases, the linear dsDNA is very stable <sup>21,22</sup>. Additionally, the stability of dsDNA is dependent on the guanine-cytosine content, the length as well as salt conditions. In 1953, Watson and Crick proposed that dsDNA is structured as a coiled, right-handed helix with bases facing towards the inside of the molecule, and alternating sugar and phosphate groups forming the backbone on the outside <sup>23</sup>. Based on X-ray fibre diffraction studies contributed by Rosalind Franklin and Maurice Wilkins, they describe dsDNA in its most common form under physiological conditions, i.e. in living cells, namely B-DNA. Characteristic for this conformation are  $\sim 10.5$  base pairs per helical turn <sup>24,25</sup>, a distance of  $\sim 0.34$  nm between the base pairs and a helix diameter of  $\sim 2$  nm. Another right-handed but more compact DNA conformation is A-DNA whereas Z-DNA is left-handed <sup>26</sup>.

### 2.3 DNA nanotechnology

In 1982, Ned Seeman proposed the idea of using DNA as basis for constructing nanometer-scaled objects and thereby pioneered in the field of DNA nanotechnology <sup>27</sup>. He solely



considered the feature of DNA to selectively hybridize based on predictable complementary Watson-Crick hydrogen bonding. If one ssDNA strand is partially complementary to more than one other ssDNA strand, a DNA junction occurs that can be designated as immobile Holliday junction. This can be expanded to complex DNA motifs including multi-arm junctions as structural units for the “bottom-up” construction of two-dimensional (2D) and three-dimensional (3D) structures. Since 1982, DNA nanotechnology has grown into a versatile, multi-disciplinary field including developments such as DNA tiles <sup>28–30</sup>, or even more complex 2D lattices <sup>31</sup> and 3D DNA crystals <sup>32</sup>.

While in the beginning the focus was on design, creation and imaging of DNA nanostructures with different shapes <sup>33–35</sup>, nowadays a variety of applications of self-assembled DNA nanostructures is explored. DNA molecules are suitable as functional nanomaterials because of a facile and automated synthesis of nearly every DNA sequence <sup>36</sup> and extremely specific complementary recognition properties expressed by base pairing and biocompatibility <sup>37</sup>. In contrast to proteins, DNA is physiochemically stable and uniform in its chemical and structural properties. To be purposeful, it is often required to modify DNA architectures with functional and/or biologically active groups and as DNA nanostructures allow for highly precise spatial placement of functional molecules at predictable positions, they are an ideal construction material for biotechnical and biomedical applications <sup>38</sup>. Hence, DNA structures have been increasingly exploited, for instant as drug delivery vehicles <sup>39–42</sup>, biosensors <sup>43,44</sup> or to improve enzymatic cascades <sup>45–47</sup>.

### 2.3.1 DNA origami

In 2006, Paul Rothemund described DNA origami as a technique for folding long, circular ssDNA strands, named scaffold strands, with the help of hundreds of small, synthetic, individual so-called staple strands into discrete and defined 2D objects <sup>48</sup> (Figure 2-3).

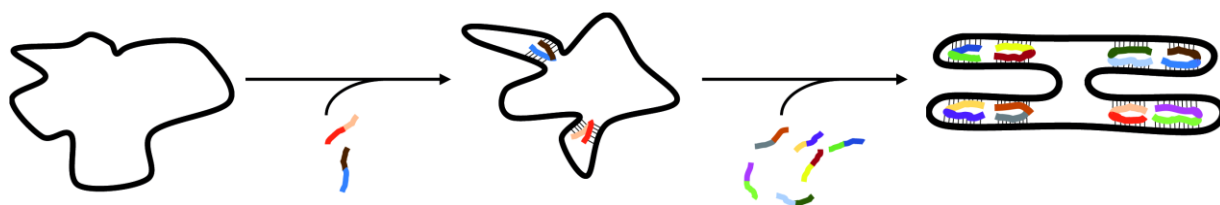


**Figure 2-3. Simplified, schematic depiction of DNA origami structure assembly.**

Parts of staple strands (multi-colored) are complementary to parts of the scaffold strand (black). In a temperature-dependent process, staple strands hybridize to the scaffold strand and fold into a DNA origami.

This temperature-based self-assembly process is feasible, since every staple strand has complementary parts to unique sections of the scaffold. After hybridization, each oligonucleotide is thus located at a precisely definable position in the folded structure. Neighboring double stranded segments are interconnected by piecewise complementary staple strands that cross from one helix to another.

DNA is highly negatively charged in aqueous milieus because of its ionized phosphate groups in the backbone. To avoid instability due to repelling forces of those phosphate groups, DNA structures are stabilized by positively charged divalent magnesium ions or monovalent sodium ions<sup>49</sup>. Because of their closely packed helices, DNA origami structures are more stable against enzymatic digestion as plasmids<sup>50</sup> and tolerate long-term storage<sup>51,52</sup>. Originally, Rothemund used a scaffold that was isolated from the bacteriophage M13mp18 with a known genome sequence of 7249 nucleotides and mixed it with approx. 200 staple strands to create flat 2D DNA origami structures. In 2009, Douglas *et al.* created extended versions scaffolds consisting of e.g. 7560 or 8634 nucleotides. In combination with the arrangement of helices in a honeycomb lattice, the synthesis of larger 3D structures with increased rigidity and complexity was feasible<sup>53</sup>. Furthermore, with the aid of the program caDNAo which was also developed by Douglas *et al.*, the design of new DNA origami structures was extremely ameliorated<sup>54</sup>. Dependent on the sequence of the scaffold, it calculates sequences for matching staple strands that allow for nanofabrication of desired DNA origami shapes. Methods like agarose gel electrophoresis, atomic force microscopy (AFM) or transmission electron microscopy (TEM) can be used to examine correct formation of DNA origami structures. Nowadays, even DNA origami structures with scaffolds consisting of 51,466 nucleotides can be produced<sup>55</sup>.

In contrast to previously known strategies to assemble large DNA structures, like DNA tiles, the DNA origami technique features beneficial characteristics: it does not require precise control of stoichiometry, is not restricted to repetitive building units and simple geometric shapes, it leads to the production of finite structures, is fast and delivers high yields<sup>56</sup>.

In this work, helices were packed on a honeycomb lattice to form two-layered block like DNA origami structures (hereafter named DOhex). As a consequence, each helix has crossovers to three adjacent helices every 7 base pairs. In general, multi-layered DNA origami structures are much more rigid than single-layered DNA origami structures. By introduction of linkers on the

ends of individual oligonucleotides, several oligonucleotides were functionalized and later incorporated at individual, unique points on the surface of the DOhex. By this, DOhex structures were engaged as molecular pegboard to place epitopes onto defined locations.

### 2.3.2 Small DNA structures

Significantly smaller and simpler than DNA origami structures, DNA junctions are composed of only a few strands (Figure 2-4). They are variable in size and symmetry, and thus can be attuned to the symmetry of their target structures. In contrast to long, linear dsDNA molecules of several hundred base-pairs, which are rather flexible over the entirety of their contour length, these small structures are assumed to have a flexible junction and typically more rigid and straight arms. This follows from the fact that the persistence length of dsDNA, qualitatively the length over which two points on its contour are not mechanically correlated by its inherent stiffness, is approx. 50 nm<sup>57</sup>. Hence, dsDNA molecules significantly below 50 nm, or 150 base-pairs, are considered rigid polymers and thus appropriate to be employed as well-defined spacers between functional molecules.

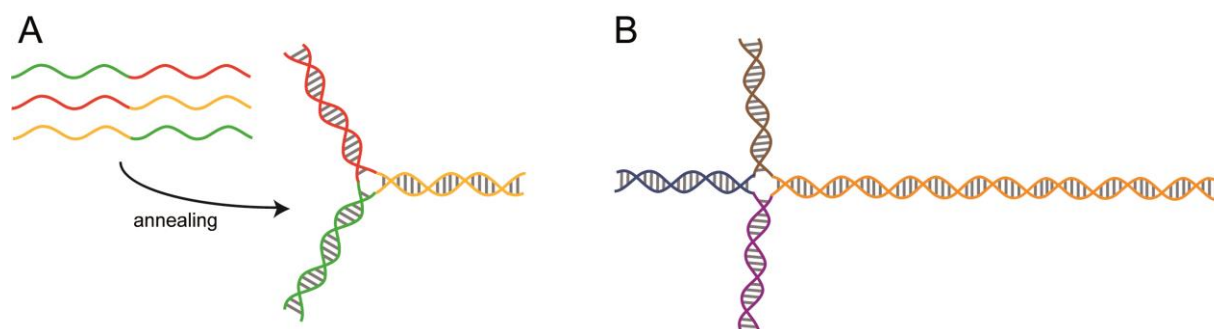


**Figure 2-4. Schematic DNA trimer and DNA 4arm structure.**

**A)** Temperature-dependent assembly of three partially complementary strands (indicated by same color) leads to the formation of a DNA trimer. **B)** DNA 4arm structure consisting of four partially complementary strands.

The DNA trimer used in this work, is one such junction that consists of three partially complementary strands which are each 30 nucleotides long. Since each strand has complementary parts to two other strands, a three-arm junction with 15 base-pair, or 5 nm long arms can be formed in a temperature-dependent process (Figure 2-4A). The ends of the arms on the DNA trimer are approximately 9 nm apart when the structure is in its electrostatically favored outstretched conformation. Trimeric DNA constructs similar in length and building were used by Sil *et al.* to cross-link immunoglobulin E (IgE)–FcεRI complexes<sup>18</sup>.

In addition, a 4-arm junction, made of four partially complementary strands was also used in some experiments presented in this work. One of the arms was designed to function as anchor to some kind of surface (orange colored arm in Figure 2-4B) while the other three arms were designed to display ligands. It adopts a tetrahedral configuration with the ligand-bearing arms approx. 8.3 nm apart.

### 2.3.3 Functionalization of DNA nanostructures with peptides

Peptides are polymers made of amino acids connected via amide bonds. In contrast to proteins, peptides are smaller ( $\leq 50$  amino acids) and lack much of their tertiary and quaternary structure. Depending on the composition of amino acid side chains, peptides have different physiochemical characteristics. They can be, for example, aliphatic/aromatic/heterocyclic, non-polar/polar or non-charged/charged (negatively or positively). Peptides interact with their targets in a non-covalent manner, e.g. via a combination of Van der Waals forces, hydrogen bonds, electrostatic interactions or hydrophobic effects. Almost all naturally occurring peptides consist of L-amino acids. Peptide synthesis strategies enable the production of not only naturally occurring peptides, but allow for synthesis of new peptides that can contain e.g. D-amino acids or non-proteinogenic amino acids such as non-natural amino acids.

Synthetic peptides are increasingly studied for their application, e.g. as bioactive compounds (e.g. antimicrobials), peptide vaccines<sup>58</sup>, in viral laboratory diagnosis<sup>59</sup> or as shuttles for therapeutic molecules<sup>60</sup> because of their small size, good biocompatibility, easy synthesis and modification, and adaptability to bind specific targets<sup>61</sup>. Techniques for the discovery and development of new peptides include e.g. phage display, screening with peptide arrays, reduction of natural ligands to identify key amino acids or *in silico* design with the help of bioinformatical tools. Phage display was developed by Smith *et al.*<sup>62</sup>. The technique involves screening of massive (approx.  $10^{10}$ – $10^{11}$  antibody variants in a library<sup>63</sup>) libraries of bacteriophages, upon which novel peptides are displayed<sup>64,65</sup>. Methods like alanine scans, where all amino acids are stepwise replaced by alanines to determine amino acids that are important for binding, help to refine the initially obtained sequence to eventually create an amino acids sequence that interacts best with the desired target. Small peptides can be easily positioned onto different kinds of carriers and nanoparticles. Whereas rather high amounts of peptide are necessary to reach biologically relevant effects, the connection of peptides via some scaffold material, which integrates them into a multivalent ligand, could potentiate the efficacy of those

peptides. To achieve this, DNA is an ideal scaffold material to precisely position and combine small molecules like synthetic peptides. Due to this, properties such as ligand density (including valency and spacing) and 3D orientation can be controlled. Chemical peptide synthesis allows for attachment of diverse modifications (e.g. fluorophores, signal sequences, etc.) or replacement of amino acids by non-natural amino acids. Addition of functional groups can be accompanied by the introduction of spacers between peptides and their scaffold molecules which can be helpful to decrease steric hinderance.

One class of short synthetic peptides are mimotopes, which are used to mimic natural antigenic sites on proteins. In comparison to the natural antigen targets, mimotopes are often advantageous as they are much smaller (usually 10 – 20 amino acids) than proteins and can be produced by automated synthesis reactions. Mimotopes will be addressed in chapter 4.

## 2.4 Characterization of therapeutic antibodies

Antibodies are proteins that take part of the humoral immune response by recognizing antigens on the surface of pathogens like viruses or bacteria. There are five different classes of antibodies: IgG, IgD, IgE, IgA, IgM.

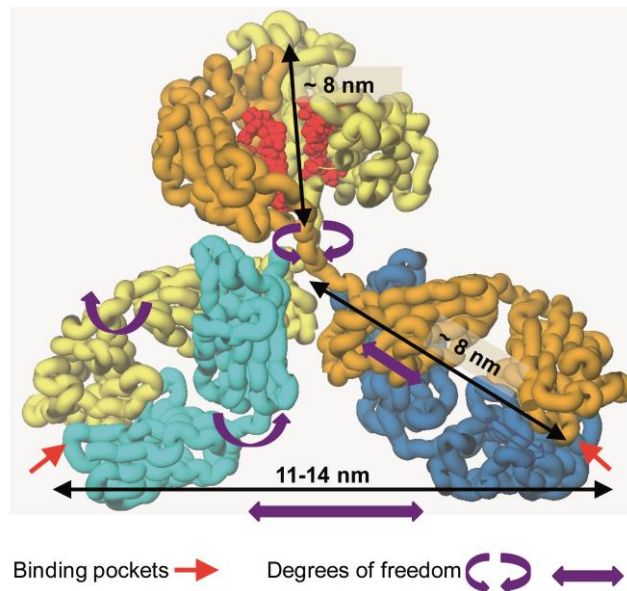


**Figure 2-5. 3D IgG antibody structure.**

Tube model of protein backbone indicates dimensions of IgG. Heavy chains are shown in yellow/orange, light chains are in blue. Red dots in Fc region represent glycosylation sites. Image was created and kindly provided by Dr. Michael Szardenings (Fraunhofer Institute for Cell Therapy and Immunology IZI, Germany).

The first class mentioned, IgG, is the most common in human serum and often used for antibody-based therapies (Figure 2-5). This type of antibody contains two antigen-binding fragments (Fab) that consist of one variable (consisting of V<sub>H</sub> and V<sub>L</sub>) and one constant (consisting of C<sub>H</sub> and C<sub>L</sub>) region. The variable region harbors the paratope, which binds to the target antigen's epitope via complementarity determining regions (CDRs). In addition, IgGs contain one constant fragment crystallizable region (Fc region) that is composed of two heavy chains that form the stem of the antibody. Located between Fab and Fc fragments is a flexible linker, the so-called hinge region. IgGs can be distinguished into the 4 subclasses IgG1, IgG2, IgG3 and IgG4. Even though their global structures are similar, their hinge regions differ significantly in length and flexibility. This influences the arrangement of the Fab arms to the Fc region and thus the functionality<sup>66</sup>.

Monoclonal antibodies (mAbs) that only target a single, defined epitope have been produced since the 1970s and by now, more than 60 therapeutic monoclonal antibodies have been approved in the US or Europe<sup>3,67</sup>. Most of the approved therapeutic mAbs are chimeric, humanized, or human IgGs. Before being permitted, the antibody's binding to its antigen as well as its stability, pharmacodynamics and pharmacokinetics need to be elucidated and tested<sup>68</sup>. Priorities of antibody engineering and production include the generation of constructs with high specificity and affinity, with the additional requirement of low immunogenicity being crucial in the case of therapeutic approaches. Methods to minimize immunogenicity have evolved from cloning antibody genes to chimeric antibodies (murine variable domains fused with human constant domains generating ~70% human antibodies)<sup>69</sup> up to humanized antibodies (85–90% human)<sup>70</sup>. However, during production (including humanization) and storage of mAbs, changes in glycosylation pattern as well as chemical instabilities like oxidation, hydrolysis or deamidation can occur<sup>71</sup>. This could influence flexibility and spatial arrangement of the antibody and possibly lead to altered immunogenicity<sup>72</sup> and/or binding affinities, and thus reduced or undesired biological activity<sup>73</sup>. The monoclonal antibodies binding  $\alpha$ -synuclein, c-Myc and actin used as test cases for bivalent binding are introduced in the following subsections.

### **2.4.1 $\alpha$ -Synuclein antibodies**

The protein  $\alpha$ -synuclein is associated with several neurodegenerative diseases, for instance Parkinson's disease and dementia with Lewy bodies. In these so-called  $\alpha$ -synucleinopathies,  $\alpha$ -synuclein is present in accumulated, insoluble oligomers or fibrils that cause cell death.

Currently available antibodies for diagnosis detect both pathological aggregates and  $\alpha$ -synuclein's monomeric physiological. This circumstance complicates immunostaining and the development of *in vivo* biomarkers <sup>74</sup>. Kovacs *et al.* reported the generation of two new antibodies 5G4 and 10D2 against  $\alpha$ -synuclein <sup>75</sup>. Both do not react with  $\beta$ - or  $\gamma$ -synuclein. Interestingly, antibody 5G4 reacted with disease-related aggregations of  $\alpha$ -synuclein much more than to the monomeric  $\alpha$ -synuclein. In contrast, 10D2 binds to the linear peptide sequence and aggregated  $\alpha$ -synuclein. Antibody 5G4 was generated by immunization of mice with peptide TKEGVVHGVATVAE that corresponds to amino acid 44–57 of  $\alpha$ -synuclein. Here, a peptide termed ED10 that consisted of a similar sequence was used as antigen for 5G4. As antigen for 10D2, the peptide sequence ED9 was derived from amino acids 118–127 of  $\alpha$ -synuclein.

#### **2.4.2 Anti-Human c-Myc antibody**

The cellular gene *c-myc* plays a crucial role in cell growth and differentiation and as irregular expression of *c-myc* is linked to neoplasms, it is considered a proto-oncogene <sup>76</sup>. It encodes e.g. the oncoprotein c-Myc (p62<sup>c-myc</sup>) which is localized in the nucleus and possesses similarities to transcription factors due to its affinity towards DNA <sup>77,78</sup>. From the sequence of *c-myc*, two peptide sequences (peptide D and G) were derived and used to raise and isolate monoclonal antibodies specific for the products of *c-myc* <sup>79</sup>. Peptide G-specific mAb Mycl-9E10 turned out to be the most sensitive antibody for immunoblotted human c-Myc.

#### **2.4.3 Anti-Actin antibody**

The protein actin is a major component of the cytoskeleton in all eukaryotic cells. It exists in three different isoforms and can be present in monomeric (G actin) and filamentous (F actin) form. Lessard *et al.* described two monoclonal antibodies which bind to epitopes located in the N-terminal two thirds of actin molecules (close to residue 50-70) <sup>80</sup>. One of the antibodies, named C4, bound broadly to many actin isoforms:  $\alpha$  (skeletal, cardiac, smooth muscle),  $\beta$  (non-muscle) and  $\gamma$  (smooth muscle and non-muscle).

### **2.5 Pathogen interactions with host cells**

Pathogens adhere to the membranes of host cells in order to escape the body's cleansing mechanisms. As a next step, most pathogens invade these host cells for growth and replication.

They use cell surface glycans or receptors, such as integrin<sup>81</sup>, for this purpose. The surfaces of all types of cells in nature are decorated with a dense array of sugars, which, in combination with glycoproteins and glycolipids, form the so-called glycocalyx. Binding of pathogens to glycans is mediated via lectins which can be categorized into hemagglutinins (mainly present on viruses) and adhesions (mainly on bacteria surfaces)<sup>82</sup>.

Glycans consist of monosaccharide subunits and can be linear or branched. Classes of glycans include e.g. glycosphingolipids, glycosaminoglycans or glycopospholipid anchors<sup>83</sup>. The scaffold of cell surface glycans commonly consist of glucose, galactose or their N-acetylated forms. Fucose and sialic acids build head groups to the terminal positions of glycans. Sialic acids are negatively charged sugars with nine-carbon backbones. Due to their position, they are easily accessible for viral pathogens and thus often the first contact. Sialic acids are widespread in animal tissues but distribution and type of sialic acids as well as linkage to the glycan structure are specific for host tissues and species. As an example, in human airways sialic acid is connected to other sugars in a  $\alpha$ -2,6 glycosidic manner, whereas in human eyes,  $\alpha$ -2,3 glycosidic bonds are formed<sup>84</sup>.

Influenza hemagglutinin (HA) and respiratory syncytial virus (RSV)-F proteins are categorized as class I viral fusion proteins because of their appearance as transmembrane homotrimers that are present as a single-chain precursor (Figure 2-6). Later, the single chain is cleaved into three sets of two domains. Due to this proteolytic processing, the viral proteins become fusogenic.

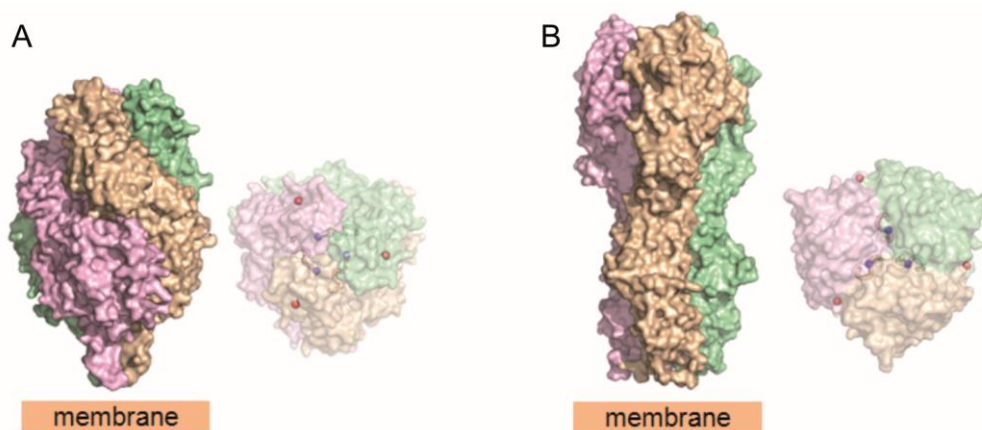


**Figure 2-6. Type I prefusion viral glycoproteins.**

Each protomer is colored differently. **A**) RSV-F protein side view (left) and top view (right). Red sphere indicates the C-terminal residue of F2, blue dots show the N-terminal residue of the fusion peptide. **B**) HA side view (left) and top view (right). Red sphere indicates the C-terminal residue of HA1, blue dots show the N-terminal residue of the fusion peptide. Image reproduced with permission from<sup>85</sup>.



Fusion of viral and host lipid bilayer is thermodynamically favored but has high kinetic barriers. To overcome these kinetic barriers, viral fusion proteins remain in a high energy, prefusion form prior to interacting with host membranes and, upon a certain trigger, undergo a conformational change into a low energy, postfusion form. The free energy obtained by this process is used to bring the membranes together<sup>86</sup>. In other words, viral proteins function as catalysts as they lower the kinetic barriers and enable fusion to host cells.

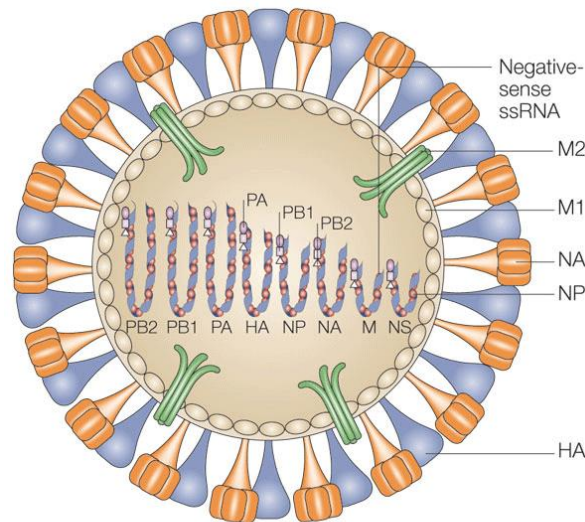
Although most bacteria live extracellularly, some bacteria, like enteroinvasive or uropathogenic *E. coli*<sup>87</sup> are able to invade human cells as they cannot multiply as efficiently outside a eukaryotic cell. Furthermore, some bacteria can secrete microbial virulence factors called toxins which help to infect hosts by harming host tissue and disarming the hosts immune system<sup>88</sup>. To give an example, enterohemorrhagic *E. coli* can produce Shiga toxins. These toxins bind to the host cell surface and are endocytosed. As a result, diseases like bloody diarrhea, hemolytic uremic syndrome and neurological abnormalities can arise.

### **2.5.1 Influenza A viruses**

Influenza A viruses (IAVs) are enveloped, mostly spherical viruses with a diameter of ~100 nm that belong to the family of *Orthomyxoviridae*. Along with influenza B viruses, they cause epidemics of respiratory infections almost every year. The genome of influenza A is a segmented, negative sense, single-stranded RNA which encodes 11 viral proteins. Among these, hemagglutinin (HA), neuraminidase (NA) and matrix 2 (M2) protein are transmembrane proteins that are located in the viral lipid bilayer referred to as envelope<sup>89</sup> (Figure 2-7). IAVs are classified into subtypes based on the combination of HA and NA proteins on the viral surface and to date, 18 HA subtypes (H1, H2...) and 11 NA subtypes (N1, N2...) are known<sup>90</sup>. As an example, A(H1N1) and A(H3N2) are the subtypes that currently co-circulate among humans worldwide.

Characteristic for influenza viruses is their ability to heavily mutate and recombine which causes the continuous emergence of new virus strains. Antigenic drift and antigenic shift are the two processes that drive these antigenic changes in order to escape host antibodies. The first one mentioned occurs due to point mutations in the viral HA and NA proteins and happens gradually and continuously as an adaptation to the host immune response. Antigen shift happens more abruptly and involves major genetic reassortments that ultimately lead to the formation of new

virus variants. Because of such antigenic variations, vaccinations against influenza A need to be adjusted and updated each year. Furthermore, these variations make it difficult to develop therapeutic antibodies which are important for the diagnosis of influenza A.



Copyright © 2005 Nature Publishing Group  
Nature Reviews | Microbiology

**Figure 2-7. Schematic diagram of an influenza A virus virion.**

HA = Hemagglutinin NA = Neuraminidase, NP = nucleoprotein, PA, PB1 and PB2 = polymerase proteins. Image reproduced with permission from <sup>91</sup>.

The trimeric transmembrane protein HA is mainly responsible for binding to the host receptor and for fusion of viral and host membrane. This  $\alpha$ -helical spike protein is a lectin that attaches to sialic acids residues on the surface of epithelial cells in the respiratory tract, establishes a stable adhesion and thus enable the virus to reach the inside of host cells via endocytosis. Whereas HAs from avian IAVs prefer receptors with  $\alpha$ -2,3-linked sialic acids, human IAVs are more specific for  $\alpha$ -2,6-linked sialic acids. Once influenza A is inside the endosome, the viral envelope fuses with the endosomal membrane and thereby the viral genome reaches the cytoplasm. HA is densely packed on the viral surface (according to estimations, one virion displays 340-400 HA trimers <sup>92</sup>) and can be categorized as class I fusion protein because it is present as a homotrimer in both prefusion and postfusion state and requires proteolytic cleavage to facilitate fusion. HA is synthesized as precursor HA0 that associates noncovalently as homotrimer and becomes infectious upon post-translationally cleavage by host proteases. It consists of a membrane-distal, globular head HA1 unit and a membrane-proximal stem HA2 unit which are connected through a disulfide bridge. The HA1 unit harbors the receptor binding site and mutates more frequently <sup>93</sup>. Once HA1 bound to sialic acids on host cells, the whole

virus is endocytosed by the host cell. An acidic pH of ~5-6 in the endosome causes the HA to undergo a conformational change. Due to this rearrangement, the hydrophobic N-terminus of HA2, the so-called fusion peptide, is no longer hidden in a hydrophobic pocket, becomes exposed and is inserted into the endosomal membrane<sup>94</sup>.

Another consequence of the low endosomal pH is the activation and opening of the M2 ion channel which acidifies the viral core and liberates the packed viral ribonucleoproteins from matrix 1 proteins underneath the envelope. The ensuing complex fusion process results in the release of the viral genome, the viral RNA-dependent RNA polymerase and viral ribonucleoproteins into the cytoplasm. Viral ribonucleoproteins contain nuclear localization signals that help to enter the host cells' nucleus where viral replication takes place. Newly synthesized viral RNA leaves the nucleus and part of it is translated by the hosts' ribosomes into the viral proteins HA, NA and M2. Viral RNA and proteins assemble at the cell surface into new virions. After budding, viral NA cleaves the new virions from the host cell.

### 2.5.2 Respiratory syncytial viruses

Respiratory syncytial virus (RSV) is a member of the *Pneumoviridae* family. It is an enveloped virus with non-segmented, negative-sense ssRNA genome and spherical (~150 nm in diameter) or filamentous (~several microns in length) shape (Figure 2-8).

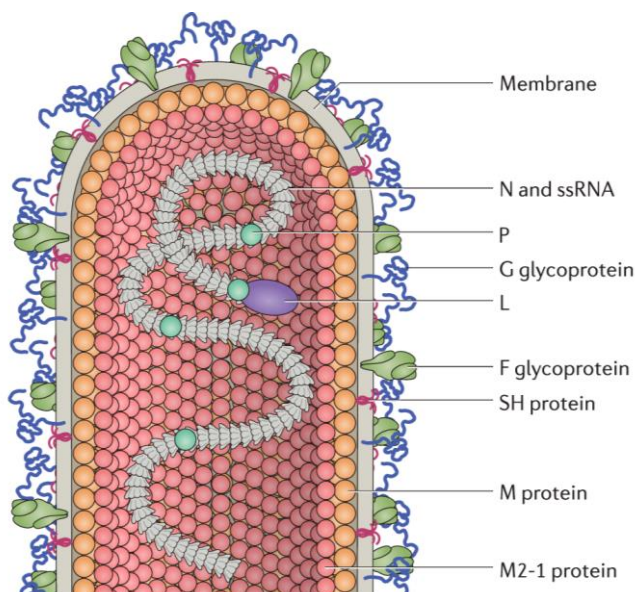


**Figure 2-8. Schematic diagram of the filamentous morphology of a RSV virion.**

G = attachment glycoprotein, F = fusion glycoprotein, SH = small hydrophobic protein, M = matrix protein, N = nucleoprotein, L = large polymerase subunit, P = phosphoprotein polymerase cofactor. Image reproduced with permission from<sup>95</sup>.

Ten genes encode for 11 proteins. Among those proteins are two non-structural (NS1 and NS2), eight structural (L, G, F, N, P, M, M2-1, SH) and one protein (M2-2) which is not yet defined. Besides the small hydrophobic protein SH, the major spike surface proteins located within the envelope are RSV-G and RSV-F that accomplish attachment to and fusion with host cells, respectively. Depending on the antigen structure of RSV-G, RS viruses can be categorized into the two subtypes RSV type A and RSV type B, whereby RSV type A is more prevalent and causes more severe diseases than RSV type B <sup>96</sup>. Diseases associated with RSV comprise lower and upper respiratory tract infections.

Most of the vaccines and immunotherapies that are currently under development target RSV-F because it is more conserved and less glycosylated than RSV-G. Furthermore, RSV-F carries the dominant neutralization epitopes. It is synthesized as inactive F0 precursor that assembles into a homotrimer. After proteolytic cleavage by furin-like protease, two disulfide-linked polypeptides, F1 and F2, are formed. In this resulting prefusion state, RSV-F exists as a “spring-loaded” trimer which is metastable. Similar to IAVs, the RSV-F fusion peptide at the hydrophobic N-terminus of F1 is hidden in the central cavity of the homotrimer. For fusion, parts of prefusion RSV-F refold, to form a so-called pre-hairpin intermediate, and the fusion peptide is inserted into a target membrane <sup>97</sup>. During the subsequent fusion process, RSV-F transforms into a highly stable postfusion conformation that displays a different antigenic topology. While for example antigenic site II and IV are found on both pre- and postfusion conformation, antigenic site Ø is only present at the apex of the prefusion RSV-F trimer <sup>98</sup>.

RSV binds to heparan sulfate proteoglycans as well as to receptors like Toll-like receptor 4, CX3C chemokine receptor 1 or nucleolin on cell surfaces <sup>99</sup>. More precisely, it infects ciliated epithelial cells of the airways.

### **2.5.3 *Escherichia coli***

Humans are colonized by different types of microbes such as fungi, viruses and bacteria which make up the so-called human microbiome. The occurrence of bacteria is mostly nonpathogenic and happens for instance in the human gut which has a commensal or/and symbiotic relationship with bacteria colonies made of up to 100 trillion microbes <sup>100</sup>. One of the many species in the human gut are bacteria belonging to the family of *Enterobacteriaceae*, with the most prominent representative being *E. coli*. *E. coli* are gram-negative, rod-shaped bacteria with lengths of

~2  $\mu\text{m}$ . Whereas the majority of *E. coli* in the human gastrointestinal microbiota are harmless, some have been associated to human diseases like gastroenteritis or Crohn's disease. Outside the gut, *E. coli* can evoke urinary tract infections, meningitis or sepsis<sup>101</sup>. Upon adhesion, bacteria reproduce and form a consortium that is termed biofilm. It enables stable adherence, chemical communication, coordination (quorum sensing) and additionally interlinks bacteria of various species<sup>102</sup>.

The surface of *E. coli* is equipped with many filamentous protein appendices which are 1–2  $\mu\text{m}$  long and ~7 nm wide protein structures called pili or fimbriae<sup>103</sup> (Figure 2-9).

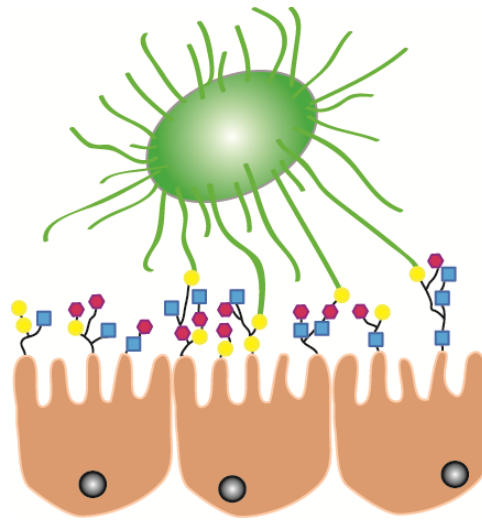


**Figure 2-9. *E. coli* adherence to epithelial cells.**

*E. coli* (green) adhere via their fimbriae to sugar chains (blue, yellow, pink) on epithelial cells (beige).

One group of representatives are type 1 fimbriae which identify ligands that contain mannose. They are widespread among enterobacteria and it is assumed that between 100 and 400 type 1 fimbriae are expressed on the surface of *E. coli*<sup>104</sup>. Those fimbriae carry lectins that mediate adhesion to host cells via carbohydrate-recognition domains. As an example, FimH, located at the lateral shaft and at the lateral ends of the fimbriae, is a lectin that targets mannose on cells such as epithelial cells in the gut, bladder or lung<sup>105,106</sup>. Its specificity and high affinity for mannose was confirmed in several studies<sup>107</sup>. Crystal structures of FimH in complex with mannose revealed that mannose is bound by a small but deep, negatively charged pocket of FimH via hydrogen bonds<sup>108</sup>.

### 2.6 Binding and activation of EphA2 receptors

Eph receptors are receptor tyrosine kinases (RTKs) that are activated by Eph family receptor interacting protein (ephrin) ligands. The Eph family receptors can be divided into two subclasses: EphA and EphB whereas the first is mainly bound by ephrin-A ligands and the second by ephrin-B ligands<sup>109,110</sup>. Since both receptor and ligand are located on the extracellular side of the cell membrane, the contact of two adjacent cells is necessary for interaction and activation<sup>111</sup>. A special feature of Eph-ephrin signaling is bidirectional signal transduction in both Eph- (“forward” signaling) and ephrin-presenting cells (“reverse” signaling). Ephrin pathways are important for angiogenesis, adult tissue homeostasis, embryogenesis, and other developmental processes. However, they are additionally key players in many pathological conditions; for example, the EphA2 receptor is widely upregulated in many cancer types (breast<sup>112</sup>, prostate<sup>113</sup>, ovarian<sup>114</sup>, lung<sup>115</sup>). EphA2 overexpression is linked to poor clinical outcome and malignant progression, but those properties are most likely independent of the ligand binding to the receptor, and instead result from crosstalk between EphA2 and Akt<sup>116,117</sup>. Interestingly, erythropoietin-producing hepatocellular carcinoma receptors (Eph receptors) can also act as tumor suppressors when activated by ephrin or ephrin-like ligands. Downstream signaling correlates with inhibition of cell proliferation, migration, invasiveness and adhesion, which are regulated via RAS-ERK<sup>118</sup>, Akt-mTORC1<sup>119</sup> and several integrin-dependent pathways<sup>120</sup>.

#### 2.6.1 Peptide SWL

The agonistic ephrin-mimicking peptide SWL was previously discovered by phage display and was shown to specifically bind EphA2 receptors on their ligand-binding domain (LBD), thereby activating downstream signaling pathways<sup>121,122</sup>. By presenting two covalently conjugated SWL peptides as dimer, the binding to EphA2 receptors could be enhanced more than 10-fold<sup>123</sup>. However, this was accompanied with the disadvantage of a decreased half-life compared to the SWL monomer, hindering thorough assessment of cooperative binding in cellular systems. In contrast to the natural ephrin ligands, which are considered to be promiscuous due to their propensity to bind and stimulate multiple Eph receptors<sup>124</sup>, SWL’s complete specificity to EphA2 eliminates the possibility of downstream interference reported to occur as a result of simultaneously triggering competing pathways<sup>125,126</sup>.

### 3 Materials and methods

All solutions were prepared using double-distilled water (ddH<sub>2</sub>O). Samples and reagents for experiments that contained viruses or cells were prepared using sterile-filtered or autoclaved solutions and filter tips. All experiments, except for microscale thermophoresis (MST) measurements, were conducted in biosafety level 2 laboratories.

#### 3.1 Equipment and consumables

5424R Microcentrifuge	Eppendorf, Germany
96 well microplate, U-bottom, clear	Greiner Bio One, Austria
96 well microplate, V-bottom, clear	Greiner Bio One, Austria
AFM cantilever BL-AC40TS	Olympus, Germany
Amicon®-Ultra-0.5 ml centrifugal filters 10K, 30K 100K molecular weight cut-off (MWCO)	EMD Millipore, Germany
AnchorChip™ (800 µm)	Bruker Daltonik, Germany
Atomic force microscope NanoWizard 3.0	JPK Instruments, Germany
Cell culture 12-well multiwell plate	Greiner Bio One, Austria
Cell culture 96-well microplate U-bottom or F- bottom	Greiner Bio One, Austria
Clear F-Bottom Immuno Nonsterile Maxisorp 96- well plates	Fisher Scientific, Germany
Cryo vial, 1.8 ml	Sarstedt, Germany
Customized magnetic plate	Fraunhofer Institute for Manufacturing Engineering and Automation IPA, Germany
DNA LoBind reaction tube (1.5 ml, 2 ml)	Eppendorf, Germany
Filter cap cell culture flask (Tissue culture treated)	Greiner Bio One, Austria
Gel documentation system Jet Imager	Intas, Germany

Incubator Heracell 240	Thermo Fisher Scientific, USA
iQue Screener, Gen 2	IntelliCyt, USA
Kimtech Science™ Precision Wipes™	Fisher Scientific, Germany
Leica DM IL microscope	Leica Microsystems, Germany
LUNA™ Automated Cell Counter	Logos Biosystems, Korea
Matrix-assisted laser desorption/ionization – time-of-flight (MALDI-TOF) MS autoflex™ speed LRF System	Bruker Daltonik, Germany
Mica “V1”, 12 mm round	Plano, Germany
Microplate reader infinite M1000	Tecan, Switzerland
Mini-PROTEAN® Tetra cell system	Bio-Rad, Germany
Monolith NT.115	Nanotemper Technologies, Germany
Monolith NT.115 capillaries	Nanotemper Technologies, Germany
NanoDrop ND-1000 ultraviolet (UV)/Vis spectrophotometer	PEQLAB Biotechnologie, Germany
Nunc™ Microplate Lids	Fisher Scientific, Germany
Parafilm® M	Sigma-Aldrich, Germany
PerfectBlue™ Horizontal Minigelsystems	PEQLAB Biotechnologie, Germany
pH Meter Lab 870	SI Analytics, Germany
Pipette tips (w/ and w/o filter)	Greiner Bio One, Austria
Plate centrifuge Multifuge 3SR	Heraeus Holding, Germany
PowerPac™ Basic Power Supply	Bio-Rad, Germany
Rotilabo®- syringe filters CME 0.22 µm	Carl Roth, Germany
Sapphire PCR tube (0.2 ml)	Greiner Bio One, Austria
TProfessional Thermocycler	Biometra, Germany
Tube, sterile (15 ml, 50 ml)	Greiner Bio One, Austria



Vortex-Genie 2	Scientific industries, USA
XP6U Ultra Micro Balance	Mettler Toledo, USA

### 3.2 Software

Besides standard software such as Microsoft Excel or Word, the following programs were used (Table 3-1).

**Table 3-1. Specific software used**

Name	Purpose	Source
Adobe Illustrator® CS4	Schematic illustrations	Adobe Systems, USA
caDNAno	DNA origami design	<a href="https://cadnano.org/">https://cadnano.org/</a>
ChemSketch	Structural chemical formulas	<a href="http://www.acdlabs.com/resources/freeware/chemsketch/">www.acdlabs.com/resources/freeware/chemsketch/</a>
GraphPad Prism 6	Graphic representation, statistical analysis	GraphPad Software, USA
Gwyddion 2.4 software	AFM image height analysis	<a href="http://gwyddion.net/">http://gwyddion.net/</a>
IC50 Calculator	Calculation of IC50 values for RSV infection assay	<a href="https://www.aatbio.com/tools/ic50-calculator">https://www.aatbio.com/tools/ic50-calculator</a>
JPK SPM and DP software	AFM imaging and processing	JPK Instruments, Germany
OligoAnalyzer Tool	Design of DNA nanostructures	<a href="https://eu.idtdna.com/pages/tools/oligoanalyzer">https://eu.idtdna.com/pages/tools/oligoanalyzer</a>

### 3.3 Chemicals

Unless otherwise stated in the following list, chemicals including salts, buffer reagents etc. were purchased from Carl Roth GmbH (Germany), Sigma-Aldrich (Germany) or VWR (USA).

3,3',5,5'-Tetramethylbenzidine (TMB) substrate	Biozol, Germany
--	-----------------

### 3 Materials and methods

---

Agarose Standard	Carl Roth, Germany
Ammonium persulfate (APS)	Carl Roth, Germany
Aprotinin	Carl Roth, Germany
Bovine serum albumin (BSA) Fraction V	Sigma-Aldrich, Germany
Dibenzylcyclooctyne (DBCO)- polyethylene glycol (PEG)4-NHS ester	Jena Bioscience, Germany
DBCO- <i>N</i> -hydroxysuccinimide ester (NHS ester)	Jena Bioscience, Germany
DBCO-Sulfo-NHS ester	Jena Bioscience, Germany
Dimethyl sulfoxide (DMSO)	Sigma-Aldrich, Germany
DNA Gel Loading Dye (6x)	Thermo Fisher Scientific, USA
EFNA1 (EphrinA1) Recombinant Human Protein	Thermo Fisher Scientific, USA
Erythrosin B Stain	BioCat, Germany
Ethanol, absolute	VWR, USA
Ethidium bromide solution	Carl Roth, Germany
GeneRuler™ 1 kb DNA Ladder	Thermo Fisher Scientific, USA
GeneRuler™ Low Range DNA Ladder	Thermo Fisher Scientific, USA
HyClone™ FBS (fetal bovine serum)	Thermo Fisher Scientific, USA
Leupeptin	Carl Roth, Germany
<i>N,N,N',N'</i> - Tetramethylethylenediamine (TEMED)	Carl Roth, Germany
NeutrAvidin™	Thermo Fisher Scientific, USA
Nonidet® P40 (Substitute) (NP-40)	Applichem, Germany
Poly-L-ornithine (0.01%)	Sigma-Aldrich, Germany
Rotiphorese® Gel 40 (29:1): 40% acrylamide/ bisacrylamide	Carl Roth, Germany
Sodium azide	Sigma-Aldrich, Germany
Sodium orthovanadate	Sigma-Aldrich, Germany

---

SYBR™ Gold nucleic acid gel stain	Life Technologies, USA
Trypsin- ethylenediaminetetraacetic acid (EDTA) (0.05%), phenol red	Thermo Fisher Scientific, USA
Trypsin, tosyl phenylalanyl chloromethyl ketone (TPCK) treated	Thermo Fisher Scientific, USA

### 3.4 Buffers

1x Origami ELISA buffer	10 mM 4-(2-hydroxyethyl)-1-piperazineethanesulfonic acid (HEPES), 10 mM MgCl <sub>2</sub> , 0.1% (v/v) Tween 20, pH 6.8 or 7.4
1x PBS	137 mM NaCl, 2.7 mM KCl, 10 mM Na <sub>2</sub> HPO <sub>4</sub> , 1.8 mM KH <sub>2</sub> PO <sub>4</sub> , pH 7.4
1x phosphate buffered saline (PBS) (EphA2 phosphorylation assay)	137 mM NaCl, 2.7 mM KCl, 8.1 mM Na <sub>2</sub> HPO <sub>4</sub> , 1.5 mM KH <sub>2</sub> PO <sub>4</sub> , pH 7.4
1x RSV blocking buffer	1x PBS, 10 mM MgCl <sub>2</sub> , 0.1% (v/v) Tween 20, 1% (v/v) BSA, pH 7.4
1x TBE buffer	89 mM tris base, 89 mM boric acid, 2 mM EDTA
1x virus ELISA buffer	1x PBS, 10 mM MgCl <sub>2</sub> , 0.1% (v/v) Tween 20, pH 7.4
Bacteria binding buffer	1x PBS, 1 mM MnCl <sub>2</sub> , 1 mM CaCl <sub>2</sub>
Block buffer (EphA2 phosphorylation assay)	1% (w/v) BSA, 0.05% NaN <sub>3</sub> in 1x PBS (EphA2 phosphorylation assay), pH 7.4
DPBS (no calcium, no magnesium)	Purchased from Thermo Fisher Scientific, USA
Dulbecco's phosphate buffered saline (DPBS) (calcium, magnesium)	Purchased from Thermo Fisher Scientific, USA

HBSP buffer	10 mM HEPES, 150 mM NaCl, 0.05% Tween 20, pH 7.4
IC Diluent #12 (EphA2 phosphorylation assay)	1% (v/v) NP-40 Alternative, 20 mM Tris (pH 8.0), 137 mM NaCl, 10% (v/v) glycerol, 2 mM EDTA, 1 mM activated sodium orthovanadate
IC Diluent #14 (EphA2 phosphorylation assay)	20 mM Tris, 137 mM NaCl, 0.1% (w/v) BSA 0.05% (v/v) Tween 20, pH 7.4
IC Diluent #9 (EphA2 phosphorylation assay)	1% (v/v) NP-40 Alternative, 20 mM Tris (pH 8.0), 137 mM NaCl, 10% (v/v) glycerol, 2 mM EDTA, 1 mM activated sodium orthovanadate, 10 µg/ml aprotinin, 10 µg/ml leupeptin
Wash buffer (EphA2 phosphorylation assay)	0.05% (v/v) Tween 20 in 1x PBS (EphA2 phosphorylation assay), pH 7.4

### 3.5 Media

Cryo medium	50% (v/v) cell medium, 30% (v/v) FBS, 20% (v/v) DMSO
HL-60 cell medium	DMEM, high glucose, GlutaMAX™ Supplement, pyruvate + 20% (v/v) FBS, sterile filtered
Madin-Darby canine kidney (MDCK) cell medium	DMEM, high glucose (4,5 g/l), GlutaMAX™ Supplement, pyruvate + 10% (v/v) FBS, sterile filtered
PC-3 cell medium	RPMI 1640 Medium, GlutaMAX™ Supplement + 10% (v/v) FBS, sterile filtrated
Virus growth medium	DMEM/7.5% (v/v) BSA + 1 µg/ml TPCK treated trypsin, sterile filtered

### 3.6 Antibodies, beads, enzymes, kits, matrices and standards

3-Hydroxypicolinic acid (3-HPA)	Bruker Daltonik, Germany
Anti-human $\alpha$ -synuclein 10D2, monoclonal	AJ Roboscreen, Germany
Anti-human $\alpha$ -synuclein 5G4, monoclonal	AJ Roboscreen, Germany
DuoSet IC Human Phospho-EphA2 kit	R&D systems, USA
Dynabeads™ MyOne™ Streptavidin T1	Thermo Fisher Scientific, USA
Goat Anti-Mouse IgG H&L horseradish peroxidase (HRP) (ab97023)	abcam, United Kingdom
Influenza A H3N2 Virions Polyclonal Antibody, HRP	Thermo Fisher Scientific, USA
IntelliCyt 6-peak and 8-peak validation beads	IntelliCyt, USA
Oligonucleotide Calibration Standard DNA	Bruker Daltonik, Germany
Phycoerythrin (PE) anti-human EphA2 Antibody	Biolegend, Germany
Purified Mouse Anti-Actin Ab-5	BD Transduction Laboratories, USA
Purified Mouse Anti-Human c-Myc	BD Pharmingen, USA
RSV Polyclonal Antibody, HRP	Thermo Fisher Scientific, USA

### 3.7 DNA, peptides and sugars

Oligonucleotides for small DNA nanostructures were designed to be partially complementary for the purpose of folding DNA structures. Unwanted formation of hairpins or self-hybridization was excluded by using the OligoAnalyzer Tool (Integrated DNA Technologies, USA). DNA was purchased from Biomers.net, Germany in high-performance liquid chromatography (HPLC) purity. Different variations of DNA sequences were used (see footers in Table 3-2).

**Table 3-2. Sequences of small DNA constructs**

Name (size)	ssDNA	DNA Sequence 5'→3'	5'	3'
30 base pair construct (~19 kDa)	30 forward (fw)	ATAATCTTGGATACGATATCACCATACGTC	1, 2	1
	30 reverse (rev)	GACGTATGGTGATATCGTATCCAAGATTAT	3	1
DNA 4arm structure (~60 kDa)	MN	ACGCTCTTTGTTCTACTGATGCTTGCCTGATCC ATGATATATATTGAGTGCTATTTAGTTTCTATCA	3	1
	N*O	TGATAGAAACTAAATATAATATGCGAGCCA	1, 2	1
	O*P*	TGGCTCGCATATTATTAGTTGTGTGTGTGT	1, 2	1
	PM*	ACACACACACA ACTAAGCACTCAATATATATCAT GGATCAGGCAAGCATCAGTAGAACAAAGAGCGT	1, 2	1
DNA trimer (~28 kDa)	ab	ACTATCTTTGGTCTATTATCTTGAGTCATC	1, 2	1, 4, 5
	b*c	GATGACTCAAGATAAACACACACACA ACTA	1, 2	1
	c*a*	TAGTTGTGTGTGTGTTAGACCAAAGATAGT	1, 2	1

<sup>1</sup> no modification, <sup>2</sup> Aminolink C6, <sup>3</sup> Biotin, <sup>4</sup> Cy3, <sup>5</sup> Atto655. Complementary segments are denoted with a star, i.e. “a” as part of strand “ab” is complementary to “a\*” in strand “c\*a\*”.

For construction of DNA origami hexagonal structures (DOhex), unmodified oligonucleotides were bought from Eurofins MWG, Germany (Table A1). Oligonucleotides with end modifications and/or for small DNA constructs were purchased from Biomers.net, Germany.

Peptides listed in Table 3-3 were used. Peptides purchased from PSL Peptide Specialty Laboratories, Germany were produced on a solid-phase (SPPS) using 9-fluorenylmethoxycarbonyl (Fmoc) chemistry. They were HPLC-purified and had a purity of at least 90% - 95%. Peptides obtained from Prof. Dr. Ines Neundorf (University of Cologne) had a purity of > 45% (ED9) and > 50% (ED10). Lyophilized peptides were stored at 4 °C. For usage, they were weighed-in on an ultra micro balance (Mettler Toledo, USA) and solubilized to concentrations of 2-5 mM in ddH<sub>2</sub>O or buffer. For PeB, after dissolving in water, drops of 0.1 M NaOH were added until the turbid solution turned clear. RSV-Peptide-6 was dissolved in DMSO. Solubilized peptides were kept at -20 °C until use.

Table 3-3. Sequences of peptides

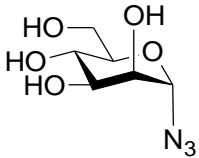
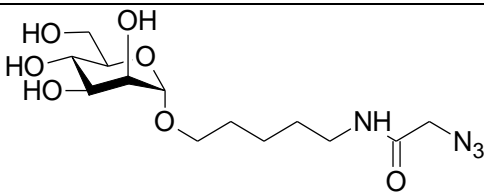
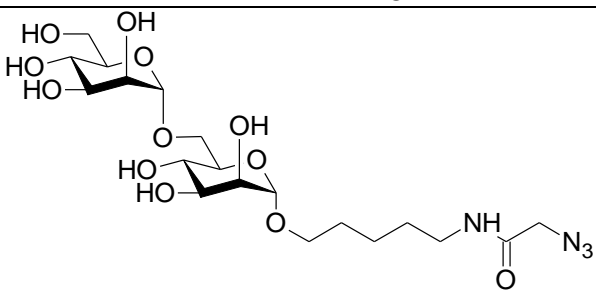
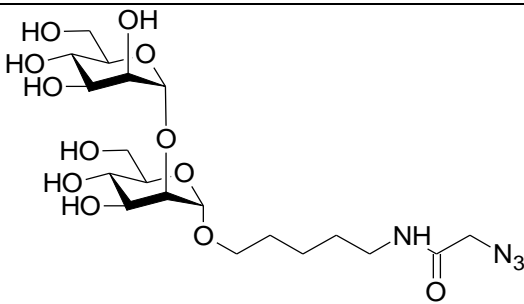
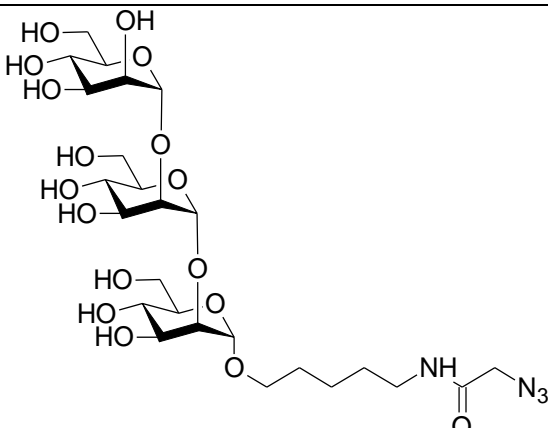
Name	Amino acid sequence in one letter code N' → C'	Modification	Supplier
Anti actin AB naïve (AN)	GDDAPRAVFPS	N-terminal: acetylated, C-terminal: Azidolysin	PSL Peptide Specialty Laboratories, Germany
Anti actin AB phage (AP)	DDSEPRAVFS	N-terminal: acetylated, C-terminal: Azidolysin	PSL Peptide Specialty Laboratories, Germany
Anti c-myc naïve (CN)	EEQKLISEEDLLR	N-terminal: acetylated, C-terminal: Azidolysin	PSL Peptide Specialty Laboratories, Germany
Anti c-myc phage (CP)	QHLVSRDLE	N-terminal: acetylated, C-terminal: Azidolysin	PSL Peptide Specialty Laboratories, Germany
ED10	GVVHGVATVAGGK	N-terminal: acetylated, C-terminal: Azidolysin	Prof. Dr. Ines Neundorf (University of Cologne)
ED9	PVDPDNEAYEGGK	N-terminal: acetylated, C-terminal: Azidolysin	Prof. Dr. Ines Neundorf (University of Cologne)
PeB	ARDFYDYDVFYYAMD	N-terminal: Azidobutyric acid, C-terminal: Amid	Maria Glanz (Leibniz- Forschungsinstitut für Molekulare Pharmakologie, Germany) and PSL Peptide Specialty Laboratories, Germany
RSV- Peptide-6	[Chg][Cpa]VSTT[Tyr3,5- I2]LPHYFDN (sequence contains non- natural amino acids <sup>1</sup> )	N-terminal: acetylated, C-terminal: PEG9, Azidolysin	PSL Peptide Specialty Laboratories, Germany
SWL	SWLAYPGAVSYRGG	N-terminal: acetylated, C-terminal: Azidolysin	PSL Peptide Specialty Laboratories, Germany

<sup>1</sup>Chg= Fmoc-L-Chg-OH (cyclohexyl-glycine), Cpa= cyclopropyl-alanine, Tyr3,5-I2= 3,5 diiodo-tyrosine

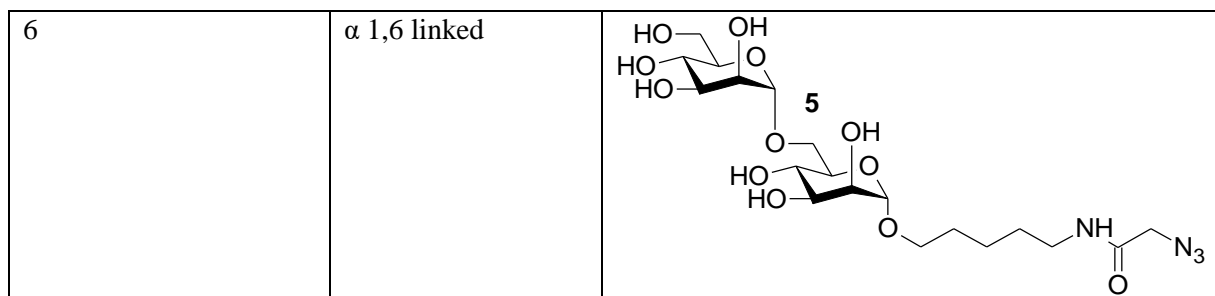
The Sugars in Table 3-4 were synthesized by Dr. Vittorio Bordoni (group of Dr. Martina Delbianco) at the Max-Planck-Institute of Colloids and Interfaces in Potsdam, Germany.

Lyophilized powder as well as 10 mM stock solutions (in ddH<sub>2</sub>O) were stored at 4 °C in the fridge.

**Table 3-4. Saccharides**

Number of Mannose monomers	Characteristic	Structure
1	Without linker	
1	With linker	
2	$\alpha$ 1,6 linked	
2	$\alpha$ 1,2 linked	
3	$\alpha$ 1,2 linked	





### 3.8 Organisms

#### 3.8.1 Cell lines

PC-3 cells (ATCC® CRL-1435™) and MDCK (NBL-2) cells, (ATCC® CCL-34™) were purchased from ATCC, USA. HL-60 cells were a kind gift from Kerstin Wenk (Universitätsklinikum Leipzig, Germany).

Cells were periodically checked for contamination with *Mycoplasma* via polymerase chain reaction (PCR).

#### 3.8.2 Viruses

IAV Strain A/X31/1 (A/Aichi/1968) subtype H3N2 is a laboratory-adapted variant of strain Hong Kong/68/H3N2 and was obtained from PD Dr. Thorsten Wolff (Robert Koch Institute, Germany). The viral titer given was  $3.8 \times 10^8$  plaque-forming units (PFU)/ml. An inactive version (processed by Dr. Daniel Lauster, Humboldt-Universität zu Berlin, Germany) of that strain was used for MST measurements.

RSV subtype A, Long strain was produced by Leila Issmail (Fraunhofer Institute for Cell Therapy and Immunology IZI, Germany) and originally came from Ruhr-Universität Bochum, Germany. The viral titer given was  $3 \times 10^8$  PFU/ml.

#### 3.8.3 Bacteria

*Escherichia coli* (Migula) Castellani and Chalmers (ATCC® 43652™, USA), O25:NM, was transformed with puc57 dsRed or puc57 green fluorescent protein (GFP) by Dr. Jasmin Fertey (Fraunhofer Institute for Cell Therapy and Immunology IZI, Germany).

### 3.9 Cultivation of cell lines

All work activities and experiments containing living cell lines were conducted under sterile conditions using a clean bench in an S2 laboratory that was spatially separated from the virus culture. Samples and reagents for cell experiments were prepared using sterile-filtered or autoclaved solutions and filter tips.

#### 3.9.1 Subcultivation

Typically, cells were grown in 75 cm<sup>2</sup> filter cap cell culture flasks (tissue culture (TC) treated) containing 10 ml of medium. They were incubated at 37 °C, 5% CO<sub>2</sub> in a humidified cell incubator (Thermo Fisher Scientific, USA) and grew as an adherent monolayer. When cells were ~70% - 80% confluent, they were split into new cell culture flasks to ensure optimal nutrient supply, removal of toxic metabolites and space for growth of new cells. For this, the old culture medium was first discarded. Cells were then carefully washed using 5 ml of pre-warmed DPBS (no calcium, no magnesium). In order to detach the cells from the culture flask, 2.5-3 ml of 0.05% Trypsin-EDTA were added on top of the cells and left to incubate for approx. 5 min at 37 °C. After the cells were detached, Trypsin-EDTA was inactivated by addition of 3 ml cell medium (containing 10% (v/v) FBS). The cells were pipetted into a 15 ml sterile tube and collected by centrifugation for 5 min at 1,150 rpm at room temperature. In a next step, the supernatant was discarded and the cell pellet was resuspended in 1 ml fresh medium. The cell suspension was then divided in different ratios (typically 1:5, 1:10 or 1:20) and seeded into new 75 cm<sup>2</sup> cell culture flasks containing 10 ml fresh medium for subsequent cultivation in the cell incubator.

#### 3.9.2 Cryopreservation

Long-time storage of cells was enabled by production of cell cryo stocks. Therefore, cells were treated as described above (3.9.1), but instead of seeding parts of the resuspended cell pellet into new flasks, 500 µl of the cell suspension were mixed with 500 µl cryo medium, filled into a cryo vial and immediately frozen by putting the vial into a -80 °C freezer. The medium for freezing cells contains a final concentration of 10% DMSO which acts as cryoprotective agent. During freezing, DMSO inhibits the formation of ice crystals which would harm the cells.

Cell lines were kept at -80 °C or in vapor phase liquid nitrogen at -156 °C. In order to culture cells, they were quickly defrosted in a 37 °C water bath and subsequently transferred into 5 ml

of medium. The mixture was centrifuged at 1,150 rpm for 7 min at room temperature. Afterwards, the supernatant was discarded, the cell pellet was resuspended in 1 ml fresh medium and transferred into a 75 cm<sup>2</sup> cell culture flask containing 10 ml of fresh medium. Cryo stocks of cell lines for long-term storage were produced from low passage numbers.

### 3.9.3 Counting

After detachment and resuspension of cells, 10 µl of cells were mixed with 10 µl of Erythrosin B Stain and pipetted into a cell counting slide (Biozym, Germany). The stain diffuses into dead or dying cells as they lack an intact cell membrane, whereas healthy cells are not affected by the stain. This slide was inserted into a cell counting machine (Logos Biosystems, Korea). The machine assesses cell viability and concentration. Taking those values into consideration, the cells were diluted in medium or DPBS to a desired concentration.

## 3.10 Quantification of DNA

Concentration and purity of nucleic acids was measured via UV-visible spectroscopy using a NanoDrop UV/Vis spectrophotometer (PEQLAB Biotechnologie, Germany). Due to heterocyclic rings in the structure of nucleotides, nucleic acids absorb light with an absorption peak at 260 nm. By applying the Beer-Lambert law, this absorption can be utilized to correlate the nucleic acid concentration. After blanking the machine with sample buffer, ~2 µl of sample were applied to measure the absorbance. Furthermore, absorbance values measured at 230 nm and 280 nm are used to calculate ratios that indicate how pure the samples are. Considered as pure are samples with ratios of ~1.8 and 1.8-2.2 for 260/280 and 260/230, respectively.

## 3.11 Synthesis of DOhex structures

### 3.11.1 Preparation of scaffold DNA

For construction of DNA origami structures, a scaffold ssDNA that is mixed with many synthetic staple ssDNA molecules, is necessary. Scaffold DNA was isolated from a modified version of bacteriophage M13mp18 with a genome of 8634 nucleotides and purified according to Castro *et al.*<sup>50</sup>. See Appendix II for sequence<sup>53</sup>.

### 3.11.2 Production of DOhex structures

Using the DNA origami software caDNAno, a hexagonal lattice-based DNA origami structure (DOhex) was designed, with approximate dimensions of 50 nm x 50 nm (see Figure 4-3). One biotin-carrying strand was extended outward from one face by appending an overhang of two thymine bases from the 5'-end of a single staple strand, and six additional staple strands on the opposite face were selectively functionalized with peptide epitopes or mimotopes. For folding, one biotinylated staple strand (Biomers.net, Germany) was mixed with peptide-conjugated DNA staple strands as well as the remaining unmodified staple strands and added in 10-fold excess to scaffold 8634 (10 nM). Reactions were mixed in PCR tubes. Two peptide-modified strands were incorporated into one DOhex structure. According to the design (Figure 4-3), these synthetic epitopes or mimotopes were arranged in different distances to each other. It is known that the distance between two helices is approximately 2.6 nm in these moderate ionic conditions, and that the distance between two nucleotides is 0.34 nm. Therefore, the distance between two 5'-ends can be calculated using Figure A 1 and the following equation:

$$\sqrt{(n_{(helices)} * helical\ distance)^2 + (n_{(nucleotides)} * nucleotide\ separation)^2} \quad (1)$$

As an example, the distance between  $\Delta$  and  $\diamond$  is:

$$\sqrt{(4 * 2.6\ nm)^2 + (4 * 0.34\ nm)^2} = 10.489\ nm \quad (2)$$

Folding was carried out in 10 mM HEPES, 10 mM MgCl<sub>2</sub> buffer by using the following temperature program (Table 3-5) in a thermocycler (Biometra, Germany). DNA is highly negatively charged in aqueous milieu because of its ionized phosphate groups in the backbone. To avoid instability due to repelling forces of those phosphate groups, DNA is stabilized by positively charged histones in nature and by positive ions like NaCl or MgCl<sub>2</sub> in DNA nanostructure formation. An initial heating step above the melting temperature separates all nonspecifically paired bases and removes secondary structures by breaking hydrogen bonds. Hybridization is achieved by following cooling steps.

**Table 3-5. Folding program for DOhex structures**

Step	Temperature	Time	go to step	loops	$\Delta$ Temperature	Cooling rate
1	65 °C	15 min	-	-	-1 °C	5 °C/s
2	64 °C	4 min	2	3	-1 °C	0.1 °C/s
3	60 °C	15 min	3	3	-1 °C	0.1 °C/s
4	56 °C	55 min	4	12	-1 °C	0.1 °C/s
5	43 °C	12 min	5	7	-1 °C	0.1 °C/s
6	35 °C	4 min	6	11	-1 °C	0.1 °C/s
7	4 °C	Pause	-	-	-	5 °C/s

After annealing, samples were purified from excess of staple strands using Amicon®-Ultra-0.5 ml centrifugal filters with 100K molecular weight cut-off (EMD Millipore, Germany) according to 3.15.2 and analyzed using AFM imaging and agarose gel electrophoresis.

### 3.12 Synthesis of small DNA nanostructures

Oligonucleotides listed in Table 3-2 were resuspended in water and the concentration was determined. To guarantee for optimal stoichiometry and high yields, all strands for one structure were mixed in equimolar amounts in PCR tubes. The mixture of oligonucleotides was supplemented with buffer, water or, in case of DNA constructs carrying RSV-Peptide-6, in DMSO, and folded using a thermocycler (Biometra, Germany). At the beginning, the mixture was heated to  $\geq 90$  °C to denature secondary structures and nonspecific base pairing. For specific base pairing, the reaction was cooled to and held at a certain annealing temperature (usually 5 K below the calculated melting temperature) for hybridization, and then further cooled to 4 °C (Table 3-6).

**Table 3-6. Folding of small DNA nanostructures**

DNA construct	Buffer condition	Temperature ramp
DNA 4arm	1x PBS	2 min at 95 °C 15 min at 52 °C Cool to 4 °C
DNA trimer	1x PBS or DMSO	2 min at 95 °C 15 min at 48 °C Cool to 4 °C

30 bp dsDNA	1x PBS, water or DMSO	2 min at 90 °C Cool to 4 °C
-------------	-----------------------	--------------------------------

Fluorescently labeled DNA trimers are hereafter termed DNA trimer<sup>Atto655</sup> or DNA trimer<sup>Cy3</sup> when built with 3'-Atto655 or 3'-Cy3 modified strand ab, respectively.

### 3.13 Modification of DNA

DNA single strands or small dsDNA constructs were modified with sugars or peptides using two consecutive reactions. First, NHS ester chemistry was used to add a DBCO molecule to the amino group-carrying 5'-end of the DNA. Afterwards, excess DBCO was removed via ethanol precipitation. In the following reaction, DBCO-DNA bound to an azide-functionalized peptide or sugar via strain-promoted alkyne-azide cycloaddition (SPAAC). This reaction was purified using Amicon® Ultra centrifugal filters or ethanol precipitation. Polyacrylamide gel electrophoresis (PAGE) and matrix-assisted laser desorption/ionization – time-of-flight (MALDI-TOF) analysis were conducted to evaluate the efficiencies of modification.

#### 3.13.1 NHS ester chemistry

DNA strands to be modified were purchased with aminolink C6 (-NH<sub>2</sub>) at the 5'-end from Biomers.net. The nucleophilic amino group reacts to N-hydroxysuccinimide (NHS) esters in an S<sub>N</sub>2 reaction, which characteristically includes the formation of a transition state (Figure 3-1). For high yields, the conjugation needs to be conducted in physiological buffer conditions (pH 6-9) and in amine-free buffers.

NH<sub>2</sub>-modified DNA molecules were incubated with a 100-fold molar excess of DBCO-NHS esters (Jena Bioscience, Germany) or DBCO-PEG4-NHS ester (Jena Bioscience, Germany) in 1x PBS pH 7.4 according to the company's instructions. Briefly, DBCO-NHS esters or DBCO-PEG4-NHS esters were freshly weighed using an ultra micro balance (Mettler Toledo, USA), solubilized in DMSO to a final concentration of 10 mM and immediately mixed with the buffered DNA solution. The reaction was left at room temperature overnight and was purified the next day via ethanol precipitation. The successful attachment of the DBCO-NHS ester or DBCO-PEG4-NHS ester linkers to DNA can be seen as a shoulder (e.g. Figure A 3) in addition

to the DNA peak at 260 nm in UV-visible spectroscopy as DBCO molecules absorb light at 309 nm.

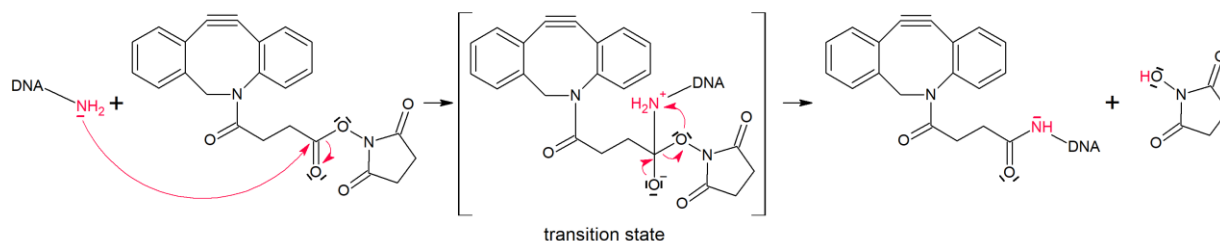


**Figure 3-1. NHS ester reaction using NH<sub>2</sub>-DNA and DBCO-NHS ester.**

Primary amino group at the DNA reacts with DBCO-NHS ester. After formation of a transition state, a stable amide bond is formed and NHS is released. Colored arrows indicate the reaction mechanism and involved atoms are shown with their free electrons.

In addition to DBCO-NHS esters and DBCO-PEG4-NHS esters, DBCO-Sulfo-NHS esters were used in the beginning of this work. The coupling to peptides appeared to be incomplete in case of PeB (see Figure 5-1A), this is why in further assays, DBCO-NHS esters or DBCO-PEG4-NHS esters were used instead of the variant containing the sulfo group.

### 3.13.2 SPAAC

The SPAAC reaction is a bioorthogonal copper-free click chemistry reaction that was developed by Agard *et al.*<sup>127</sup>. The term click chemistry was established by Sharpless *et al.* in 2001<sup>128</sup> and describes Copper-catalyzed azide-alkyne cycloadditions that are based on the mechanism of a Huisgen 1,3 dipolar cycloaddition<sup>129</sup>. The addition of Cu(I) was needed to perform the cycloaddition under physiological conditions with high yields and in a fast and selective manner. In copper-free click chemistry, instead of toxic Cu(I), a ring strain provides energy (18 kcal/mol of ring strain) to activate alkynes for the covalent reaction with azides to efficiently form stable triazoles (Figure 3-2). Due to this, the reaction happens quickly, is efficient and can be executed in almost every solvent. As a strained alkyne, the molecule DBCO was used in this work because it is reported to perform excellent reactions with azide groups<sup>130</sup>.

Bioconjugation was achieved by adding azide-modified peptides or sugars in 10 - 20-fold molar excess to DBCO-modified DNA. The reaction was incubated at room temperature overnight.

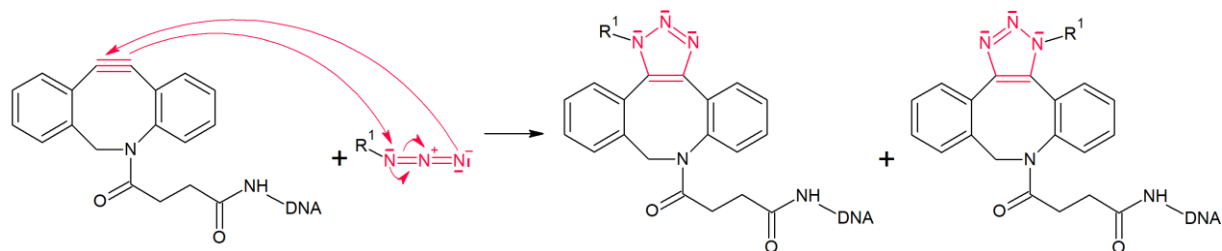


**Figure 3-2. SPAAC reaction using DBCO-DNA and an azide molecule.**

DBCO-DNA reacts with an azide molecule ( $R^1 = \text{sugar or peptide}$ ). As a result, two distinct regioisomers are formed. Colored arrows indicate the reaction mechanism and involved atoms are shown with their free electrons.

### 3.14 Verification of DNA structure folding and functionalization

Correct folding of DNA origami structures as well as functionalization of ssDNA or small DNA nanostructures was confirmed by gel electrophoresis. Electrophoretic separation of charged particles is dependent on their size, shape and charge<sup>131</sup>. As their phosphate backbone is negatively charged, DNA molecules are able to migrate through an electric field towards the anode. Since their charge is proportional to their size, smaller DNA molecules travel faster towards the plus pole than larger DNA molecules. The gel is a porous matrix consisting of either agarose (suitable for big DNA structures like DNA origami) or polyacrylamide (suitable for smaller DNA structures and ssDNA). Depending on the concentration of agarose or polyacrylamide, the pore sizes of the gel can vary from 200-500 nm for agarose and 5-100 nm for acrylamide<sup>132</sup>.

Another method to verify correct folding of DNA origami structures is AFM imaging.

#### 3.14.1 Agarose gel electrophoresis

Gels made of 1.5% (w/v) agarose were used for the analysis of larger DNA origami structures prior to the experiments. Agarose gel electrophoresis was performed using PerfectBlue™ Horizontal Minigelsystems (PEQLAB Biotechnologie, Germany). Agarose was mixed with 0.5x TBE buffer containing 10 mM  $\text{MgCl}_2$  and boiled in a microwave until the agarose powder was completely melted. The solution was cooled down to  $\sim 45^\circ\text{C}$  and poured into a gel casting tray with inserted comb. After polymerization, samples were applied and the gel was run in 0.5x TBE buffer containing 10 mM  $\text{MgCl}_2$  in an electrophoresis chamber at 70 V in  $4^\circ\text{C}$  for approx. 3 h. Gels were then stained in an ethidium bromide bath (0.5  $\mu\text{g/ml}$ ) for approx. 30 min. Ethidium bromide is an intercalating dye that binds between base pairs and thereby gains an enhancement in fluorescence when excited with UV light.



### 3.14.2 Native PAGE

The coupling of peptides, sugars or DBCO groups to either ssDNA or small DNA nanostructures was always evaluated prior to experiments by native gels with polyacrylamide content of 8% (v/v) – 20% (v/v). PAGE was carried out using a Mini-PROTEAN® Tetra cell system and its components (Bio-Rad, Germany). First, polyacrylamide was mixed with water, TBE buffer (final concentration of 1x) and then 0.1% (v/v) TEMED, which serves as reaction catalyzer, and 0.1% (w/v) APS, which initiates the reaction, were added. The gel was poured between two glass plates that were secured in a casting frame. Immediately after pouring, the comb was inserted carefully and the gel was left to polymerize for approx. 30 min. Then, the gel was fixed in the electrode assembly module and placed into an electrophoresis chamber which was filled with running buffer (0.5x TBE). After removing the comb, the slots were rinsed with buffer, the samples were applied to the pockets and the electrophoresis was performed at 100 – 120 V for approx. 1-1.5 h (depending on the denseness of the gel) at room temperature. A dilution of 1x SYBR™ Gold nucleic acid gel stain in 0.5x TBE was used to stain the gel for approx. 20 min before imaging it under UV light. SYBR™ Gold exhibits fluorescence enhancement upon binding to both ssDNA and dsDNA.

### 3.14.3 AFM imaging

Appearance, stability and folding efficiency of DNA origami structures can be evaluated via atomic force microscopy (AFM) imaging. For this type of scanning probe microscopy, a sharp tip moves along the sample surface. It is attached to a flexible cantilever which bends towards or away from the surface due to attractive or repulsive interactions between sample and tip. A laser is directed at the cantilever and from there reflected to a detector that converts the change in deflection into an image. AFM can be conducted in different modes: contact mode (tip touches sample constantly), non-contact mode (tip is always above the sample) or tapping/AC mode (tip touches sample periodically). The latter is most suitable for scanning soft, biological samples like DNA since frictional forces are weaker than in contact mode <sup>133</sup>.

Freshly cleaned and cleaved mica surface (Plano, Germany) was treated with 100 µl Poly-L-ornithine for 10 min. Poly-L-ornithine is positively charged and thus suitable to immobilize negatively charged DNA to mica <sup>134</sup>. After washing the mica with 1x Origami ELISA buffer, purified DOhex structures were applied and incubated for 10 min. Approximately 1 ml of buffer was added to the fluid cell and imaged in tapping mode using cantilever BL-AC40TS-CS2

(Olympus, Germany) and the atomic force microscope NanoWizard 3.0. (JPK Instruments, Germany).

## **3.15 Purification and concentration of DNA**

### **3.15.1 Ethanol precipitation**

Ethanol precipitation was carried out to purify DNA from excess of DBCO-NHS ester, DBCO-PEG4-NHS ester or RSV-Peptide-6 and during the production of scaffold for DNA origami structures. In principle, the solubility of DNA is decreased by addition of salts that neutralize the negative charge of DNA and by addition of ethanol which is less polar than water.

To achieve precipitation, the DNA was mixed with 0.1 volumes 3 M Sodium acetate and 2 volumes of pure ethanol. Immediately afterwards, the DNA was frozen for 5 min in liquid nitrogen and subsequently incubated on ice for 30-60 min. DNA was pelleted by centrifugation at 15,000 rpm, at 4 °C for 1 h. The supernatant was carefully removed and after the DNA pellet was dry (approx. 10 min), it was resuspended in ddH<sub>2</sub>O or buffer.

### **3.15.2 Spin filtration**

Amicon® Ultra centrifugal filters (EMD Millipore, Germany) were used to either separate modified DNA constructs from small unbound molecules like peptides or sugars after conjugation or to remove staple strands that were not incorporated into DNA origami structures. As this is done by ultracentrifugation, the samples are also concentrated since the volume is reduced. Due to defined filter pore sizes, large DNA molecules are detained whereas small peptides, sugars or ssDNA pass the filter and are discarded. For purification of DNA trimer, DNA 4arm or DNA origami structures, Amicon® filters with MWCO of 10K, 30K or 100K were used, respectively.

At first, the filter was washed with 500 µl of sample buffer by spinning at 13,000 rpm, 8-9 min, 4 °C and discarding the flow-through. Next, sample was added and the filter were topped up to 500 µl with buffer before centrifugation was repeated. Again, flow-through was discarded and washing with buffer was repeated at least twice. In the end, the sample was either pipetted out of the filters or collected by spinning filters upside down in a new tube as recommended by the manufacturers.

### 3.16 MALDI-TOF

To find out whether coupling of peptides to ssDNA and removal of excess of peptides via spin filtration was complete, MALDI-TOF mass spectrometry was conducted. Here, the DNA sample is co-crystallized with a 3-HPA matrix<sup>135</sup> and exposed to pulsed laser light. The energy of the laser is absorbed by the matrix and transferred to the DNA sample which results in ablation and desorption. In this way, sample molecules are protonated or deprotonated and consequently ionized. The molecular weights of these ions can be analyzed by time-of-flight mass spectrometry. For analysis of ssDNA, an Autoflex Speed mass spectrometer (Bruker Daltonik, Germany) was used in linear positive mode.

First, 0.5 µl of 3-HPA matrix (half-saturated, dissolved in water/acetonitrile (50:50) with 10 mg/ml diammonium hydrogen citrate) were spotted on the AnchorChip target and dried at room temperature. Then, 0.5 µl of the DNA sample were spotted and dried at room temperature. Before measurement, the machine was calibrated using the Oligonucleotide Calibration Standard (Bruker Daltonik, Germany).

### 3.17 ELISA

The ELISA method allows for detection and quantification of specific binding events in a parallel, high-throughput manner. After immobilizing one binding partner on the bottom of a plate, the binding of a second partner can be evaluated by enzymatic conversion of a substrate into a colored product. The resulting color signals are proportional to the number of bound molecules and can be measured by an absorbance reader. Several washing steps ensure the removal of nonspecifically bound components. In each ELISA, the samples were applied as triplicates and ELISAs were repeated once or twice.

#### 3.17.1 Binding of antibodies to peptides on DOhex structures

This indirect ELISA method determines how strong antibodies bind to epitopes presented on DOhex structures and further elucidates binding profiles based on the distances between two epitopes or mimotopes (Figure 3-3). Clear F-Bottom Immuno Nonsterile Maxisorp 96-well plates (Fisher Scientific, Germany) were coated with 500 ng/well NeutrAvidin™ (Thermo Fisher Scientific, USA) in 0.1 M NaHCO<sub>3</sub> pH 8.0 buffer, covered with a lid and incubated at 4 °C overnight. The following day, all steps were carried out at room temperature and incubation

took place under gentle agitation with working volumes of 100  $\mu\text{l}$ /well for samples and antibodies. Plates were washed three times with 200  $\mu\text{l}$ /well 1x Origami ELISA buffer and incubated with 100 ng/well – 500 ng/well biotin- and epitope-carrying DNA origami structures for 1 h. In addition, each ELISA was equipped with negative controls (wells containing buffer only, wells containing only the first antibody, wells containing dsDNA) and one positive control (wells containing dsDNA that was conjugated to the epitope) which are shown as schematic in Figure 4-2. After washing three times, plates were incubated with the primary binding antibody diluted in 1x Origami ELISA buffer for 1 h. Afterwards, plates were washed three times with 1x Origami ELISA buffer and incubated with a secondary antibody (Goat Anti-Mouse IgG H&L (HRP), abcam, UK) for 1 h. The plates were washed three times and incubated with freshly mixed TMB A and TMB B substrate solution (in a ratio of 1:1) until the wells turned distinctly blue or for up to 30 min. The reason for those colorimetric reactions was the conversion of TMB substrate by the enzyme HRP. Subsequently, enzymatic reactions were stopped by adding 50  $\mu\text{l}$ /well 1 M  $\text{H}_2\text{SO}_4$ . Absorbance was measured at 450 nm and at 520 nm (subtracted as reference value) using a microplate reader infinite M1000 (Tecan, Switzerland).

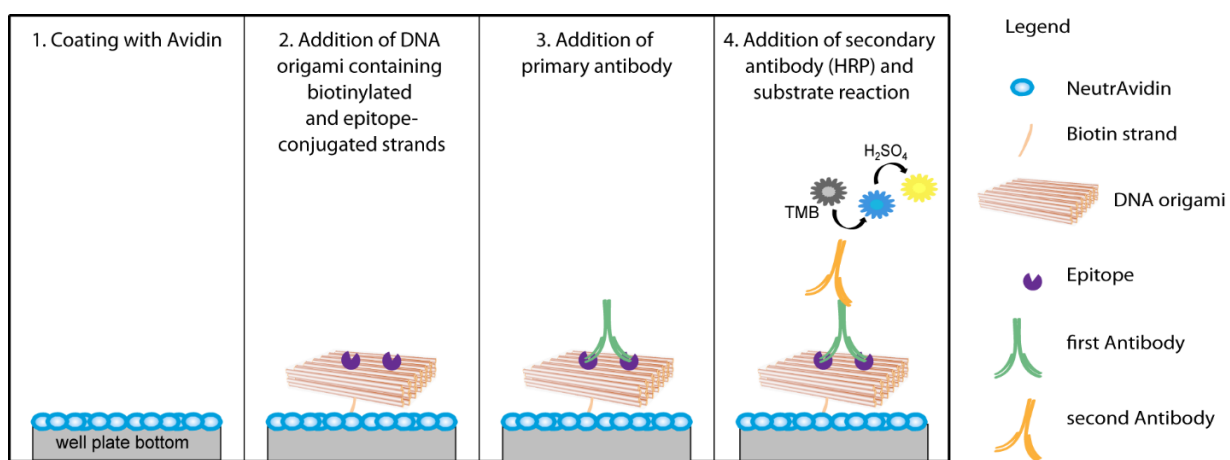


**Figure 3-3. Schematic ELISA principle using DOhex structures.**

HRP = Horse reddish peroxidase, TMB = 3,3',5,5'-Tetramethylbenzidine. Components are not in scale.

### 3.17.2 Binding of viruses to peptide-functionalized dsDNA constructs

In order to determine whether influenza A as well as RSV bind specifically to peptide-decorated 30 bp dsDNA constructs, direct ELISAs were conducted. At first, Clear F-Bottom Immuno Nonsterile Maxisorp 96-well plates were coated with 500 ng/well NeutrAvidin™ in 0.1 M  $\text{NaHCO}_3$  pH 8.0 buffer. They were closed with a lid and incubated at 4 °C overnight. The next day, the ELISA was conducted at room temperature and under gentle agitation with working

volumes of 100  $\mu$ l/well for samples and antibodies. The NeutrAvidin<sup>TM</sup> coated plate was washed three times with 1x virus ELISA buffer and treated with biotin- and peptide-carrying 30 bp dsDNA structures or appropriate controls (wells containing buffer only, wells containing only the first antibody, wells containing 30 bp dsDNA) for 1 h. Next, in case of influenza A, the plate wells were washed three times with 1x virus ELISA buffer and incubated with various dilutions of viruses (freshly defrosted and vortexed before used) for 1 h. In case of RSV, washing prior to addition of antibody, as well as dilution of antibody was done using 1x RSV blocking buffer. After washing three times, the plate was incubated for 1 h with either Influenza A H3N2 Virions Polyclonal Antibody, HRP (Thermo Fisher Scientific, Germany) 1:200 dilution or RSV Polyclonal Antibody, HRP (Thermo Fisher Scientific, Germany) 1:500 dilution for detecting Influenza A or RSV, respectively. Then, the plate was washed three times using 1x RSV blocking buffer for RSV ELISAs and 1x virus ELISA buffer for influenza A X31 ELISAs. Next, TMB A and TMB B substrate solution were freshly mixed in a ratio of 1:1 and incubated on the wells until the solution turned blue. The HRP reaction was stopped by addition of 50  $\mu$ l/well 1 M H<sub>2</sub>SO<sub>4</sub>. A microplate reader infinite M1000 (Tecan, Switzerland) was used to measure absorbances at 450 nm and 520 nm.

### **3.17.3 EphA2 phosphorylation assay**

Levels of EphA2 phosphorylation were determined using the DuoSet IC Human Phospho-EphA2 kit which is based on a sandwich ELISA (Figure 3-4). Therefore, all required solutions were prepared in accordance to the manufacturer's instructions.

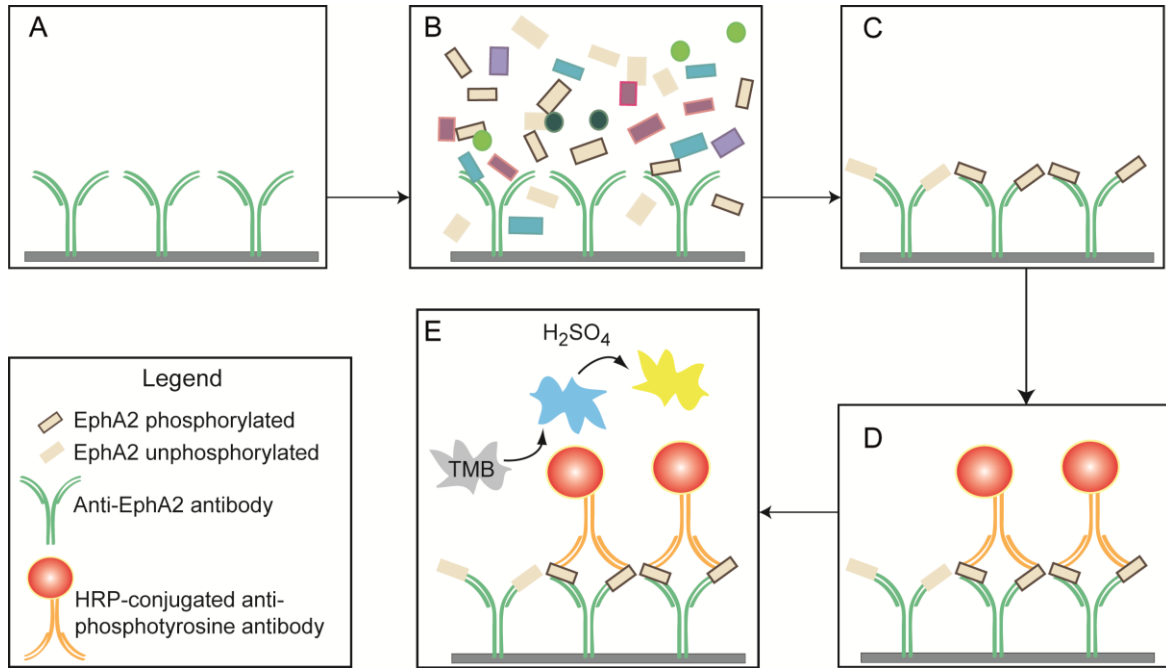


**Figure 3-4. EphA2 phosphorylation assay principle.**

**A)** ELISA plate well bottom coated with anti-EphA2 antibodies. **B)** Addition of cell lysate. **C)** Phosphorylated and unphosphorylated EphA2 receptors bind to anti-EphA2 antibodies. **D)** HRP-conjugated anti-phosphotyrosine antibody binds to phosphotyrosines of phosphorylated EphA2 antibodies. **E)** TMB substrate is converted by HRP, substrate reaction is stopped by addition of sulfuric acid. Components are not in scale.

One day before the assay,  $1 \times 10^6$  PC-3 cells were seeded into a cell culture 12-well multiwell plate and human EphA2 capture antibodies were coated to a clear F-Bottom Immuno Nonsterile Maxisorp 96-well plate according to the manufacturer's instructions. On the day of the experiment, cells were serum-starved for 4 h by changing to medium without FBS. Next, medium was removed and cells were treated with either 1xSWL-DNA trimer, 2xSWL-DNA trimer, 3xSWL-DNA trimer, natural ligand ephrin-A1, SWL peptide, DNA trimer only or 1x PBS/10 mM  $\text{MgCl}_2$  as negative control for 30 min at 37 °C. Cells were lysed using 250  $\mu\text{l}$ /well lysis buffer and assayed as indicated by manufacturer's instructions. Manifold washing was conducted after every step and the whole procedure was executed at room temperature. In brief, 96-well ELISA plates carrying human EphA2 capture antibodies were incubated with cell lysates of afore treated PC-3 cells. This was followed by the addition of anti-phospho-tyrosine-HRP antibodies which converts TMB substrate solution into a blue solution. Plates were incubated with TMB for 25 min (ligands in Figure 6-6) or 8 min (ephrin-A1 in Figure A 8). This reaction was stopped by adding 50  $\mu\text{l}$ /well 1 M  $\text{H}_2\text{SO}_4$  and absorbance was measured at 450 nm and at 520 nm in a microplate reader (Tecan, Germany); the latter was subtracted as reference value. To normalize values from concentration series, controls (only 1x PBS/10 mM  $\text{MgCl}_2$ ) were subtracted, too. Data was kindly analyzed by Dr. Martin

Sajfutdinow (Fraunhofer Institute for Cell Therapy and Immunology IZI, Germany), who fitted to the equation:

$$A = A_{min} + \frac{(A_{max} - A_{min})}{1 + \left(\frac{x}{EC50}\right)^{-b}} \quad (3)$$

where  $A$  is the observed absorbance,  $A_{min}$  and  $A_{max}$  are minimal and maximal absorbance respectively, and  $b$  is the Hill coefficient.

### 3.18 MST

Microscale thermophoresis enables the characterization of interactions between two molecules in solution<sup>136,137</sup>. It is based on the preferential drift of molecules in a temperature gradient, usually towards the direction of colder temperatures. If a molecule interacts with a binding partner, its mobility changes and can be tracked when one of the binding partners is fluorescently labeled. At first, a spot within the solution is warmed up by a laser which typically results in a movement of molecules out of the heated spot and leads to a local decrease in fluorescence. When the laser is switched off, the solution cools down and consequently the molecules move back into the spot, leading the local fluorescence to increase again. If molecules move like this, the process is called positive thermophoresis. When molecules move from the cold into the heated spot, the process is called negative thermophoresis. Basically, thermophoretic mobility is dependent on the temperature as well as charge, size and solvation shell of the molecules, and changes, if molecules interact with others. In this work, MST measurements were applied to study the binding of fluorescently labeled, PeB-modified DNA trimers to inactive influenza viruses.

Prior to the binding experiment, a capillary check (so-called cap scan) was performed to determine an optimal concentration of the fluorescent DNA trimers to reach recommended values of 200-300 fluorescence units (FU) for the measurement. As fluorescent DNA trimers were diluted 1:2 with inactive IAV X31, dilutions of 400 FU were prepared in HBSP buffer. Inactive IAV X31 were thawed, vortexed for 1-2 min, diluted to 1 mg/ml in HBSP buffer and 2-fold serially diluted (10  $\mu$ l per dilution) to a lowest concentration of 0.03  $\mu$ g/ml. Then, 10  $\mu$ l of the determined concentration of Atto655-labeled DNA trimers with PeB (3xPeB-DNA

trimer<sup>Atto655</sup>) or as control without PeB (0xPeB-DNA trimer<sup>Atto655</sup>) were added to the virus dilution series. Each dilution was filled into a Monolith NT.115 standard capillary (NanoTemper Technologies, Germany) and inserted into a Monolith NT.115 (NanoTemper Technologies, Germany). Data was evaluated using the MO.Affinity Analysis Software (NanoTemper Technologies, Germany).

### 3.19 Hemagglutination inhibition assay

The hemagglutination inhibition (HAI) assay is a commonly used assay to test whether inhibitors bind to HA and thus hinder viruses from agglutinating erythrocytes. HA proteins are capable of agglutinating erythrocytes once they bind to sialic acid on their surface. As a result, erythrocytes will stay in solution as cross-linked gel, instead of settling on the bottom of a plate or tube and form a visible red dot as they would normally do (Figure 3-5).

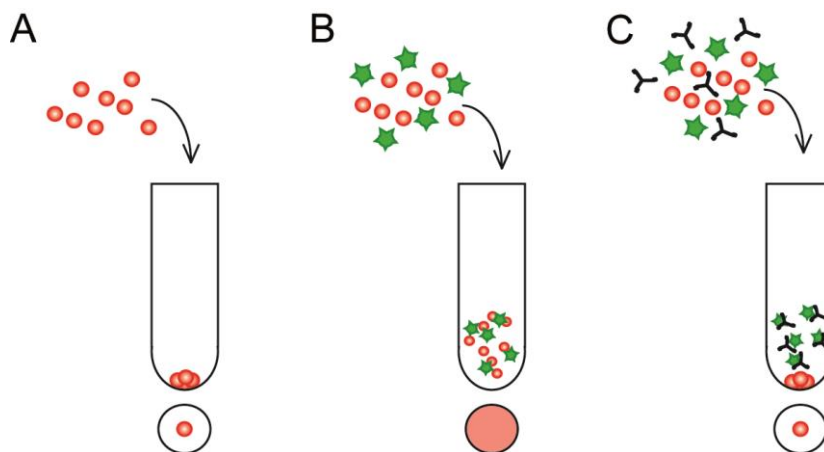


**Figure 3-5. Principle of HAI assay, side view (top) and bottom view (below).**

A) Red blood cells (red) settle at the bottom of a vial. B) Addition of IAV (green) leads to agglutination, red blood cells stay in solution. C) Addition of viral inhibitor (like 3xPeB-DNA trimer, black) prevents IAV from binding to red blood cells. As a result, red blood cells settle at the bottom of the vial. Components are not in scale.

HAI assays were performed by Dr. Daniel Lauster (Humboldt-Universität zu Berlin, Germany) according to Mammen *et al.* and Cross *et al.*<sup>138,139</sup>. In brief, inactivated X31 were used and adjusted to a titer of either 2 or 4 hemagglutination units (HAU) per 5  $\mu$ l. PeB-DNA trimers were applied to a clear 96 well microplate with U-bottom and diluted with DPBS (no calcium, no magnesium) in a 1:2 series. Then, X31 was added to the wells and incubated for 30 min at room temperature under slight agitation. Afterwards, 50  $\mu$ l of a 1% solution of human erythrocytes (equals  $\sim 2 \times 10^6$  cells/ $\mu$ l, obtained from German Red Cross Berlin, Germany) was



added and incubated for 1 h. The lowest concentration of PeB-DNA trimers that reached inhibition of hemagglutination complies the hemagglutination inhibition constant  $K_i$ HAI.

### **3.20 Flow cytometry**

Flow cytometry allows for analysis of size and inner complexity of single cells or particles (e.g. beads). Therefore, cells, located in a liquid stream, pass beams of laser light and consequently scatter light into several detectors. In line with the laser beam is a detector which recognizes the forward-scattered light (FSC) or diffraction of light that depends on the volume of cells. Another detector is positioned perpendicular to the light beam and measures the side-scattered light (SSC) or light refraction. This provides insight into the morphology and granularity of cells. Furthermore, flow cytometers are equipped with fluorescent detectors to examine fluorescently labeled cells or particles.

#### **3.20.1 Influenza A infection inhibition assay**

Upon infection with IAV X31, cells exhibit cytopathic effects (CPEs) such as rounding and detachment from the surface. Cell death is associated with shrinkage of cells; an effect that can be detected in flow cytometry as changes in FSC signals. By comparison of death and living cells, infection of MDCK cells with IAV X31 was estimated.

First,  $1.5 \times 10^4$  MDCK cells were seeded into a cell culture 96-well microplate with F-bottom (Greiner Bio One, Austria). The next day, 3xPeB-DNA trimers, PeB peptide, DNA trimer only or DPBS (calcium, magnesium) were mixed with IAV X31 (freshly defrosted and vortexed before used, final concentration of  $3.8 \times 10^5$  PFU/ml) and incubated for 30 min at 37 °C. All samples and virus dilutions were prepared with DPBS (calcium, magnesium). Cells were washed using DPBS (calcium, magnesium) and treated with prepared sample-virus mixtures, IAV X31 or DPBS (calcium, magnesium) for 1 h at 37 °C. After incubation, the samples were aspirated and the wells were incubated with virus growth medium for 2 days until a CPE was clearly visible in the IAV X31 only treated wells. Microscopic images were taken as described in 3.21.1. Then, the supernatant was transferred into new tubes. Attached cells on the well bottom were detached according to 3.9.1 and added to their corresponding supernatant into the tubes. This was done to compare all cells that are present in one well because dead cells that are not adherent anymore should also be analyzed by flow cytometry. Tubes were centrifuged at

1,150 rpm for 5 min at room temperature. The supernatant was discarded and the pellet was resuspended in 50  $\mu$ l/well DPBS (calcium, magnesium) analyzed using an iQue screener (IntelliCyt, USA).

#### 3.20.2 Bacteria binding assay

DNA 4arm structures containing one biotin molecule and three sugar molecules were built. The sugar molecules tested were mannose-based mono-, di-, tri- or hexasaccharides.

The following process was conducted by Dr. Jasmin Fertey (Fraunhofer Institute for Cell Therapy and Immunology IZI, Germany). First, biotin-labeled, sugar-modified DNA 4arm constructs were bound to *E. coli* (stably expressing either GFP or dsRed). Then, these complexes were used to bind Dynabeads™ MyOne™ Streptavidin T1 (Thermo Fisher Scientific, USA) via biotin (Figure 3-6). Due to the beads and with the help of a magnet, these complexes could be purified from unbound components. The goal was to compare the different sugar molecules for their ability to capture bacteria and to analyze this ability via flow cytometry.

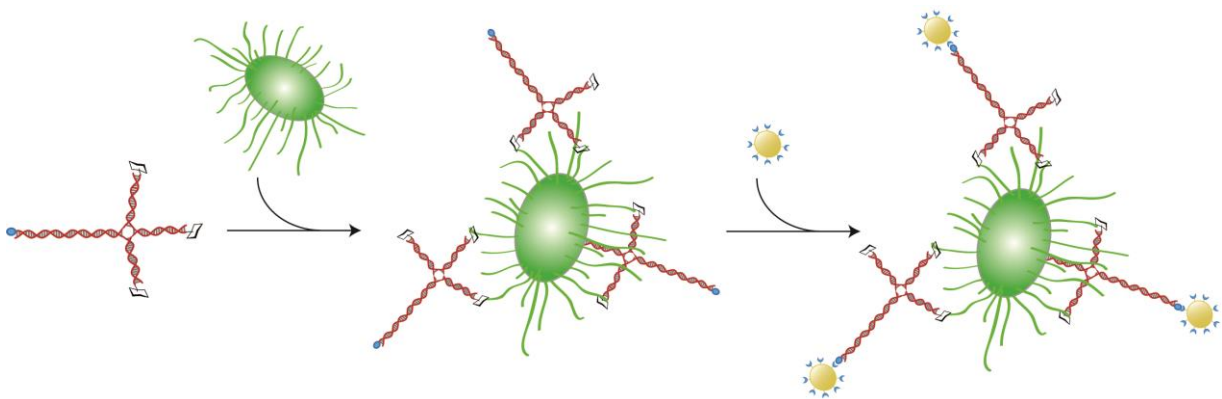


**Figure 3-6. Schematic bacteria binding assay.**

Sugar-conjugated (black), biotin-modified (blue) DNA 4arm structures (red) were incubated with *E. coli* bacteria (green). Bacteria were captured via streptavidin-coated (blue) beads (golden). Components are not in scale.

In brief, fluorescently labeled *E. coli* bacteria were grown overnight in ampicillin-supplemented Mueller-Hinton-Bouillon. According to previous studies, this kind of medium is supposed to induce the growth of pili<sup>140</sup>. The next day, *E. coli* were centrifuged at 4,000 rpm, 5 min at 4°C and washed twice with 1x PBS. The final pellet was resuspended in bacteria binding buffer. An OD<sub>600</sub> was adjusted to values between 0.4-0.6. Next, for each reaction, 45  $\mu$ l bacteria were mixed with 2  $\mu$ g DNA 4arm-sugar construct in a tube and filled up to 50  $\mu$ l with bacteria binding buffer. The mixture was incubated at 4 °C overnight. In parallel, 1  $\mu$ l beads per reaction were

blocked with 24  $\mu$ l bacteria binding buffer containing 0.2% BSA at 4 °C overnight. The next day, 25  $\mu$ l beads per reaction were added to 25  $\mu$ l of bacteria/DNA 4arm-sugar construct and incubated for 2 h at room temperature. Afterwards, the samples were transferred into a clear 96 well microplate with U-bottom and washed three times using a customized magnetic plate (Fraunhofer Institute for Manufacturing Engineering and Automation IPA, Germany) as well as bacteria binding buffer (100  $\mu$ l/well). The plate was analyzed using an iQue screener (IntelliCyt, USA) with detection filters 533/30 (FL1-A) for GFP labeled bacteria and 585/40 (FL2-A) for dsRed labeled bacteria.

### **3.20.3 EphA2 expression assay**

To confirm expression of EphA2 receptors on the cell membrane of PC-3 cells, they were probed with a PE anti-human EphA2 antibody (Biolegend, Germany) according to manufacturer's instructions. In brief, PC-3 cells were detached as described in 3.9.1 and a number of  $4 \times 10^4$  solubilized PC-3 cells were incubated with PE anti-human EphA2 antibody (Biolegend, Germany) for 30 min at 4 °C. Cells were washed with DPBS (no calcium, no magnesium) twice, collected by centrifugation and resuspended in 1x PBS/1% (w/v) BSA. In addition, HL-60 suspension cells were washed with DPBS (no calcium, no magnesium) and treated with the antibody in the same manner. Samples were analyzed using an iQue screener (IntelliCyt, USA) with detection filters 585/40 for PE.

### **3.20.4 EphA2 binding assay**

Binding of SWL-DNA trimers to PC-3 cells was assessed using a high-throughput flow cytometer. The day before assaying,  $1 \times 10^4$  PC-3 cells were seeded into a cell culture 96-well microplate with U-bottom. After serum starvation for 4 h, cells were washed with DPBS (no calcium, no magnesium), treated with serial dilutions of Cy3-labeled DNA trimers conjugated to three, two, one or no peptide SWL (3xSWL-DNA trimer<sup>Cy3</sup>, 2xSWL-DNA trimer<sup>Cy3</sup>, 1xSWL-DNA trimer<sup>Cy3</sup>, 0xSWL-DNA trimer<sup>Cy3</sup>, respectively) for 30 min at room temperature. Subsequently, cells were washed with DPBS (no calcium, no magnesium) and detached as described in 3.9.1. After centrifugation, cells were resuspended in 1x PBS/1% (w/v) BSA and analyzed using an iQue screener (IntelliCyt, USA) with detection filters 585/40 for Cy3.

### **3.21 Microscopic observation of cells**

Besides the following methods, cells were routinely visualized using a phase-contrast light microscopy. Thereby growth, confluency and phenotypical health (lack of bacterial or fungal contaminations) could be monitored.

#### **3.21.1 Detection of CPE in MDCK cells**

One day before treatment,  $1.5 \times 10^4$  MDCK cells were seeded into a cell culture 96-well F-bottom microplate and stored in the incubator overnight. The next day, samples were prepared and cells were treated as described in 3.20.1 until CPE was visible. Then, photos were taken using an inverting contrasting Leica DM IL microscope (Leica Microsystems, Germany) with 10x objective.

#### **3.21.2 PC-3 cell rounding assay**

PC-3 cells were checked for changes in cell morphology upon activation of EphA2 receptors and following signaling pathways. Briefly, sub-confluent PC-3 cells in cell culture 96-well microplate with F-bottom were serum-starved for 4 h and then incubated for up to 1 h with either 3xSWL-DNA trimer (20  $\mu$ M), natural ligand ephrin-A1 (1.5  $\mu$ g/ml), SWL peptide (150  $\mu$ M), DNA trimer only (20  $\mu$ M) or 1x PBS/10 mM  $\text{MgCl}_2$  as control. Microscopic images of PC-3 cells in the same spot were taken at different time points using an inverting contrasting Leica DM IL microscope (Leica Microsystems, Germany) with 10x objective to assess cell contraction and rounding.

## 4 Evaluating the binding of antibodies to epitopes separated by specific distances

### 4.1 Importance and aim

During manufacturing of mAbs, unwanted alterations in flexibility, angular orientation or any other physical and/or geometrical parameters between the two variable regions can result in changed binding affinities. Furthermore, non-canonical antibody modalities such as domain swapping<sup>141</sup> or antigen clasping<sup>142</sup>, as well as antibody-like formats such as reprobodies<sup>143</sup> necessitate new tools for investigating their geometry-specific multivalent binding.

In order to detect such changes or characterize different types of binding modes, there is great interest to develop effective functional tools to characterize the flexibility and conformation of mAbs, and the resulting impact on target binding. Until now, structural characterization is mostly done with mass spectrometry<sup>68</sup>. Recently, Jay *et al.* reviewed several imaging techniques to characterize antibody structures and found that individual-particle electron tomography (IPET) is the most suitable method for determination of structural dynamics<sup>3</sup>. A kit for determining antibody binding to antigens was introduced by the company Dynamic Biosensors GmbH<sup>144</sup>. Its focus lies on measuring the linear distances between two fab fragments which may be crucial for strong binding to antigens. Using neutron scattering, the distance between two antigen-binding sites of IgG antibodies was determined to be in the range of 11 to 14 nm<sup>145</sup>. In a recent study by Högberg and co-workers, a surface plasmon resonance (SPR)-based method was introduced to study the binding of antibodies to two antigens that are separated in various distances<sup>146</sup>. They discovered that IgGs prefer binding to epitopes that are separated by distances of 16 nm. While providing valuable information, all of these methods require expensive and/or highly specialized experimental platforms to carry out. This, combined with the degree of experience and training often needed to perform these methods with the necessary accuracy, highlights the need for methods that can be integrated into standard laboratory platforms.

In contrast to the aforementioned methods, an Enzyme Linked Immunosorbent Assay (ELISA) is easy to handle, inexpensive and can be conducted in a high throughput manner while at the same time maintaining high sensitivity and specificity. Therefore, an ELISA setup combined

with DNA-based templating of peptide-based epitopes was utilized to map the binding properties of several types of antibodies. DNA nanostructures are capable of spatially arranging different functional molecules, and due to the sub-nanometer resolution range for double-stranded DNA, the position of single molecules can be precisely controlled<sup>147</sup>. In this work, rigid DNA origami structures were used as substrates for positioning the peptide epitopes. The goal was the development of a universally accessible assay method that ascertains the extent to which mAbs are able to bind to two short peptide sequences that are attached onto DNA structures and separated in different distances to each other. If the two epitopes are arranged in a way which is reachable for both binding regions of the antibody, then the binding interaction is expected to be bivalent, and thus very strong in comparison to a single binding interaction between a binding region and epitope. In contrast, if the distance between the epitopes is too small or too big, the antibody cannot bind in a stable bivalent manner (Figure 4-1), and thus the strength of interaction would be more comparable to the monovalent case.

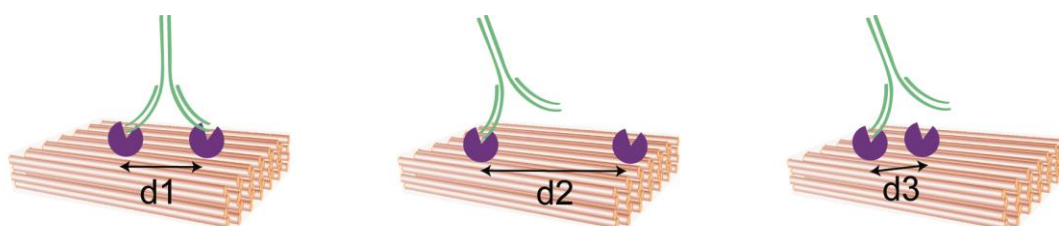


**Figure 4-1. Schematic of antibodies binding to DOhex structures.**

Measurement of spacing between the antibody's Fab fragments via binding of those to two ligands which are placed in distinct distances on the DOhex. Distance  $d_1$ , made by position of epitopes (violet), matches the accessibility of the antibody (green) whereas  $d_2$  and  $d_3$  are too far apart or too close, respectively. Components are not in scale.

Here, the focus lied on testing IgG antibodies since those are very well characterized, but also offer different variants for examining non-canonical binding modes. A main characteristic of IgGs is their huge intrinsic flexibility that helps them to adopt many conformations<sup>148</sup>. It is also known that the hinge region of the most abundant subclass IgG1 is very flexible and consists of 15 amino acids<sup>66</sup>. However, not only the hinge region determines the distances between antibody Fab fragments. A factor that controls the flexibility of Fab fragments is the angle between variable and constant region (called elbow angle)<sup>149</sup>. In humans, antibody light chains occur in  $\kappa$  and  $\lambda$  isoforms, which differ in their elbow angle. Stanfield *et al.* found that Fab fragment structures with  $\lambda$  chains tend to have a larger elbow angle than Fab fragments with  $\kappa$  chains<sup>149</sup>.

For establishing the DNA origami-integrated assay method, the ability of two anti- $\alpha$ -synuclein antibodies to bind to peptide pairs on DOhex structures was tested. To characterize the overall robustness of the system for both therapeutic and diagnostic/imaging antibodies and verify its ability to differentiate between binding modes, additional antibody-peptide pairs were tested with the DOhex ELISA setup: a commercially available anti-Actin antibody and an Anti-Human c-Myc antibody were probed for binding to two unique target peptides each. Those peptides were either directly derived from the target protein sequence (“naïve peptide”) or newly developed via phage display (“phage peptide”) by Dr. Michael Szardenings (Fraunhofer Institute for Cell Therapy and Immunology IZI, Germany). Epitopes selected from phage-display were also called mimotopes as they mimic the structure of the natural epitope.

Every ELISA was equipped with appropriate controls to exclude nonspecific binding and to find out whether the epitope can be bound by the antibody when attached to DNA nanostructures (Figure 4-2). Because the secondary antibody was the same for all ELISAs shown in this chapter, it could be used as baseline for background binding to compare general binding intensities.

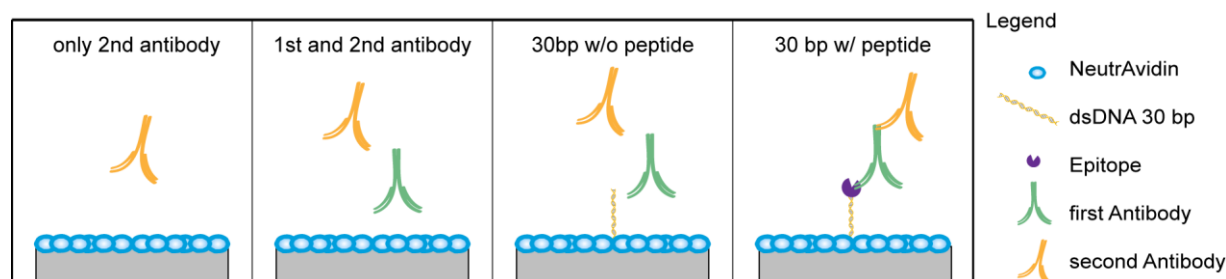


**Figure 4-2. Control samples for ELISA.**

After addition of a secondary antibody, the ELISA was continued as described in 3.17.1. From left to right, three negative controls and one positive control is shown.

ELISA components were added as indicated in section 3.17.1. After addition of DOhex structures (or controls) and the antibodies to be tested, the resulting binding interaction was verified by using a Goat Anti-Mouse IgG H&L (HRP) (abcam, UK) antibody that functioned as secondary antibody. ELISAs were further processed as described in 3.17.1. In order to compare independently performed ELISA assays, all values were normalized to the inter-peptide distance of 16.27 nm. This distance was closest to the most optimal space between two antigens suggested by Shaw *et al.*<sup>146</sup>. In the plots, the level of antibody binding to epitopes on the structures is represented by each bar.

## 4.2 Design of DOhex structures

DOhex structures with dimensions of  $\sim 50 \times 50$  nm were designed on a hexagonal lattice using the software caDNA<sup>54,150</sup> as shown in Figure A 2. They consist of two layers and were used as “molecular pegboard” to place epitopes onto defined locations (Figure A 1). By introduction of functionalizable linkers on the 5′-ends of individual staple oligonucleotides, a total number of six locations on one side of the structure could be functionalized with epitopes. During the process of folding, peptide-functionalized staples were incorporated at individual, unique points on the surface of the DOhex (Figure 4-3B) with the desired inter-peptide spacing. The oligonucleotides are illustrated as symbols ( $\circ$ ,  $\times$ ,  $\times$ ,  $\diamond$ ,  $\Delta$  and  $\square$ ). In order to avoid the possibility of one antibody bridging two neighboring DOhex structures to bind one epitope on each DOhex structure, strands for functionalization were selected to appear in the center of the structure (Figure 4-3B). Pairs of epitope-modified oligonucleotides were used to create different linear distances on the DOhex surface ranging from approx. 2 to 25 nm. The quality of coupling was determined via PAGE (Figure 4-4B). By including different pairs of epitope-carrying DNA strands in the DOhex assembly reactions (with the other four staples corresponding to the unused sites being unmodified), different distances between could be displayed. In addition, one of the staple strands on the other side of the DOhex was biotinylated for mounting DOhex structures to a NeutrAvidin™ coating on the ELISA plate well bottom. Correct folding of the DOhex structures was confirmed via AFM (Figure 4-3A) and agarose gel electrophoresis (Figure 4-4A).

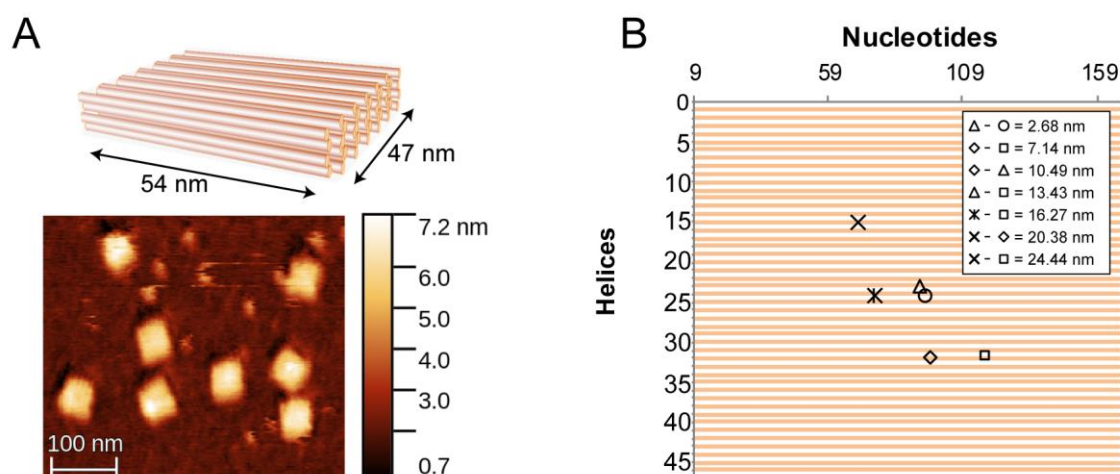


**Figure 4-3. Appearance of DOhex structure.**

**A)** Dimensions of DOhex structure (top) and AFM image of several DOhex structures on mica (bottom). **B)** Arrangement of six epitopes on surface of DOhex, view from the top. The inset displays inter-peptide distances that can be reached by combining two positions.



After folding, DOhex structures were filtered using Amicon® Ultra centrifugal filters with 100K MWCO. This step was essential to exchange buffer from folding buffer to 1x Origami ELISA buffer that contained Tween 20 to prevent nonspecific binding. In addition, this step was important as elimination of unbound biotin strands guarantees for optimal binding of DOhex structures to NeutrAvidin™-coated ELISA plate bottom. The lane in Figure 4-4A corresponding to unpurified DOhex shows an additional, faster cloud due to remaining unincorporated staple strands (“not pure”). After purification using Amicon Ultra-0.5 mL Centrifugal Filters with 100K MWCO, this second band is almost gone (“pure”).

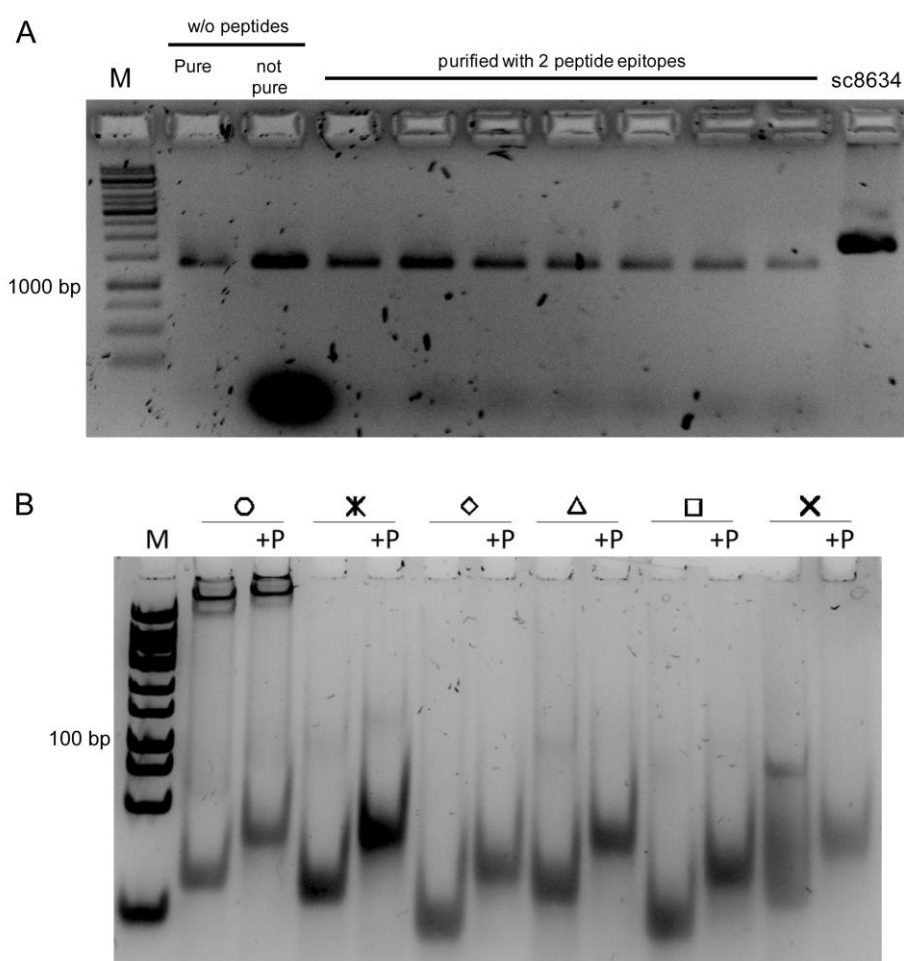


**Figure 4-4. Analysis of conjugated DOhex structures.**

**A)** Verification of DOhex folding. 1.5% (w/v) agarose gel showing DOhex structures with different combinations of peptide-containing strands. Gel was stained with ethidium bromide afterwards. Sc8634 = scaffold strand 8634. M = GeneRuler 1 kb DNA Ladder (Thermo Fisher Scientific, USA) serves as control, not as ruler. **B)** 15% (v/v) native PAGE. Representative image shows conjugation of six staple strands (legend for characters can be found in Figure A 1) with ED10. Each strand was applied with DBCO modification and after addition of ED10 (“+P”). The gel was stained with SYBR® Gold Nucleic Acid Gel Stain (Thermo Fisher Scientific, USA) and imaged under UV light. M = GeneRuler™ Low Range DNA Ladder (Thermo Fisher Scientific, USA).

Conjugation of peptide epitopes to staple strands could be proved by native PAGE. As an example, the gel in Figure 4-4B shows staple strands modified with peptide ED10. The upward shift indicates the successful addition of peptide to DNA. Only staples with a conjugation yield of > ~90% were used for folding. Additional upper bands for the strands with the circle symbol indicate aggregation and were already present in the unmodified freshly dissolved version of the strand without DBCO modification.

Folded and filtered DOhex structures were subsequently utilized to perform ELISA experiments. Biotinylated DOhex structures without peptide epitopes on the surface served as controls.

### 4.3 $\alpha$ -synuclein antibodies

The ability of two  $\alpha$ -synuclein antibodies 5G4 and 10D2 to bind to peptide epitopes separated in various distances was assessed. Therefore, DOhex structures displaying either two peptides ED10 or two peptides ED9 in different distances to each other, were coated onto ELISA plates and incubated with 5G4 and 10D2, respectively. After incubation, ELISAs were further processed as described in 3.17.1.

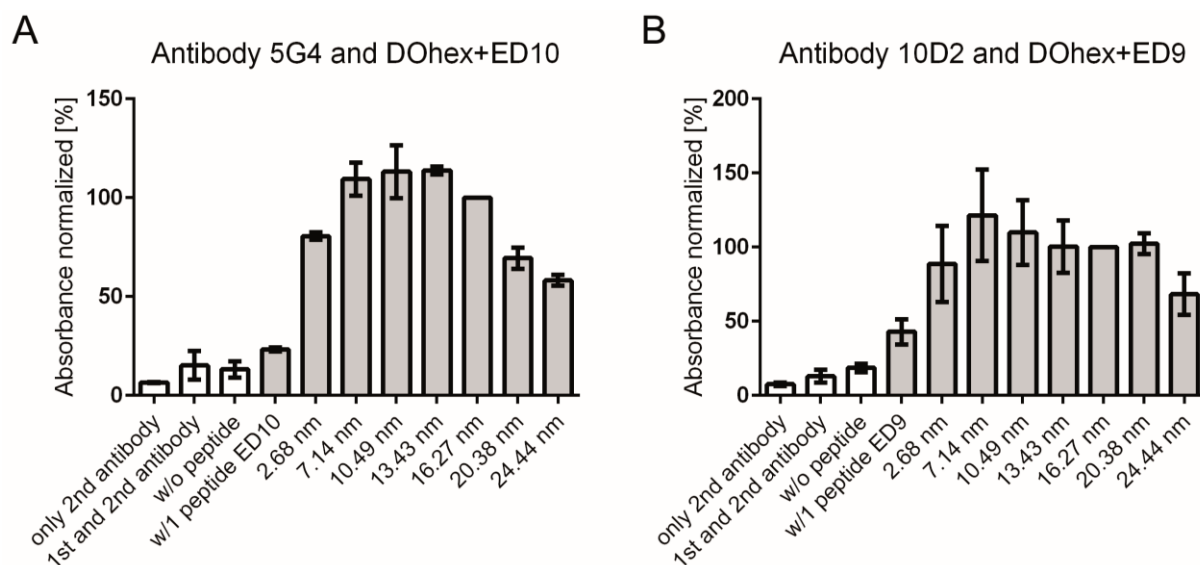


**Figure 4-5.  $\alpha$ -Synuclein antibodies binding to ED10 and ED9 on DOhex structures.**

Mean values of net absorbance ( $A_{450\text{ nm}} - A_{520\text{ nm}}$ ) of three times triplicates  $\pm$  standard deviations were normalized to an inter-peptide distance of 16.27 nm. White bars on the left side of the graph show control samples. **A)** Antibody 5G4 was diluted to a concentration of 0.9  $\mu\text{g/ml}$ ; the secondary antibody (Goat Anti-Mouse IgG H&L (HRP) was diluted 1:5000. **B)** Antibody 10D2 was diluted to a concentration of 0.3  $\mu\text{g/ml}$ ; the secondary antibody (Goat Anti-Mouse IgG H&L (HRP) was diluted 1:15000.

Figure 4-5A indicates that antibody 5G4 bound epitopes in distances from 7.14 nm – 16.27 nm the best. Distances  $\geq 20.38$  nm and  $\leq 2.68$  nm resulted in weaker binding and/or faster dissociation. DOhex structures displaying one ED10 peptide show absorbance signals that were about four times lower (~23%) than signals from DOhex structures carrying epitopes placed in distances from 7.14 nm – 16.27 nm (~100%).

Antibody 10D2 also showed low affinity towards DOhex only and bound a broader spectrum of distances of ED9 starting from  $\geq 2.68$  nm – 20.38 nm (Figure 4-5B). Interestingly, absorbance signals caused by DOhex structures carrying one ED9 peptide were about half as high (~43%) as signals from DOhex structures carrying two peptides (~100%).

Nonspecific binding of 5G4 or 10D2 to unmodified DOhex structures could not be detected. Also, both  $\alpha$ -synuclein antibodies and the secondary antibody did not nonspecifically bind to the NeutrAvidin™ coated wells.

### 4.4 Anti c-Myc antibody

The anti c-Myc antibody Myc1-9E10 and a part of the described peptide G, used here as the “naïve peptide” (CN)<sup>79</sup> were chosen to examine binding. A crystal structure of this complex was already analyzed<sup>151</sup>. Interestingly, this indicated that one single peptide (denoted as “tag” in the publication) is simultaneously bound by two Fab fragments of one antibody. This mode of binding can be more broadly defined as “antigen clasping”<sup>142</sup>. One Fab fragment binds the core sequence LISE of the peptide whereas the other Fab fragment binds to the termini of the peptide (amino acids EQ and LN of C-terminal epitope). By means of phage display, a mimotope for the Anti-Human c-Myc antibody was found and determined as “phage peptide” (CP). While lacking the flanking EQ and LN motifs that enable binding to a secondary Fab fragment, it was still observed to bind the antibody, and was also evaluated in DOhex-integrated ELISAs.

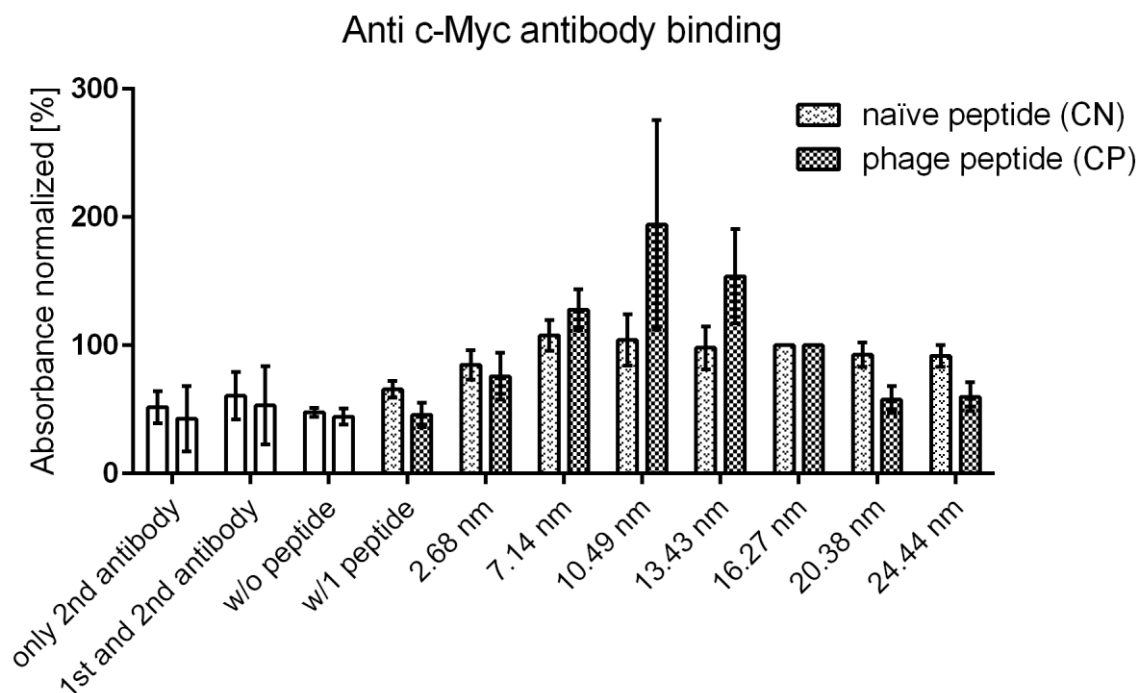


**Figure 4-6. Anti c-Myc antibody binding to CP and CN on DOhex structures.**

Mean values of net absorbance (A450 nm - A520 nm) of three times triplicates  $\pm$  standard deviations were normalized to an inter-peptide distance of 16.27 nm. White bars on the left side of the graph show control samples. Anti-Human c-Myc antibody was diluted to a concentration of 0.05  $\mu\text{g/ml}$ . The secondary antibody (Goat Anti-Mouse IgG H&L (HRP), abcam, UK) was diluted 1:4000.

Obvious binding differences, resulting from displaying CN peptides pairs at different distances from each other, were not detectable, although clear differences were observed for DOhex without, with one or with two CN peptides (Figure 4-6). Starting from 7.14 nm, binding was still observed for distances up to 24.44 nm, however with only slight decrease towards greater distances. Even at larger inter-peptide distances, a stronger binding signal was observed for all pairwise combinations of two peptides than for the control with only a single peptide on DOhex.

In contrast to that, DOhex structures carrying CP peptides revealed increased antibody binding for distances between 7.14 nm - 13.43 nm which is a shorter distance than previously suggested as the optimal range between antigens<sup>146</sup>. Binding at larger distances, particularly over 20 nm, was roughly comparable to that for DOhex bearing a single peptide. Neither antibodies show any evidence of nonspecific binding to the DNA of the underlying structures. Whereas DOhex structures with one CP peptide reach absorbance values of  $\sim 46\%$ , two mimotopes in distances from 7.14 nm – 13.43 nm give values that are about three times higher ( $\sim 159\%$ ).

In comparison to signals from ELISAs using  $\alpha$ -synuclein antibodies, the signals were in general lower which was indicated by the higher background of the antibodies only controls.

#### 4.5 Anti-Actin antibody

Binding of anti-Actin C4 to two epitopes was assessed via ELISA, too. These epitopes were either part of the sequence for rabbit actin<sup>152</sup> and termed “naïve peptide” (AN) or a ”phage peptide” (AP) that has been derived by phage display.

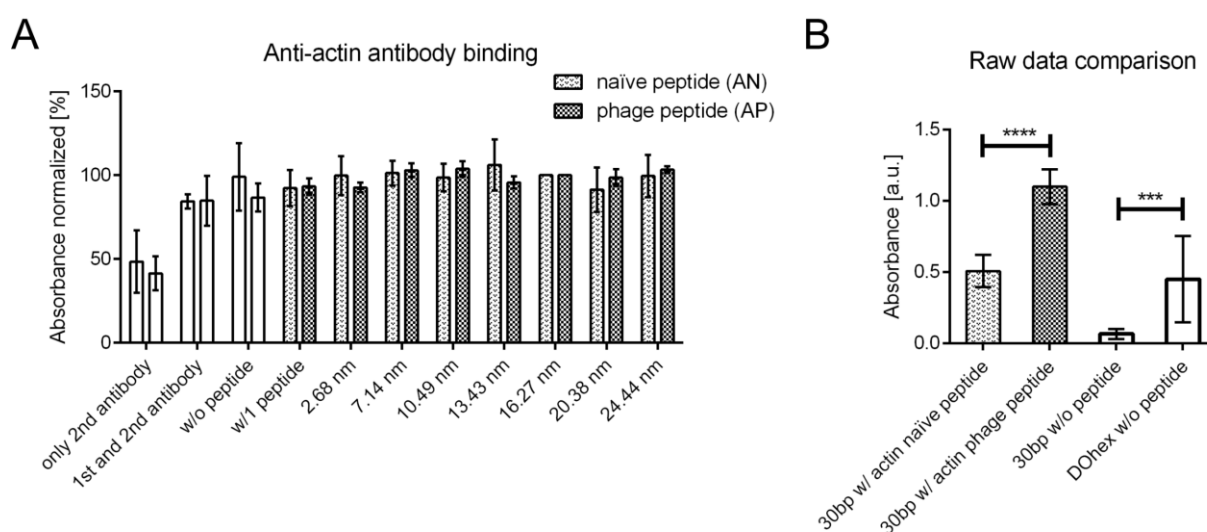


**Figure 4-7. Anti-actin antibody binding to AP and AN on DOhex structures.**

**A)** Mean values of net absorbance ( $A_{450\text{ nm}} - A_{520\text{ nm}}$ ) of three times triplicates  $\pm$  standard deviations were normalized to an inter-peptide distance of 16.27 nm. White bars on the left side of the graph show control samples. Anti-Actin antibody was diluted to a concentration of 0.5  $\mu\text{g/ml}$ . The secondary antibody (Goat Anti-Mouse IgG H&L (HRP), abcam, UK) was diluted 1:5000. **B)** DOhex structure w/o peptide, biotinylated double-stranded DNA (30 base pairs) carrying either one naïve peptide, one phage peptide or no peptide were tested for antibody binding. Shown are mean values of net absorbance ( $A_{450\text{ nm}} - A_{520\text{ nm}}$ ) of five replicates  $\pm$  standard deviation. One-way ANOVA followed by Tukey’s test was used for determination of p values (\*\*\*\*,  $p \leq 0.0001$ ; \*\*\*,  $p \leq 0.001$ ).

In comparison to signals from ELISAs using  $\alpha$ -synuclein antibodies, the signals were in general lower which was indicated by the higher background of the secondary antibody control (Figure 4-7A). High background binding of anti-Actin antibody to NeutrAvidin™ coated wells could be detected, too. Additionally, high absorbance signals from wells containing DOhex structures w/o peptides occurred, indicating the presence of nonspecific binding between the antibody and underlying DNA origami structure. Presentation of one or two peptides on DOhex structures did not lead to an increase in binding. Consequently, the anti-actin antibody showed no clear binding to AN or to AP placed in at different distance on DOhex structures.

To identify if the antibody preferentially binds more strongly to one of the two peptides, raw absorbance data of an ELISA positive control (biotinylated dsDNA carrying either AN or AP) was plotted. Figure 4-7B displays that the antibody has significantly higher affinity to the mimotope (AP) than to the version of the naïve epitope (AN). Binding to unmodified dsDNA is low. Interestingly, binding of the anti-actin antibody to both DNA structures without peptides was significantly different. While binding to dsDNA w/o peptide is comparatively low, binding to DOhex w/o peptide was found to be higher.

### 4.6 Discussion

Antibodies bind their epitopes in a multivalent manner. While for instance IgG antibodies typically bind their target bivalently, IgA antibodies have four binding sites and IgM antibodies exist as decamer and bind pentavalently<sup>153,154</sup>. In this chapter, an ELISA-based method to study the bivalent binding of antibody Fab fragment to their epitopes was introduced.

DNA origami structures were designed to serve as platform for displaying two epitopes that were ~2.5 nm to 25 nm apart. DNA origami structures allow for accurate placement of molecules like epitopes on their surface. Furthermore, theoretical distances between attached molecules can be calculated. Nevertheless, these distances can slightly vary due to structural fluctuations of the DOhex structures or the choice of linking molecules (e.g. spacers) between the DNA strands and peptides. DNA origami structures are exposed to a variety of electrostatic, hydrophobic, thermal and solvation forces. Those can affect structural dynamics and local mechanical properties<sup>155</sup>. In order to more accurately validate the data obtained by ELISA experiments, it would be necessary to confirm the mathematically determined distances in an experimental setup or via computational modelling. Possible options are for instance the program CanDo<sup>50,156</sup>, all-atom molecular dynamics simulations as described by Yoo *et al.*<sup>155</sup> or by small-angle X-ray scattering using gold nanoparticles<sup>157</sup>. Taking into the account the introduced linkers, e.g. the aminolink C6 on ssDNA and DBCO that has been added during conjugation, it can be assumed that the attached peptides are flexible to some extent and might be able to bend slightly towards Fab fragments of antibodies in proximity.

For  $\alpha$ -synuclein antibodies, explicit signatures of the antibodies' affinity to the peptide could be determined. Antibody 5G4 could bind well to epitopes that were 7.14 nm – 16.27 nm apart. In

comparison, signals from binding to DOhex structures with only one ED10 peptide were only very low. Those findings are consistent with literature<sup>75</sup> reporting that 5G4 primarily attaches to aggregations of many  $\alpha$ -synuclein proteins organized in a plaque rather than to single monomeric targets. Antibody 10D2 was able to bind epitopes in all tested distances  $\geq 2.68$  nm to similar extends. This might be attributed to its capacity of binding monomeric and a variation of aggregated  $\alpha$ -synuclein forms. Therefore, the distance between the epitopes would not matter as long as the peptides are accessible for the antibody.

The ELISAs involving 5G4 and 10D2 seem to demonstrate the difference between a multivalent and an additive effect. In case of 5G4, presentation of two epitopes led to an increase in binding signals that were about more than four times higher than signals arising from DOhex structures with one epitope. This usually indicates that one antibody can bind simultaneously with both Fab fragments to its target epitopes on the DOhex structure, i.e. a multivalent binding effect. In contrast to that is the binding profile of 10D2. DOhex structures with two ED9 epitopes led to signals that were only double compared to structures carrying one ED9 peptide, and furthermore showed no dependence upon distance. Looking at Fig. 1a of the supplemental material of<sup>75</sup> it becomes clear that 10D2 binds monomeric and  $\alpha$ -synuclein aggregations of different sizes. In contrast to that, 5G4 binds to aggregations of  $\alpha$ -synuclein of a distinct size and not to monomeric  $\alpha$ -synuclein. This also matches the results of the ELISAs conducted in this project.

For the anti c-Myc antibody clone 9E10, comparing distance-dependent binding profiles for two target peptides highlighted the difference between its two binding modes. Comparing CN with the sequence of the “tag” peptide in the paper by Höhne and co-workers<sup>151</sup>, it becomes clear that the core part KLISEED is conserved and that only minor differences can be found in the terminal flanking sequences. The core part is known to be normally bound by the CDR H3 of the antibody’s Fab fragment. The N-terminal amino acids EQ and the C-terminal amino acids LN are able to simultaneously bind to the two Fab fragments. While the LN motif is altered to LL in peptide CN and furthermore serves as the anchor point to the underlying DOhex structure, and thus likely loses its affinity for secondary binding, the N-terminus EG is nevertheless conserved and would be expected to participate in the “antigen clasping” binding mode. Since this effect of binding was seen for Fab fragments in solution as well as for the whole antibody in solution, this is expected to be applicable for the conditions in the ELISA setup here. Resultingly, binding of the Anti c-Myc antibody to two CN peptides on the surface of DOhex structures did not seem to be dependent on the distance between both peptides. This could be

due to the fact that one antibody binds to one CN peptide with both Fab fragments and therefore, the distance between two peptides does not matter that much. In accordance with that, it is also likely that two antibodies bind to one CN one DOhex. Either of these mechanisms would explain why the binding signals do not severely change for greater distances.

Table 4-1 provides a sequence comparison between “tag”, CN and CP. In contrast, peptide CP is not as negatively charged as CN and the core structure HLVSERD differs in three amino acids from the core of CN (KLISEED). Aside from the exchange of E to R (negatively charged amino acid is replaced by positively charged amino acid) in the second-to-last position of the core motif, all other exchanges are like-for-like; the two other amino acids K and I were replaced by H (like K positively charged) and V (like I with hydrophobic side chain), respectively. Due to this it was assumed that the core of CP still likely displayed normal binding to a single Fab fragment. However, in comparison to the “tag” and CN sequences, the N- and C-terminal ends of CP would not be expected to participate in non-canonical antigen clasping of two Fab fragments. In the case of the C-terminal end, its direct chemical anchoring to the DNA strand at the surface of the DOhex structure as well as the replacement of an uncharged amino acid (N) with a negatively charged one (E) are expected to make the site both sterically unavailable and physiochemically unsuitable for binding. At the N-terminus of CN, the loss of the negatively-charged amino acid E is also expected to eliminate its affinity to bind the antibody Fab fragments.

**Table 4-1. Comparison of CN and CP peptides**

“Tag” peptide		E	Q	K	L	I	S	E	E	D	L	N	
CN	E	E	Q	K	L	I	S	E	E	D	L	L	R
CP			Q	H	L	V	S	E	R	D	L	E	
Like-for-like exchange CN → CP?				+		h			x			x	

+ = yes, both positively charged, h = yes, both hydrophobic, x = no, exchanges of amino acids with different charges

These factors indicate that while CP is still able to participate in “normal” binding to a single Fab fragment at its core, its participation in antigen clasping is missing in comparison to “tag” and CN. Therefore, it is likely that CP can be only bound by one Fab fragment and thus, one antibody binds to two CP peptides in a typical bivalent interaction. To conclude, CN might be able to retain the ability to simultaneously bind to two Fab fragments whereas CP enables only binding to one Fab fragment.



Unfortunately, the Anti-actin antibody did not show an enhanced affinity towards DOhex structures displaying the AP and AN peptides. The antibody bound to all variations of DOhex structures with same affinity (Figure 4-7A). This could be due to geometrical constraints of the antibody sterically inhibiting the simultaneous binding of both Fab fragments to peptides on the planar origami surface, or some other factor such as charge-based repulsion. Unfortunately, structural data such as X-ray crystallography or cryo-EM is not available for this antibody. Based on overall binding levels, AP bound significantly better to the anti-Actin antibody than AN. Both AP and AN have the sequence PRAVF in the center in common and differ at the N- and C-terminal ends. AP is one amino acid shorter and is higher negatively charged than AN. A difference in binding could be detected between the controls made of dsDNA w/o peptide and DOhex structures w/o peptide. The reason for this might be the elevated local amount of negative charges coming from densely packed DOhex structures. It is possible that this charge contributed to a repulsion of the antibody thus the signals were not clearly higher than background signals that arose from unspecific binding of the anti-Actin antibody to the NeutrAvidin™ coated plate surface.

The method presented here is a novel solution to determine binding and flexibility of antibody Fab fragments. The data obtained for  $\alpha$ -synuclein antibodies and the Anti c-Myc antibody binding to different epitopes was largely consistent with previous structural and functional studies. First, the  $\alpha$ -synuclein antibodies support the differences between one antibody targeting  $\alpha$ -synuclein aggregations only and the other antibody targeting both monomeric and aggregated forms of  $\alpha$ -synuclein. Second, the results for the anti c-Myc antibody allow for differentiation between normal and non-canonical (antigen clasping) binding modes. To sum up, for these three antibodies, defined binding signatures could be determined and reproduced. Limitations of the method occurred when examining the anti-Actin antibody and might also occur with other antibodies.



## 5 Capturing pathogens via peptide- or sugar-coupled DNA nanostructures

Multivalent strategies have previously been used in studies for developing viral inhibitors for noroviruses<sup>158</sup>, influenza<sup>159</sup> or human immunodeficiency viruses (HIV)<sup>160</sup>. Additionally, multivalent ligands for binding *E. coli*<sup>161–163</sup> as well as for binding bacterial toxins<sup>164</sup> have previously been reported. In contrast to these predominantly polyvalent approaches, the objective of the projects presented in this chapter was to bind and block surface structures of pathogens in an oligovalent manner. This is different from the aforementioned polyvalent approaches, where binding inhibitors are presented in a structurally undefined arrangement on a scaffold. In the oligovalent setups described in this chapter, valency and spacing of ligands were strictly controlled by target-oriented positioning onto small DNA nanostructures. Ligands that are displayed on DNA constructs in an oligovalent way could be valuable inhibitors for pathogens as they are presumably more active than in their monovalent appearance. The functionalized DNA constructs used in this chapter function as something that could be roughly described as “synthetic antibodies”. Unlike antibodies, they can comprise more than two binding units and the attachment of functional molecules such as fluorophores is straightforward. The design, development, synthesis and quality control of new antibodies is a time consuming and costly process. As an alternative, short peptides derived from the antibody’s paratope that specifically bind the antibody’s epitope are much easier to produce. Those small peptides can be mounted onto DNA nanostructures and their position can be easily adjusted to the desired target structures.

Another interesting advantage of DNA is the material itself. Studies on dengue viruses furnish evidence that DNA nanostructures also electrostatically catch and separate virions from the host cell membrane through their negative charges<sup>165</sup>.

In this work, the fusion proteins of the viral respiratory pathogens influenza A (namely HA) and RSV (namely RSV-F) were bound by oligovalent peptide-DNA ligands in order to prevent them from attaching to host cell membranes. In the case of RSV, another goal was to lock the fusion protein in its prefusion conformation and thus impede the virus from invading host cell membranes. Furthermore, different mannose-based sugar compounds were presented on DNA

structures and offered to an *E. coli* strain in order to find the best *E. coli* binding sugar-DNA structure.

### 5.1 Global burden of pathogenic infections

#### 5.1.1 Influenza A virus

Influenza viruses cause respiratory diseases in humans, commonly known as the “flu”. Outbreaks of influenza viruses are known at least since the Middle Ages. Seasonal influenza outbreaks involve influenza A and B and occur every year in winter (in temperate climates). In worst cases, influenza A viruses (IAV) can spread transnationally and hence becomes a so-called pandemic. IAV pandemics are often associated with high levels of morbidity and mortality. The most severe IAV pandemic in recent history lasted from 1918 until 1920, was caused by an H1N1 strain and was called Spanish flu. It was exceptional deadly and accountable for ~50 million deaths<sup>166</sup>. The most recent influenza pandemic, called swine flu, happened from 2009-2010 and was mainly caused by the new strain A(H1N1)pdm09. Currently, the new strain from 2009, A(H1N1)pdm09, and A(H3N2) influenza viruses are circulating in humans. IAVs infect nose, throat and lungs, and in cases of uncomplicated infection cause symptoms like nasal discharge, coughing, fever and breathing difficulties. Healthy people react to annual influenza epidemics with immune responses and suffer from mild upper respiratory tract infection. However, in people with severe or progressive clinical illness (e.g. chronic pulmonary or cardiac disease or diabetes mellitus), infants or adults aged 65 years and older, the viruses can expand into the lower respiratory tract. Those people are at risk of developing severe breathing problems, bronchitis, otitis media and/or viral pneumonia that can be fatal. According to estimations from December 2017, respiratory deaths related to seasonal influenza increased to 290,000-650,000 worldwide<sup>167</sup>. Thus, seasonal influenza is a tremendous threat to human health worldwide.

At present, three classes of antiviral drugs have been approved for treatment of influenza infection: Adamantane derivatives (e.g. amantadine and rimantadine) which block the M2 ion channel and are solely active against IAV, a selective inhibitor of influenza cap-dependent endonuclease (baloxavir), and NA inhibitors (Relenza™ (zanamivir), Tamiflu™ (oseltamivir), Inavir™ (laninamivir octanoate) and Rapivab™ (peramivir)) which inhibit both influenza A and

B. Unfortunately, all currently circulating influenza viruses have acquired resistance to adamantane drugs and consequently those drugs are not used anymore<sup>168</sup>. Additionally, some strains resistant to NA inhibitors have already emerged and spread, thus making treatment options even more difficult<sup>169</sup>. Therefore, new antiviral drugs are urgently needed. Since around 80% of viral surface glycoproteins are HA trimers, and since their regions responsible for binding and fusion are highly conserved, they are increasingly becoming a potential target antigen for new drugs. In the wake of this, a number of broadly neutralizing antibodies targeting the stem and head regions of HA have been identified<sup>170</sup>.

Currently, influenza vaccines are the best possible prophylaxis of seasonal influenza. Those vaccines contain inactivated influenza viruses from different strains that are predicted to circulate in the upcoming influenza season. Due to antigenic changes in HA and NA over time and therewith associated resistance, influenza vaccines have to be updated and administered annually<sup>171</sup>. Influenza vaccinations help to decrease the severity and the rate of influenza infections. Scientist aim to develop vaccines that are long-lasting and confer a broad protection against seasonal as well as pandemic influenza viruses.

### 5.1.2 RSV

While in most cases, RSV infections of healthy adults manifest in mild respiratory symptoms, infants, elderly or immunocompromised people are prone to develop respiratory tract infection such as bronchiolitis or pneumonia. A study estimated that in 2015, 33.1 million cases of acute lower respiratory infections worldwide were associated with RSV. They entailed about 59,600 in-hospital deaths in children under the age of 5 years and 27,300 in-hospital deaths in children younger than 6 months<sup>172</sup>. Most cases of acute lower respiratory infections and associated deaths resulting from an infection with RSV occur in developing countries. In industrial countries, mortality associated with RSV infections is rare, but the economic burden due to medical needs is nevertheless enormous. RSV infections occur seasonally and are widespread. It is anticipated that almost all children have been infected with RSV by 2 years of age<sup>173</sup>. Furthermore, RSV infections during childhood can lead to asthma and persistent wheezing<sup>174</sup>.

Treatment of RSV infections is basically symptom management and supportive care. The only licensed drug against RSV is Ribavirin. It is a nucleoside analogue that inhibits RNA transcription and is given in cases of acute RSV infection. Unfortunately, it has little or no

significant effect on reduction of RSV load, is very expensive and not recommended for routine use because of safety concerns<sup>175–177</sup>. Furthermore, it does not specifically act on RSV but also on other viruses like influenza or adenoviruses.

As of today, there is no effective vaccine against RSV infection on the market. The mAb palivizumab (Synagis®) was approved as immunoprophylactic by the Food and Drug Administration (FDA) in 1998 and can prevent RSV infection of infants. It targets the highly conserved antigenic site II which is accessible on both prefusion and postfusion RSV-F<sup>98</sup>. Due to high costs and the need for repeated administration, palivizumab is only given to high-risk patients and difficult to obtain in developing countries.

Antibodies against RSV-F can hinder viruses from entering cells and thus reduce illnesses caused by RSV. The antibody motavizumab is more potent than palivizumab and also targets both pre- and postfusion RSV-F<sup>178</sup>, but failed due to concerns on the risk/benefit profile<sup>179</sup>. However, it has been presumed that most RSV-neutralization activity only comes from antibodies specifically targeting prefusion RSV-F<sup>180</sup>. In 2013, McLellan *et al.*, characterized a set of prefusion-specific antibodies, namely D25, AM22, and 5C4, that bound to antigenic site Ø of prefusion RSV-F and appeared to be more potent than Palivizumab<sup>85,181</sup>. Antibody D25 is able to bind to single monomeric RSV-F protomers and supposedly freezes it in its prefusion conformation.

### 5.1.3 *E. coli*

In addition to viral infections, bacterial infections present major global health problems and affect young children in particular. Bacteremia, meningitis, and respiratory tract infections comprise the most prevalent severe neonatal infections and occur upon infection with pathogens like *Escherichia coli*, *Klebsiella* sp., *Staphylococcus aureus* and *Streptococcus pyogenes*<sup>103</sup>. As a consequence of bacteremia (presence of bacteria in the blood), systemic responses of the body's immune system can evoke sepsis. The most common human diseases caused by strains of *E. coli* are urinary tract infections and diarrhea. Urinary tract infections have been estimated to affect about 150 million people worldwide each year<sup>182</sup>. In the urinary tract, FimH targets the glycoprotein uroplakin Ia that presents high-mannose type *N*-glycans and is located on the mucosal surface of the bladder. In 2016, enterotoxigenic *E. coli* diarrhea led to 51,186 deaths among all age groups globally<sup>183</sup>. Particularly, low- income and middle-income countries are

affected the most. Although antibiotics can be used to successfully treat patients with bacterial infections, the emergence of antibiotic resistant bacterial strains becomes an increasing concern. Another aspect is the formation of biofilms. While in the gut, biofilms can be advantageous for both bacteria and host, biofilm formation on medical devices and implants is problematic due to their entrenched structure which makes it difficult for antibiotics to neutralize all bacteria in a biofilm. Biofilms cannot easily be removed by disinfectants, antibiotics or mechanically<sup>184</sup>.

## 5.2 Binding and blocking influenza A via peptide-DNA constructs

### 5.2.1 Aim

HA of IAV was the first described lectin and as the name suggests, hemagglutinin induces agglutination of erythrocytes<sup>185</sup>. In 1995, Mammen *et al.* could prove that a variety of polymeric inhibitors containing sialic acid hindered IAVs to bind to erythrocytes<sup>138</sup>. They found that besides binding affinity also steric stabilization as well as temperature have an influence on multivalently induced binding inhibition. A few years later, the same group could show that due to multivalency, the binding of several HA trimers to sialic acid receptors on erythrocytes had an affinity of  $10^{13} \text{ M}^{-1}$ . In comparison, an affinity of  $10^3 \text{ M}^{-1}$  was found for monovalent binding between sialic acid and a single HA receptor<sup>4</sup>. Findings like this prove that binding HA in a multivalent manner is a promising approach to detect or block IAV.

In 2016, Memczak *et al.* presented peptides derived from the CDRs of the HA-binding monoclonal antibody HC19<sup>186</sup>. This antibody binds to a discontinuous receptor binding site in the HA1 unit that is conserved among several influenza serotypes and acts as competitive HA inhibitor<sup>187,188</sup>. Among the presented peptides, two were able to bind to influenza A/Aichi/2/68 H3N2 at the sialic acid binding site of HA1. One of them, PeB, exhibited an inhibitor constant  $K_i\text{HAI}$  of  $235 \pm 15 \mu\text{M}$  in HAI assays and  $\text{IC}_{50}$  values of  $32 \pm 5 \mu\text{M}$  in infection inhibition assays. As values like these are rather high for medical applications, the aim of this project was to improve the efficacy of PeB by multivalent presentation of several PeB peptides. Since HA is a homotrimeric receptor, three peptides PeB were conjugated to the DNA trimer structures which function as scaffold material. As reported by Papp *et al.*, the distance between two HA trimers is 10 nm and the receptor binding sites within one HA trimer are 4 nm apart<sup>189</sup>. The flexibility of the DNA trimer junction might allow the attached PeB peptides to bind to the homomers of either one HA trimer or to two homomers from different neighboring HA trimers.

In order to confirm that PeB remains active when attached to DNA, ELISA assays were conducted. Differences in binding to IAV dependent on valency were examined in MST experiments. The ability of PeB-DNA trimers to block HA and thus hinder IAVs from infecting cells was tested via HAI assays, flow cytometry analysis of cells and microscopic imaging.

### 5.2.2 Construction of PeB-DNA nanostructures

Peptide PeB (published by Memczak *et al.* <sup>186</sup>) was attached to NH<sub>2</sub>-modified DNA strands via NHS ester- and copper-free click chemistry (see 3.13). For HAI assays and infection inhibition assays, DNA trimers carrying three PeB peptides were constructed. Usually, ab-NH<sub>2</sub>, b\*c-NH<sub>2</sub>, c\*a\*-NH<sub>2</sub> were modified with DBCO-NHS esters and incubated overnight. After ethanol precipitation on the next day, the strands were incubated with PeB overnight and folded into DNA trimers the next day. After folding, excess of unbound PeB was removed using Amicon® Ultra centrifugal filters with 10K MWCO. PeB-modified 30 bp dsDNA molecules were used in ELISAs. Therefore, PeB-modified 30 fw ssDNA was mixed with 30 rev ssDNA 5'-biotin in equimolar ratios. Removal of excess of PeB was not necessary because only the biotin-modified strand binds strongly to the NeutrAvidin™ coated well bottoms of the ELISA plates, so any unconjugated peptide would be removed in washing steps, before the measurement took place.

For MST measurements, the strand ab was used as 5'-NH<sub>2</sub> and 3'-Atto655 modified version to build 0-3xPeB-DNA trimers<sup>Atto655</sup>. For DNA trimers<sup>Atto655</sup> carrying no, one, two or three PeB peptides, PeB-modified DNA strands were replaced by three, two, one or no unmodified strand, respectively. When conjugated at the ends of the arms on the DNA trimer, PeB peptides are approximately 9 nm apart when the structure is in outstretched conformation.

In the beginning of the work, a DBCO-Sulfo-NHS ester was used for conjugating DBCO to NH<sub>2</sub>-modified DNA. PAGE analysis revealed that conjugation of PeB to DNA trimers was incomplete since there were multiple bands visible (Figure 5-1A sample 2-3x PeB-DNA trimer). Those bands originate from DNA trimers bearing one PeB (weak lowest band), two PeB (band above) and three PeB (highest band).



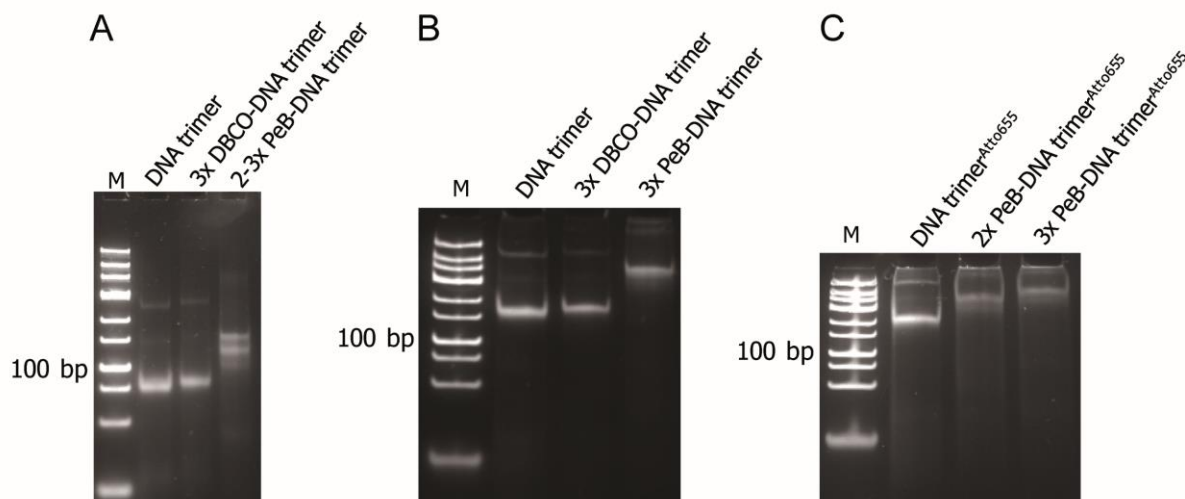


**Figure 5-1. PAGEs: Addition of PeB peptides to DNA trimers.**

The partially complementary strands ab, b\*c, c\*a\* were assembled to DNA trimers and modified with DBCO-NHS ester for addition of three PeB peptides (3xPeB-DNA trimer). **A)** 8% (v/v) native PAGE showing incomplete conjugation of PeB to DNA trimers. DBCO-Sulfo-NHS esters were used as linkers. **B)** 15% (v/v) native PAGE showing complete conjugation of PeB. DBCO-NHS esters were used as linkers. **C)** 15% (v/v) native PAGE showing DNA trimers<sup>Atto655</sup> modified with PeB for MST measurements. Gels were stained with SYBR® Gold Nucleic Acid Gel Stain and imaged under UV light. M = GeneRuler™ Low Range DNA Ladder (Thermo Fisher Scientific, USA) serves as control, not as ruler.

After replacing DBCO-Sulfo-NHS ester with DBCO-NHS ester, coupling of PeB to DNA structures resulted in much better conjugation yields that were visible as one single band (Figure 5-1B). This band ran slower through the gel than unmodified DNA trimers which clearly indicated an increase of molecular weight due to the attachment of peptides. Furthermore, the Atto655 dye on the 3'-end of the ab-NH<sub>2</sub> strand did not interfere with DNA trimer folding or conjugation (Figure 5-1C).

### 5.2.3 Binding of PeB-DNA trimers to IAV X31

To assess whether DNA-coupled peptides PeB bind to IAV X31, binding studies utilizing ELISA and MST measurements were conducted.

The binding properties of active IAV X31 were assessed via ELISA measurements. Therefore, 30 bp dsDNA constructs with 5'-biotin group on one strand (30 rev) and 5'-NH<sub>2</sub> group on the other strand (30 fw) were used. PeB was attached to the 5'-NH<sub>2</sub> group of 30 fw ssDNA as described in 3.13 (PAGE not shown).

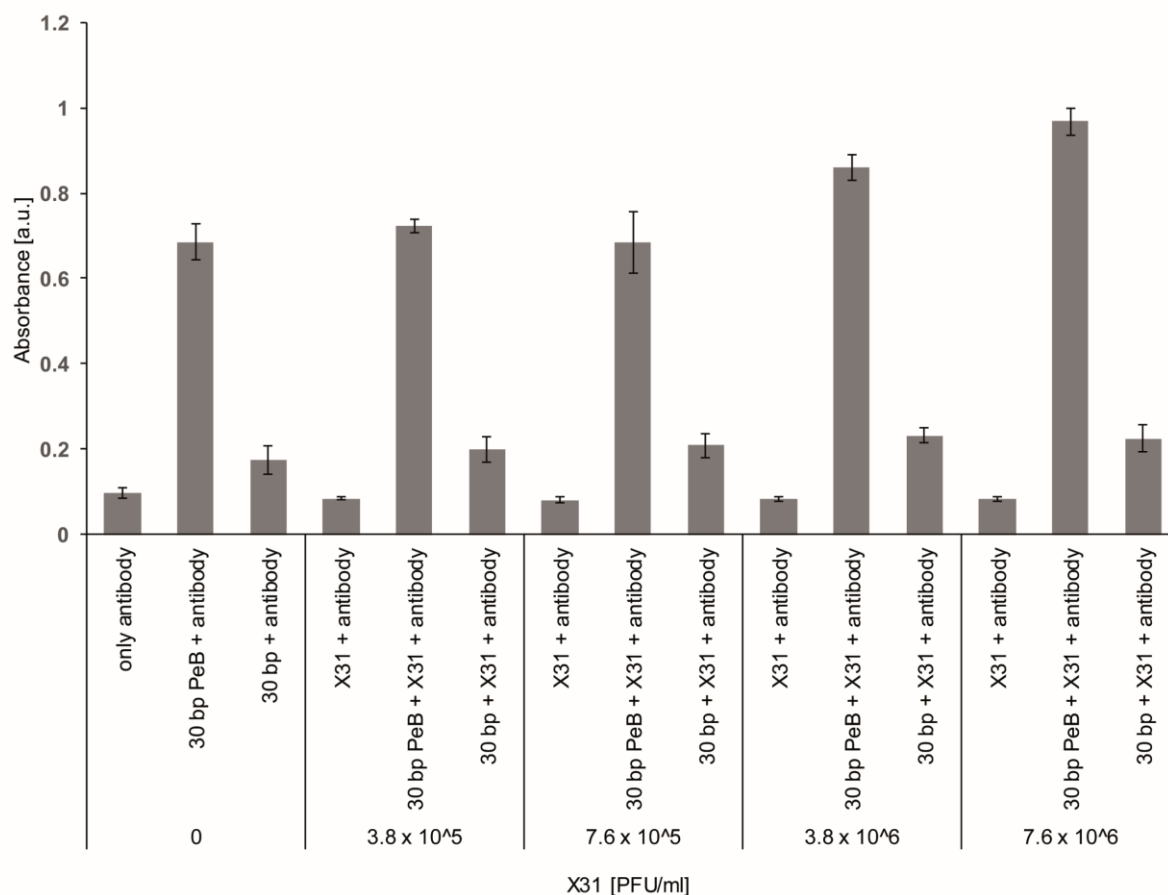


**Figure 5-2. IAV ELISA.**

Different dilutions of active IAV X31 were tested for binding to biotin-modified dsDNA constructs 30 bp (80 nM) and 30 bp PeB (80 nM) and probed using IAV H3N2 Virions Polyclonal Antibody, HRP. The experiment was executed three times and the bars show mean values of triplicates  $\pm$  standard deviation of one representative experiment.

The results in Figure 5-2 indicated an increase in absorbance signal dependent on the concentration of IAV X31. Moreover, the antibody seemed to nonspecifically bind to PeB-carrying dsDNA, too. Blocking with buffer containing 1% BSA, led to an increase in unspecific binding (data not shown). Only at higher virus concentrations ( $\geq 3.8 \times 10^6$  PFU/ml), the absorbance signal was clearly above the background signal provoked by nonspecific binding of the antibody.

The MST experiments shown here were performed by Dr. Walter Stöcklein (Fraunhofer Institute for Cell Therapy and Immunology, Branch Bioanalytics and Bioprocesses, Germany) in a biosafety level 1 laboratory. Therefore, IAV X31 had to be inactivated prior to the measurements. UV-inactivated (5 min, 220 nm on ice) IAV X31 were obtained from Dr. Daniel Lauster (Humboldt-Universität zu Berlin, Germany). Because one binding partner has to be fluorescently labeled, DNA trimers<sup>Atto655</sup> were manufactured. Atto655 absorbs and emits light

in the red spectral range and was therefore suitable for the MST device (Monolith NT.115, NanoTemper Technologies, Germany). For assembly of DNA trimers<sup>Atto655</sup> with different amounts of PeB, PeB-modified strands were mixed with unmodified DNA strands. MST experiments were set up as a titration experiment where concentrations of DNA trimers<sup>Atto655</sup> were kept constant and mixed with different dilutions of inactive IAV X31.

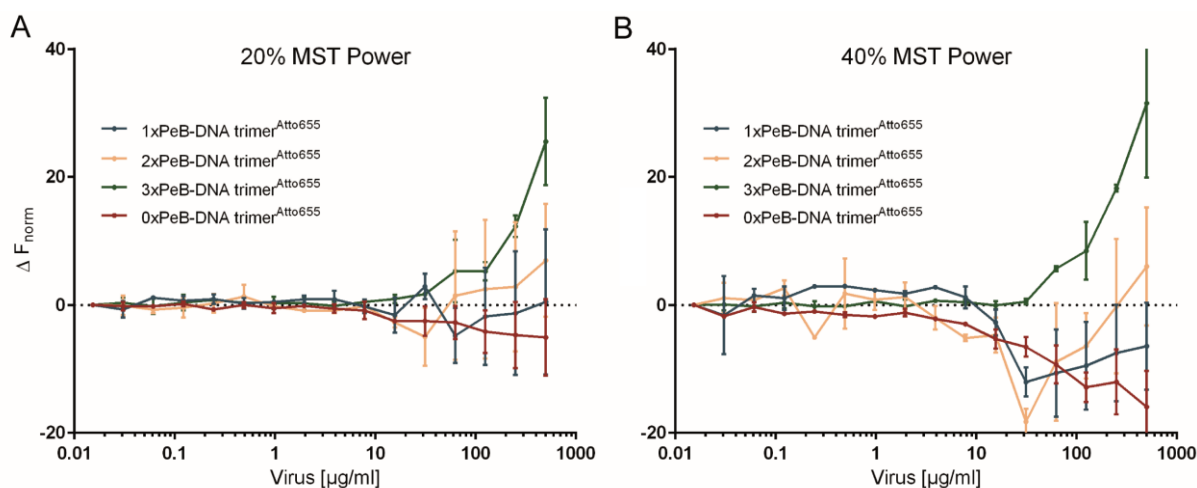


**Figure 5-3. MST analysis of PeB-DNA trimers<sup>Atto655</sup> binding to IAV X31.**

Different dilutions of inactive IAV X31 were incubated with fluorescently labeled DNA trimers carrying different amounts of PeB peptide. The graph represents mean values of duplicates  $\pm$  standard deviation. **A)** Measurement using 20% MST power. **B)** Measurement using 40% MST power.

First, the capillary shape was evaluated (Figure A 4). The symmetrical fluorescence peak without extra shoulders indicated the absence of unspecific binding of the samples to the edges of the capillaries. In Figure 5-3, the value  $\Delta F_{\text{norm}}$  describes the ratio between  $F_{\text{hot}}$  (after laser heating) /  $F_{\text{initial}}$  (before laser heating) and after subtraction of the baseline. Positive thermophoresis (positive  $\Delta F_{\text{norm}}$ ) as well as binding of 3xPeB-DNA trimer<sup>Atto655</sup> to IAV X31 could be detected for virus concentrations  $\geq 62.5 \mu\text{g/ml}$ . DNA trimers<sup>Atto655</sup> carrying less than 3 PeB peptides showed a negative change in fluorescence and did not clearly bind to IAV X31. Application of 40% MST power led to a more distinct separation of the curves (Figure 5-3B).

#### 5.2.4 Blocking IAV X31

Besides verification of binding, the PeB-DNA trimers were tested for their ability to impede IAV X31 virus from binding to red blood cells in HA inhibition assays. In addition, the influence of PeB-modified DNA trimers in influenza infection assays using MDCK cells was examined.

HA inhibition assays depicted in Figure 5-4 were conducted by Dr. Daniel Lauster (Humboldt-Universität zu Berlin). Tests comprised incompletely modified DNA trimers (2-3xPeB-DNA trimer, see Figure 5-1A,), completely modified DNA trimers (3xPeB-DNA trimers, see Figure 5-1B) and unmodified 0xPeB-DNA trimers as controls.

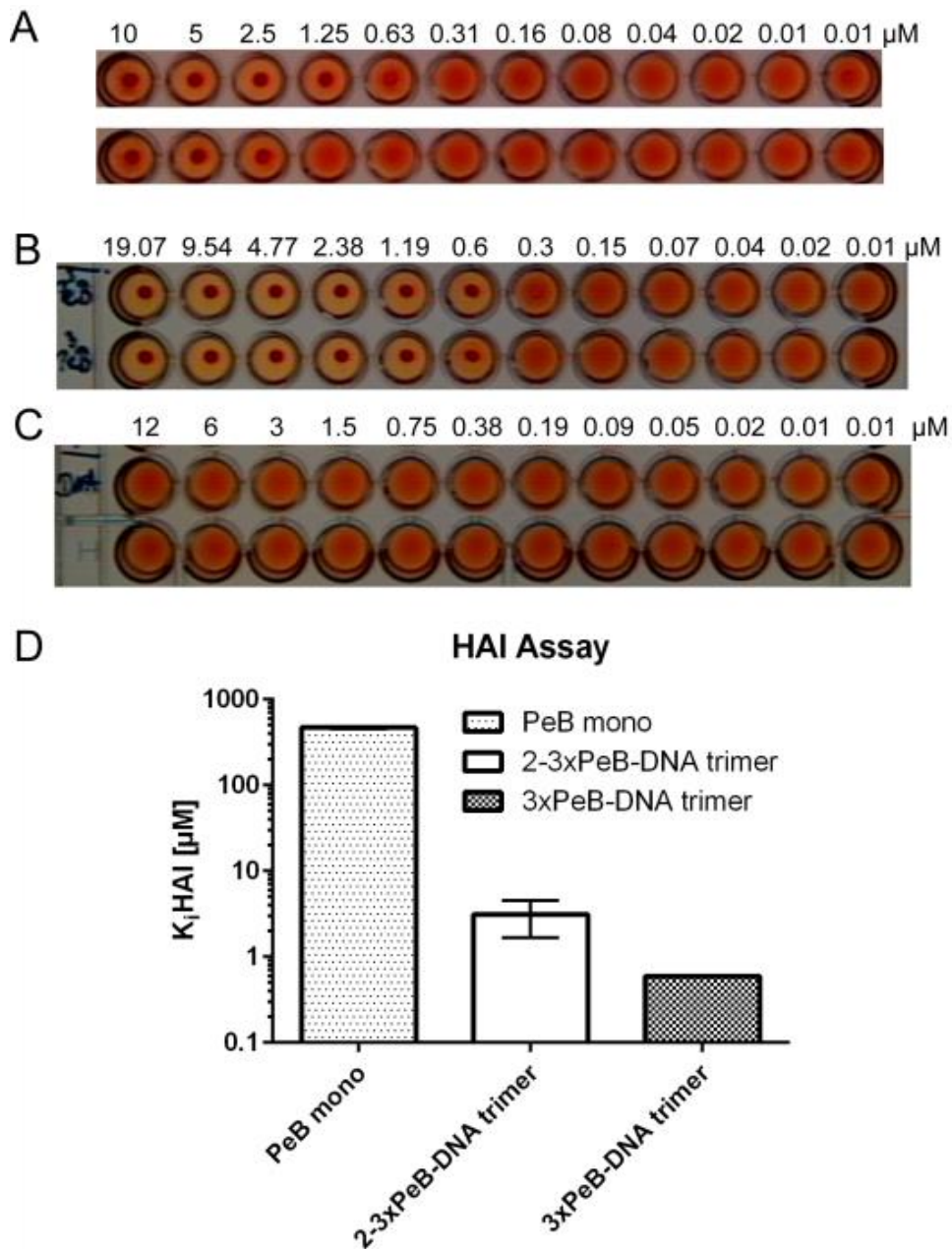


**Figure 5-4. HAI Assay using PeB-modified DNA trimers on IAV X31.**

**A)-C)** Raw data of HA inhibition assays. Concentrations are given in terms of nanoparticle, i.e. DNA construct. **A)** Dilution of 2-3xPeB-DNA trimer mixed with 2 HAU virus (upper row) and with 4 HAU (lower row). **B)** Dilution of 3xPeB-DNA trimer mixed with 4 HAU virus in duplicates. **C)** Dilution of 0xPeB-DNA trimer mixed with 4 HAU virus in duplicates. **D)** Inhibitor constant  $K_i$  HAI in concentrations of nanoparticle, i.e. DNA construct. Values were normalized to 4 HAU. Assays were conducted by Dr. Daniel Lauster (Humboldt-Universität zu Berlin).

Figure 5-4A displays inhibition of hemagglutination as the formation of red dots on the bottom of the wells for concentrations of 1.25  $\mu\text{M}$  2-3xPeB-DNA trimer for 2 HAU and 2.5  $\mu\text{M}$  3xPeB-DNA trimer for 4 HAU. Concentrations lower than these did not hinder viruses from binding to erythrocytes. As a result, the red blood cells are kept in solution and do not form red dots at the bottom. For the completely conjugated DNA trimer (3xPeB-DNA trimer), inhibition of hemagglutination was visible for values as low as 600 nM (Figure 5-4B). DNA trimers without PeB peptides did not inhibit IAV X31 from binding to erythrocytes (Figure 5-4C). The concentrations mentioned here refer to nanoparticles, i.e. DNA trimers. In Figure 5-4D, values for PeB-DNA trimers were compared to PeB only ( $K_i\text{HAI}_{\text{peptide}} = 469.8 \mu\text{M}$ , determined by Daniel Lauster). In order to compare all values in terms of peptide concentration,  $K_i\text{HAI}$  values from DNA constructs can be multiplied by 2.5 (for 2-3 PeB per DNA trimer) or by 3 (for 3 PeB per DNA trimer). For 3xPeB-DNA trimer ( $K_i\text{HAI}_{\text{peptide}} = 1.8 \mu\text{M}$ ), an enhancement factor  $\beta$  of 261 was calculated. The enhancement factor per entity/complex is 783.

To determine whether PeB-DNA trimers are able to inhibit IAV X31 from infecting hosts *in vitro*, MDCK cells were seeded and treated when grown as confluent cell monolayer. Prior to treatment of cells, IAV X31 were incubated with 0xPeB-DNA trimer, 3xPeB-DNA trimer, PeB only or DPBS (calcium, magnesium) as control.

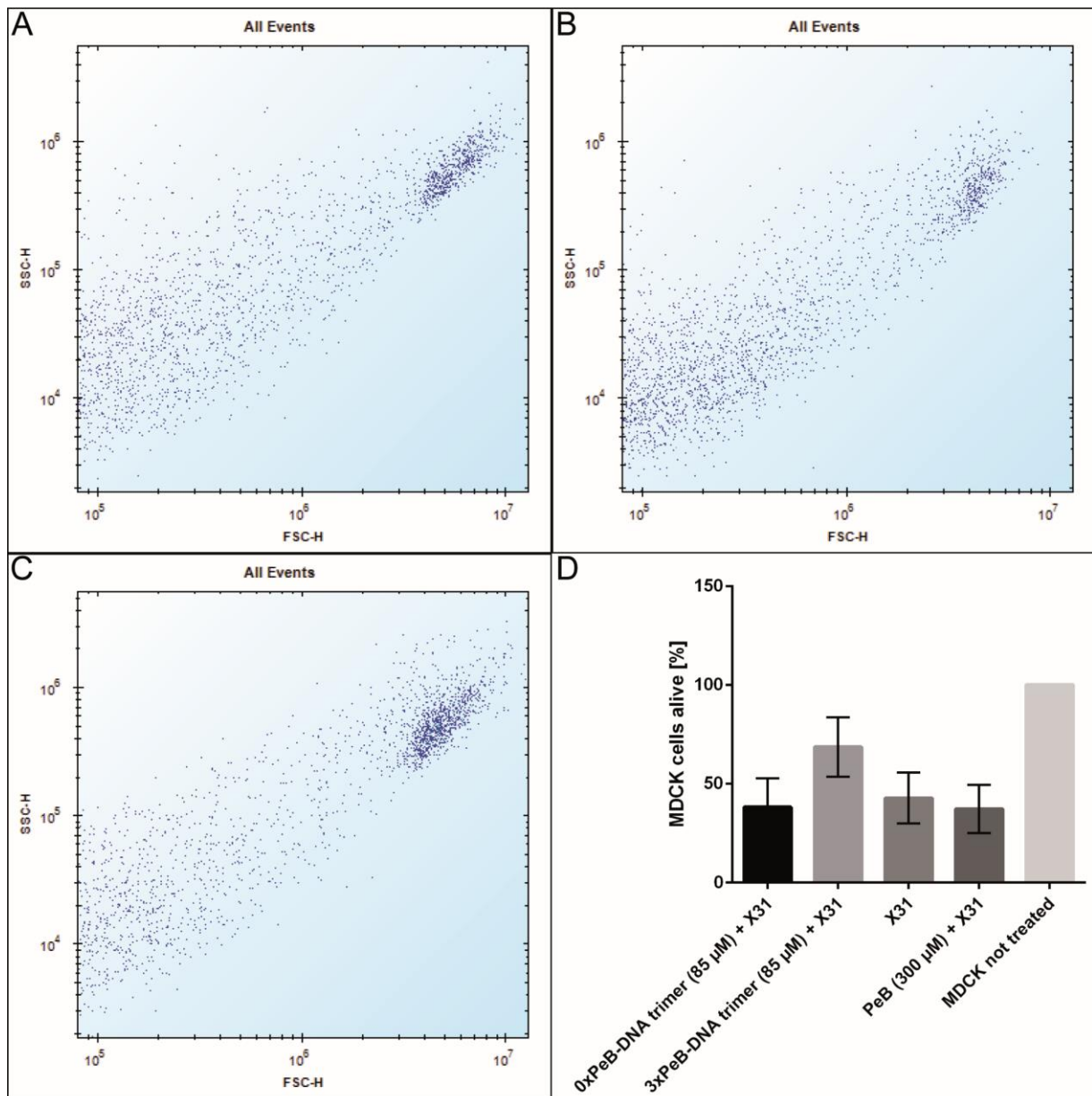


**Figure 5-5. IAV infection inhibition assay using flow cytometry.**

**A)** Dot plot of MDCK cells. **B)** Dot plot of MDCK cells treated with IAV X31 only. **C)** Dot plot of MDCK cells treated with IAV X31 pre-incubated with 3xPeB-DNA trimers (85  $\mu$ M). **D)** MDCK cells not treated or treated with IAV X31 ( $3.8 \times 10^4$  PFU), IAV X31 ( $3.8 \times 10^4$  PFU) pre-incubated with 0xPeB-DNA trimers (85  $\mu$ M), IAV X31 ( $3.8 \times 10^4$  PFU) pre-incubated with 3xPeB-DNA trimers (85  $\mu$ M) or IAV X31 ( $3.8 \times 10^4$  PFU) pre-incubated with PeB (300  $\mu$ M). Graph represents mean values of three measurements  $\pm$  standard deviation normalized to not treated MDCK cells.

A comparison of raw data uncovered that most of the measured events formed distinct populations for untreated MDCK cells (Figure 5-5A) and MDCK cells treated with 3xPeB-DNA trimers incubated IAV X31 (Figure 5-5C). That was different for MDCK cells treated with IAV X31 only (Figure 5-5B) or treated with unmodified DNA trimers (0xPeB-DNA trimers) incubated IAV X31 (not shown), which gave more diffuse signals. As FCS and SSC values of



these cells differed, the cell population appeared in an altered shape. For analysis, the distinct cell population of untreated MDCK cells was gated and used as standard. Indeed, the analysis of influenza infection inhibition assays disclosed a higher amount of viable MDCK cells when IAV X31 where pretreated with 3xPeB-DNA trimers. This effect was rather weak and not significantly different from the other samples that contained IAV X31 (Figure 5-5D). Interestingly, 85  $\mu\text{M}$  of 3xPeB-DNA trimers delivered a higher percentage of living MDCK cells than 300  $\mu\text{M}$  PeB.

In addition to analysis of infection via flow cytometry, a reliable method to trace cell infection with IAVs is microscopic evaluation. Infections of cells can be seen in inverted light microscopy as CPE and/or cell death. CPEs phenotypically manifest as cells round up and detach and/or develop abnormal morphologies. Photos of cells were taken and presented in Figure 5-6.

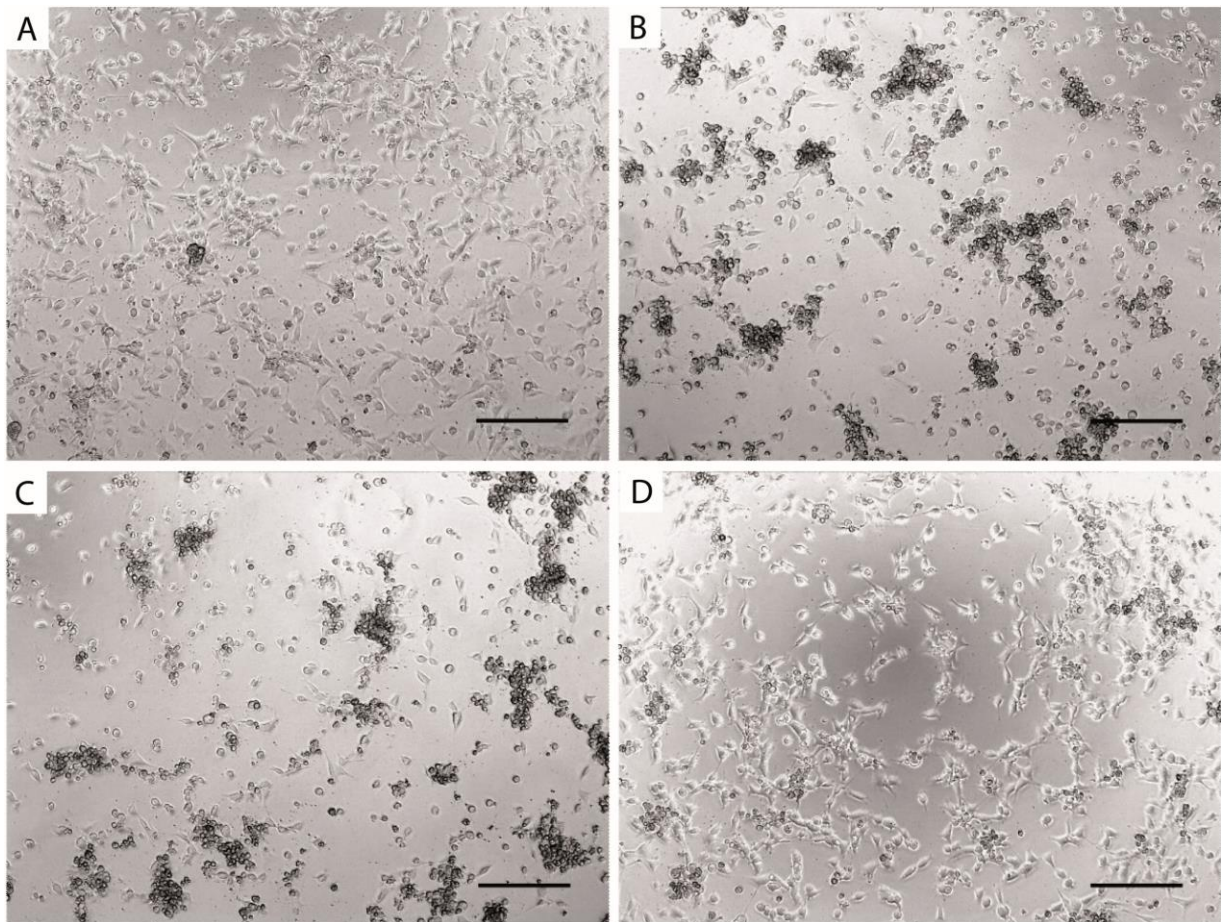


**Figure 5-6. Photos of MDCK cells after IAV X31 infection inhibition assay.**

MDCK cell monolayer treated with **A)** DPBS (calcium, magnesium), **B)** IAV X31 ( $3.8 \times 10^4$  PFU), **C)** IAV X31 ( $3.8 \times 10^4$  PFU) pre-incubated with 0xPeB-DNA trimer (85  $\mu\text{M}$ ). **D)** IAV X31 ( $3.8 \times 10^4$  PFU) pre-incubated with 3xPeB-DNA trimer (85  $\mu\text{M}$ ). Scale bar = 100  $\mu\text{m}$ .

Images B and C given in Figure 5-6 show detached cells and adjacent cells tethered to each other to form floating cell bonds that appear to have a higher contrast. A normal MDCK cell monolayer was depicted in Figure 5-6A. All cells are attached and appear in their physiological morphology. Attached cells were also seen when they were treated with IAV X31 that were pretreated with 3xPeB-DNA trimers at a concentration of 85  $\mu\text{M}$ . Only a few floating cell associations (left bottom corner of Figure 5-6D) were visible; most of the cells were outstretched and did not show symptoms of cytopathic effects.

### 5.2.5 Discussion

Adherence of the IAV to host cells requires multivalent interactions between HA and sialic acid structures. Previous studies substantiate that presentation of three sialic acid ligands enormously increases the affinity for HA<sup>190,191</sup>. The HA-binding peptide PeB was found to attach to its target in micromolar concentrations<sup>186</sup>. The scope of this project was to exploit whether an oligovalent presentation of up to three peptides PeB on DNA nanostructures potentiates the affinity of PeB to HA and consequently hinders IAVs from sticking to sugar structures on cells.

For the conjugation of PeB to DNA strands, NHS ester and copper-free click chemistry reactions were executed. Initial conjugations using DBCO-Sulfo-NHS esters as linkers revealed that not all DNA strands could be modified with PeB. Using DBCO-NHS esters helped to overcome this problem and resulted in complete conjugation. Therefore, DBCO-NHS esters were used as linkers for all other modifications (except for the first HAI Assay) in this work.

In order to test binding to active IAV X31, an ELISA setup was established. For simple binding analysis, dsDNA functionalized with one PeB peptide was tested for binding to different virus concentrations. Interestingly, only high concentrations of viruses showed binding above the background signal. In order to obtain more informative results and to determine binding constants, it would be necessary to reach saturation, hence higher viral concentrations are required. One possibility to reach higher titers is the production of viruses in chicken eggs instead of cell cultures<sup>192</sup>. Additionally, MST measurements were performed where, in contrast to ELISAs, the ligand is not tethered to a well bottom but in solution. In MST measurements utilizing DNA trimers with varying amounts of PeB, it became apparent that 3xPeB-DNA trimers resulted in a positive thermophoresis signal when incubated with inactive IAVs. In contrast, all other DNA constructs showed negative thermophoresis. Generally, bigger



molecules display a trend towards positive thermophoresis and as virus-bound 3xPeB-DNA trimers become bigger and undergo changes in their hydrate shell, it was suggested that positive thermophoresis might appear due to stable binding. This would further imply that DNA constructs carrying only one or two PeB molecules could not bind inactive IAVs with a high stability compared to those with three PeB molecules. DNA trimers without PeB did not nonspecifically bind the inactive viruses. The analysis does not allow for determination of binding data such as half-maximal effective concentration (EC50) values because saturation could not be achieved.

The results obtained by ELISA and MST experiments proved that PeB, when conjugated to DNA constructs, maintained its ability to bind both active as well as inactive IAV X31. Interestingly, neither DNA trimers conjugated to one PeB, nor DNA trimers conjugated to two PeB peptides showed any significant binding to IAV X31 in MST experiments, while in ELISAs, the presence of one PeB on dsDNA led to measurable binding. The reason for this could be that during inactivation, IAV X31 lost part of its activity and thus attached less efficiently to PeB in MST tests. A more likely explanation would be that the dense coating of PeB-dsDNA onto ELISA plates automatically led to a multivalent presentation of PeB. In a future experiment, coating of different densities of dsDNA-PeB constructs could shed light on whether binding of the viruses to PeB-DNA is indeed multivalent or increases linearly with the number of dsDNA-PeB constructs.

In the attempt to block the agglutination and binding activity of HA, IAV X31 were incubated with 3xPeB-DNA trimers as only these DNA structures exhibited binding to IAV X31 in MST experiments. The effect was tested via HAI assays, flow cytometric analysis and microscopic examination of CPEs. Inhibition of viral agglutination of erythrocytes worked with nanomolar  $K_i$ HAI values of DNA structures carrying three PeB peptides, and to a lesser extent with mixtures of structures carrying either two and three peptides due to incomplete conjugation. High hydrophobicity of PeB ruled out HAI assays of monovalent peptides with 4 HAU, since PeB nonspecifically bound and linked erythrocytes. As a consequence, less PeB could be available for binding IAV X31, which could distort the results. However, when attached to DNA trimers, the solubility and effectivity of PeB could be improved and therefore IAV X31 at concentrations of 4 HAU could also be neutralized. Unfortunately, it was not possible to reproduce the results of those HAI assays later on. A reason for this could be degradation of the DNA constructs due to long-time storage or variations in the blood used for HAI assays, the

latter being a typical pitfall of this particular technique. Due to this, different methods to assess virus inhibition were applied. Flow cytometry is a technique to identify populations of cells and to discriminate dead from living cells as the latter clearly appear as a separate and well-defined population. Viral infection leads to CPE and apoptosis of cells<sup>193</sup>. Apoptosis, also known as programmed cell death, causes biological and morphological changes in cells which results in a less clearly defined cell population as seen in typical flow cytometry scatter plots. Apoptotic cells undergo cellular shrinkage and fragment into apoptotic bodies, both features are detectable in flow cytometry by decreasing FSC and increasing SSC signals, respectively<sup>194</sup>. Those effects appeared in outlines in MDCK cells treated with IAV X31, but not in untreated MDCK cells or MDCK cells when IAV X31 were pretreated with 3xPeB-DNA trimers. In the end, direct microscopic observation of cells remained as the method of choice<sup>195</sup>. Here, explicit cytopathic effects could be detected in MDCK cells treated with IAV X31 and MDCK cells treated with IAV X31 pre-incubated with 0xPeB-DNA trimers, but not in MDCK cells treated with IAV X31 pre-incubated with 3xPeB-DNA trimers. Even though it could be shown that DNA as a scaffold material for 3 peptides PeB can block HA in lower concentrations than PeB only, a concentration of 85  $\mu\text{M}$  is still too high for therapeutic applications.

Apart from DNA, other materials have been exploited as multivalent scaffold for HA binding ligands. In a study from 2015 by Lauster *et al.*, a peptide variant of PeB was conjugated to stearic acids in order to enable a multivalent presentation. Even though inhibitory effects of the peptides could be ameliorated due to stearylation, they found that these modified peptides nonspecifically bound to the cell membranes<sup>196</sup>. A few other peptides binding to HA of IAV types H1N1 and H3N2 were reported by Matsubara *et al.*<sup>197</sup>. Their inhibitory effect could be increased by alkylation. Another solution for multivalent presentation of HA targeting peptides was presented by Hüttl and co-workers<sup>198</sup>. Micelles formed by peptide amphiphiles showed improved biological activity compared to naïve peptides. Bandlow *et al.* examined the spacing of HA molecules by bivalently arranging sialylated sugar HA ligands in different distances on flexible PEG conjugates and on rigid DNA-peptide nucleic acid (PNA) complexes. They found that flexible PEG conjugates showed only weak binding affinities compared to DNA-PNA complexes. The highest affinity was achieved when sialyl N-Acetyllactosamine ligands on DNA-PNA were separated in distances between 5.2 – 5.9 nm which was presumably owed to two sugars binding to a single HA trimer<sup>199</sup>.

### 5.3 Binding and inhibiting RSV via peptide-DNA constructs

#### 5.3.1 Aim

Human respiratory syncytial virus is a major cause for lower respiratory tract diseases in infants and immunocompromised adults. However, for prevention and treatment of RSV infections, there are only a few medicines available.

In the course of a collaborative project with the groups of Dr. Thomas Grunwald (Fraunhofer Institute for Cell Therapy and Immunology IZI, Germany) and Dr. Mirko Buchholz (Fraunhofer Institute for Cell Therapy and Immunology IZI-MWT, Germany), novel, highly-selective, short synthetic peptides were derived from the anti-prefusion RSV-F antibody D25. These peptides target epitopes at the antigenic site Ø on the apex of prefusion RSV-F and were shown to inhibit the transition to postfusion RSV-F. After optimization of the amino acid sequence (truncations, alanine scanning, replacement of natural amino acids with non-natural amino acids), the best binding peptide, named RSV-Peptide-6, was tested in binding and infection inhibition assays. After confirming affinity towards RS viruses, three of these peptides were attached to DNA nanostructures in an oligovalent strategy. The first aim of this project was to enhance binding of RSV-Peptide-6-DNA nanostructures to RSV. Since RSV-F is a trimeric protein, the binding affinity of the RSV-Peptide-6 could be increased by oligovalently presenting three peptides to RSV-F on a DNA trimer. The second goal was to block and thus disturb the RSV-F activity using these constructs. Eventually, inhibition of RSV-F would disrupt viral fusion with and entry into host cells and could prevent RSV infection. For evaluation of the inhibitory potential of RSV-Peptide-6-DNA constructs, RSV infection assays of host cells in the presence of the constructs were examined by Leila Issmail (Fraunhofer Institute for Cell Therapy and Immunology IZI, Germany) and compared to RSV-Peptide-6 as well as unmodified DNA trimers only.

#### 5.3.2 Construction of RSV-Peptide-6-DNA nanostructures

DNA trimers and 30 bp constructs carrying RSV-Peptide-6 were produced differently than described before (see Figure 5-7A). Because of its hydrophobicity, RSV-Peptide-6 could not be solubilized in aqueous solutions but was dissolved in DMSO. First, ssDNA strands were modified with DBCO-PEG4-NHS ester because it was assumed that due to the PEG chain, the solubility in aqueous solutions of the peptide could be increased. After ethanol precipitation, the

ssDNA was dissolved in DMSO and also folding was carried out in DMSO. Since the addition of RSV-Peptide-6 did not cause visible aggregations, the structures were further purified by ethanol precipitation. Purification via Amicon® Ultra centrifugal filters was not possible here since DMSO at concentrations  $\leq 5\%$  may cause filter materials to leak out of the component parts as per manufacturer's instructions.

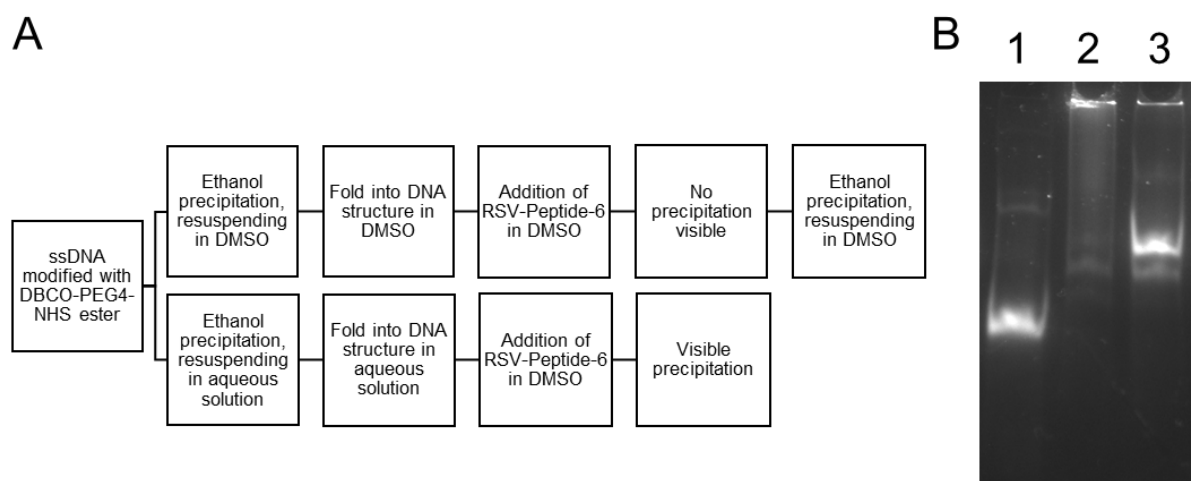


**Figure 5-7. Production of RSV-Peptide-6 modified DNA structures in DMSO.**

**A)** Synthetic pathway of RSV-Peptide-6 modified DNA structures in DMSO to avoid aggregation. **B)** Modification and purification in DMSO. Lane 1) DNA trimer unmodified in DMSO, Lane 2) 3xRSV-Peptide-6-DNA trimer in DMSO, Lane 3) 3xRSV-Peptide-6-DNA trimer in DMSO after ethanol precipitation. The 10% (v/v) native PAGE gel was stained with SYBR® Gold Nucleic Acid Gel Stain and imaged under UV light.

In Figure 5-7B it is shown that DNA trimers can assemble in non-aqueous solutions like DMSO (lane 1). Addition of RSV-Peptide-6 still leads to aggregations that were not visible by eye but could be seen in the pockets of the PAGE (lane 2). After ethanol precipitation, that was necessary to remove unbound peptides, aggregations could be reduced and the band displaying RSV-Peptide-6 conjugated DNA trimers was more intense (lane 3). The appearance of a less intense band slightly below the main band in lane 3 indicates that there were a small percentage of 2xRSV-Peptide-6-DNA trimers besides the desired 3xRSV-Peptide-6-DNA trimer.

Binding of dsDNA functionalized with RSV-Peptide-6 to active RSV was assessed using an ELISA approach. Therefore, two complementary ssDNA strands with a length of 30 nucleotides were purchased with 5'-biotin group (30 rev) and 5'-NH<sub>2</sub> group (30 fw). The strand 30 fw 5'-NH<sub>2</sub> was modified with RSV-Peptide-6 in DMSO as described above (Figure 5-7A). In parallel, 30 rev 5'-biotin was ethanol precipitated and resuspended in DMSO, too. Both strands were assembled in a thermocycler, evaluated using native PAGE (results not shown) and

subsequently incubated on a NeutrAvidin™ coated ELISA plate. The ELISAs were conducted as described in 3.17.2 using different dilutions of active RSV.

### 5.3.3 Binding of dsDNA modified with RSV-Peptide-6 to RSV

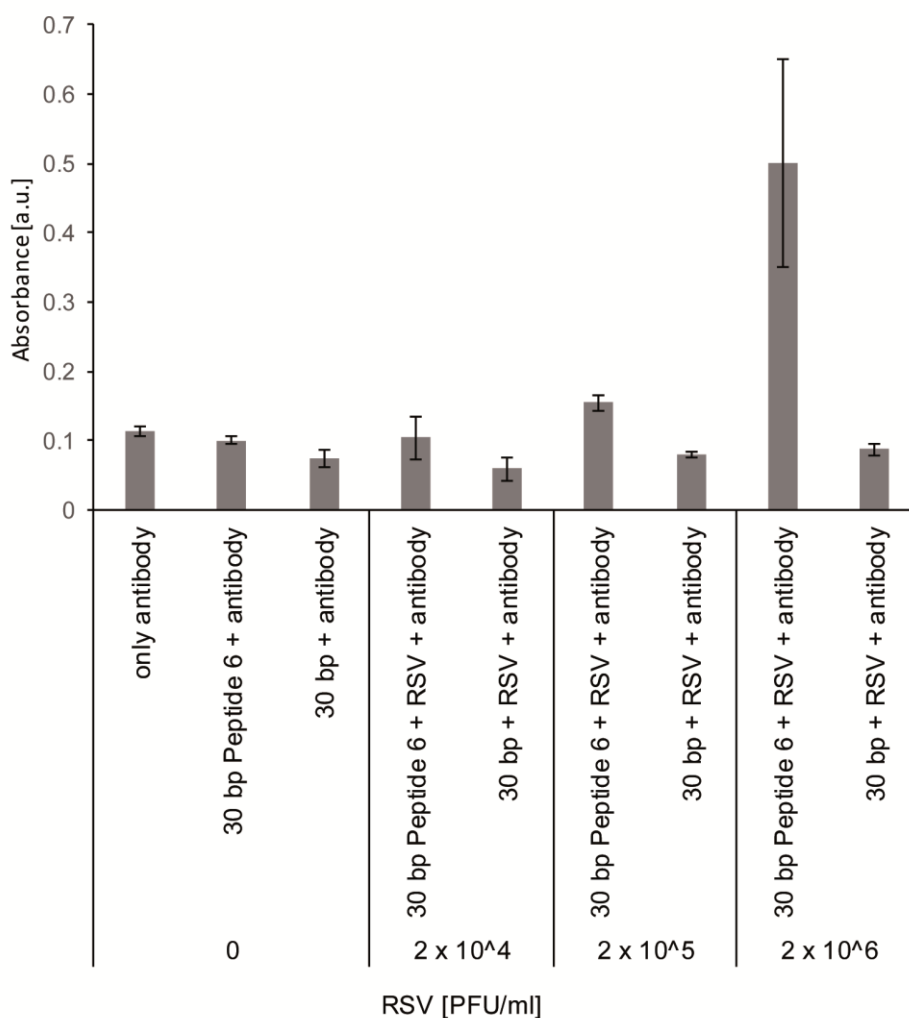


**Figure 5-8. RSV ELISA.**

Different dilutions of active RSV were tested for binding to biotin-modified dsDNA constructs 30 bp (46 nM) and 30 bp RSV-Peptide-6 (46 nM) and probed using RSV Polyclonal Antibody, HRP. The experiment was executed three times and the bars show mean values of triplicates  $\pm$  standard deviation of one representative experiment which was conducted by Basma Altattan (Fraunhofer Institute for Cell Therapy and Immunology IZI, Germany).

The diagram in Figure 5-8 illustrates the binding of active RSV to RSV-Peptide-6 attached to dsDNA on an ELISA plate bottom. A slightly elevated absorbance signal could be observed at a virus concentration of  $2 \times 10^5$  PFU/ml. Clearly elevated absorbance signals at a higher viral concentration ( $2 \times 10^6$  PFU/ml) indicated binding to RSV-Peptide-6 immobilized via dsDNA. Nonspecific binding of the antibody to the plate bottom or DNA only is within the background signal.

### 5.3.4 RSV infection inhibition assay

In order to investigate whether the newly developed RSV-binding peptides not only bind RSV but are also able to hinder the viruses from infecting host cells, RSV infection inhibition assays were conducted by Leila Issmail (Fraunhofer Institute for Cell Therapy and Immunology IZI, Germany). RSV-Peptide-6-carrying DNA trimers were produced in DMSO like outlined for 30 bp RSV-Peptide-6 (section 5.3.2) and in Figure 5-7A. These constructs were compared to the performance of monovalent RSV-Peptide-6 and to unmodified DNA trimers, both dissolved in DMSO, too. For the production of unmodified DNA trimers that were used as control, unmodified DNA trimer strands (ab, b\*c, c\*a\*) were used but still incubated with the adequate amount of peptide. They were purified via ethanol precipitation just like the modified DNA trimers. This step was necessary to preclude the possibility that RSV-Peptide-6 molecules bound nonspecifically to DNA trimers and were not completely removed by the final ethanol precipitation step. Before the samples were pre-incubated with RSV, they were diluted in high-glucose DMEM (GlutaMAX™) medium supplemented with 1% penicillin – streptomycin. This step did not cause peptide aggregations that were visible by eye or light microscopy.

Plotted in Figure 5-9 was the infectivity of RSV against different concentrations of samples. The tool IC50 calculator (AAT Bioquest) was used to plot IC50 data (Figure 5-9C, D) and calculate IC50 values using the equation:

$$Y = min \frac{(max - min)}{1 + (\frac{x}{IC50})^b} \quad (4)$$

where  $b$  is the Hill coefficient.

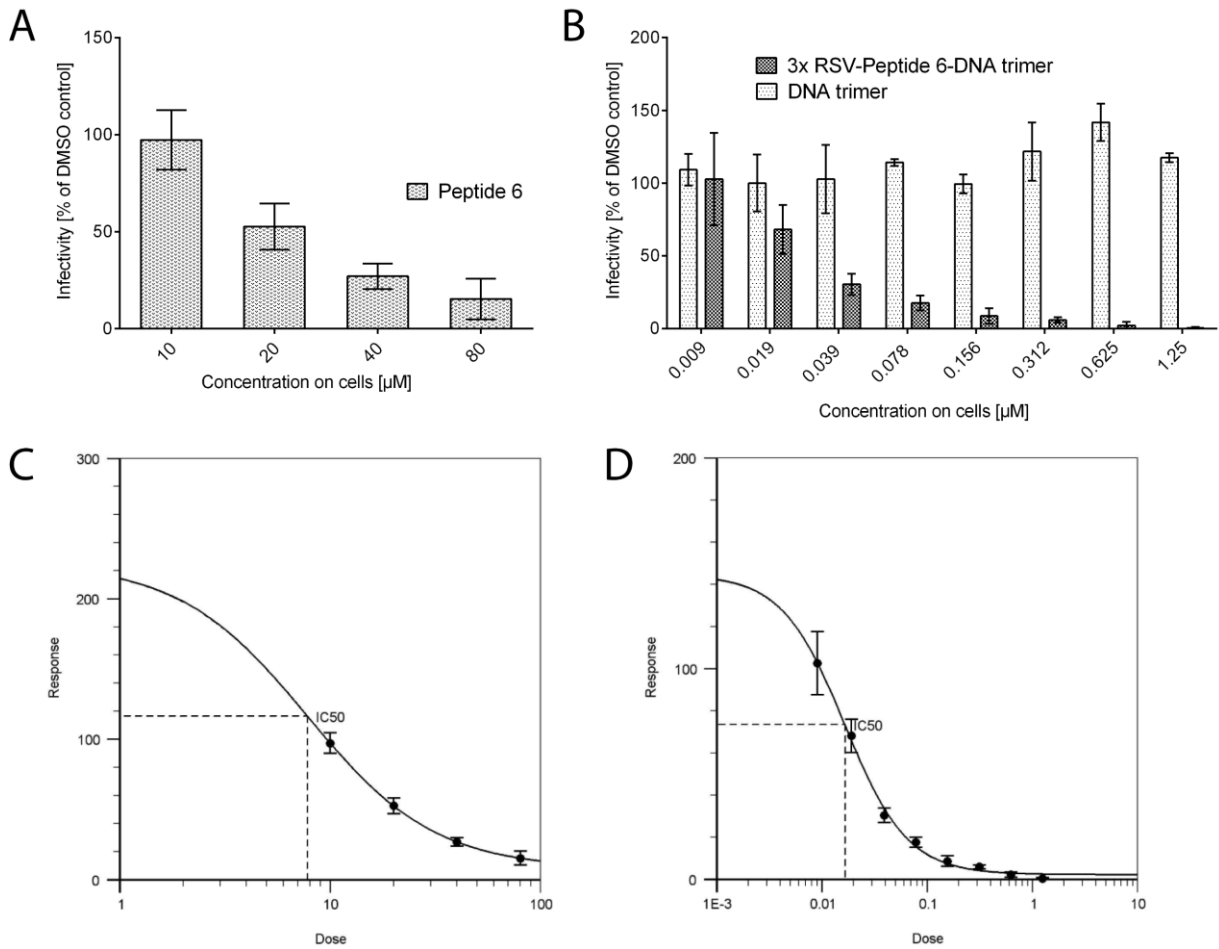


**Figure 5-9. RSV infection inhibition assay.**

Plaque reduction assay on human epithelial cells (HEp-2) using recombinant RSV expressing green fluorescent protein. RSV (100 PFU / 25 µl) were pre-incubated with 2-fold dilution series of peptid-DNA structures at 37 °C for 10 min. HEp-2 cells were treated with virus-compound mixtures and controls for 45 h at 37 °C, 5%CO<sub>2</sub>. Fluorescent plaques were counted using AID ELiSpot reader. Experiments were conducted by Leila Issmail (Fraunhofer Institute for Cell Therapy and Immunology IZI, Germany). **A**) Infection inhibition assay using various dilutions of RSV-Peptide-6. Concentrations are given in terms of peptide. **B**) Infection inhibition assay using various dilutions of 3xRSV-Peptide-6-DNA trimers and DNA trimers only (served as control). Concentrations are given in term of DNA construct carrying mainly three peptides. **C**) IC<sub>50</sub> calculation of infection inhibition assay using various dilutions of RSV-Peptide-6. **D**) IC<sub>50</sub> calculation of infection inhibition assay using various dilutions of RSV-Peptide-6-DNA trimers.

Pretreated viruses that co-express GFP were incubated on Hep-2 cells for almost 2 days before fluorescent plaques caused by the viruses were counted. Figure 5-9A depicts that the infectivity is decreased by increasing concentrations of RSV-Peptide-6. Infectivity was as low as ~15% when RSV-Peptide-6 at a concentration of 80 µM was applied. An IC<sub>50</sub> value of 7.782 µM was calculated. Figure 5-9B illustrates infectivity against concentrations of DNA nanostructures. In order to directly compare these results to Figure 5-9A in terms of the absolute number of active peptides, one can multiply the concentrations by 2.5, as each DNA trimer carries two to three

RSV-Peptide-6 molecules or by 3 as the majority of constructs carries three peptides. To exactly determine to which percentage one DNA trimer carries three peptides, more detailed analyses would be necessary. As can be seen in Figure 5-9B DNA trimers without peptides did not decrease the infectivity of RSV, but 3xRSV-Peptide 6-DNA trimers, resulted in a concentration-dependent decrease of infectivity. DNA construct concentrations of 1.25  $\mu\text{M}$  resulted in infection inhibition of  $\sim 100\%$  and an  $\text{IC}_{50}$  value of 0.017  $\mu\text{M}$  (in terms of discrete entity). Comparing both  $\text{IC}_{50}$  values in terms of entity, an enhancement factor  $\beta$  of 458 was calculated.

### 5.3.5 Discussion

RSV infections are prevalent and cause symptoms ranging from a mild cold to severe pneumonia and bronchiolitis. As of today, no antiviral drugs which are specific for treatment of RSV infections are available. In the course of this project, oligovalent presentation of novel RSV-F targeting peptides aimed to inhibit RSV from infection host cells *in vitro*. As the peptides had hydrophobic properties, conjugation to DNA structures had to be done in organic solvents like DMSO. To further increase solubility, a PEG containing linker was chosen.

ELISA assays were performed to evaluate binding of dsDNA functionalized with one RSV-Peptide-6 to different concentrations of active RSV. It was found, that only high concentrations of RSV bound to the RSV-Peptide-6 ligand. The viruses used for the presented experiments were purified and concentrated via ultracentrifugation through a 20% sucrose layer. Similar to influenza ELISAs depicted in Figure 5-2, a major drawback of this approach is the lack of higher viral concentrations that would allow for more measurements employing RSV concentrations above  $2 \times 10^6$  PFU/ml. To overcome this problem, RSV could be concentrated by ultracentrifugation through sucrose gradients. Even though this method is most commonly used, it remains problematic as RSV tends to considerably lose its infectivity<sup>200-202</sup>. Moreover, for conducting meaningful studies on binding of peptide-functionalized DNA structures to RSV, it would be advantageous to study binding kinetics between the nanostructures and the well characterized protein RSV-F instead of binding to whole viruses. RS viruses have inhomogeneous sizes and shapes which makes it almost impossible to determine reliable molecular weight values.

Monovalent activity of RSV-Peptide-6 was compared to the activity of trivalent RSV-Peptide-6 on DNA trimers in infection inhibition assays (Figure 5-9). Indeed, the oligovalent



presentation could enhance the inhibitory effect of the monovalent peptides. To our knowledge, this is the first study that uses multivalently presented peptides to target RSV-F. Recently, Cagno *et al.*, have proposed a new approach to turn reversible virustatic mechanisms into irreversible virucidal deactivation<sup>203</sup>. They used nanoparticles coated with undecanesulfonic acid-containing ligands that mimic heparan sulfate proteoglycans. Compared to nanoparticles coated with 3-mercaptopethylsulfonate that are virostatic, undecanesulfonic acid-containing ligands are longer and can bind RSV in a multivalent manner. As a result, global virus deformation and irreversible loss of infectivity could be induced. The undecanesulfonic acid-containing nanoparticles are hydrophobic.

Due to these findings, the aim for future studies is to vary the RSV-Peptide-6 conjugated DNA nanostructures in length and flexibility to further improve RSV infection inhibition.

It remains questionable whether HEp-2 cells constitute an appropriate model system for RSV infection assays. It has been reported by Johnson and co-workers, that heparan sulfate occurs on cells like HEp-2 cells, but is missing at the apical surface of differentiated ciliated epithelial cells which make up the primary location for RSV replication<sup>204</sup>.

Compared to the performance of peptide-DNA constructs used to block IAV, the constructs used to block RSV have a much stronger inhibitory effect. Although both constructs show binding to their target viruses, there is a drastic difference in terms of infection inhibition for both for the monovalent and oligovalent approach. The explanation could be that RSV-Peptide-6 acts as a functional blocker that prevents conformational change. In contrast to that is the anti-IAV peptide PeB which is described as a competitive binding inhibitor only. The blocking of function might act as natural amplification factor as it has a big effect on following signal pathways, whereas blocking of binding is simply competition which can be annulled.

By now, binding and neutralization properties of D25 could be improved which led to the generation of the new antibody MEDI8897<sup>205,206</sup>.

## **5.4 Evaluating the binding of different sugar-DNA constructs to *E. coli***

### **5.4.1 Aim**

It is known that chains of sugars on the surface of epithelial cells are used by pathogens to identify, adhere and infect those cells. Stable and effective microbial adhesion is realized by

multivalent ligand-receptor interactions. In the case of *Enterobacteriaceae* like *E. coli*, this adhesion is mediated through Type 1 fimbriae which are also referred to as “mannose-sensitive” fimbriae since they bind to D-mannose structures<sup>184,207</sup>.

Here, different sorts of synthetically produced mannose molecules were examined for their binding to *E. coli*. Therefore, DNA 4arm structures carrying one sugar on each of the three short arms and a biotin molecule on the longer, fourth arm were produced. The biotin molecule allows the catching and purification of *E. coli* bound to sugars on the DNA structures via streptavidin-coated magnetic beads. The usage of DNA structures as linkers enables the creation of precise arrangements of defined mannose chains with single-nanometer spatial resolution. The goal of this subproject was the establishment of a high-throughput assay that allows for a quick assessment of interactions between a variety of sugars and pathogens like bacteria. This was realized by flow cytometry in a 96 well plate format.

### 5.4.2 Construction of sugar-modified DNA 4arm structures

For the construction of DNA 4arm structures carrying three sugar molecules, oligonucleotides N\*O (5'-NH<sub>2</sub>), O\*P\* (5'-NH<sub>2</sub>) and PM\* (5'-NH<sub>2</sub>) were functionalized with DBCO according to 3.13.1. After removal of excess of DBCO-NHS ester via ethanol precipitation, the three strands were mixed with MN (5'-biotin) in 1x PBS and folded as described in 3.12. DBCO-DNA 4arm structures were incubated with various azide-functionalized sugar molecules which were obtained from Dr. Vittorio Bordoni (Max-Planck-Institute of Colloids and Interfaces, Germany). Amicon® Ultra centrifugal filters with 30K MWCO were employed to clear unbound sugar molecules from sugar-carrying DNA 4arm structures. The coupling process was verified via 10% (v/v) native PAGE (Figure 5-10).

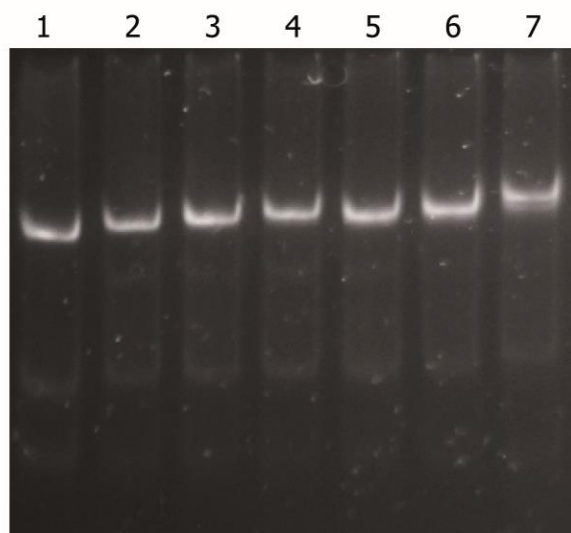


**Figure 5-10. PAGE: DNA 4arm structures conjugated to different mannose molecules.**

DNA 4arm structures (lane 1) were modified with three sugar molecules. Those were: Lane 2) Monosaccharide w/o linker; lane 3) Monosaccharide w/ linker; lane 4) Disaccharide 1,6 linked; lane 5) Disaccharide 1,2 linked; lane 6) Trisaccharide 1,2 linked; lane 7) Hexasaccharide 1,6 linked. The 10% (v/v) native PAGE gel was stained with SYBR® Gold Nucleic Acid Gel Stain and imaged under UV light.

Figure 5-10 clearly shows a decelerated migration of sugar-modified DNA 4arm structures (lanes 2-7) in comparison unmodified DNA 4arm structures (lane 1). The change in height of the bands corresponded to the size of attached sugars and increased from left to right. In addition, only one band per lane can be seen which indicates the formation of a uniform population of correctly folded and modified DNA constructs.

### 5.4.3 Bacteria binding assay

The produced sugar-carrying DNA 4arm structures were incubated with fluorescent *E. coli* and magnetic beads in a clear 96 well microplate with U-bottom by Dr. Jasmin Fertey (Fraunhofer Institute for Cell Therapy and Immunology IZI, Germany) as described in 3.20.2. Analysis was performed using an iQue screener (IntelliCyt, USA). Populations were gated by fluorescence (detection filters 533/30 for GFP labeled bacteria and 585/40 for dsRed labeled bacteria, see gates in Figure A 5) and plotted as fluorescent events as percentage of all events. Due to repeated washing it was assumed that detected fluorescence signals only originate from bound bacteria.

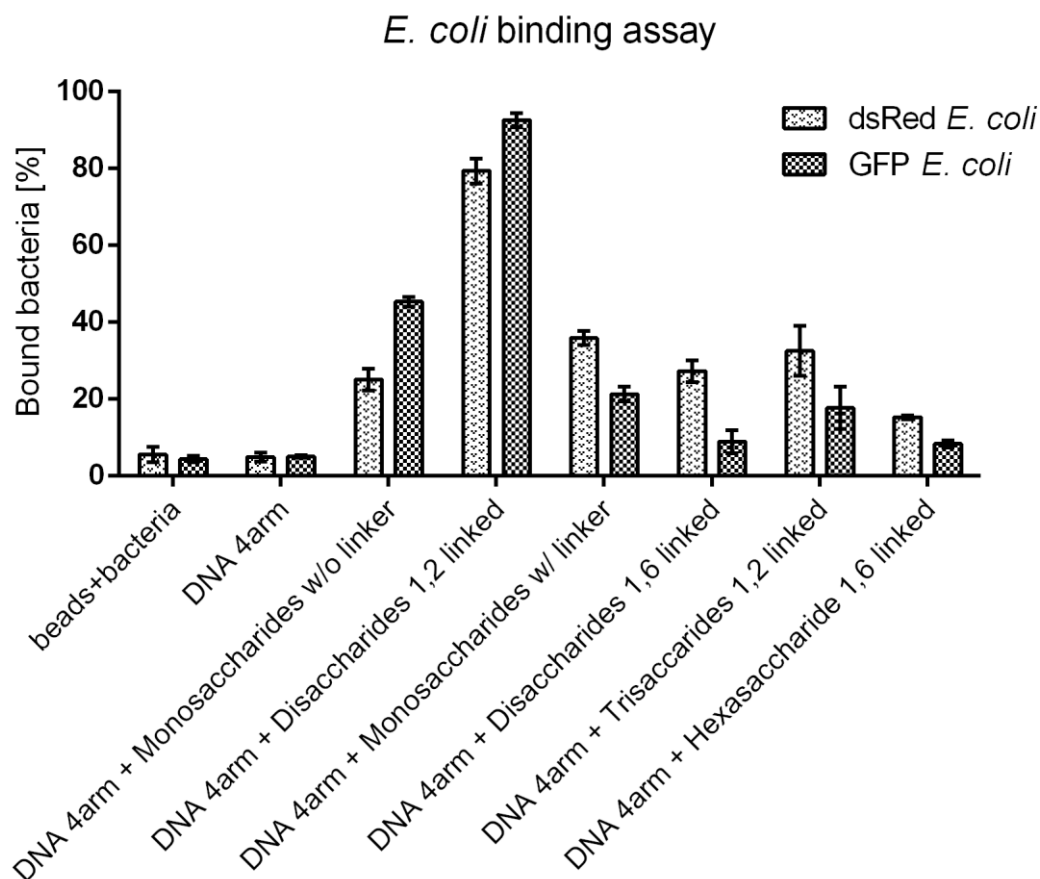


**Figure 5-11. Binding of fluorescent *E. coli* to mannose molecules on DNA 4arm structures.**

Measured events were gated for fluorescent bacteria. Shown are normalized values of bound bacteria as percent of all detected events. The samples “beads+bacteria” and “DNA 4arm” are controls. All linkages are  $\alpha$ -linkages. Raw dot plots are shown in Figure A 5.

As indicated in Figure 5-11, *E. coli* did not bind nonspecifically to “naked” DNA 4 arm structures or beads but to sugar-conjugated 4 arm structures in varying degrees depending on the specific type of sugar. DNA 4 arm + Disaccharides 1,2 linked and both DNA 4 arm + Monosaccharides (with and without linker) rank among the best binders whereas longer and more complex sugar structures show a decreased binding to *E. coli*.

#### 5.4.4 Discussion

*E. coli* attach to host cell surface carbohydrates via  $\alpha$ -mannoside-specific type 1 fimbriae. Type 1 fimbriae play a key factor in diseases like urinary tract infections, neonatal meningitis and Crohn’s disease<sup>184</sup>. Antibiotic therapies have negative impacts as increased intake contributes to the development of antibiotic resistances and additionally harms the beneficial gut microbiota. In particular, the growth of bacterial resistances to traditional antibiotics reinforces the need for novel antibacterial therapies. A promising approach is to target and block the interaction of FimH with mannosylated host receptors.

The results obtained by Langermann *et al.* suggest that blocking bacterial adhesion of uropathogenic *E. coli* to mannose-containing receptors with FimH vaccines compromises bacterial infections causing bladder inflammations<sup>208</sup>. In 2013, a study demonstrated that multivalent presentation of n-Heptyl  $\alpha$ -d-mannoside led to FimH inhibition *in vivo*<sup>209</sup>. Long retention times of the multivalent derivatives in the bladder of mice led to the conclusion that these FimH inhibitors could be suitable drug candidates against urinary tract infections. Consequently, FimH is an attractive target as its mannose-binding pocket is highly conserved across all known FimHs, except for the FimH of O157:H7 enterohaemorrhagic *E. coli*<sup>210</sup>.

In the course of a bigger project, the goal is to develop multivalent arrangements of new glycan formulations. Those compounds can eventually function as anti-adhesives that hinder bacteria from binding to and infecting host cells. An initial step of that project was the creation of a high-throughput assay to screen synthetic mannose structures attached to DNA structures for their ability to bind *E. coli* bacteria. Therefore, DNA 4arm structures presenting three of the same mannose structures were bound to labeled *E. coli*. The unlabeled *E. coli* strain used was found to cause diarrhea. Interestingly, the large glycan oligomannose-9 also carries three terminal  $\alpha$  1,2 linked mannosides on its three arms. The affinity for binding to FimH was shown to increase with a factor of three for oligomannose-9 over Man- $\alpha$ -1,2Man, which indicated that the binding of oligomannose-9 is not polyvalent<sup>184</sup>. Thus, it can be concluded, that not all three mannose residues simultaneously bind to FimH molecules.

In concordance with findings in the literature, the best binding sugars were 1,2 linked mannose disaccharides<sup>211</sup>. However, another study detected 1,3 linked mannose disaccharides as better FimH binders<sup>210</sup> and another study identified mannose oligosaccharides as better binders than mannose disaccharides<sup>212</sup>. Those differences very likely depend on assay and linker conditions as well as on the expression of pili. Interestingly, no correlation between FimH variations among different *E. coli* pathotypes and the affinities or specificities for oligomannosides could be detected<sup>210</sup>. More recent analyses of crystal structures and kinetic characterizations showed that FimH is able to similarly recognize terminal  $\alpha$ 1,2-;  $\alpha$ 1,3-; and  $\alpha$ 1,6-linked mannosides of natural high-mannose type *N*-glycans present in the bladder<sup>213</sup>.

The method presented here is robust and delivers reproducible results. For future studies, different DNA architectures that vary in flexibility, symmetry and sugar structures can be

examined with the developed method. Moreover, this technique can be expanded to other bacteria or to viruses.

## 6 Pinpointed stimulation of EphA2 receptors via DNA-templated oligovalence

### 6.1 Importance and aim

The activation of canonical EphA2 receptor signaling through ligands has been implicated in the suppression of tumor growth and therefore EphA2 receptors are increasingly studied as potential therapeutic targets<sup>120,214</sup>. In addition, these receptors are internalized upon ligand binding and their expression in normal tissues is low compared to cancerous tissue, making them suitable to specifically deliver anti-cancer agents<sup>215,216</sup> or serve as specific tissue markers for imaging agents<sup>217,218</sup>.

A DNA-templated approach was adopted, where up to three SWL peptide monomers were bound to stable DNA nanostructures and the influence of this oligovalent presentation was examined on PC-3 prostate cancer cells that overexpress the EphA2 receptor. Upon binding of the dimeric ephrin ligand to a pair of Eph receptors, their dimerization is followed by autophosphorylation of tyrosine residues in the cytosolic domain of the receptors and subsequent activation of signaling pathways. In contrast to most RTKs, downstream Eph-ephrin signaling requires the formation of higher-order clusters<sup>219</sup>. Since the association of as few as three ligand-receptor complexes has been shown to cause oligomerization<sup>220,221</sup> a three-valent DNA template called DNA trimer was chosen for this study (Figure 6-1).

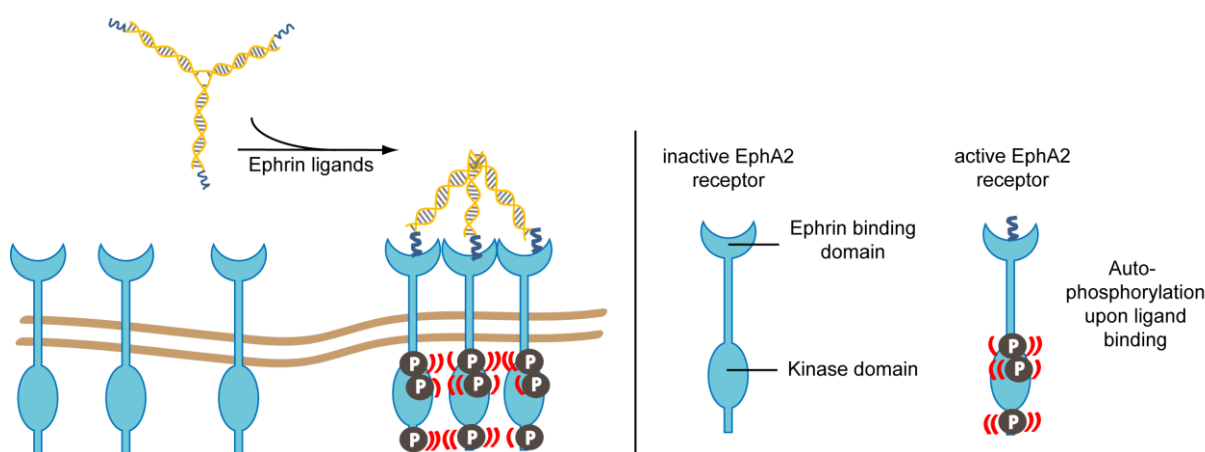


**Figure 6-1. SWL-coupled DNA trimer and its action on EphA2 receptors.**

EphA2 (light blue) cluster formation and subsequent autophosphorylation due to the presence of three peptides SWL (dark blue) attached to DNA trimers (orange). Inactive Eph receptors are loosely distributed on cell membranes and become ordered when activated<sup>222</sup>.

A related DNA-based approach to activate EphA2 signaling pathways by controlling cluster proximity was introduced by Shaw *et al.* in 2014<sup>14</sup>. They engineered a large DNA origami structure (approximately 5 MDa in size) that positions pairs of dimeric ephrin-A5 protein ligands at two different distances from each other, 43 nm and 100 nm. Here, a comparatively small SWL peptide (1.7 kDa) was chosen instead of natural ephrin protein ligands (e.g. ephrin-A1 with molecular weight of approx. 21 kDa) since these mimic the binding and stimulation activity of the full ligand, albeit with specificity to EphA2, while still allowing the exploitation of sub-nanometer spatial resolution that DNA can provide<sup>147</sup>.

### 6.2 Construction of SWL-DNA trimers

The DNA trimer consists of three partially complementary strands, has a molecular mass of approximately 28 kDa when unmodified, and a mass of approximately 34 kDa when modified with three monomeric SWL peptides. When conjugated at the ends of the arms on the DNA trimer, SWL peptides are approximately 9 nm apart when the structure is in outstretched conformation. Although the structure's arms are rigid on these length scales (DNA persistence length is 50 nm), the junction in the middle supplies the DNA trimers with needed flexibility for adjusting to the exact conformation of the EphA2 LBD. Furthermore nanostructures built from DNA or other modified nucleotide variants are very stable molecules<sup>223</sup> and therefore can be more suitable to survive in a biological environment than peptides alone<sup>123</sup> (Figure A 6).

For DNA trimers carrying zero, one, two or three SWL peptides, 5'-NH<sub>2</sub>-modified DNA strands were replaced by three, two, one and no unmodified strand, respectively. For flow cytometry, the strand ab was used as 5'-NH<sub>2</sub> and 3'-Cy3 modified version. In order to place SWL peptides onto the DNA trimer, NHS ester reactions as well as copper-free click chemistry reactions<sup>127,128,224-226</sup> were performed to attain nearly quantitative yields as proved by PAGE (Figure 6-2).

Figure 6-2 illustrates the stepwise assembly of DNA trimers. Due to the addition of strand b\*c to ab, the molecular weight increased which caused a decelerated migration through the gel and a corresponding shift in the height of the bands. The correct formation of DNA trimers was indicated by the existence of a single band. The conjugation to different numbers of SWL peptides led to further gains in molecular weights. Therefore, the changes in height of the bands were evaluated as successful modifications. A weak band below the prominent band can be seen



in the lane loaded with 3xSWL-DNA trimers and corresponds to not completely functionalized 2xSWL-DNA trimers.

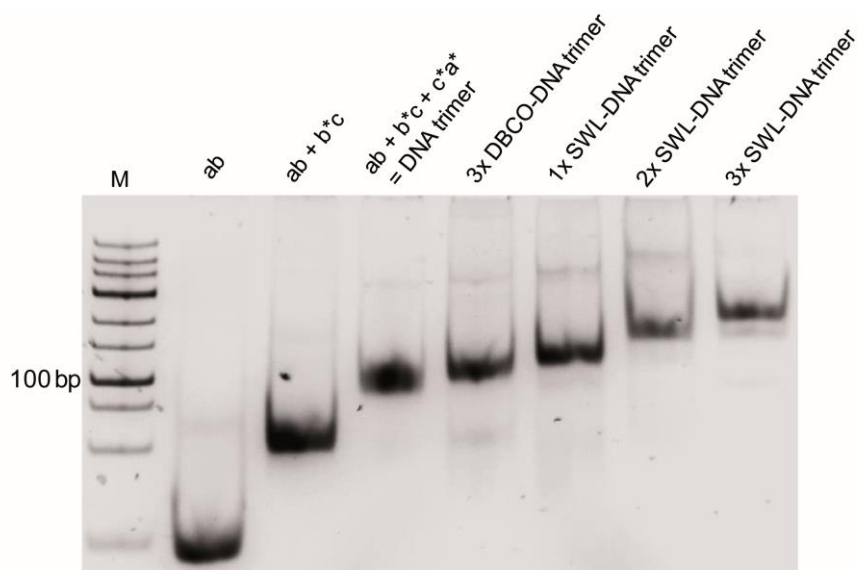


**Figure 6-2. PAGE: Assembly of DNA trimers and addition of SWL peptides.**

The partially complementary strands ab, b\*c, c\*a\* were assembled to DNA trimers and modified with DBCO-NHS ester for addition of three SWL peptides (3xSWL-DNA trimer). The 10% (v/v) native PAGE gel was stained with SYBR® Gold Nucleic Acid Gel Stain and imaged under UV light. M = GeneRuler™ Low Range DNA Ladder (Thermo Fisher Scientific, USA) serves as control, not as ruler.

The overnight incubation of DBCO-modified DNA trimers with SWL peptide for conjugation was followed by Amicon® purification to remove unbound SWL molecules from the solution. To verify whether this purification was successful, MALDI-TOF analysis was performed. Owing to the type of MALDI-TOF, only ssDNA strands could be analyzed (Figure 6-3). SWL-coupled DNA strand ab (expected mass 11.3 kDa) was examined before purification with Amicon® 3 K filter. The peak at 11.5 kDa confirms the covalent conjugation of SWL to oligonucleotides (double ionized peak at 5.8 kDa). Oligonucleotides that were not coupled to SWL peptide could not be detected (peak would be at 9.3 kDa) and a peak at 1.7 kDa corresponds to free SWL peptide. This peak is relatively high in comparison to both DNA peaks. In comparison, Amicon® 3 K purified SWL-oligonucleotides disclosed a remarkable difference in intensity for SWL-oligonucleotides to uncoupled SWL. The peak for free SWL is within the noise range whereas higher peaks are visible for DNA-SWL conjugates.

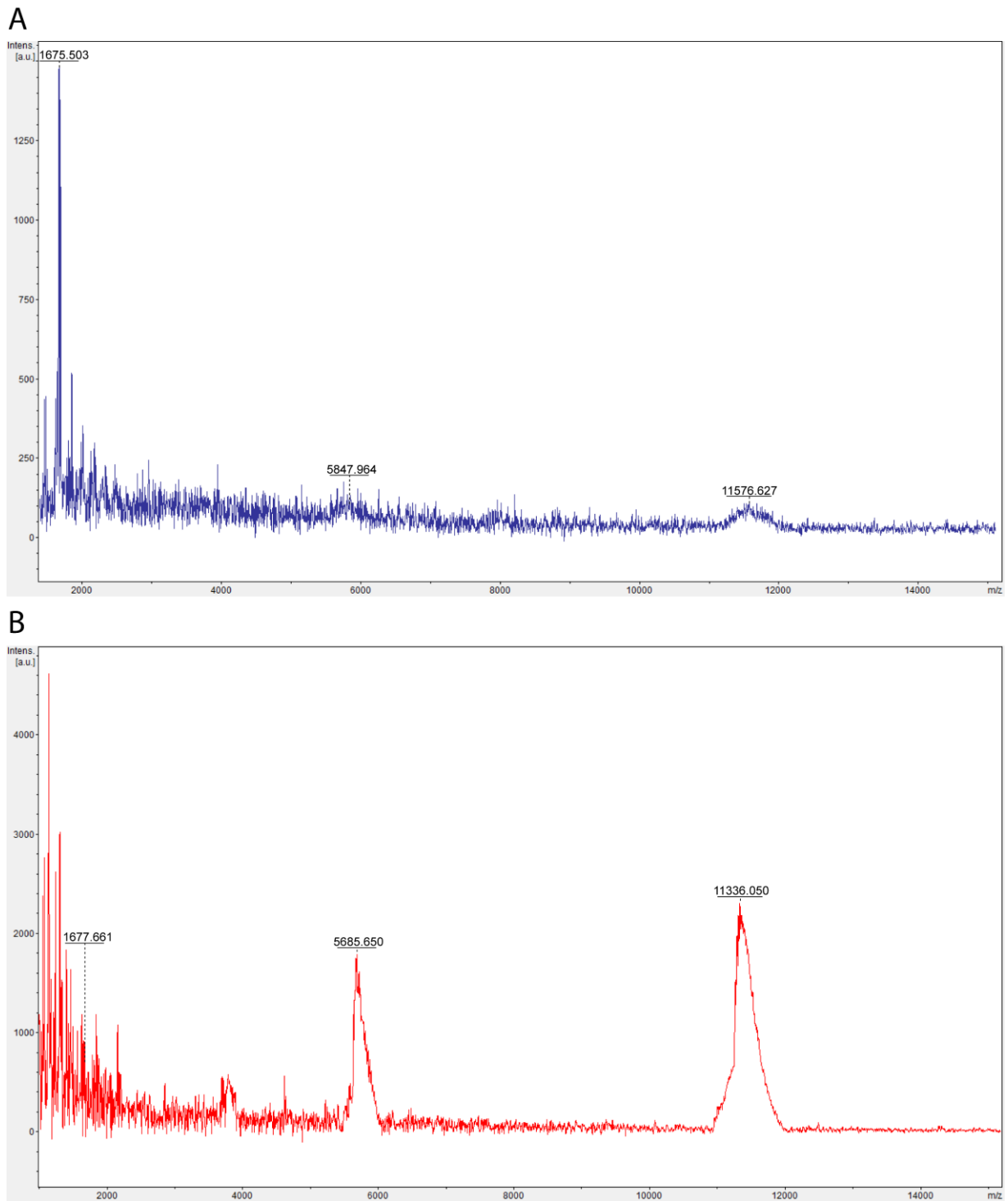


**Figure 6-3. Mass spectra of oligonucleotides coupled to SWL peptides.**  
A) SWL-coupled oligonucleotides before purification with Amicon® 3 K filter is shown in blue. B) Mass spectra of Amicon® 3 K purified SWL-oligonucleotides is shown in red.

### 6.3 Binding of SWL-DNA trimers to PC-3 cells

To confirm the overexpression of EphA2 in PC-3 cells, expression was initially probed using a PE labeled anti-human EphA2 antibody in flow cytometry experiments. As a negative control HL-60 cells, which should only express these receptors after maturation<sup>227</sup>, were tested, too. As Figure 6-4 reveals, PC-3 cells treated with PE anti-human EphA2 antibody showed enhanced fluorescence signals compared to untreated PC-3 cells. Fluorescence signals from HL-60 cells were not elevated which confirms that these cells lack an EphA2 expression.

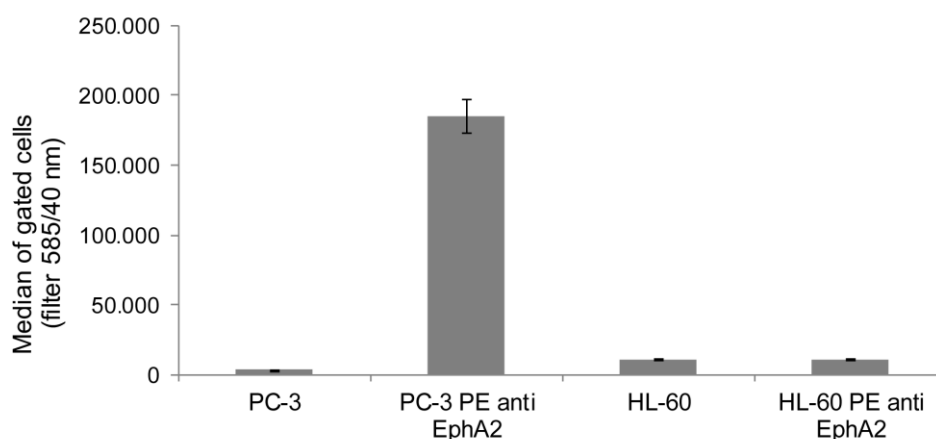


**Figure 6-4. Flow cytometry analysis of EphA2 expression.**

Displayed are average values of gated cells with standard deviation presented as error bars.

EphA2-expressing PC-3 cells were treated with different concentrations of DNA trimers<sup>Cy3</sup> carrying between 0-3 SWL peptides, and were subsequently analyzed via flow cytometry (Figure 6-5). As expected, binding curves revealed that the construct with three SWL peptides (3xSWL-DNA trimer<sup>Cy3</sup>) displays highest binding activity. In comparison, the binding activity of structures carrying one SWL peptide is nearly indistinguishable from nonspecific interactions occurring between the bare DNA trimer<sup>Cy3</sup> and cells. Structures carrying two peptides do display moderate binding, although at approximately one-quarter of the levels of the three-peptide structures at the highest concentration.

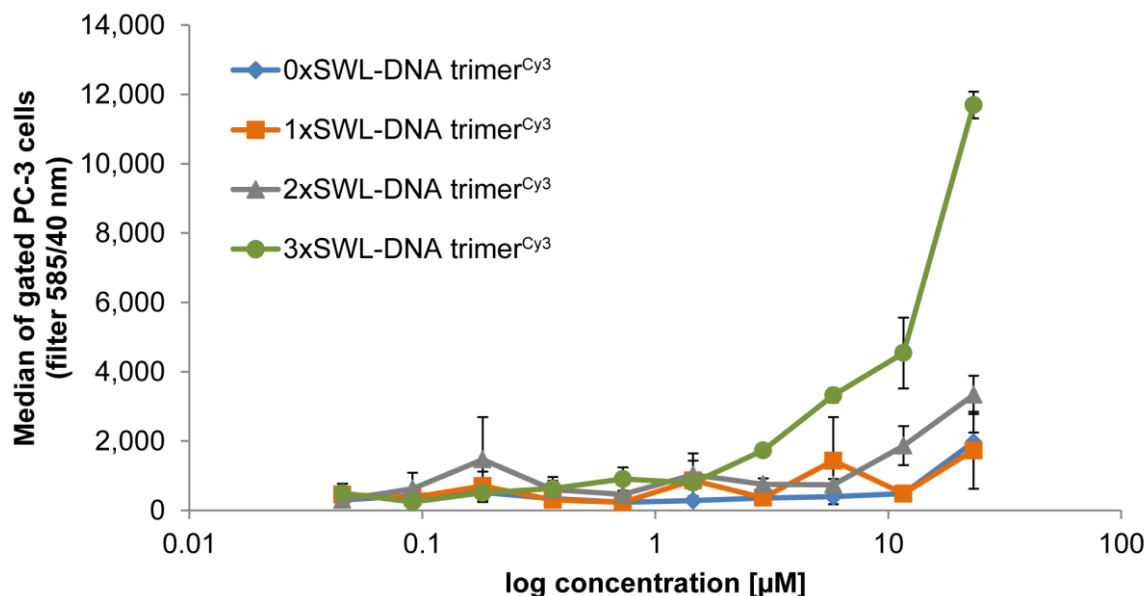


**Figure 6-5. Binding of SWL-coupled DNA trimers<sup>Cy3</sup> to EphA2-expressing PC-3 cells.**

Serum-starved PC-3 cells were treated with SWL-DNA trimer<sup>Cy3</sup> constructs (carrying 0-3 peptides SWL) in duplicates for 30 min at room temperature. Cells were gated and normalized by cell number. Displayed on the y-axis are average values of emission which were observed using a 585/40 nm filter (FL2-A) with standard deviation presented as error bars. The x-axis indicates concentrations of the constructs in terms of DNA. Scatter plots of raw data can be found in Figure A 7.

For both the two- and three-peptide variants, the highest concentration of 25 µM was not sufficient to reach saturation of binding, as was particularly evident in the latter case. This lack of saturation likely results from the active internalization via endocytosis following activation of EphA2 pathways<sup>228</sup>, leading to an accumulation of fluorescent molecules within the cell interior. Nevertheless, the onset of binding above 1.5 µM for the 3xSWL-DNA trimer<sup>Cy3</sup> is clear, compared to the 1xSWL-DNA trimers<sup>Cy3</sup> and 2xSWL-DNA trimers<sup>Cy3</sup>, both of which do not show any comparable amount of binding below the maximum concentration. Due to the functional connection between receptor binding and internalization, biochemical signaling events and phenotype changes resulting from treatment with the DNA-peptide constructs were also examined.

#### 6.4 Confirmation of EphA2 pathway activation via receptor phosphorylation

The efficacy and potency of EphA2 receptor phosphorylation resulting from binding of the various constructs (monomeric peptide, mono-, bi- and trivalent presentation on the DNA trimer and positive/negative controls) was quantified by sandwich ELISA detecting first EphA2

receptors and second phospho-tyrosines. The phosphorylation of EphA2 receptors resulting from the application of different concentrations of the ligands enabled the calculation of approximate EC50 values for the DNA-peptide constructs by least-square analysis (Figure 6-6, Table 6-1, equation (3))<sup>229</sup>. As expected, the negative control of DNA trimers without any SWL peptides did not lead to any clearly enhanced phosphorylation of tyrosine residues whereas 3xSWL-DNA trimers led to the highest phosphorylation signal (EC50 = 0.0190 ± 0.0046 μM), i.e. overall efficacy, followed by 2xSWL-DNA trimers (EC50 = 0.0572 ± 0.0113 μM) and 1xSWL-DNA trimers (EC50 = 2.7427 ± 1.9837 μM) for concentrations up to 30 μM. For SWL, concentrations up to 500 μM were tested and fitting revealed an EC50 value of 153.8287 ± 115.3869 μM. DNA trimers without any SWL (0xSWL-DNA trimer) did not evoke phosphorylation of EphA2 receptors, and accordingly the absorbance signal is within the background (approximately 0 in Figure 6-6). Figure A 8 presents the data obtained for the natural ligand ephrin-A1 (EC50 = 0.0027 ± 0.0005 μM).

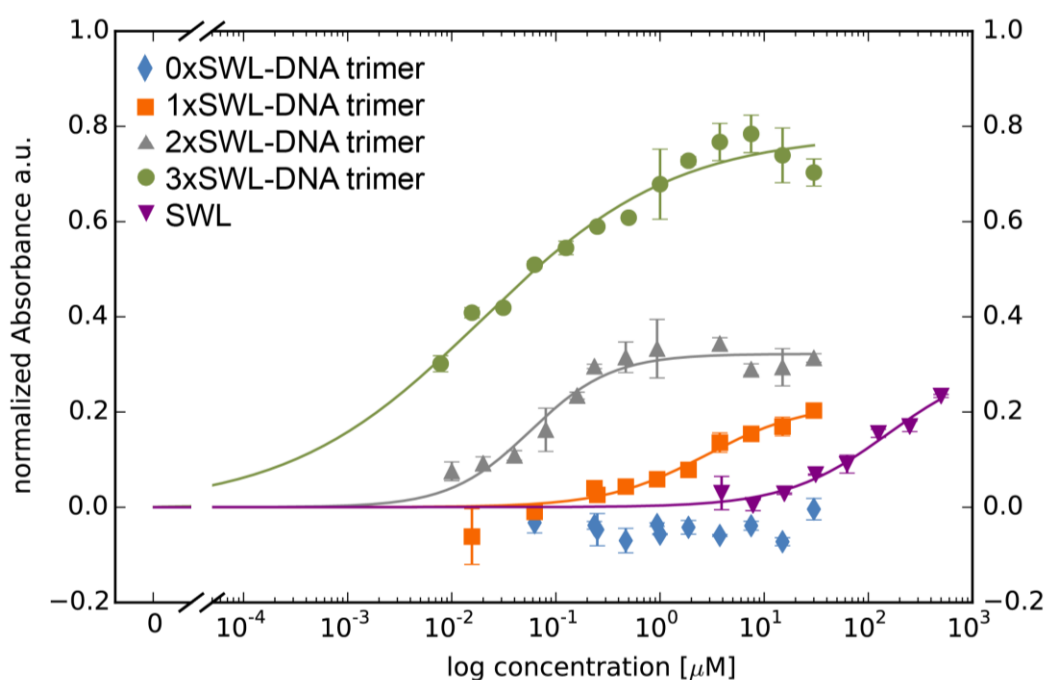


**Figure 6-6. Quantitative analysis of phosphorylation of EphA2 receptors.**

Serum-starved PC-3 cells were treated with different concentrations of constructs in duplicates for 30 min at 37 °C. Cells were washed with 1x PBS twice and further treated according to the manufacturer's instructions. Displayed data points are averages of normalized net absorbance (difference between absorbance at 520 nm versus 450 nm); the net absorbance signal in the presence of different entity concentrations was normalized to the signal from treatment with 1x PBS/ 10 mM MgCl<sub>2</sub> only (without any peptide or DNA constructs) resulting in normalized absorbance. Standard deviation is presented as error bars. The x-axis indicates concentrations of the constructs in terms of DNA for 0xSWL-DNA trimer – 3xSWL-DNA trimer and the concentration of the peptide for SWL. It should be understood that the x-axis displays concentrations for whole entities not for binding entities (in this case SWL molecules).

**Table 6-1. EC50 values of different ligands for EphA2 receptor phosphorylation**

Values result from fitting to equation (3) and are also shown as solid lines in Figure 6-6.

<b>Ligand</b>	<b>EC50 [<math>\mu\text{M}</math>] (mean <math>\pm</math> standard deviation)</b>
SWL	153.8287 $\pm$ 115.3869
ephrin-A1	0.0027 $\pm$ 0.0005
1xSWL-DNA trimer	2.7427 $\pm$ 1.9837
2xSWL-DNA trimer	0.0572 $\pm$ 0.0113
3xSWL-DNA trimer	0.0190 $\pm$ 0.0046

## 6.5 PC-3 cell rounding caused by EphA2 activation

Phosphorylation of EphA2 receptors is required for subsequent signaling pathways in EphA2 receptor presenting cells, therefore it is expected that multivalent presentation of the peptide on the trimeric DNA construct will lead to the most significant cell phenotype changes. As a result of downstream processes resulting from EphA2 activation, PC-3 cells retract their membrane protrusions and "round up," adopting a compact morphology <sup>120</sup>. The overall impact of monomeric SWL peptide or the SWL-DNA trimer displaying different numbers of peptides on cell morphology was qualitatively assessed via microscopic imaging, as seen in Figure 6-7. For 3xSWL-DNA trimers, a concentration of 20  $\mu\text{M}$ , well above the measured EC50 values, was used while concentrations of the natural ligand and monovalent SWL were chosen according to previous reports.

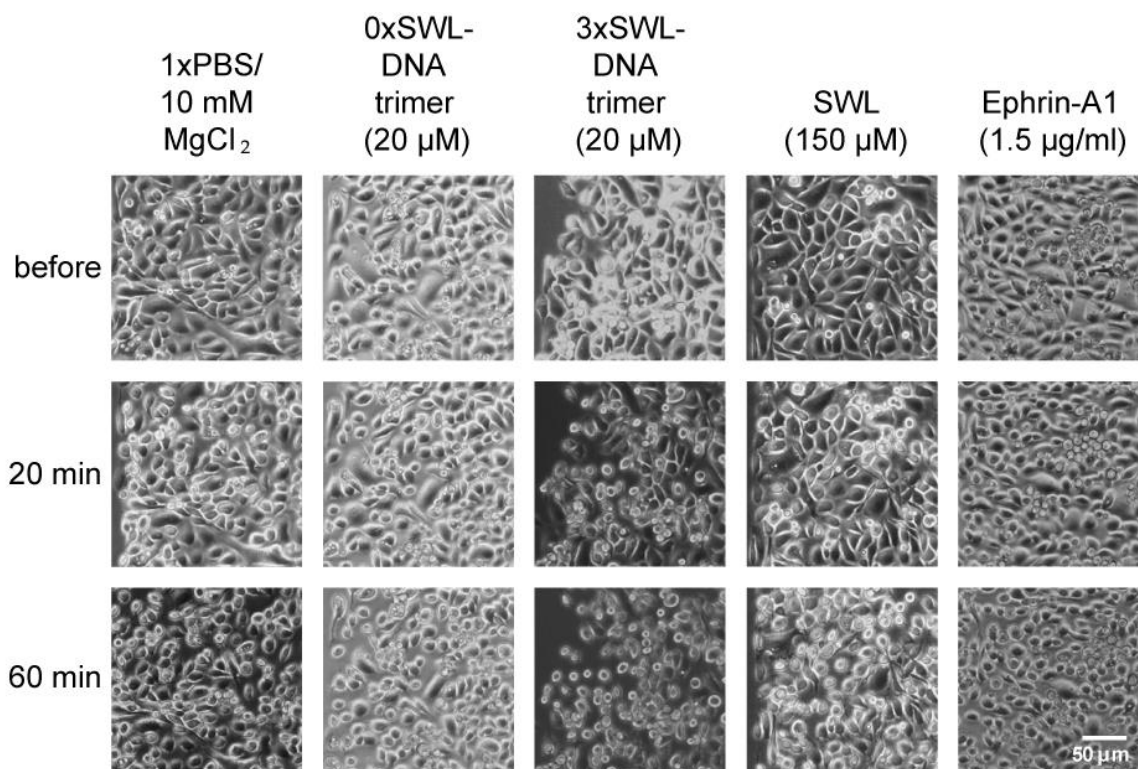


**Figure 6-7. PC-3 cell rounding.**

Cells were seeded the day before and serum-starved for 4 h prior treatment. Samples were diluted in 1x PBS and incubated on cells for indicated times. Cell morphology was observed and 20 and 60 minutes to account for inherent rounding effects from serum starvation.

Slight rounding of cells following starvation was seen as a baseline effect for all samples, likely due to the lack of nutrients and medium. As expected, the most prominent differences were seen for 3xSWL-DNA trimers. At a concentration of 20  $\mu\text{M}$ , rounding of cells was already observed after 20 min, and was ubiquitous in the sample after 60 min of treatment. By contrast, after 20 minutes a significant amount of rounding beyond the likely starvation-induced effects was not significantly clear for the 1xSWL-DNA or 2xSWL-DNA structures (Figure A 9). A 150  $\mu\text{M}$  concentration of the monomeric peptide showed no noticeable change in morphology after 20 minutes when compared to the negative controls of PBS and the DNA structure without any peptides.

In comparison to the 3xSWL-DNA structure, only moderate changes in morphology were observed to arise from the application of 1.5  $\mu\text{g/ml}$  of the natural ephrin-A1 ligand after 20 and 60 minutes. This concentration is approx. 27 times the EC50 value of 2.654 nM as shown in Figure A 8. Downstream impact on morphological phenotype is clearly suppressed despite the fact that the natural ligand did still lead to high levels of EphA2 phosphorylation, as seen in Figure A 8 and Figure 6-6. While seemingly contradictory, this is consistent with some previous

reports where additional stimulation of the Rho-ROCK1 signaling pathway by external serum factors is necessary to cause significant levels of cell rounding following serum starvation<sup>230</sup>.

### 6.6 Discussion

It was shown that even simple DNA nanostructures consisting of a few strands are not only limited to serving as functional carriers for bioactive peptides such as SWL but can also enhance their activity and trigger specific downstream signaling pathways in a pinpointed manner. These rationally designed, structural scaffolds not only hold the peptides in a controlled spatial average distribution while still maintaining flexibility at the central joint to finely adjust to the arrangement of binding sites; they also preserve their functionality and provide the basis for oligovalent binding to target structures, and thus an enhanced efficacy when compared to the monovalent peptides.

The binding of SWL-DNA trimers<sup>Cy3</sup> to PC-3 cells via EphA2 receptors was analyzed using flow cytometry to determine binding curves (Figure 6-5). Preparation limitations impeded the production and testing of higher concentrations of the constructs. Therefore, saturation could not be achieved, likely due to the fact that EphA2 receptors are internalized upon activation<sup>228</sup>, leading to an accumulation of fluorescence within the cells. In this case, saturation, if reached, would likely correspond to the actively driven depletion of expressed EphA2 receptors from the surface of the cells, rather than equilibrium kinetics of binding between the DNA peptide constructs and the receptors. Thus, half-maximal effective concentration (EC50) values or other binding constants could not be quantitatively determined for flow cytometry data. Nevertheless, enhanced concentration-dependent fluorescence signals for cells treated with the 3xSWL-DNA trimer<sup>Cy3</sup> compared to the 0–2 peptide variants clearly show an increased affinity due to higher-order presentation of SWL.

In a sandwich ELISA to quantify phosphorylation of tyrosine residues (Figure 6-6), the results underline the presence of an oligovalent effect, as 3xSWL-DNA trimers are both more potent and more efficacious than monomeric SWL peptides. Interestingly, all SWL-conjugated DNA trimers are more potent than the monovalent, unconjugated SWL peptide. SWL and 1xSWL-DNA seem to have a similar efficacy although it should be noted that the maximum effect could not be reached due to practical limitations, implying that the calculated EC50 value could be



higher. However, it is clear that 1xSWL-DNA trimers can reach similar phosphorylation signals with a much lower concentration, indicating that the presence of the DNA structure improves potency. An explanation could be that the attachment of SWL to DNA already improves its stability and/or binding properties. More specifically, the larger DNA construct could shield the attached peptide from proteases, which was indeed previously implicated as a limitation for the covalently dimerized SWL variant<sup>123</sup>. Furthermore, DNA is known to nonspecifically stick to the outer plasma membrane of cells, which would generally increase the chances for the DNA-peptide conjugate structures to interact with any surface receptors such as EphA2 as compared to the peptide by itself.

The 2xSWL-DNA and 3xSWL-DNA constructs have a noticeably elevated performance compared to 1xSWL-DNA and SWL, as shown in Figure 6-6. The attachment of two peptides on the DNA structure drastically decreases the EC50, by nearly a factor of 50 compared to 1xSWL-DNA, which portends the influence of an oligovalent effect. This is further enhanced when 3 peptides, the suggested minimum for inducing Eph receptor clustering<sup>221</sup>, are attached to the DNA structure. While the apparent EC50 value is only further decreased by a factor of three, the overall phosphorylation efficacy more than doubles, as compared to the monomeric peptide as well as both the mono- and bivalent DNA-peptide conjugates. The natural ligand ephrin-A1 remained most potent and efficacious when tested for EphA2 receptor phosphorylation in different concentrations (Figure A 8). As expected, 0xSWL-DNA trimer did not lead to phosphorylation at any concentration, and therefore an EC50 value was not calculated. Moreover, comparatively low signals seen for PC-3 cells treated only with PBS confirmed that even though EphA2 receptors are indeed highly expressed (indicated by the PBS control in Figure 6-4) they are only slightly activated.

Even though the degree of activation from even the trivalent DNA construct is greatly surpassed by that achieved by the natural ephrin-A1 ligand (Table 6-1, Figure A 8), two factors could mitigate a direct comparison. First, it is expected that a short, linear, likely flexible peptide fragment will be entropically disfavored from specifically binding to and activating its target when compared to an active polypeptide region held in a rigidly defined conformation within a folded protein. Second, as noted before, ephrin-A1 is known to bind and activate most, if not all A-type Eph receptors, several of which are expressed in PC-3 cells<sup>231</sup>. While the natural ligand is clearly more efficient at stimulating phosphorylation of EphA2 dimers, this does not capture

the extent to which cross-stimulation of other EphA receptors interferes with downstream pathways<sup>125,126</sup>. Indeed, recently reported findings from Singh *et al.*, point out that different types of ephrin ligands, including the SWL peptide used here, give rise to diverse activities of EphA2 receptor signaling<sup>232</sup>.

This second point is of particular importance when observing the effects on cell phenotype; namely the “rounding up” of cells following treatment. While the application of the full ligand in excess of its measured EC50 value for tyrosine phosphorylation did show some moderate signs of morphological changes after 20 min (Figure 6-7) consistent with previous observations on serum-starved PC-3 cells<sup>230</sup>, this was clearly surpassed by effects resulting from application of the 3xSWL-DNA constructs. Even though visual, microscopic interpretation of cell morphology is to some extent a qualitative art, this nonetheless suggests that pinpointed stimulation with the EphA2-specific peptide along with the promotion of receptor clustering is a potent trigger of this particular phenotype change. This discrepancy with the significantly more efficient tyrosine phosphorylation by the natural ligand does support the possibility of negative feedback resulting from the cross-stimulation of different EphA receptors.

More generally, the presentation of highly specific peptide fragments on simple DNA scaffolds in the way shown here potentially provides a two-pronged tool for helping to unravel the complexity of signaling pathways involving promiscuous binding between a ligand and multiple receptors<sup>233</sup>. Beyond the A- and B-classes of Eph receptors, the binding of a single ligand to a set of multiple receptors (or vice versa) is a common occurrence in diverse processes such as immune recognition<sup>234</sup>, tissue and organ development<sup>235</sup>, programmed cell death also known as apoptosis<sup>236,237</sup> and many others. DNA-scaffolded presentation of short peptide epitopes known to be specific to a particular receptor, such as cell death receptors<sup>238,239</sup>, would enable a systematic examination of these pathways with a pinpointed resolution in terms of biochemical pathways and degree of multimerization in signaling events.

## 7 Conclusion and outlook

In this study, it was shown that DNA nanostructures can serve as versatile tools to precisely arrange biomolecules to target different types of biological systems. The connection of individual bioactive binding units on DNA structural scaffolds leads to the emergence of multivalent ligands. According to the principle of multivalency, those engage in much stronger interactions with their corresponding receptors than single binding units would do due to their inherent cooperativity. To construct these ligands, copper-free click chemistry reactions were conducted. Those types of reactions are beneficial over potentially toxic copper-catalyzed click chemistry reactions as they do not require the removal of potentially cytotoxic copper<sup>240</sup> afterwards. Instead of copper, the ring strain of the DBCO linker molecule, that functions as a tether for the binding units on the multivalent ligand, provides enough energy to catalyze the coupling reaction. The formation of regioisomeric mixtures of triazoles in copper-free click chemistry reactions does not hinder their applications in biorthogonal chemistry<sup>241–243</sup>.

DNA structures of different sizes were employed in this work, which enabled the precise generation of ligand arrangements with spacings ranging from under 5 to ~ 50 nm. In order to place two antibody binding peptides (epitopes) on the planar surface linear distances of up to ~ 25 nm, a large DNA origami structure was used. A variety of DNA origami structures were designed to test several different inter-ligand distances as well as the monovalent case for comparison, and binding of the respective antibody was assessed in an ELISA approach. The presented method is straightforward and the obtained results largely confirm antibody binding properties reported in literature, as well as show different types of signatures for different non-canonical modes of antibody binding. Even though the method has limitations and not all antibodies seem to be suitable, it contributes to a better characterization of antibody binding properties.

Small DNA nanostructures were coupled to bioactive peptides or mannose structures to target receptors on the surface of different types of pathogens, specifically respiratory viruses and enterobacteria. As model systems for viruses, influenza A and RSV were utilized. Both harbor homotrimeric glycoproteins that facilitate binding to and fusion with host cell membranes. Therefore, DNA nanostructures with three ligand-presenting arms were equipped with up to three peptides that were designed to specifically bind to and inhibit the viral receptor. Here, both

a steric binding inhibitor (peptide PeB for influenza A) and a fusion inhibitor (RSV-Peptide-6 for RSV) were chosen in order to assess differences in multivalent amplification when applied to blocking simple binding interactions versus active functions. For influenza A, only the enhanced binding of peptide-functionalized DNA structures to the viruses could be detected, however their ability to inhibit infectiveness was increased to a much lesser degree. In the case of RSV, inhibition of the viral receptor responsible for blocking could be significantly increased due to oligovalent presentation of three binding peptides on DNA structures, resulting in an enhancement of anti-infection efficacy of several hundred times. Due to these results, it can be assumed that inhibitors that block conformational changes critical to fusion are more successful than inhibitors that only sterically compete for binding pockets. Furthermore, the findings imply that the concept of presenting virus-binding peptides on DNA structures could be transferred to other viruses with multimeric receptors, e.g. HIV or severe acute respiratory syndrome coronavirus (SARS-CoV), to hinder them from infecting host cells.

As a model system for oligovalent binding to bacterial surface, *E. coli* bacteria were chosen. Since most bacteria such as *E. coli* mainly bind to sugar molecules on the surfaces on host cells, the focus here was on the identification of mannose structures that could be bound best by *E. coli*. Therefore, a new and robust high throughput method was developed involving the presentation of different oligosaccharides on DNA structures, and different types of mannose-based compounds were screened. The strongest interactions found was between *E. coli* and 1,2 linked mannose disaccharides, which matches previous findings reported the literature. In the future, unlabeled *E. coli* and other species (e.g. *Klebsiella pneumoniae*) can be tested with the new method.

In the last subproject, DNA-peptide nanostructures functioned as oligovalent ligands for activating EphA2 mediated signaling pathways. A central point was the variation of ligand valency from zero to three EphA2 activating peptides (called SWL) per DNA structure, in order to assess the impact of forced dimerization of receptors, and the formation of a “minimal cluster” of three receptors. Effects on binding and phosphorylation of EphA2 receptors as well as phenotypical alterations of prostate cancer cells expressing EphA2 receptors were examined. From the research that has been carried out, it became clear the DNA structures harboring three SWL peptides had the greatest effect. It could be shown that DNA scaffolds can increase the potency of weak signaling peptides through oligovalent presentation and serve as potential tools for examination of complex signaling pathways.

The results in this work were obtained *in vitro*. For chapters 5 and 6, future *in vivo* studies are of great importance to validate the effects of functional DNA nanostructures in whole, intact organisms. Until now, only a few studies that utilize DNA origami-based materials as *in vivo* drug delivery systems exist and were summarized in a review by Jiang *et al.*<sup>244</sup>. In order to develop functionalized DNA structures that are successful *in vivo*, detailed information on pharmacokinetics (e.g. half-life and clearance mechanisms), pharmacodynamics (e.g. side effects and specificity) and immunogenicity must be examined. In this context it has been argued that natural DNA and RNA (including small DNA nanostructures) are susceptible to nuclease degradation upon introduction into living organisms. Due to this, chemical modifications of nucleobases, the phosphodiester backbone and/or sugar moieties have led to the development of nucleic acid analogues with altered properties<sup>245,246</sup>. Most prominent among these are locked nucleic acids (LNAs), PNAs, Morpholino<sup>247</sup> and xeno nucleic acids (XNA)<sup>248</sup> which are reported to have improved biostability compared to DNA and RNA.

In summary, it was shown that DNA nanostructures can be applied in a wide range of biological systems. They are an exceptionally useful tool for the directed, multivalent positioning of bioactive molecules and at the same time provide stability and controllability in valency and flexibility. This work provides insights about opportunities and limitations of utilizing oligovalent DNA-based ligands to interact with antibodies, viruses, bacteria and cell receptors and delivers new techniques to assess those interactions.



---

## 8 References

1. Gaston, J. *et al.* Intracellular delivery of therapeutic antibodies into specific cells using antibody-peptide fusions. *Sci. Rep.* **9**, 18688 (2019).
2. Linko, V., Ora, A. & Kostianen, M. A. DNA Nanostructures as Smart Drug-Delivery Vehicles and Molecular Devices. *Trends Biotechnol.* **33**, 586–594 (2015).
3. Jay, J. *et al.* IgG Antibody 3D Structures and Dynamics. *Antibodies* **7**, 18 (2018).
4. Mammen, M., Choi, S.-K. & Whitesides, G. M. Polyvalent Interactions in Biological Systems: Implications for Design and Use of Multivalent Ligands and Inhibitors. *Angew. Chem. Int. Ed. Engl.* **37**, 2754–2794 (1998).
5. Lisabeth, E. M., Falivelli, G. & Pasquale, E. B. Eph Receptor Signaling and Ephrins. *Cold Spring Harb. Perspect. Biol.* **5**, a009159–a009159 (2013).
6. Fasting, C. *et al.* Multivalency as a chemical organization and action principle. *Angew. Chem. Int. Ed. Engl.* **51**, 10472–98 (2012).
7. Krishnamurthy, V. M., Estroff, L. A. & Whitesides, G. M. Multivalency in Ligand Design. in *Fragment-based Approaches in Drug Discovery* vol. 34 11–53 (2006).
8. Lundquist, J. J. & Toone, E. J. The Cluster Glycoside Effect. *Chem. Rev.* **102**, 555–578 (2002).
9. Merritt, E. A. *et al.* Characterization and Crystal Structure of a High-Affinity Pentavalent Receptor-Binding Inhibitor for Cholera Toxin and *E. coli* Heat-Labile Enterotoxin. *J. Am. Chem. Soc.* **124**, 8818–8824 (2002).
10. Nangreave, J., Yan, H. & Liu, Y. DNA Nanostructures as Models for Evaluating the Role of Enthalpy and Entropy in Polyvalent Binding. *J. Am. Chem. Soc.* **133**, 4490–4497 (2011).
11. Paar, J. M., Harris, N. T., Holowka, D. & Baird, B. Bivalent Ligands with Rigid Double-Stranded DNA Spacers Reveal Structural Constraints on Signaling by FcεRI. *J. Immunol.* **169**, 856–864 (2002).
12. Rinker, S., Ke, Y., Liu, Y., Chhabra, R. & Yan, H. Self-assembled DNA nanostructures for distance-dependent multivalent ligand–protein binding. *Nat. Nanotechnol.* **3**, 418–422 (2008).
13. Li, J. *et al.* Self-assembled multivalent DNA nanostructures for noninvasive intracellular delivery of immunostimulatory CpG oligonucleotides. *ACS Nano* **5**, 8783–9 (2011).
14. Shaw, A. *et al.* Spatial control of membrane receptor function using ligand nanocalipers.

- Nat. Methods* **11**, 841–846 (2014).
15. Eberhard, H., Diezmann, F. & Seitz, O. DNA as a molecular ruler: interrogation of a tandem SH2 domain with self-assembled, bivalent DNA-peptide complexes. *Angew. Chem. Int. Ed. Engl.* **50**, 4146–50 (2011).
  16. Dubel, N., Liese, S., Scherz, F. & Seitz, O. Exploring the Limits of Bivalency by DNA-Based Spatial Screening. *Angew. Chemie Int. Ed.* **58**, 907–911 (2019).
  17. Abendroth, F. *et al.* DNA-controlled bivalent presentation of ligands for the estrogen receptor. *Angew. Chem. Int. Ed. Engl.* **50**, 8592–6 (2011).
  18. Sil, D., Lee, J. B., Luo, D., Holowka, D. & Baird, B. Trivalent Ligands with Rigid DNA Spacers Reveal Structural Requirements For IgE Receptor Signaling in RBL Mast Cells. *ACS Chem. Biol.* **2**, 674–684 (2007).
  19. Kiessling, L. L. & Lamanna, A. C. Multivalency in Biological Systems. in 345–357 (2003). doi:10.1007/978-94-007-0958-4\_26.
  20. Pray, L. A. Discovery of DNA Double Helix: Watson and Crick. *Nat. Educ.* **1**, 100 (2008).
  21. Blanco, A. & Blanco, G. Nucleic Acids. in *Medical Biochemistry* vol. 44 121–140 (Elsevier, 2017).
  22. Yakovchuk, P. Base-stacking and base-pairing contributions into thermal stability of the DNA double helix. *Nucleic Acids Res.* **34**, 564–574 (2006).
  23. WATSON, J. D. & CRICK, F. H. C. Molecular Structure of Nucleic Acids: A Structure for Deoxyribose Nucleic Acid. *Nature* **171**, 737–738 (1953).
  24. Wang, J. C. Helical repeat of DNA in solution. *Proc. Natl. Acad. Sci.* **76**, 200–203 (1979).
  25. Rhodes, D. & Klug, A. Helical periodicity of DNA determined by enzyme digestion. *Nature* **286**, 573–578 (1980).
  26. Ussery, D. W. DNA Structure: A-, B- and Z-DNA Helix Families. in *Encyclopedia of Life Sciences* (John Wiley & Sons, Ltd, 2002). doi:10.1038/npg.els.0003122.
  27. Seeman, N. C. Nucleic acid junctions and lattices. *J. Theor. Biol.* **99**, 237–47 (1982).
  28. Wei, B., Dai, M. & Yin, P. Complex shapes self-assembled from single-stranded DNA tiles. *Nature* **485**, 623–6 (2012).
  29. LaBean, T. H. *et al.* Construction, Analysis, Ligation, and Self-Assembly of DNA Triple Crossover Complexes. *J. Am. Chem. Soc.* **122**, 1848–1860 (2000).
  30. Fu, T. J. & Seeman, N. C. DNA double-crossover molecules. *Biochemistry* **32**, 3211–3220 (1993).



31. He, Y., Chen, Y., Liu, H., Ribbe, A. E. & Mao, C. Self-Assembly of Hexagonal DNA Two-Dimensional (2D) Arrays. *J. Am. Chem. Soc.* **127**, 12202–12203 (2005).
32. Zheng, J. *et al.* From molecular to macroscopic via the rational design of a self-assembled 3D DNA crystal. *Nature* **461**, 74–7 (2009).
33. Dietz, H., Douglas, S. & Shih, W. Folding DNA into twisted and curved nanoscale shapes. *Science (80-. )*. **325**, 725–730 (2009).
34. Han, D. *et al.* DNA origami with complex curvatures in three-dimensional space. *Science* **332**, 342–6 (2011).
35. Goodman, R. P. *et al.* Rapid chiral assembly of rigid DNA building blocks for molecular nanofabrication. *Science* **310**, 1661–5 (2005).
36. Kosuri, S. & Church, G. M. Large-scale de novo DNA synthesis: technologies and applications. *Nat. Methods* **11**, 499–507 (2014).
37. Ko, S., Liu, H., Chen, Y. & Mao, C. DNA nanotubes as combinatorial vehicles for cellular delivery. *Biomacromolecules* **9**, 3039–3043 (2008).
38. Smith, D., Schüller, V., Engst, C., Rädler, J. & Liedl, T. Nucleic acid nanostructures for biomedical applications. *Nanomedicine* **8**, 105–121 (2013).
39. Charoenphol, P. & Bermudez, H. Design and application of multifunctional DNA nanocarriers for therapeutic delivery. *Acta Biomater.* **10**, 1683–91 (2014).
40. Jiang, Q. *et al.* DNA origami as a carrier for circumvention of drug resistance. *J. Am. Chem. Soc.* **134**, 13396–403 (2012).
41. Douglas, S. M., Bachelet, I. & Church, G. M. A logic-gated nanorobot for targeted transport of molecular payloads. *Science* **335**, 831–4 (2012).
42. Zhao, Y. *et al.* DNA Origami Delivery System for Cancer Therapy with Tunable Release Properties. *ACS Nano* **6**, 8684–8691 (2012).
43. Zhou, G. *et al.* Multivalent capture and detection of cancer cells with DNA nanostructured biosensors and multibranched hybridization chain reaction amplification. *Anal. Chem.* **86**, 7843–8 (2014).
44. Pei, H. *et al.* Scaffolded biosensors with designed DNA nanostructures. *NPG Asia Mater.* **5**, e51 (2013).
45. Fu, J., Liu, M., Liu, Y., Woodbury, N. W. & Yan, H. Interenzyme Substrate Diffusion for an Enzyme Cascade Organized on Spatially Addressable DNA Nanostructures. *J. Am. Chem. Soc.* **134**, 5516–5519 (2012).
46. Liu, M. *et al.* A Three-Enzyme Pathway with an Optimised Geometric Arrangement to

- Facilitate Substrate Transfer. *Chembiochem* **17**, 1097–101 (2016).
47. Yang, Y. R. *et al.* 2D Enzyme Cascade Network with Efficient Substrate Channeling by Swinging Arms. *ChemBioChem* **19**, 212–216 (2018).
  48. Rothmund, P. W. K. Folding DNA to create nanoscale shapes and patterns. *Nature* **440**, 297–302 (2006).
  49. Martin, T. G. & Dietz, H. Magnesium-free self-assembly of multi-layer DNA objects. *Nat. Commun.* **3**, 1103 (2012).
  50. Castro, C. E. *et al.* A primer to scaffolded DNA origami. *Nat. Methods* **8**, 221–229 (2011).
  51. Kielar, C. *et al.* Effect of Staple Age on DNA Origami Nanostructure Assembly and Stability. *Molecules* **24**, 2577 (2019).
  52. Xin, Y. *et al.* Cryopreservation of DNA Origami Nanostructures. *Small* **16**, 1905959 (2020).
  53. Douglas, S. M. *et al.* Self-assembly of DNA into nanoscale three-dimensional shapes. *Nature* **459**, 414–8 (2009).
  54. Douglas, S. M. *et al.* Rapid prototyping of 3D DNA-origami shapes with caDNAno. *Nucleic Acids Res.* **37**, 5001–6 (2009).
  55. Marchi Alexandria N., Saaem Ishtiaq, Vogen Briana N., Brown Stanley & LaBean Thomas H. Toward Larger DNA Origami. *Nano Lett.* **14**, 5740–5747 (2014).
  56. Saccà, B. & Niemeyer, C. M. DNA origami: the art of folding DNA. *Angew. Chem. Int. Ed. Engl.* **51**, 58–66 (2012).
  57. Marko, J. F. & Cocco, S. The micromechanics of DNA. *Phys. World* **16**, 37–41 (2003).
  58. Knittelfelder, R., Riemer, A. B. & Jensen-Jarolim, E. Mimotope vaccination – from allergy to cancer. *Expert Opin. Biol. Ther.* **9**, 493–506 (2009).
  59. Leinikki, P. *et al.* Synthetic Peptides as Diagnostic Tools in Virology. in *Advances in Virus Research* vol. 42 149–186 (1993).
  60. Lindgren, M., Hällbrink, M., Prochiantz, A. & Langel, Ü. Cell-penetrating peptides. *Trends Pharmacol. Sci.* **21**, 99–103 (2000).
  61. AlDeghather, D., Smaglo, B. G. & Weiner, L. M. Beyond peptides and mAbs-current status and future perspectives for biotherapeutics with novel constructs. *J. Clin. Pharmacol.* **55**, S4–S20 (2015).
  62. Smith, G. P. Filamentous fusion phage: novel expression vectors that display cloned antigens on the virion surface. *Science* **228**, 1315–7 (1985).
  63. Almagro, J. C., Pedraza-Escalona, M., Arrieta, H. I. & Pérez-Tapia, S. M. Phage Display

- Libraries for Antibody Therapeutic Discovery and Development. *Antibodies* **8**, 44 (2019).
64. Smith, B. G. P. & Scott, J. K. Libraries of Peptides and Proteins Displayed on Filamentous Phage. *Methods* **217**, 228–257 (1993).
  65. Szardenings, M. Phage display of random peptide libraries: applications, limits, and potential. *J. Recept. Signal Transduct. Res.* **23**, 307–49 (2003).
  66. Vidarsson, G., Dekkers, G. & Rispens, T. IgG Subclasses and Allotypes: From Structure to Effector Functions. *Front. Immunol.* **5**, 1–17 (2014).
  67. Ecker, D. M., Jones, S. D. & Levine, H. L. The therapeutic monoclonal antibody market. *MAbs* **7**, 9–14 (2015).
  68. Beck, A., Wagner-Rousset, E., Ayoub, D., Van Dorsselaer, A. & Sanglier-Cianférani, S. Characterization of Therapeutic Antibodies and Related Products. *Anal. Chem.* **85**, 715–736 (2013).
  69. Neuberger, M. S. *et al.* A hapten-specific chimaeric IgE antibody with human physiological effector function. *Nature* **314**, 268–270 (1985).
  70. Jones, P. T., Dear, P. H., Foote, J., Neuberger, M. S. & Winter, G. Replacing the complementarity-determining regions in a human antibody with those from a mouse. *Nature* **321**, 522–525 (1986).
  71. Manning, M. C., Chou, D. K., Murphy, B. M., Payne, R. W. & Katayama, D. S. Stability of Protein Pharmaceuticals: An Update. *Pharm. Res.* **27**, 544–575 (2010).
  72. Suzanne, H., Daan, J. C., Huub, S. & Wim, J. Structure-immunogenicity relationships of therapeutic proteins. *Pharm. Res.* **21**, 27–45 (2004).
  73. Wright, A. & Morrison, S. L. Effect of glycosylation on antibody function: implications for genetic engineering. *Trends Biotechnol.* **15**, 26–32 (1997).
  74. Kovacs, G. G. *et al.* Intracellular processing of disease-associated  $\alpha$ -synuclein in the human brain suggests prion-like cell-to-cell spread. *Neurobiol. Dis.* **69**, 76–92 (2014).
  75. Kovacs, G. G. *et al.* An antibody with high reactivity for disease-associated  $\alpha$ -synuclein reveals extensive brain pathology. *Acta Neuropathol.* **124**, 37–50 (2012).
  76. Evan, G. I. & Littlewood, T. D. The role of c-myc in cell growth. *Curr. Opin. Genet. Dev.* **3**, 44–49 (1993).
  77. DePinho, R. A., Schreiber-Agus, N. & Alt, F. W. myc Family Oncogenes in the Development of Normal and Neoplastic Cells. in 1–46 (1991). doi:10.1016/S0065-230X(08)60994-X.
  78. Ramsay, G., Evan, G. I. & Bishop, J. M. The protein encoded by the human proto-

- oncogene c-myc. *Proc. Natl. Acad. Sci. U. S. A.* **81**, 7742–7746 (1984).
79. Evan, G. I., Lewis, G. K., Ramsay, G. & Bishop, J. M. Isolation of monoclonal antibodies specific for human c-myc proto-oncogene product. *Mol. Cell. Biol.* **5**, 3610–3616 (1985).
80. Lessard, J. L. Two monoclonal antibodies to actin: One muscle selective and one generally reactive. *Cell Motil. Cytoskeleton* **10**, 349–362 (1988).
81. Stewart, P. L. & Nemerow, G. R. Cell integrins: commonly used receptors for diverse viral pathogens. *Trends Microbiol.* **15**, 500–507 (2007).
82. Nizet, V., Varki, A. & Aebi, M. *Microbial Lectins: Hemagglutinins, Adhesins, and Toxins. Essentials of Glycobiology* (2017). doi:10.1101/glycobiology.3e.037.
83. Varki, A. Glycan-based interactions involving vertebrate sialic-acid-recognizing proteins. *Nature* **446**, 1023–9 (2007).
84. Rustmeier, Strebl & Stehle. The Symmetry of Viral Sialic Acid Binding Sites—Implications for Antiviral Strategies. *Viruses* **11**, 947 (2019).
85. McLellan, J. S. *et al.* Structure of RSV Fusion Glycoprotein Trimer Bound to a Prefusion-Specific Neutralizing Antibody. *Science (80-. )*. **340**, 1113–1117 (2013).
86. Harrison, S. C. Viral membrane fusion. *Nat. Struct. Mol. Biol.* **15**, 690–698 (2008).
87. Martinez, J. J. Type 1 pilus-mediated bacterial invasion of bladder epithelial cells. *EMBO J.* **19**, 2803–2812 (2000).
88. de Bernard, M. & Montecucco, C. Bacterial Toxins. in *Inflammation - From Molecular and Cellular Mechanisms to the Clinic* 81–98 (Wiley-VCH Verlag GmbH & Co. KGaA, 2017). doi:10.1002/9783527692156.ch4.
89. Samji, T. Influenza A: understanding the viral life cycle. *Yale J. Biol. Med.* **82**, 153–9 (2009).
90. Liu, J.-H., Chang, C.-C., Chen, C.-W., Wong, L.-T. & Chu, Y.-W. Conservation region finding for influenza A viruses by machine learning methods of N-linked glycosylation sites and B-cell epitopes. *Math. Biosci.* **315**, 108217 (2019).
91. Horimoto, T. & Kawaoka, Y. Influenza: lessons from past pandemics, warnings from current incidents. *Nat. Rev. Microbiol.* **3**, 591–600 (2005).
92. Harris, A. *et al.* Influenza virus pleiomorphy characterized by cryoelectron tomography. *Proc. Natl. Acad. Sci.* **103**, 19123–19127 (2006).
93. Plotkin, J. B. & Dushoff, J. Codon bias and frequency-dependent selection on the hemagglutinin epitopes of influenza A virus. *Proc. Natl. Acad. Sci.* **100**, 7152–7157 (2003).

- 
94. Steinhauer, D. A. Role of Hemagglutinin Cleavage for the Pathogenicity of Influenza Virus. *Virology* **258**, 1–20 (1999).
  95. Battles, M. B. & McLellan, J. S. Respiratory syncytial virus entry and how to block it. *Nat. Rev. Microbiol.* **17**, 233–245 (2019).
  96. Esposito, S. *et al.* Characteristics and Their Clinical Relevance of Respiratory Syncytial Virus Types and Genotypes Circulating in Northern Italy in Five Consecutive Winter Seasons. *PLoS One* **10**, e0129369 (2015).
  97. Rossey, I., McLellan, J. S., Saelens, X. & Schepens, B. Clinical Potential of Prefusion RSV F-specific Antibodies. *Trends Microbiol.* **26**, 209–219 (2018).
  98. Ye, X. *et al.* Antigenic Site-Specific Competitive Antibody Responses to the Fusion Protein of Respiratory Syncytial Virus Were Associated With Viral Clearance in Hematopoietic Cell Transplantation Adults. *Front. Immunol.* **10**, 1–10 (2019).
  99. Griffiths, C., Drews, S. J. & Marchant, D. J. Respiratory Syncytial Virus: Infection, Detection, and New Options for Prevention and Treatment. *Clin. Microbiol. Rev.* **30**, 277–319 (2017).
  100. Chow, J., Lee, S. M., Shen, Y., Khosravi, A. & Mazmanian, S. K. Host–Bacterial Symbiosis in Health and Disease. in 243–274 (2010). doi:10.1016/B978-0-12-381300-8.00008-3.
  101. Kaper, J. B., Nataro, J. P. & Mobley, H. L. T. Pathogenic Escherichia coli. *Nat. Rev. Microbiol.* **2**, 123–140 (2004).
  102. Hartmann, M. & Lindhorst, T. K. The Bacterial Lectin FimH, a Target for Drug Discovery - Carbohydrate Inhibitors of Type 1 Fimbriae-Mediated Bacterial Adhesion. *European J. Org. Chem.* **2011**, 3583–3609 (2011).
  103. Hartmann, M., Horst, A. K., Klemm, P. & Lindhorst, T. K. A kit for the investigation of live Escherichia colicell adhesion to glycosylated surfaces. *Chem. Commun.* **46**, 330–332 (2010).
  104. Lindhorst, T. K., Kieburg, C. & Krallmann-Wenzel, U. Inhibition of the type 1 fimbriae-mediated adhesion of Escherichia coli to erythrocytes by multiantennary alpha-mannosyl clusters: the effect of multivalency. *Glycoconj. J.* **15**, 605–13 (1998).
  105. Krogfelt, K. A., Bergmans, H. & Klemm, P. Direct evidence that the FimH protein is the mannose-specific adhesin of Escherichia coli type 1 fimbriae. *Infect. Immun.* **58**, 1995–8 (1990).
  106. Jones, C. H. *et al.* FimH adhesin of type 1 pili is assembled into a fibrillar tip structure in

- the Enterobacteriaceae. *Proc. Natl. Acad. Sci.* **92**, 2081–2085 (1995).
107. Bouckaert, J. *et al.* Receptor binding studies disclose a novel class of high-affinity inhibitors of the Escherichia coli FimH adhesin. *Mol. Microbiol.* **55**, 441–455 (2004).
108. Hung, C.-S. *et al.* Structural basis of tropism of Escherichia coli to the bladder during urinary tract infection. *Mol. Microbiol.* **44**, 903–915 (2002).
109. Pasquale, E. B. Eph–ephrin promiscuity is now crystal clear. *Nat. Neurosci.* **7**, 417–418 (2004).
110. Pasquale, E. B. Eph receptor signalling casts a wide net on cell behaviour. *Nat. Rev. Mol. Cell Biol.* **6**, 462–75 (2005).
111. Blits-Huizinga, C. T., Nelersa, C. M., Malhotra, A. & Liebl, D. J. Ephrins and their receptors: binding versus biology. *IUBMB Life* **56**, 257–65 (2004).
112. Zelinski, D. P., Zantek, N. D., Stewart, J. C., Irizarry, A. R. & Kinch, M. S. EphA2 overexpression causes tumorigenesis of mammary epithelial cells. *Cancer Res.* **61**, 2301–6 (2001).
113. Walker-Daniels, J. *et al.* Overexpression of the EphA2 tyrosine kinase in prostate cancer. *Prostate* **41**, 275–280 (1999).
114. Thaker, P. H. *et al.* EphA2 expression is associated with aggressive features in ovarian carcinoma. *Clin. Cancer Res.* **10**, 5145–50 (2004).
115. Kinch, M. S., Moore, M.-B. & Harpole, D. H. Predictive value of the EphA2 receptor tyrosine kinase in lung cancer recurrence and survival. *Clin. Cancer Res.* **9**, 613–8 (2003).
116. Miao, H. *et al.* EphA2 Mediates Ligand-Dependent Inhibition and Ligand-Independent Promotion of Cell Migration and Invasion via a Reciprocal Regulatory Loop with Akt. *Cancer Cell* **16**, 9–20 (2009).
117. Barquilla, A. & Pasquale, E. B. Eph receptors and ephrins: therapeutic opportunities. *Annu. Rev. Pharmacol. Toxicol.* **55**, 465–87 (2015).
118. Miao, H. *et al.* Activation of EphA receptor tyrosine kinase inhibits the Ras/MAPK pathway. *Nat. Cell Biol.* **3**, 527–530 (2001).
119. Yang, N.-Y. *et al.* Crosstalk of the EphA2 receptor with a serine/threonine phosphatase suppresses the Akt-mTORC1 pathway in cancer cells. *Cell. Signal.* **23**, 201–212 (2011).
120. Miao, H., Burnett, E., Kinch, M., Simon, E. & Wang, B. Activation of EphA2 kinase suppresses integrin function and causes focal-adhesion-kinase dephosphorylation. *Nat. Cell Biol.* **2**, 62–9 (2000).
121. Koolpe, M., Dail, M. & Pasquale, E. B. An ephrin mimetic peptide that selectively targets

- the EphA2 receptor. *J. Biol. Chem.* **277**, 46974–9 (2002).
122. Mitra, S. *et al.* Structure-activity relationship analysis of peptides targeting the EphA2 receptor. *Biochemistry* **49**, 6687–95 (2010).
123. Duggineni, S. *et al.* Design and Synthesis of Potent Bivalent Peptide Agonists Targeting the EphA2 Receptor. *ACS Med. Chem. Lett.* **4**, (2013).
124. Coulthard, M. G. *et al.* Eph/ephrin signaling in injury and inflammation. *Am. J. Pathol.* **181**, 1493–1503 (2012).
125. Falivelli, G. *et al.* Attenuation of eph receptor kinase activation in cancer cells by coexpressed ephrin ligands. *PLoS One* **8**, e81445 (2013).
126. Astin, J. W. *et al.* Competition amongst Eph receptors regulates contact inhibition of locomotion and invasiveness in prostate cancer cells. *Nat. Cell Biol.* **12**, 1194–1204 (2010).
127. Agard, N. J., Prescher, J. A. & Bertozzi, C. R. A Strain-Promoted [3 + 2] Azide–Alkyne Cycloaddition for Covalent Modification of Biomolecules in Living Systems. *J. Am. Chem. Soc.* **126**, 15046–15047 (2004).
128. Kolb, H. C., Finn, M. G. & Sharpless, K. B. Click Chemistry: Diverse Chemical Function from a Few Good Reactions. *Angew. Chem. Int. Ed. Engl.* **40**, 2004–2021 (2001).
129. Huisgen, R. 1,3-Dipolar Cycloadditions. Past and Future. *Angew. Chemie Int. Ed. English* **2**, 565–598 (1963).
130. Debets, M. F. *et al.* Aza-dibenzocyclooctynes for fast and efficient enzyme PEGylation via copper-free (3+2) cycloaddition. *Chem. Commun.* **46**, 97–99 (2010).
131. Fritsch, R. J. & Krause, I. ELECTROPHORESIS. in *Encyclopedia of Food Sciences and Nutrition* 2055–2062 (Elsevier, 2003). doi:10.1016/B0-12-227055-X/01409-7.
132. Viovy, J.-L. Electrophoresis of DNA and other polyelectrolytes: Physical mechanisms. *Rev. Mod. Phys.* **72**, 813–872 (2000).
133. Hansma, P. K. *et al.* Tapping mode atomic force microscopy in liquids. *Appl. Phys. Lett.* **64**, 1738 (1994).
134. Podesta, A. *et al.* Atomic force microscopy study of DNA deposited on poly L-ornithine-coated mica. *J. Microsc.* **215**, 236–40 (2004).
135. Wu, K. J., Steding, A. & Becker, C. H. Matrix-assisted laser desorption time-of-flight mass spectrometry of oligonucleotides using 3-hydroxypicolinic acid as an ultraviolet-sensitive matrix. *Rapid Commun. Mass Spectrom.* **7**, 142–146 (1993).
136. Jerabek-Willemsen, M., Wienken, C. J., Braun, D., Baaske, P. & Duhr, S. Molecular

- Interaction Studies Using Microscale Thermophoresis. *Assay Drug Dev. Technol.* **9**, 342–353 (2011).
137. Zillner, K. *et al.* Microscale thermophoresis as a sensitive method to quantify protein: nucleic acid interactions in solution. *Methods Mol. Biol.* **815**, 241–52 (2012).
138. Mammen, M., Dahmann, G. & Whitesides, G. M. Effective inhibitors of hemagglutination by influenza virus synthesized from polymers having active ester groups. Insight into mechanism of inhibition. *J. Med. Chem.* **38**, 4179–90 (1995).
139. Cross, G. Hemagglutination inhibition assays. *Semin. Avian Exot. Pet Med.* **11**, 15–18 (2002).
140. Levine, M. M. *et al.* Immunity to enterotoxigenic *Escherichia coli*. *Infect. Immun.* **23**, 729–36 (1979).
141. Calarese, D. A. Antibody Domain Exchange Is an Immunological Solution to Carbohydrate Cluster Recognition. *Science (80-. )*. **300**, 2065–2071 (2003).
142. Hattori, T. *et al.* Antigen clasping by two antigen-binding sites of an exceptionally specific antibody for histone methylation. *Proc. Natl. Acad. Sci.* **113**, 2092–2097 (2016).
143. Lee, S.-C. *et al.* Design of a binding scaffold based on variable lymphocyte receptors of jawless vertebrates by module engineering. *Proc. Natl. Acad. Sci.* **109**, 3299–3304 (2012).
144. Reusch, J. & Rant, U. *Advanced Biophysical Analysis of Mono-and Bispecific Antibody Formats with the switchSENSE® Biosensor Platform*. [www.dynamic-biosensors.com](http://www.dynamic-biosensors.com).
145. Sosnick, T. R., Benjamin, D. C., Novotny, J., Seeger, P. A. & Trewthella, J. Distances between the antigen-binding sites of three murine antibody subclasses measured using neutron and X-ray scattering. *Biochemistry* **31**, 1779–86 (1992).
146. Shaw, A. *et al.* Binding to nanopatterned antigens is dominated by the spatial tolerance of antibodies. *Nat. Nanotechnol.* **14**, 184–190 (2019).
147. Funke, J. J. & Dietz, H. Placing molecules with Bohr radius resolution using DNA origami. *Nat. Nanotechnol.* **11**, 47–52 (2016).
148. Burton, D. R. Antibody: the flexible adaptor molecule. *Trends Biochem. Sci.* **15**, 64–69 (1990).
149. Stanfield, R. L., Zemla, A., Wilson, I. A. & Rupp, B. Antibody Elbow Angles are Influenced by their Light Chain Class. *J. Mol. Biol.* **357**, 1566–1574 (2006).
150. Amoako, G. *et al.* 3D DNA origami designed with caDNAno. *Chinese Sci. Bull.* **58**, 3019–3022 (2013).



- 
151. Krauß, N. *et al.* The structure of the anti-c-myc antibody 9E10 Fab fragment/epitope peptide complex reveals a novel binding mode dominated by the heavy chain hypervariable loops. *Proteins Struct. Funct. Bioinforma.* **73**, 552–565 (2008).
  152. Elzinga, M., Collins, J. H., Kuehl, W. M. & Adelstein, R. S. Complete Amino-Acid Sequence of Actin of Rabbit Skeletal Muscle. *Proc. Natl. Acad. Sci.* **70**, 2687–2691 (1973).
  153. Crothers, D. M. & Metzger, H. The influence of polyvalency on the binding properties of antibodies. *Immunochemistry* **9**, 341–357 (1972).
  154. Kiessling, L. L., Strong, L. E. & Gestwicki, J. E. Chapter 29. Principles for multivalent ligand design. in *Annual Reports in Medicinal Chemistry* vol. 35 321–330 (2000).
  155. Yoo, J. & Aksimentiev, A. In situ structure and dynamics of DNA origami determined through molecular dynamics simulations. *Proc. Natl. Acad. Sci. U. S. A.* **110**, 20099–104 (2013).
  156. Kim, D.-N., Kilchherr, F., Dietz, H. & Bathe, M. Quantitative prediction of 3D solution shape and flexibility of nucleic acid nanostructures. *Nucleic Acids Res.* **40**, 2862–2868 (2012).
  157. Hartl, C. *et al.* Position Accuracy of Gold Nanoparticles on DNA Origami Structures Studied with Small-Angle X-ray Scattering. *Nano Lett.* **18**, 2609–2615 (2018).
  158. Rademacher, C. *et al.* Targeting norovirus infection - Multivalent entry inhibitor design based on NMR experiments. *Chem. - A Eur. J.* **17**, 7442–7453 (2011).
  159. Papp, I. *et al.* Inhibition of influenza virus activity by multivalent glycoarchitectures with matched sizes. *Chembiochem* **12**, 887–95 (2011).
  160. Danial, M., Root, M. J. & Klok, H.-A. Polyvalent Side Chain Peptide–Synthetic Polymer Conjugates as HIV-1 Entry Inhibitors. *Biomacromolecules* **13**, 1438–1447 (2012).
  161. Kötter, S., Krallmann-Wenzel, U., Ehlers, S. & Lindhorst, T. K. Multivalent ligands for the mannose-specific lectin on type 1 fimbriae of *Escherichia coli* : syntheses and testing of trivalent  $\alpha$ -D-mannoside clusters. *J. Chem. Soc. Perkin Trans. 1* 2193–2200 (1998) doi:10.1039/a801985a.
  162. Autar, R. *et al.* Adhesion Inhibition of F1C-Fimbriated *Escherichia coli* and *Pseudomonas aeruginosa* PAK and PAO by Multivalent Carbohydrate Ligands. *ChemBioChem* **4**, 1317–1325 (2003).
  163. Gu, L. *et al.* Single-walled carbon nanotubes displaying multivalent ligands for capturing pathogens. *Chem. Commun.* 874 (2005) doi:10.1039/b415015e.

164. Kitov, P. I. *et al.* Shiga-like toxins are neutralized by tailored multivalent carbohydrate ligands. *Nature* **403**, 669–672 (2000).
165. Kwon, P. S. *et al.* Designer DNA architecture offers precise and multivalent spatial pattern-recognition for viral sensing and inhibition. *Nat. Chem.* (2019) doi:10.1038/s41557-019-0369-8.
166. Johnson, N. P. A. S. & Mueller, J. Updating the Accounts: Global Mortality of the 1918-1920 “Spanish” Influenza Pandemic. *Bull. Hist. Med.* **76**, 105–115 (2002).
167. Iuliano, A. D. *et al.* Estimates of global seasonal influenza-associated respiratory mortality: a modelling study. *Lancet* **391**, 1285–1300 (2018).
168. Hussain, M., Galvin, H., Haw, T. Y., Nutsford, A. & Husain, M. Drug resistance in influenza A virus: the epidemiology and management. *Infect. Drug Resist.* **Volume 10**, 121–134 (2017).
169. van der Vries, E., Schutten, M., Fraaij, P., Boucher, C. & Osterhaus, A. Influenza Virus Resistance to Antiviral Therapy. in *Advances in pharmacology (San Diego, Calif.)* vol. 67 217–246 (Copyright © 2013 Elsevier Inc. All rights reserved., 2013).
170. Corti, D. *et al.* Tackling influenza with broadly neutralizing antibodies. *Curr. Opin. Virol.* **24**, 60–69 (2017).
171. World Health Organization. WHO Global Influenza. Surveillance Network. Manual for the laboratory diagnosis and virological surveillance of influenza. 153 (2011).
172. Shi, T. *et al.* Global, regional, and national disease burden estimates of acute lower respiratory infections due to respiratory syncytial virus in young children in 2015: a systematic review and modelling study. *Lancet* **390**, 946–958 (2017).
173. Stein, R. T. *et al.* Respiratory syncytial virus hospitalization and mortality: Systematic review and meta-analysis. *Pediatr. Pulmonol.* **52**, 556–569 (2017).
174. Bacharier, L. B. *et al.* Determinants of asthma after severe respiratory syncytial virus bronchiolitis. *J. Allergy Clin. Immunol.* **130**, 91-100.e3 (2012).
175. DEVINCENZO, J. P. Therapy of respiratory syncytial virus infection. *Pediatr. Infect. Dis. J.* **19**, 786–790 (2000).
176. Lieberthal, A. S. *et al.* Diagnosis and management of bronchiolitis. *Pediatrics* **118**, 1774–1793 (2006).
177. Ventre, K. & Randolph, A. Ribavirin for respiratory syncytial virus infection of the lower respiratory tract in infants and young children. in *Cochrane Database of Systematic*

- 
- Reviews* (ed. Ventre, K.) (John Wiley & Sons, Ltd, 2007). doi:10.1002/14651858.CD000181.pub3.
178. McLellan, J. S. *et al.* Structural basis of respiratory syncytial virus neutralization by motavizumab. *Nat. Struct. Mol. Biol.* **17**, 248–250 (2010).
  179. Mazur, N. I., van Delden, J. J. M. & Bont, L. J. Respiratory syncytial virus trials and beyond. *Lancet Infect. Dis.* **15**, 1363–1365 (2015).
  180. Magro, M. *et al.* Neutralizing antibodies against the preactive form of respiratory syncytial virus fusion protein offer unique possibilities for clinical intervention. *Proc. Natl. Acad. Sci.* **109**, 3089–3094 (2012).
  181. Kwakkenbos, M. J. *et al.* Generation of stable monoclonal antibody-producing B cell receptor-positive human memory B cells by genetic programming. *Nat. Med.* **16**, 123–128 (2010).
  182. Harding, G. K. M. & Ronald, A. R. The management of urinary infections; what have we learned in the past decade? *Int. J. Antimicrob. Agents* **4**, 83–88 (1994).
  183. Khalil, I. A. *et al.* Morbidity and mortality due to shigella and enterotoxigenic *Escherichia coli* diarrhoea: the Global Burden of Disease Study 1990–2016. *Lancet Infect. Dis.* **18**, 1229–1240 (2018).
  184. Knight, S. D. & Bouckaert, J. Structure, Function, and Assembly of Type 1 Fimbriae. in *Peptide-Based Materials* vol. 310 67–107 (2009).
  185. Hirst, G. K. ADSORPTION OF INFLUENZA HEMAGGLUTININS AND VIRUS BY RED BLOOD CELLS. *J. Exp. Med.* **76**, 195–209 (1942).
  186. Memczak, H. *et al.* Anti-Hemagglutinin Antibody Derived Lead Peptides for Inhibitors of Influenza Virus Binding. *PLoS One* **11**, e0159074 (2016).
  187. Bizebard, T. *et al.* Refined three-dimensional structure of the Fab fragment of a murine IgG1, $\lambda$  antibody. *Acta Crystallogr. Sect. D Biol. Crystallogr.* **50**, 768–777 (1994).
  188. Fleury, D., Wharton, S. A., Skehel, J. J., Knossow, M. & Bizebard, T. Antigen distortion allows influenza virus to escape neutralization. *Nat. Struct. Biol.* **5**, 119–123 (1998).
  189. Papp, I. *et al.* Inhibition of influenza virus infection by multivalent sialic-acid-functionalized gold nanoparticles. *Small* **6**, 2900–6 (2010).
  190. Yamabe, M., Kaihatsu, K. & Ebara, Y. Sialyllactose-Modified Three-Way Junction DNA as Binding Inhibitor of Influenza Virus Hemagglutinin. *Bioconjug. Chem.* **29**, 1490–1494 (2018).
  191. Lu, W. *et al.* Enhanced Inhibition of Influenza A Virus Adhesion by Di- and Trivalent

- Hemagglutinin Inhibitors. *J. Med. Chem.* **62**, 6398–6404 (2019).
192. Balish, A. L., Katz, J. M. & Klimov, A. I. Influenza: Propagation, Quantification, and Storage. in *Current Protocols in Microbiology* 15G.1.1-15G.1.24 (John Wiley & Sons, Inc., 2013). doi:10.1002/9780471729259.mc15g01s29.
193. Takizawa, T. *et al.* Induction of programmed cell death (apoptosis) by influenza virus infection in tissue culture cells. *J. Gen. Virol.* **74**, 2347–2355 (1993).
194. Vermes, I., Haanen, C. & Reutelingsperger, C. Flow cytometry of apoptotic cell death. *J. Immunol. Methods* **243**, 167–190 (2000).
195. Einfeld, A. J., Neumann, G. & Kawaoka, Y. Influenza A virus isolation, culture and identification. *Nat. Protoc.* **9**, 2663–81 (2014).
196. Lauster, D. *et al.* Potential of acylated peptides to target the influenza A virus. *Beilstein J. Org. Chem.* **11**, 589–595 (2015).
197. Matsubara, T. *et al.* Sialic Acid-Mimic Peptides As Hemagglutinin Inhibitors for Anti-Influenza Therapy. *J. Med. Chem.* **53**, 4441–4449 (2010).
198. Hüttl, C. *et al.* Self-assembled peptide amphiphiles function as multivalent binder with increased hemagglutinin affinity. *BMC Biotechnol.* **13**, 51 (2013).
199. Bandlow, V. *et al.* Spatial Screening of Hemagglutinin on Influenza A Virus Particles: Sialyl-LacNAc Displays on DNA and PEG Scaffolds Reveal the Requirements for Bivalency Enhanced Interactions with Weak Monovalent Binders. *J. Am. Chem. Soc.* **139**, 16389–16397 (2017).
200. Ueba, O. Respiratory syncytial virus. I. Concentration and purification of the infectious virus. *Acta Med. Okayama* **32**, 265–72 (1978).
201. Trépanier, P., Payment, P. & Trudel, M. Concentration of human respiratory syncytial virus using ammonium sulfate, polyethylene glycol or hollow fiber ultrafiltration. *J. Virol. Methods* **3**, 201–211 (1981).
202. Mbiguino, A. & Menezes, J. Purification of human respiratory syncytial virus: superiority of sucrose gradient over percoll, renografin, and metrizamide gradients. *J. Virol. Methods* **31**, 161–170 (1991).
203. Cagno, V. *et al.* Broad-spectrum non-toxic antiviral nanoparticles with a virucidal inhibition mechanism. *Nat. Mater.* **17**, 195–203 (2018).
204. Johnson, S. M. *et al.* Respiratory Syncytial Virus Uses CX3CR1 as a Receptor on Primary Human Airway Epithelial Cultures. *PLoS Pathog.* **11**, e1005318 (2015).
205. Griffin, M. P. *et al.* Safety, Tolerability, and Pharmacokinetics of MEDI8897, the

- Respiratory Syncytial Virus Prefusion F-Targeting Monoclonal Antibody with an Extended Half-Life, in Healthy Adults. *Antimicrob. Agents Chemother.* **61**, e01714-16 (2017).
206. Zhu, Q. *et al.* A highly potent extended half-life antibody as a potential rsv vaccine surrogate for all infants. *Sci. Transl. Med.* **9**, 1–12 (2017).
207. Ofek, I. & Beachey, E. H. Mannose binding and epithelial cell adherence of Escherichia coli. *Infect. Immun.* **22**, 247–54 (1978).
208. Langermann, S. *et al.* Vaccination with FimH Adhesin Protects Cynomolgus Monkeys from Colonization and Infection by Uropathogenic Escherichia coli . *J. Infect. Dis.* **181**, 774–778 (2000).
209. Bouckaert, J. *et al.* Heptyl  $\alpha$ -D-Mannosides Grafted on a  $\beta$ -Cyclodextrin Core To Interfere with Escherichia coli Adhesion: An In Vivo Multivalent Effect. *Chem. - A Eur. J.* **19**, 7847–7855 (2013).
210. Bouckaert, J. *et al.* The affinity of the FimH fimbrial adhesin is receptor-driven and quasi-independent of Escherichia coli pathotypes. *Mol. Microbiol.* **61**, 1556–1568 (2006).
211. Ajisaka, K. *et al.* Preferential binding of E. coli with type 1 fimbria to d- mannobiose with the Man $\alpha$ 1 $\rightarrow$ 2Man structure. *Biosci. Biotechnol. Biochem.* **80**, 128–134 (2016).
212. Firon, N., Ofek, I. & Sharon, N. Interaction of mannose-containing oligosaccharides with the fimbrial lectin of Escherichia coli. *Biochem. Biophys. Res. Commun.* **105**, 1426–32 (1982).
213. Sauer, M. M. *et al.* Binding of the Bacterial Adhesin FimH to Its Natural, Multivalent High-Mannose Type Glycan Targets. *J. Am. Chem. Soc.* **141**, 936–944 (2019).
214. Petty, A. *et al.* A Small Molecule Agonist of EphA2 Receptor Tyrosine Kinase Inhibits Tumor Cell Migration In Vitro and Prostate Cancer Metastasis In Vivo. *PLoS One* **7**, e42120 (2012).
215. Wang, S. *et al.* Novel Targeted System To Deliver Chemotherapeutic Drugs to EphA2-Expressing Cancer Cells. *J. Med. Chem.* **55**, 2427–2436 (2012).
216. Tandon, M., Vemula, S. V. & Mittal, S. K. Emerging strategies for EphA2 receptor targeting for cancer therapeutics. *Expert Opin. Ther. Targets* **15**, 31–51 (2011).
217. Liu, Y. *et al.* <sup>99m</sup>Tc-labeled SWL specific peptide for targeting EphA2 receptor. *Nucl. Med. Biol.* **41**, 450–456 (2014).
218. Cai, W. *et al.* Quantitative radioimmunoPET imaging of EphA2 in tumor-bearing mice. *Eur. J. Nucl. Med. Mol. Imaging* **34**, 2024–2036 (2007).

219. Stein, E. *et al.* Eph receptors discriminate specific ligand oligomers to determine alternative signaling complexes, attachment, and assembly responses. *Genes Dev.* **12**, 667–678 (1998).
220. Smith, F. M. *et al.* Dissecting the EphA3/Ephrin-A5 Interactions Using a Novel Functional Mutagenesis Screen. *J. Biol. Chem.* **279**, 9522–9531 (2004).
221. Xu, Q., Lin, W.-C., Petit, R. S. & Groves, J. T. EphA2 Receptor Activation by Monomeric Ephrin-A1 on Supported Membranes. *Biophys. J.* **101**, 2731–2739 (2011).
222. Himanen, J. P. *et al.* Architecture of Eph receptor clusters. *Proc. Natl. Acad. Sci.* **107**, 10860–10865 (2010).
223. Keum, J.-W. & Bermudez, H. Enhanced resistance of DNA nanostructures to enzymatic digestion. *Chem. Commun. (Camb)*. 7036–8 (2009) doi:10.1039/b917661f.
224. Baskin, J. M. *et al.* Copper-free click chemistry for dynamic in vivo imaging. *Proc. Natl. Acad. Sci. U. S. A.* **104**, 16793–7 (2007).
225. Jewett, J. C. & Bertozzi, C. R. Cu-free click cycloaddition reactions in chemical biology. *Chem. Soc. Rev.* **39**, 1272 (2010).
226. Lorenz, J. S. *et al.* Synthetic Transient Crosslinks Program the Mechanics of Soft, Biopolymer-Based Materials. *Adv. Mater.* **30**, 1706092 (2018).
227. Mukai, M., Suruga, N., Saeki, N. & Ogawa, K. EphA receptors and ephrin-A ligands are upregulated by monocytic differentiation/maturation and promote cell adhesion and protrusion formation in HL60 monocytes. *BMC Cell Biol.* **18**, 28 (2017).
228. Walker-Daniels, J., Riese, D. J. & Kinch, M. S. c-Cbl-dependent EphA2 protein degradation is induced by ligand binding. *Mol. Cancer Res.* **1**, 79–87 (2002).
229. Sebaugh, J. L. Guidelines for accurate EC50/IC50 estimation. *Pharm. Stat.* **10**, 128–134 (2011).
230. Huang, X., Wu, D., Jin, H., Stupack, D. & Wang, J. Y. J. Induction of cell retraction by the combined actions of Abl–CrkII and Rho–ROCK1 signaling. *J. Cell Biol.* **183**, 711–723 (2008).
231. Fox, B. P., Tabone, C. J. & Kandpal, R. P. Potential clinical relevance of Eph receptors and ephrin ligands expressed in prostate carcinoma cell lines. *Biochem. Biophys. Res. Commun.* **342**, 1263–1272 (2006).
232. Singh, D. R., Kanvinde, P., King, C., Pasquale, E. B. & Hristova, K. The EphA2 receptor is activated through induction of distinct, ligand-dependent oligomeric structures. *Commun. Biol.* **1**, 15 (2018).

- 
233. Schreiber, G. & Keating, A. E. Protein binding specificity versus promiscuity. *Curr. Opin. Struct. Biol.* **21**, 50–61 (2011).
234. Eisen, H. N. *et al.* Promiscuous binding of extracellular peptides to cell surface class I MHC protein. *Proc. Natl. Acad. Sci.* **109**, 4580–4585 (2012).
235. Mueller, T. D. & Nickel, J. Promiscuity and specificity in BMP receptor activation. *FEBS Lett.* **586**, 1846–1859 (2012).
236. Ashkenazi, A. Death Receptors: Signaling and Modulation. *Science (80-. )*. **281**, 1305–1308 (1998).
237. Wajant, H., Pfizenmaier, K. & Scheurich, P. TNF-related apoptosis inducing ligand (TRAIL) and its receptors in tumor surveillance and cancer therapy. *Apoptosis* **7**, 449–59 (2002).
238. Okochi, M., Nakanishi, M., Kato, R., Kobayashi, T. & Honda, H. High-throughput screening of cell death inducible short peptides from TNF-related apoptosis-inducing ligand sequence. *FEBS Lett.* **580**, 885–889 (2006).
239. Tur, V. *et al.* DR4-selective Tumor Necrosis Factor-related Apoptosis-inducing Ligand (TRAIL) Variants Obtained by Structure-based Design. *J. Biol. Chem.* **283**, 20560–20568 (2008).
240. Gaetke, L. M. & Chow, C. K. Copper toxicity, oxidative stress, and antioxidant nutrients. *Toxicology* **189**, 147–63 (2003).
241. van der Linden, W. A. *et al.* Two-step bioorthogonal activity-based proteasome profiling using copper-free click reagents: A comparative study. *Bioorg. Med. Chem.* **20**, 662–666 (2012).
242. Koo, H. *et al.* Bioorthogonal copper-free click chemistry in vivo for tumor-targeted delivery of nanoparticles. *Angew. Chem. Int. Ed. Engl.* **51**, 11836–40 (2012).
243. Yoon, H. I. *et al.* Bioorthogonal Copper Free Click Chemistry for Labeling and Tracking of Chondrocytes In Vivo. *Bioconjug. Chem.* **27**, 927–936 (2016).
244. Jiang, Q., Liu, S., Liu, J., Wang, Z. & Ding, B. Rationally Designed DNA-Origami Nanomaterials for Drug Delivery In Vivo. *Adv. Mater.* **31**, 1804785 (2019).
245. Pinheiro, V. B. & Holliger, P. Towards XNA nanotechnology: new materials from synthetic genetic polymers. *Trends Biotechnol.* **32**, 321–328 (2014).
246. Morihiro, K., Kasahara, Y. & Obika, S. Biological applications of xeno nucleic acids. *Mol. Biosyst.* **13**, 235–245 (2017).
247. Karkare, S. & Bhatnagar, D. Promising nucleic acid analogs and mimics: characteristic

- features and applications of PNA, LNA, and morpholino. *Appl. Microbiol. Biotechnol.* **71**, 575–586 (2006).
248. Chaput, J. C. & Herdewijn, P. What Is XNA? *Angew. Chemie Int. Ed.* **58**, 11570–11572 (2019).



## Appendix

### I. Lists of figures and tables

#### List of figures

Figure 2-1. Multivalent interactions. ....	3
Figure 2-2. The molecular structure of dsDNA. ....	6
Figure 2-3. Simplified, schematic depiction of DNA origami structure assembly. ....	7
Figure 2-4. Schematic DNA trimer and DNA 4arm structure. ....	9
Figure 2-5. 3D IgG antibody structure. ....	11
Figure 2-6. Type I prefusion viral glycoproteins. ....	14
Figure 2-7. Schematic diagram of an influenza A virus virion. ....	16
Figure 2-8. Schematic diagram of the filamentous morphology of a RSV virion. ....	17
Figure 2-9. <i>E. coli</i> adherence to epithelial cells. ....	19
Figure 3-1. NHS ester reaction using NH <sub>2</sub> -DNA and DBCO-NHS ester. ....	37
Figure 3-2. SPAAC reaction using DBCO-DNA and an azide molecule. ....	38
Figure 3-3. Schematic ELISA principle using DOhex structures. ....	42
Figure 3-4. EphA2 phosphorylation assay principle. ....	44
Figure 3-5. Principle of HAI assay, side view (top) and bottom view (below). ....	46
Figure 3-6. Schematic bacteria binding assay. ....	48
Figure 4-1. Schematic of antibodies binding to DOhex structures. ....	52
Figure 4-2. Control samples for ELISA. ....	53
Figure 4-3. Appearance of DOhex structure. ....	54
Figure 4-4. Analysis of conjugated DOhex structures. ....	55
Figure 4-5. $\alpha$ -Synuclein antibodies binding to ED10 and ED9 on DOhex structures. ....	56
Figure 4-6. Anti c-Myc antibody binding to CP and CN on DOhex structures. ....	58
Figure 4-7. Anti-actin antibody binding to AP and AN on DOhex structures. ....	59
Figure 5-1. PAGEs: Addition of PeB peptides to DNA trimers. ....	71
Figure 5-2. IAV ELISA. ....	72
Figure 5-3. MST analysis of PeB-DNA trimers <sup>Atto655</sup> binding to IAV X31. ....	73
Figure 5-4. HAI Assay using PeB-modified DNA trimers on IAV X31. ....	74
Figure 5-5. IAV infection inhibition assay using flow cytometry. ....	76
Figure 5-6. Photos of MDCK cells after IAV X31 infection inhibition assay. ....	77

Figure 5-7. Production of RSV-Peptide-6 modified DNA structures in DMSO. ....	82
Figure 5-8. RSV ELISA. ....	83
Figure 5-9. RSV infection inhibition assay. ....	85
Figure 5-10. PAGE: DNA 4arm structures conjugated to different mannose molecules. ....	89
Figure 5-11. Binding of fluorescent <i>E. coli</i> to mannose molecules on DNA 4arm structures..	90
Figure 6-1. SWL-coupled DNA trimer and its action on EphA2 receptors. ....	93
Figure 6-2. PAGE: Assembly of DNA trimers and addition of SWL peptides. ....	95
Figure 6-3. Mass spectra of oligonucleotides coupled to SWL peptides. ....	96
Figure 6-4. Flow cytometry analysis of EphA2 expression. ....	97
Figure 6-5. Binding of SWL-coupled DNA trimers <sup>Cy3</sup> to EphA2-expressing PC-3 cells. ....	98
Figure 6-6. Quantitative analysis of phosphorylation of EphA2 receptors. ....	99
Figure 6-7. PC-3 cell rounding. ....	101
Figure A 1. Modifiable 5'-ends on DOhex structure. ....	134
Figure A 2. Detailed caDNAno design of DOhex. ....	135
Figure A 3. Raw NanoDrop image of unmodified and DBCO-modified 4arm strands. ....	138
Figure A 4. Raw data of MST capillary shapes. ....	138
Figure A 5. Flow cytometry dot plots of bacteria binding assay. ....	139
Figure A 6. PAGE: Stability of 3xSWL-DNA trimers in biological surroundings. ....	139
Figure A 7. Flow cytometry dot plots of SWL-functionalized DNA trimers to PC-3 cells. ..	140
Figure A 8. Dose-response curve of EphA2 phosphorylation due to ephrin-A1 treatment....	141
Figure A 9. PC-3 cell rounding upon treatment with 1x- and 2xSWL-DNA trimers. ....	141

---

**List of tables**

Table 3-1. Specific software used .....	23
Table 3-2. Sequences of small DNA constructs .....	28
Table 3-3. Sequences of peptides .....	29
Table 3-4. Saccharides .....	30
Table 3-5. Folding program for DOhex structures .....	35
Table 3-6. Folding of small DNA nanostructures .....	35
Table 4-1. Comparison of CN and CP peptides .....	62
Table 6-1. EC50 values of different ligands for EphA2 receptor phosphorylation .....	100
Table A 1. DNA sequences of staple strands. Positions are written as helix[nucleotide].....	130

## II. DNA Sequences and design for DNA origami hexagonal structure

**Table A 1. DNA sequences of staple strands. Positions are written as helix[nucleotide].**

5'-end	3'-end	Sequence 5' → 3'
0[108]	6[102]	CGAGGTGAATTTCTTAAACTCTTCAACAGTTGAT
0[34]	3[35]	CGATATACCGCTTTATACGTAAGAGGGCAA
0[55]	4[60]	CAACCATCCTCAGCAGTTTCCAACACTCATCTTTGATC
0[73]	3[84]	TTGCTCGGAACCTAAAGAGCGATTATACCAAGC
1[129]	2[116]	ACAATGTATCGGTTTATCAGCTTGCAGTGAGATTT
1[137]	5[143]	AGGTCCAGACACAACGCTGTAGCTCAGAACCCGT
1[144]	9[136]	GCGGAGAAGGTATTATTATGGCTTTTGATGATCAT
1[60]	8[53]	AAAAAGAACCCTTGAGACTGGCTCATT
10[122]	16[116]	GCCGAAACAAACCAGCAATGAGGGAGTCACAATCA
10[38]	16[32]	CCTCTTACAGGCAACAGGCGGATGGGTTGATTCCC
10[73]	5[86]	ATTATTTAGACTGGATAGCGTCCTTACATAACACC
11[101]	19[93]	AAATATTAGCGAGCAAGGAACGGAATACCCGTTAA
11[108]	0[109]	CGGATGACAGGGTTGATCCAGGCGTCAGCGGTTT
11[117]	17[122]	AGCCACCACATTTTCGAATGAAAAAACCGATTAT
11[130]	1[128]	ACCCACCAGAGAATAGGTTAGCGGGGA
11[24]	0[21]	AGGCAGACGACACGGTCAAAAGCTGTTAAAGGTTCCGGTC
11[31]	17[37]	TGCAAAAGAAGTTTAAACTATTATAAGGCAAGTCG
11[54]	17[59]	GGGTAATAGCATTGAAGGATTGCTTAACATTTTA
11[66]	0[56]	AATGCGAGGCAGGACAGATCTTGACGACAGCAGCCGACAATGACAA
12[152]	6[150]	GTCAGACGCCACCCAGAGCCCAGGAGGTCCT
13[131]	7[136]	GAATTAGAGTAAATCCTACAGGACCTATTTCCGGA
13[144]	24[143]	TAACCGAACAACCGTAGTAATTTGTTTATCCGCTT
13[151]	7[160]	TAGACCGACTATGGAAAGTCATACCTGAAACATGAAAG
13[52]	5[44]	AAGCTCCCCCTCAAATGCTTTTGCCCTATCATGAA
13[93]	18[80]	CTTTTTTTGCCATCAATACTGCGGAAGAGGAAGATTC
14[108]	6[116]	AGCAGCCTTGAAGTTTTAATAAACAGTTAATGCTC
14[115]	11[107]	CACCCGTCACCGTCATAGCCCCCTTAC
14[24]	6[32]	AGAGACGGAACAAATCTACTGACGAGAAACACACG
15[129]	11[129]	AAGGTAAATATTTTGGGATAGCAGCGGTTTCATCGGCGGGA
15[31]	11[23]	TTTGTGAGGATCCCTGACAGTTCAGAAAACGAGAG
15[59]	20[60]	GAATGAAGTTTCATTCCATAACCTGCCAATAACAAAAACATTATGATTT
15[80]	9[86]	CATGTTTTACCAAAGACACACAAATATCGCGTCTA
16[115]	21[121]	ATAGAGACTCCGGAAACGAGCCCAATAATAAGACAAAAGTTCA
16[142]	19[143]	CGGAATAAGTGTTAGCAAAGTTACAACAATGAAAT
16[31]	20[39]	AATTATACATTGCAAAGAATAAAGCTAAATCGTAA
17[123]	25[115]	TACAACAGCCTATTTTGCGCGAGGCGTTTACATC
17[38]	25[30]	CAAATGGAGCAACCCCGTTGTTAAATCAGCTTAA
17[45]	13[51]	TCAATATAACACTTAGAGCTTAATTCCGGAAGGCA
17[60]	25[52]	GCTTCAGGTCAGCCCCAGTTAAATTCGCATGTAG
18[79]	23[92]	TACGGCGCGATTGAGAGGTATAAGCAAATGTTT

19[109]	14[109]	TTACAATAATCCGAAAAGT
19[144]	30[143]	AGCAGAATTATTTACAGTGTAGAATTCATCGAATT
19[45]	8[46]	GTACATCATACGTCAGAACAAACTCTAGAAAGCAG
19[67]	8[66]	GTAAGTAGCAATCAAACAAAGCGATTTAGGTTAA
19[84]	13[92]	GAAGCGAGGCATCACCCGAAAAGA
19[94]	27[93]	CCCACAAGAATGCGCTAAGAAACGACAAGAACGGGTAGTCGA
2[108]	4[102]	GGATTTTGCTAAACAAACACCCATGTACCGTAATA
2[115]	10[123]	CTGTGTTTCGTCACCAGTCCACCACTAGCCCGGCC
20[157]	13[150]	CATTAGACGGGAATAGCTCAGATAGTCAG
20[31]	14[25]	GCCTGAGTAATTCAGAGCATTAGCAGTCTTTATAG
20[38]	31[37]	ATGCACAGTCAACGTTGGCGTCTGGTAACCAATAG
20[59]	31[58]	TAGATGATATTTTGACCGGCTTTCACGCATTCCAG
20[80]	31[79]	CAACGATAAATTCGTTGGGAGCGAGCCAGTGCTGA
21[108]	14[116]	TTTGTTATCCCATGATTAATAATTCGACATTCAACCGATAAT
21[137]	13[130]	GCCACTGAACACCCTGAAGCAAGACAGAAGGCCATC
21[151]	15[155]	AATCAGAGCCAAAATACCAAAGACAATTATTCA
21[24]	15[30]	AAAGGAATCGACCATTAGCTGCGAAAGAGGTCATT
23[52]	19[44]	GAAAATTGCCTATCAATAACCCTCATATATTTGTT
23[74]	19[66]	ATTATCTACATCTAGCTGCAAGGATAAAAAATCCCT
24[142]	27[143]	ATCCGGTATTTTTTATTACCAATCTTATCAACAAT
24[24]	20[32]	TTTTTGTCATCATATGTAACAAGAGCCGGAGAAT
25[116]	29[122]	GAGTTTCCTTGCTAATGCAGAACGAAAGTACGTAG
25[130]	21[136]	CGTCTAAGAACACCAGCTACAATCCAGTTAAGCA
25[31]	29[37]	TTCGTGTAGATAGGGGACGACGACAGCAACTGGGG
25[53]	29[59]	CCATAATGGGCTCAGGAAGATCGGCCATTCTTAA
26[129]	15[128]	AATCTGAAAATCAAATAGCAGTATTTATTTGGG
26[87]	20[81]	ATTCTAATGCCGGAGAAATATCAGAGACTTTATTT
27[144]	38[143]	AGAGAGCCAGCCATATTGCTATTAGAGAGACAAAC
27[94]	35[93]	CAATAAACACGTAATTCGTATAAAATAGCTTAGATTTGAAA
28[157]	21[150]	GAGGCATTTTCTAAGTCCACGAGCAAGAG
28[45]	17[44]	CTGCGTATCGGATAGGTCAATCACCGAGAGTCTGG
28[66]	22[67]	AAGCCACTCCACGGCGGACAACCGTAAG
29[123]	40[121]	GGCAGAATCCATTTATCGTAGATTTGTTTGGGAAGG
29[151]	23[156]	AACGAATCATTAGGAATATAGAAGTGAATCTTAC
29[31]	21[23]	GAAATTGGGAAGGGCGATCAGTTTGGGGCGCAGAG
29[38]	40[39]	GGATACCTTTTTCTGGAAGCGGCAGACGGGGTAGA
29[45]	23[51]	CTGCTGCGTATCCTTCCTTAAATTTTTGATAATCA
29[60]	40[58]	GTTACGACTGGAGAGGTTGGTGACTTCAGGAGAGTG
29[67]	23[73]	AACTATTATTTCAACATATATTTTAAAACAGGAAG
29[93]	34[80]	GTTTCATGTCCAGACTTCTGGTGCCGGTTTTCCCGGC
3[131]	7[123]	CTGTTAGTAAATGAATATAGAAAGGTTTTGCCCCC
3[36]	10[39]	AAGAATAAATCCGGGGAACCAAC
3[45]	7[37]	CTAAATTAACGGGTAAATGCGGGACAAATCACAG
3[85]	6[80]	GCGAGAAGAGGCTTTGAGGAGAGGGTATTCA
30[115]	21[107]	TGCGCTCAACACGACAAAAGGTAATAATGTTCAATCATTCTTT

## Appendix

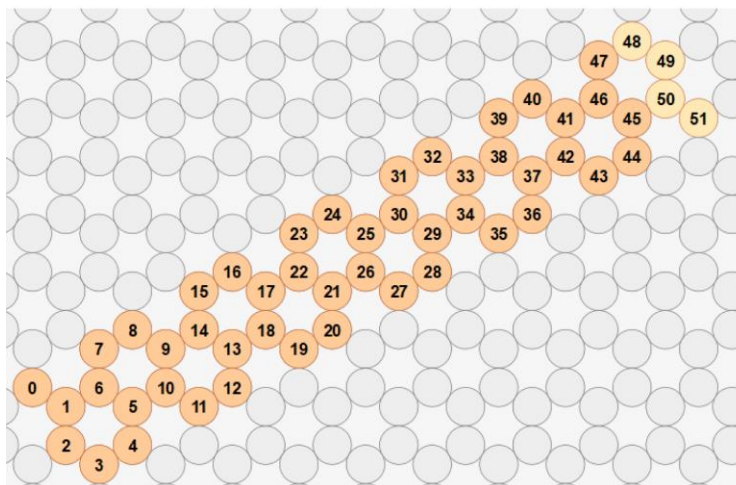
30[136]	26[130]	AAAAAGAATCGTAATAAGAGAATATCGCCTGTAAT
30[142]	34[136]	ACTCGTGTGAAATGCTGATGCAAATAGGTCTATTA
31[38]	35[30]	AAGACGAAGACGCCTGGTAGGAGGACCATGAAGGA
31[45]	28[46]	ACAGCGCAACAACCCTCAAAGGCGAGCCATTCAGG
31[59]	35[51]	CAATTGTGGCGATCCGATGTAAACAGGGATTTGCA
31[66]	28[67]	AATGCGCCGCCAAGCTTGCCAGGGAAACCAGGCA
31[80]	30[88]	ACCACCAGGTTTTAGTTAACGTAAAACG
32[85]	35[74]	TATCTGCCACTCATTGGAGCGAAGCAGGCACCAGG
33[24]	29[30]	TGCCCCGTTTCAGTTCAGCATCAGAAACAGTTCAGGC
34[135]	42[143]	ATTAATGAAACAGTACGAATTATTTCGCCTGTTTA
34[79]	39[93]	AGAATTAACCTCCTGTTTGCATATGATGTATGAT
35[129]	25[129]	TTTTTCCCTTTTAATTGGCCTGTAAAGC
35[24]	24[25]	TGCTTTGGTAAGCCAGCTGGGATTATCAAAAACAT
35[31]	41[37]	TGAACGGGAAAAAACTCTTGCTAACAAGGAGAGT
35[52]	41[58]	ATACATCAAACCTGAGCTTAAGTCCGTAGCTGAACC
35[75]	29[92]	AGAACGAGGATATTCACGTGAAGAGTCACGAC
35[94]	42[97]	TTAATTACATTACAAACAACAGTAATAATACAT
36[122]	41[121]	GCAATCGGGAGTAGATTAACA
36[157]	29[150]	CGCGCAGAGGCATAAATCAATCGTCTAAC
36[85]	46[80]	CTAACAGTAAGTTTCTATAAACAGAGTATTAGAT
37[108]	30[116]	TACCTTAACGTAGAGTCAGCGAGAACTTCTGACCTAAATATA
37[115]	30[109]	TACAAAGAAGATGATGAATAACAATCATAGCGGCCAACGTTA
37[151]	31[156]	CTTGACAGTATACCTTTATATGTATAAATAAGGC
37[52]	29[44]	AACGGAAACAGCAAAATCGAAACCAGACGCAGGTG
37[74]	29[66]	ACCGGGAAACTGCGTGTGCCGCGAATGCATGGGGT
38[129]	30[137]	TTGCAAAATCATCCAATCTTTGAAATACCGACAGA
38[142]	42[136]	AGATAATGGATGCGGAACAAAGAACGTATTAGCAC
39[101]	46[102]	CATCTATTCCTGATTATCTGGGATTTAGAAGTCTA
39[131]	35[128]	ACTTCTGAAAATAAAGAACGGATTCATTTCAATTACCCTT
39[27]	35[23]	TCGCTATTTAATCGAAGCGTAAACGAGCAGCGTGA AAC
39[94]	32[86]	GGCAATTCCTGGGAAGACCTCAGGCTACTA
4[101]	11[100]	GCAATCGAGAGAGGTTGAGGCAGATTTCATAATCA
4[154]	1[143]	CGCCACCCATTCCACAGTTTTGTCTCTTAATT
4[59]	15[58]	GCCTTGAAAGATAGTAAGAGTTGAGAACCAGAGCT
4[71]	1[59]	ATTTGTATCACCCCACTTTTTCATGAGGAAGCG
40[120]	43[114]	AGCGGAATTTTTACAAGAGCCGTA AAA
40[38]	43[37]	TAACGCTTGTGATGCCAGTTTATAAAGATTGGGCG
40[57]	43[59]	AGATCGGTTGATGATGAACGACAGTGCAGATCCG
40[72]	43[85]	CATTCGGGTTTTGCTGATCCATGCAGACATCAC
41[122]	46[137]	ATTCACAGACATCACCAGTCACACGACCAGTATAA
41[38]	46[53]	CTGTGGGGATTGCCATTGCAACAGGAAAAACGATC
41[45]	37[51]	GTCATTGTAAATGGAGGTCAATGGGCTGGAAGAGC
41[59]	46[74]	GTACCATAAACTCATGGAAATACCTACATTTTAA
41[67]	37[73]	ACACAAAGGATGCAGGTGAGTATCATCAAGCGGAA
42[135]	45[150]	TAATATCTGGTCAGTTGAGTATTAACCGAACGAAC

42[142]	47[153]	GGAAATCCTTGAAAGCGATAAAAGGGACATT
42[45]	31[44]	ATTGACTGGAAAGTTTCTCTTATCAAGATGAAATT
42[66]	31[65]	CGTTTGAAGACACTGCACTCGAAGTTTGTGAGAAA
42[96]	45[107]	TTGATTAGCATCACCTTGCTAGCAAATTAATGCGCGA
43[115]	45[123]	TATCAAACCCTAGTGCCATAAAA
43[38]	41[44]	TTATTTCCATGTGACTGATACCGTGCCTCGCAGT
43[60]	41[66]	GTGTATAGAGATTATCACGAGTACAATATTATCAA
43[86]	36[86]	GAAAATCTTTACTGTTGTTCCGAATTCAAGAAAAGCG
44[153]	37[150]	GGCGGTCGCAAATCAAATATCATTG
44[28]	33[23]	TATAAGTCAGCAAAAATGAGTATGGGAGTAACAAGAAGT
44[80]	44[81]	TGTAACGATACTTGCCCTCTCTGTTGAAAAATCTGGTGTTTA
45[108]	37[114]	ACTGTGAATGGATTAGACATCATCAAATATAATCCTGATTTAGGTTTT
45[115]	37[107]	GCCCCGCTGAGAGCCAGCGAACCTCCAATAGACAG
45[124]	39[130]	CATCGCCATACGTGGCGACAACCTACCACCAATTAT
45[151]	39[157]	CACCTGACCTTGCCCGAATCATTTAGGGTTAGAAC
45[20]	39[26]	GCAATGTGTCTGAACCACAGCGAAAATGCTACGCA
46[101]	45[114]	TTAGGGATTATTTACATTGGCAGATATATTTTATA
46[136]	38[130]	GAATTAATAACACCCGCTGCAACCAATCAACAACCTAAAAACAATAAA
46[52]	42[46]	CTCGCAAAATTTCCGCATACAAATACAATGTTTAC
46[73]	42[67]	ACCCGGTGAAGATGAAGGTATAGATCTTGTCTAC
46[79]	46[93]	GATTGACGCTCAATCGTCTGAAATTCTAC
46[92]	40[73]	AAAACATATATCTTACAGCTGACGCTGGCATTTCG
47[20]	44[29]	ACAATATTACCGCCATATTTTACGAGAAAAAGGTT
5[144]	16[143]	ACTGCCACCAAGCCAGATGAGCCATGACGGAACCA
5[45]	0[35]	CTGACATTACCTCGTCACCGCCACGCATAAC
5[80]	15[79]	ACAGGCCAAAACATTCAATTTAATTCAA
5[87]	5[79]	AGGCGCATACGGCCCAATAGAACAAAGTACAATGT
6[101]	9[100]	AAGTTGCCCGTACGGGGTCAAGTCCAGGTCAGACG
6[115]	2[109]	AGTAATAAGTACCTCATTTTCAGGGACACTGAATG
6[149]	1[136]	CAAAATAATAGCTCCAAAAGGAGCCTTTAATCTAA
6[31]	2[21]	TAACATCATAACGACCTGCTCCATGAAACGAAATGCCAC
6[79]	6[91]	TCACCTTAATCATTGGAGTAACAGGCGGCTG
6[90]	0[74]	GCTGACCGCAACGGCAGCTTGATACCGATAG
7[124]	11[116]	TGGTGTACTGGTAATATATTCACCCAGCATACCG
7[137]	3[130]	ACCATTAGGATGTATCACGCCACCCTCAGAGACAAA
7[38]	11[30]	AACGGACGTTGGGAAGAAAACATTAGTTTACCTTT
8[45]	3[44]	TCAGAGTAGTAAATTGGGGGATATTCCAACCTTGATAAATTGTGTGACA
8[52]	11[53]	ATACATTCATCAGCAACAAGAGG
8[65]	4[72]	GAATGGTTAATTTCAAAGAGTAATGAACGGCGGAG
9[101]	17[97]	ATTGCCATTACAAAGGGCATATGGTTTACCAGAGAAAAG
9[137]	13[143]	TAAGAACCACGCCTCCCTCAGAGCCTGTAGCACCG
9[87]	10[74]	ATGCTTTGAATTACCTTATGCGATTAATACCAGGA
15[70]	11[65]	TGTAGCTCGAGCTTAGATTAATCGTCATAAATATTTAA
16[76]	19[83]	AAGTACGCATTTGGTAATAGTATACTTTGCGGGA
17[98]	24[96]	AACTGGCAATCCAACCTTAAATCCCGACTT

21[122]	32[119]	AAAAGGCTGTCAACAAGCTAGTATCTTAATGGGCAAGAC
22[66]	15[69]	GCTAATATTTTGTGTCTGATAATGC
23[112]	19[108]	TAGTTGCATATTATTTTAAACGCAGAGGGTAATTGATGAG
23[93]	16[77]	TGAAGATGGGTAGCTATTTGCTGAAACGAATATGCAACTA
24[76]	26[88]	AACGTTATAAATGTGAACAAAGCCAGCTTCCGGCACCGCGACGG
24[95]	32[98]	GCGGGCCTTAAACCAAGTAAATTCCTATTTCATAACTTTT
30[108]	23[111]	TACACCGCACTGCGAACCTCAAGAT
30[87]	24[77]	ACGGTAACAACAGATTTAAATTGTA
32[118]	36[123]	AAAGAACATAGTGATTGAAAATTCATTTGAATTACTGA
32[97]	39[100]	TCAAATAACAAGACGCTGAGACAGATGAATT

Oligonucleotides marked in blue were ordered with 5′-NH<sub>2</sub> group from Biomers.net GmbH, Germany and used for modification with peptides or sugars. Marked in yellow is the oligonucleotide that was ordered with two extra thymines and a biotin group at the 5′-end from Biomers.net GmbH, Germany.

A



B

Symbol	Position of 5′ end	
	Helix	Nucleotide
Cross	✕	15 70
Triangle	△	23 93
Star	✱	24 76
Circle	○	24 95
Diamond	◇	32 97
Square	□	32 118

**Figure A 1. Modifiable 5′-ends on DOhex structure.**

**A)** Cross-section of DOhex in caDNAno. Staple strands having 5′-ends on helices 15, 23, 24 and 32 were used for peptide attachment. One strand with 5′-end on helix 11 was selected to carry biotin. **B)** Corresponding table.



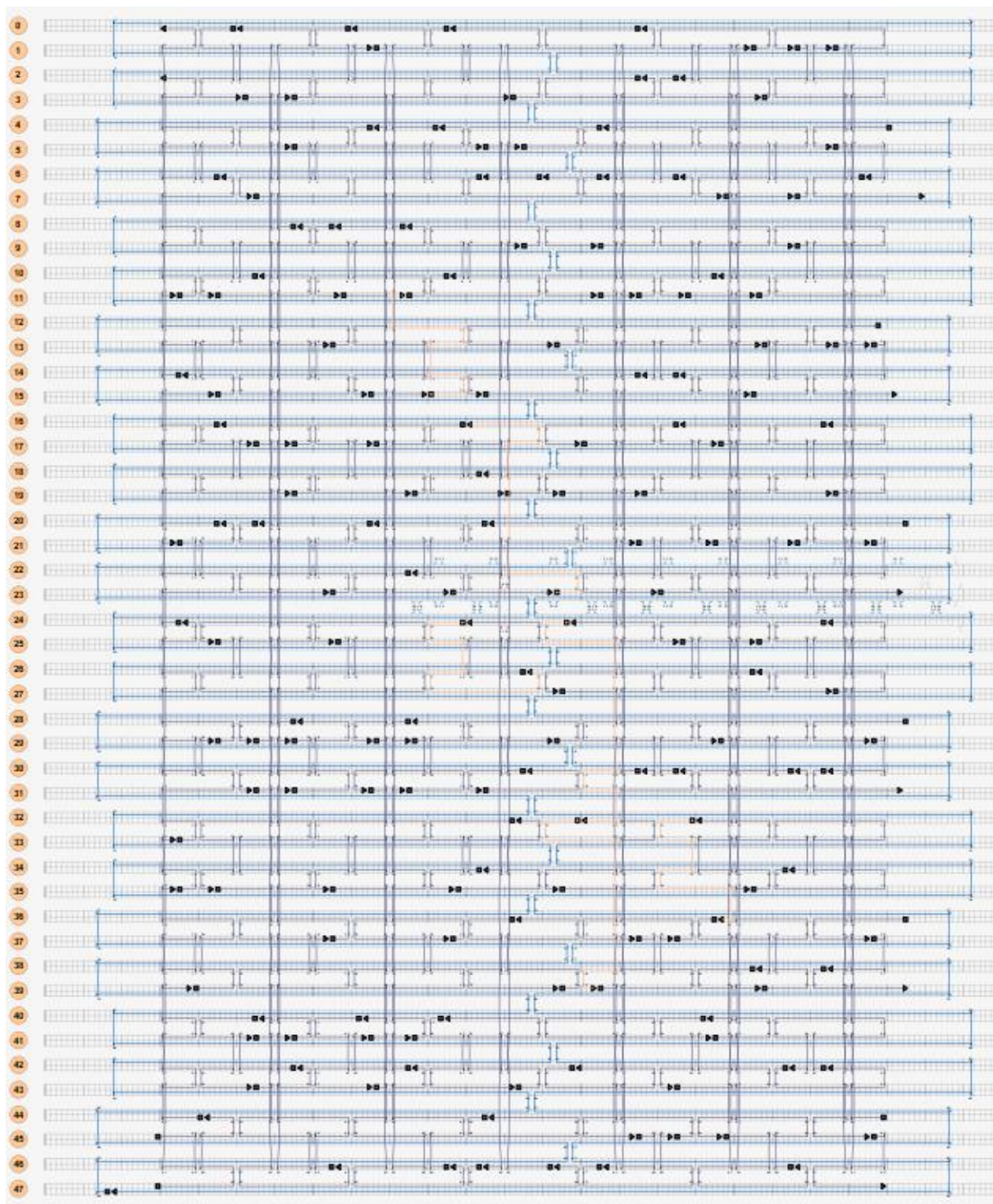


**Figure A 2. Detailed caDNAno design of DOhex.**

Image shows 3D multilayer DOhex layout projected onto a 2D diagram. Helices are numbered on the left, nucleotides are counted from left to right. Blue line = scaffold 8634, grey = unmodified staple strands, orange = modifiable staple strands. Arrowheads indicate 3'-ends, squares indicate 5'-ends.

**Sequence for scaffold strand 8634**

AATGCTACTACTATTAGTAGAATTGATGCCACCTTTTCAGCTCGCGCCCAAATGAAAATATAGCTAAACAGGTTATTGACCATTGCGAAATGTA  
TCTAATGGTCAAACATACTACTCGTTTCGAGAAATGGGAATCAACTGTTATATGGAATGAAACTTCCAGACACCGTACTTTAGTTGCATATTTA  
AAACATGTTGAGCTACAGCATTATATTCAGCAATTAAGCTCTAAGCCATCCGCAAAAATGACCTCTTATCAAAAAGGAGCAATTAAGGTACTCTC  
TAATCCTGACCTGTTGGAGTTTGGCTCCGGTCTGGTTTCGCTTTGAAGCTCGAATTAACGCGATATTGAAGTCTTCCGGCTTCTCTTAATCTT  
TTTGATGCAATCCGCTTTGCTCTGACTATAATAGTCAGGGTAAAGACCTGATTTTTGATTATGGTCATTTCTGTTTTCTGAACTGTTAAAGCAT  
TTGAGGGGATTCAATGAATATTTATGACGATTCCGAGTATTGGACGCTATCCAGTCTAAACATTTTACTATTACCCCTCTGGCAAACTTCTT  
TTGCAAAAAGCCTCTCGCTATTTTGGTTTTATCGTCGTCTGGTAAACGAGGGTTATGATAGTGTGCTTACTATGCCTCGTAATCTTTTGGCG  
TTATGATCTGCATTAGTTGAATGGTATTCTAAATCTCAACTGATGAATCTTCTACTCTGTAATAATGTTGTTCCGTTAGTTCTGTTTTATTAACG  
TAGATTTTTCTTCCCAACGCTCTGACTGGTATAATGAGCCAGTCTTAAAAATCGCATAAGGTAATTCACAATGATTAAGTTGAAATTAACCATC  
TCAAGCCCAATTTACTACTCGTTCTGGTGTTCCTGTCAGGGCAAGCCTTATCTACTGAATGAGCAGCTTTGTTACGTTGATTTGGGTAATGAATAT  
CCGGTCTTGTCAAGATTACTCTGTGAAGGTCAGCCAGCCTATGCGCTGGTCTGTACACCGTTCACTGTCTCTTTCAAAGTTGGTCAGTTTCG  
GTTCCCTTATGATTGACCGTCTGCGCTCGTTCCGGTAAGTAACATGGAGCAGGTCGCGGATTCGACACAATTTATCAGGCGATGATACAAATC  
TCCGTTGACTTTGTTTCGCGCTGGTATAATCGCTGGGGTCAAAGATGAGTGTATTTAGTGTATTCTTTTGCCTTTCTGTTTTAGGTTGGTGCCTT  
CGTAGTGGCATTACGATTTTACCCGTTAATGAAAATCTCTCATGAAAAAGTCTTATGCTCTCAAAGCCTCTGTAGCCGTTGCTACCCCTGTTCC  
GATGCTGTCTTTCTGCTGAGGGTACGATCCCGCAAAAAGCGCCCTTAACTCCCTGCAAGCCTCAGCGACCGAATATATCGGTTATGCGTGGG  
CGATGGTGTGTCATTGTCGGCGCAACTATCGGTATCAAGCTGTTTAAAGAAATTCACCTCGAAAAGCAAGCTGATAAACCGATACAATTAAGGC  
TCCTTTTGGAGCCTTTTTTTGGAGATTTTCAACGTGAAAAAATTTATTCGCAATCTCTTATGTTGTTCTTTCTATTCTACTCCGCTGAAACTG  
TTGAAAGTTGTTTAGCAAAATCCATACAGAAAATTCATTTACTAACGCTCGAAAAGACGACAAAATTTAGATCGTTACGCTAACTATGAGGGC  
TGCTGTGGAATGCTACAGGCGTTGTAGTTGTACTGGTGACGAACTCAGTGTACGGTACATGGGTTCTATTGGGCTGCTATCCCTGAAAAT  
GAGGGTGGTGGCTCTGAGGGTGGCGGTTCTGAGGGTGGCGGTTCTGAGGGTGGCGGTTACTAAACCTCTGAGTACGGTGATACACCTATTCCGGG  
CTATACTTATATCAACCTCTCGACGGCACTTATCCGCTGGTACTGAGCAAAAACCCGCTAATCCTAATCTTCTTTGAGGAGTCTCAGCCTCTT  
AATACTTTATGTTTCAAGATAATAGGTTCCGAAATAGGCAGGGGCACTTAACTGTTTATACGGGCACTGTTACTCAAGGCACTGACCCCGTTAA  
AACTTATTACCAGTACACTCTGTATCATCAAAAAGCCATGTATGACGCTTACTGGAACGGTAAATTCAGAGACTGCGCTTTCCATTCTGGCTTTAA  
TGAGGATTTATTTGTTTGAATATCAAGGCCAATCGTCTGACCTGCCTCAACCTCTGTCAATGCTGGCGCGGCTCTGGTGGTGGTTCTGGTGG  
CGGCTCTGAGGGTGGTGGCTCTGAGGGTGGCGGTTCTGAGGGTGGCGGCTCTGAGGGAGGCGGTTCCGGTGGTGGCTCTGGTTCGGTGATTTTG  
ATTATGAAAAGATGGCAACGCTAATAAGGGGCTATGACCGAAAATGCCGATGAAAACGCGCTACAGTCTGACGCTAAAGGCAAACTTGATTC  
TGTCGCTACTGATTACGGTGTCTATCGATGGTTTATTGGTACGTTTCCGGCTTGTAAATGTAATGGTGTACTGGTGATTTTGTGGCTCT  
AATCCCAAAATGGCTCAAGTCGGTACGGTGATAATTACCTTTAATGAATAATTTCCGTCATATTTACCTTCCCTCCCTCAATCGGTTGAATGTC  
GCCCTTTTGTCTTTGGCGCTGGTAAACCATATGAATTTCTATTGATTGTGACAAAATAAACTTATCCGTTGGTGTCTTTGCGTTTCTTTATATGTT  
GCCACCTTATGATGATTTTCTACGTTTGTCTAACATACTGCGTAAATAAGGAGTCTTAAATCATGCCAGTTCTTTGGGATTCCGTTATTATTGGC  
TTTCTCGGTTTCTTCTGGTAACTTTGTTCCGCTATCTGCTTACTTTCTTAAAAAGGGCTTCGGTAAAGATAGCTATTGCTATTTCAATTGTTCTTG  
CTCTTATTATTGGGCTTAACTCAATTTGTTGGGTTATCTCTCTGATATTAGCGCTCAATTACCTCTGACTTTGTTACAGGTTGTTCAAGTTAATCTC  
CCGCTAATGCGCTTCCCTGTTTTATGTTATTTCTCTGTAAAAGGCTGCTAATTTCAATTTTACGTTAAACAAAAATCGTTTCTTATTGGATTG  
GGATAAATAATATGGCTGTTTATTTTGTAAGTGGCAAAATAGGCTCTGAAAAGACGCTCGTTAGCGTTGGTAAGATTCAGGATAAAAATTGAGCT  
GGGTGCAAAATAGCAACTAATCTGATTTAAGGCTTCAAAACCTCCCGCAAGTCGGGAGGTTTCGCTAAAACGCTCGCGTTCTTAGAATACCGGA  
TAAGCCTTCTATATCTGATTGCTTGTCTATTGGCGCGGTAATGATTCCTACGATGAAAATAAAAACGCTTGTCTGTTCTCGATGAGTGGGATC  
TTGGTTAATACCGTCTTGGAAATGATAAGGAAAGACAGCCGATTATTGATTGGTTTCTACATGCTCGTAAATAGGATGGGATATTATTTTCTT  
GTTACAGGACTTATCTATTGTTGATAAACAGGCGCTTCTGCAATTAGCTGAACATGTTGTTTATTGTCGCTCTGGACAGAACTTTACCTTTG  
TCGGTACTTTATATCTTATTACTGGCTCGAAAATGCCTCTGCCTAAATACATGTTGGCGTTGTTAAATATGGCGATTCTCAATTAAGCCCTAC  
TGTTGAGCGTTGGCTTTATACTGGTAAGAATTTGTATAACGCATATGATACTAAACAGGCTTTTTCTAGTAATATGATTCCGGTGTATTCTTAT  
TTAACGCTTATTATACACCGTCCGTTATTTCAAACCATTAATTTAGGTCAGAAGATGAAATTAACATAAAATATTTGAAAAGTTTCTCGC  
GTTCTTTGCTTGGCATTGGATTGTCATCAGCATTACATATAGTTATATAACCAACCTAAGCCGGAGGTTAAAAAGGTAGTCTCTCAGACCTAT  
GATTTGATAAAATCACTATTGACTCTTCTCAGCGTCTAATCTAAGCTATCGCTATGTTTCAAGGATTCTAAGGGAAAAATTAATTAATAGCGAC  
GATTTACAGAAGCAAGGTTATCTACTACATATATGATTATGTAAGTGTTCATTAATAAAAGGTAATTCAAATGAAATGTTAAATGTAATTA  
TTTTGTTTTCTGATGTTGTTTTCATCATCTTCTTTGCTCAGGTAATTGAAATGAATAATTCGCTCTGCGGATTTTGTAACTGGTATTCAAAGC  
AATCAGGCGAATCCGTTATTGTTTCCCGATGTAAGGTAAGTACTGTTACTGTATATTCATCTGACGTTAAACCTGAAAATCTACGCAATTTCTTTAT  
TCTGTTTTACGTGCAAAATAATTTGATATGGTAGGTTCTAACCCTTCCATTATTCAGAAGTATAATCCAAACAATCAGGATTATATTGATGAATTG  
CCATCATCTGATAAATCAGGAATATGATGATAATCCGCTCCTCTGGTGGTTTCTTTGTTCCGCAAAAATGATAATGTTACTCAAACTTTTAAATTA  
ATAACGTTCCGGGCAAGGATTAATACGAGTTGTCGAATGTTTGTAAAGTCTAATACTTCTAAATCTCAAATGTAATATCTATTGACGGCTCTA  
ATCTATTAGTTGTTAGTGTCTTAAAGATATTTAGATAACCTTCTCAATTTCTTCAACTGTTGATTGCAACTGACCAGATATTGATTGAGGG  
TTTGATATTGAGGTTACAGAAGGTGATGCTTTAGATTTTCAATTTGCTGTGGCTCTCAGCGTGGCAGTGTGACGGCGGTGTTAACTGACCGC  
CTCACCTCTGTTTTATCTTCTGCTGGTGGTTCGTTCCGTTATTTAATGGCGATGTTTTAGGGCTATCAGTTGCGCATTAAGACTAATAGCCATT  
CAAAAATATTGCTGTGCCAGTATCTTACGCTTTCAGGTCAGAAGGTTCTATCTGTTGGCCAGAATGTCCCTTTTATTACTGGTCTGTGAC  
TGGTGAATCTGCCAATGTAATAATCCATTTACAGACGATTGAGCGTCAAAATGTAGGATTTCCATGAGCGTTTTCTGTTGCAATGGCTGGCGG  
TAATATTGTTCTGGATATTACCAGCAAGCCGATAGTTTGGAGTTCTTACTCAGGCAAGTGTATTACTAATCAAGAAGTATTGCTACAAC

GGTTAATTTGCGTGATGGACAGACTCTTTTACTCGGTGGCCTCACTGATTATAAAAAACTTCTCAGGATTTGCGGTACCGTTCTGTCTAAAAAT  
CCCTTTAATCGGCCTCTGTAGCTCCCGCTCTGATTCTAACGAGGAAAGCAGTTATACGTGCTCGTCAAAGCAACCATAGTACGCGCCCTGTA  
GCGGCGCATTAAAGCGCGCGGGTGTGGTGGTTACGCGCAGCGTGACCGCTACACTTGCAGCGCCCTAGCGCCCGCTCTTTTCGCTTTTCCCTT  
CCTTTCTCGCCACGTTTCGCCGGCTTTCCCGTCAAGCTCTAAATCGGGGGCTCCCTTTAGGGTTCCGATTTAGTGCCTTACGGCACCTCGACCCCAA  
AAAACTTGATTTGGGTGATGGTTCACGTAGTGGGCCATCGCCCTGATAGACGGTTTTTCGCCCTTTGACGTTGGAGTCCACGTTCTTAATAGTGG  
ACTCTGTTCCAAACCTGGAACAACACTCAACCCTATCTCGGGCTATCTTTTGATTATAAGGGATTTTGGCGATTTGGAACCACCATCAAACAG  
GATTTTCGCCTGCTGGGGCAAACCAGCGTGGACCGCTTGCTGCAACTCTCTCAGGGCCAGGCGGTGAAGGGCAATCAGCTGTTGCCCGTCTCACT  
GGTGAAGAAAGAAAAACCACCTGGCGCCCAATACGCAAAACCGCTCTCCCGCGCGTTGGCCGATTCATTAATGACGTGGCACGACAGGTTTCCC  
GACTGGAAGCGGGCAGTAGCGCAACGCAATTAATGTGAGTTAGTCACTCATTAGGCACCCAGGCTTTACACTTTATGCTTCCGGCTCGTAT  
GTTGTGTGGAATTGTGAGCGGATAACAATTCACACAGGAAACAGCTATGACCATGATTACGAATTCGAGCTCGGTACCCGGGGATCCATTCTCC  
TGTGACTCGGAAGTGCATTTATCATCTCCATAAAAACAAACCCGCGTAGCGAGTTACAGATAAAAATAAATCCCGCGAGTGCAGGAGTTGTTATG  
TAATATTGGGTTAATCATCTATATGTTTTGTACAGAGAGGGCAAGTATCGTTTCCACCGTACTCGTGATAATAATTTTGCACGGTATCAGTCATTT  
CTGCGCATTGACAGAAATGGGGATTTGTCTTATTAGACTTATAAACTTCATGGAATATTTGTATGCCGACTTATATCTATACTTACATCTACATA  
AACACCTTCGTGATGCTGCATGGAGACAAGACACCGGATCTGCACAACATTGATAACGCCCAATCTTTTGTCTCAGACTCTAACTATTGATACT  
CATTTATAAACTCCTTGCAATGTATGTCGTTTCAGCTAAACGGTATCAGCAATGTTTATGTAAAGAAACAGTAAGATAAATACTCAACCCGATGTTT  
GAGTACGGTCATCATCTGACACTACAGACTCTGGCATCGCTGTGAAGACGACGCGAAATTCAGCATTTTACAAGCGTTATCTTTTACAAAACCG  
ATCTCACTCTCCTTTGATGCGAATGCCAGCGTCAGACATCATATGCAGATACTCACTGCATCCTGAACCCATTGACCTCCAACCCCGTAATAGCG  
ATGCGTAATGATGTCGATGTTACTAACGGGCTTTGTTTCGATTAAGTCCGCGAGAACTTCCAGGTCACCAGTGCAGTGGTTGATAACAGGAG  
TCTTCCCAGGATGGCGAACAACAAGAACTGGTTTCCGTCTTACGGACTTCGTTGCTTTCCAGTTTAGCAATACGCTTACTCCCATCCGAGATAA  
CACCTTCGTAATACTCAGCTGCTCGTTGAGTTTGTATTTGCTGTTTCAAGCTCAACACGCGATTTCCCTACTGTTAGCGCAATATCTCGTTCTC  
CTGGTCGCGCGGTTTGATGTATTGCTGGTTTCTTTCCCGTTCATCCAGCAGTCCAGCACAAATCGATGGTGTACCAATTCATGGAAGGTTCTGC  
GTCAAATCCCAGTCGTCATGCATTGCCTGCTCTGCCGTTACGCGAGTGCCTGAGAGTTAATTTGCTCACTTCGAACCTCTCTGTTTACTGATAA  
GTTCCAGATCCTCCTGGCAACTTGCACAAGTCCGACAACCTGAACGACCAGGCGCTTTCGTTTATCTATCGGATCGCCACACTCACAACAATGA  
GTGGCAGATATAGCCTGGTGGTTCAGGCGGCGCATTTTTATTGCTGTGTTGCGCTGTAATTCTTCTATTTCTGATGCTGAATCAATGATGCTGCCA  
TCTTTCAATTAATCCCTGAACTGTTGGTTAATACGCATGAGGGTGAATGCGAATAATAAAGCTTGGCACTGGCCGCTGTTTTACAACGTCGTGACTG  
GGAAAACCTGGCGTTACCCAACCTAATCGCCTTGCAGCACATCCCCTTTCCGCGAGTGGCGTAATAGCGAAGAGGCCCGCACCGATCGCCCTT  
CCCAACAGTTGCGCAGCCTGAATGGCGAATGGCGCTTTGCCCTGGTTCCGGCACCAGAAAGCGGTGCCGAAAGCTGGCTGGAGTGGCATCTTCT  
GAGGCCGATACTGTCGTCGTCCTTCAAACCTGGCAGATGCACGGTTACGATGCGCCATCTACACCAACGTGACCTATCCCATTACGGTCAATCC  
GCCGTTTGTCCACGGAGAAATCCGACGGGTTGTTACTCGCTCACATTTAATGTTGATGAAAGCTGGCTACAGGAAGGCCAGACGCGAATATTTT  
TGATGGCGTTCTATGGTTAAAAAATGAGCTGATTTAACAAAAATTAATGCGAATTTTAAACAAAAATTAACGTTTACAATTTAAATATTTGCT  
TATAAATCTTCTGTTTTTGGGGCTTTTCTGATTATCAACCGGGTACATATGATTGACATGCTAGTTTTACGATTACCGTTCATCGATTCTCTTGT  
TTGCTCCAGACTCTCAGGCAATGACCTGATAGCCTTTGTAGATCTCTAAAAATAGCTACCCTCTCCGGCATTAAATTTATCAGCTAGAACGGTTGA  
ATATCATATTGATGGTGATTGACTGTCTCCGGCCTTTCTCACCTTTTGAATCTTTACCTACACATTACTCAGGCATTGCATTTAAAAATATATGAG  
GGTTCTAAAAATTTTATCCTTGCCTTGAATAAAGGCTTCTCCCGCAAAAGTATTACAGGGTCATAATGTTTTTGGTACAACCGATTTAGCTTTAT  
GCTCTGAGGCTTATGCTTAATTTGCTAATTTGCTTTCCTGCTGATGATTTATTGGATGTT

### III. Additional and raw data

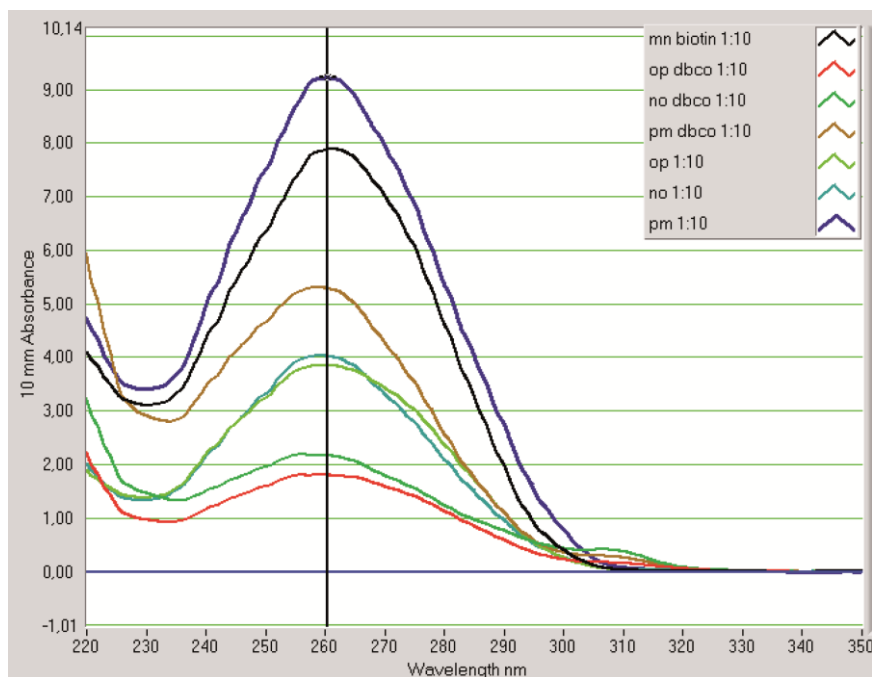


**Figure A 3. Raw NanoDrop image of unmodified and DBCO-modified 4arm strands.**

DNA absorbance at 260 nm was visible as peak for all examined DNA strands. In addition, shoulders at 309 nm were observed for DNA strands conjugated to DBCO (red “op dbco”, green “no dbco” and brown “pm dbco” curve).

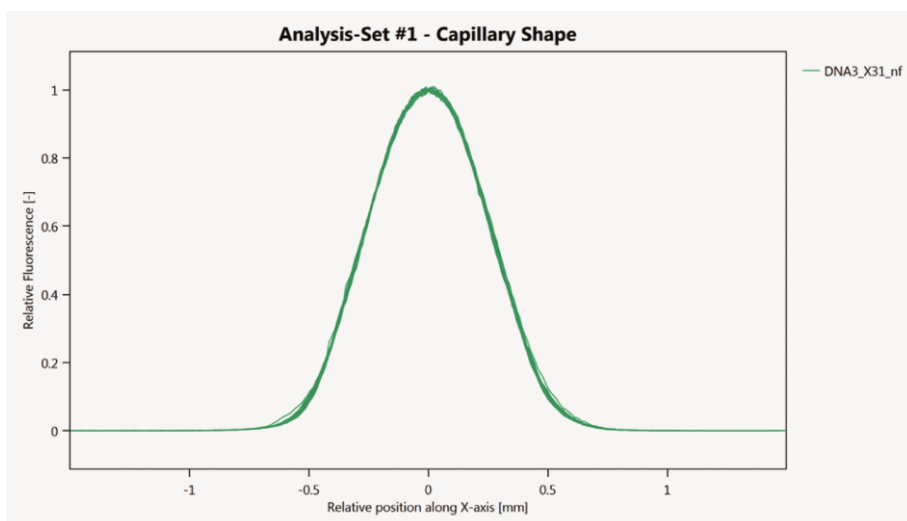


**Figure A 4. Raw data of MST capillary shapes.**

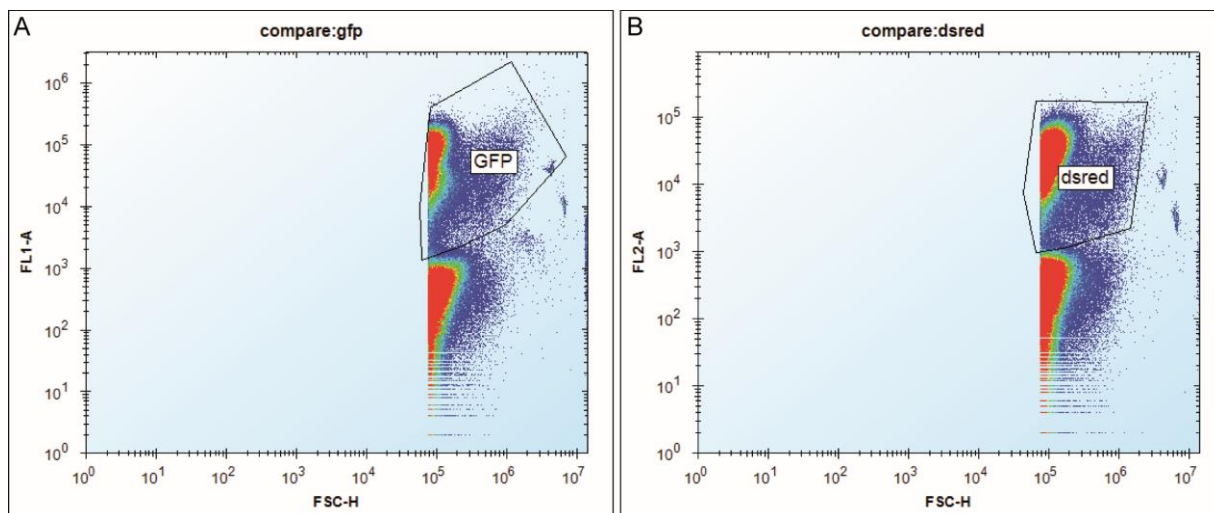


**Figure A 5. Flow cytometry dot plots of bacteria binding assay.**

**A)** GFP bacteria captured via sugar-functionalized 4arm structures attached to magnetic beads can be seen as population with elevated fluorescent signals in FL1-A (533/30). **B)** DsRed bacteria captured via sugar-functionalized 4arm structures attached to magnetic beads can be seen as population with elevated fluorescent signals in FL2-A (585/40).

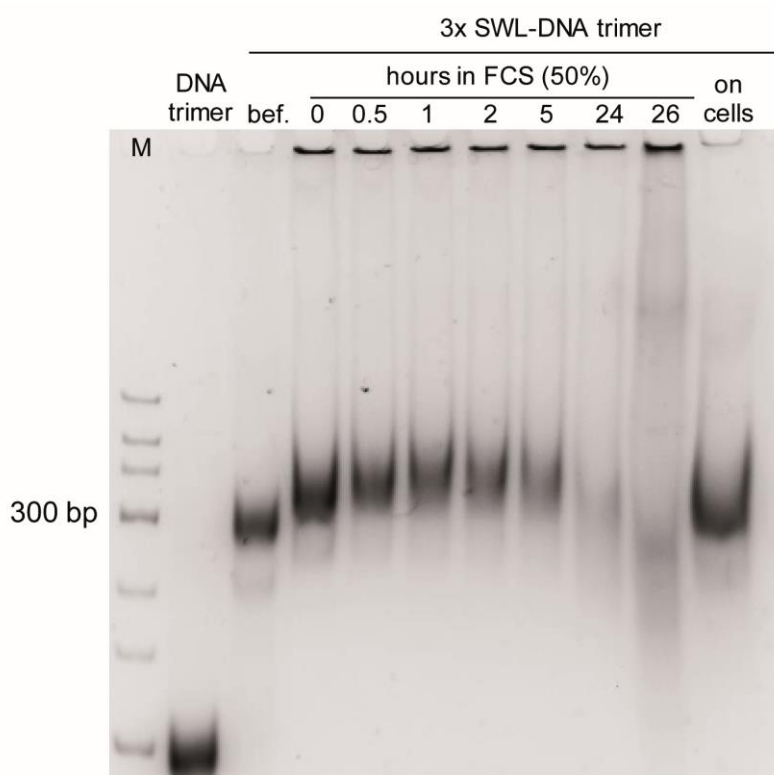


**Figure A 6. PAGE: Stability of 3xSWL-DNA trimers in biological surroundings.**

Stability of 3xSWL-DNA trimers in 50% (v/v) FBS and incubated with PC-3 cells at 37 °C. Constructs were incubated in 50% (v/v) FBS over time, analyzed on 10% (v/v) native PAGE and stained with SYBR® Gold Nucleic Acid Gel Stain and imaged under UV light. Unmodified DNA trimers serve as control. Sample “bef.” = 3xSWL-DNA trimers before addition of FCS, sample is in 1× PBS/10 mM MgCl<sub>2</sub>. Addition of FCS led to upward shift in gel. Structures were stable over 5 h and degraded after 24 h. When incubated with PC-3 cells in serum-free medium, 3xSWL-DNA trimers were stable for at least 24 h (far right band). M = GeneRuler™ Low Range DNA Ladder (Thermo Fisher Scientific, USA) serves as control, not as ruler.



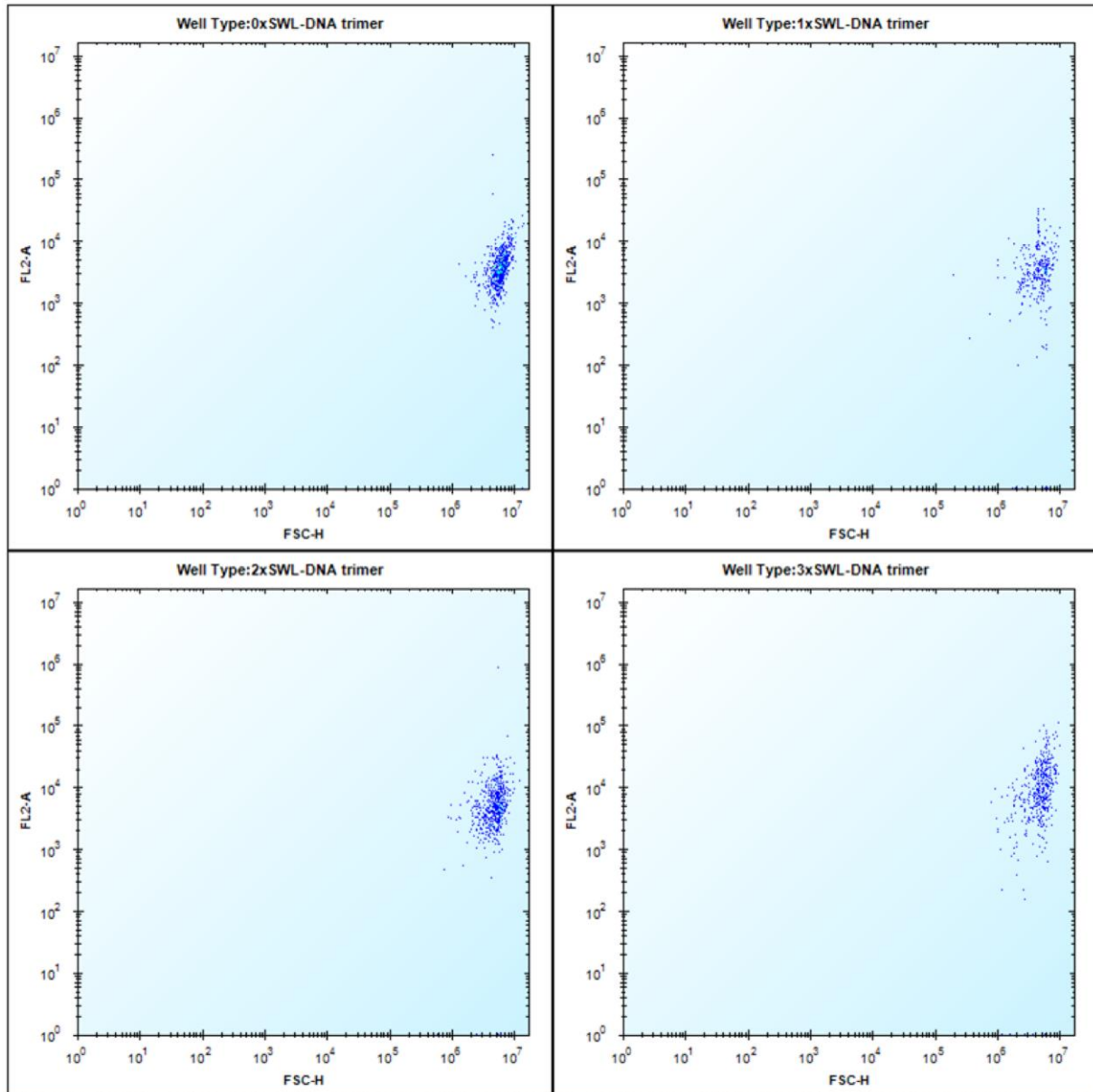


**Figure A 7. Flow cytometry dot plots of SWL-functionalized DNA trimers to PC-3 cells.**

Elevated signals at up to intensities of  $10^5$  in FL2-A (filter 585/40) indicated enhanced binding of 3xSWL-DNA trimers<sup>Cy3</sup> to PC-3 cells.

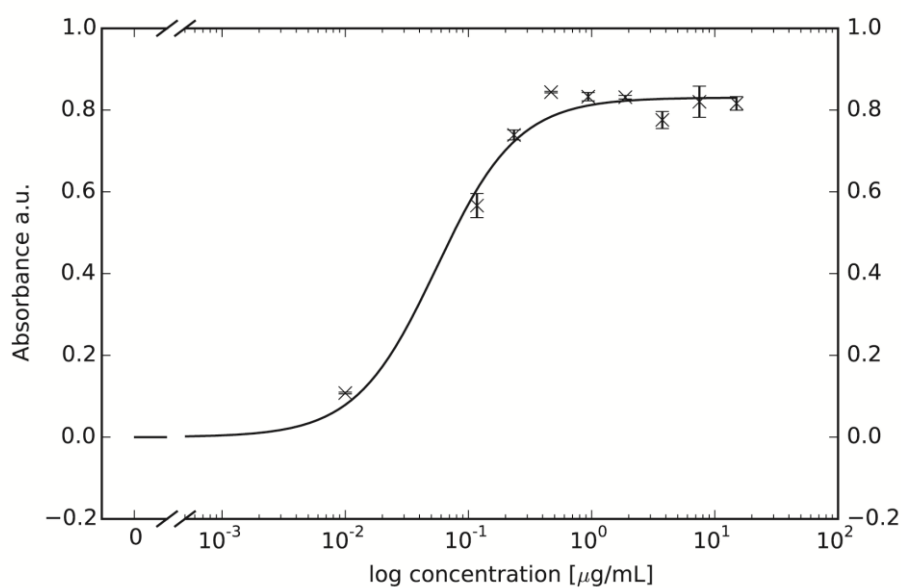


**Figure A 8. Dose-response curve of EphA2 phosphorylation due to ephrin-A1 treatment.**

Displayed values are averages of net absorbance (difference between absorbance at 520 nm versus 450 nm) with standard deviation presented as error bars. The calculated EC<sub>50</sub> value is  $0.0552 \pm 0.0103 \mu\text{g/mL}$  which equals 2.65 nM

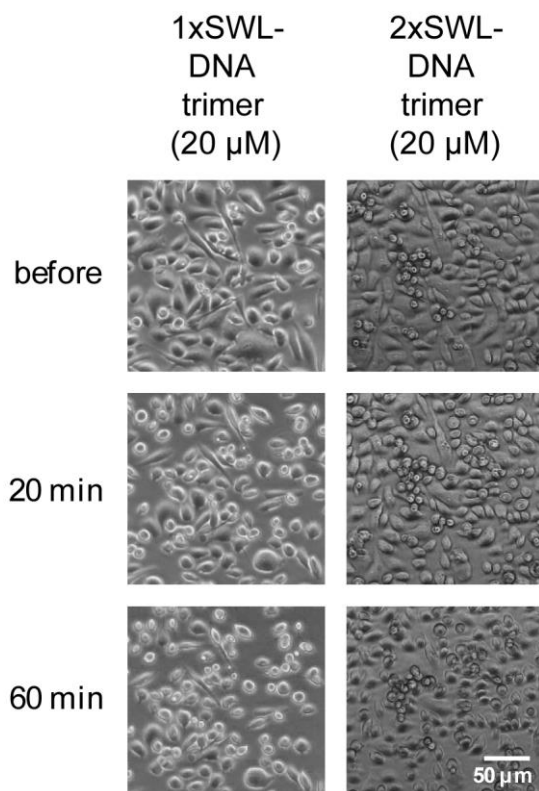


**Figure A 9. PC-3 cell rounding upon treatment with 1x- and 2xSWL-DNA trimers.**  
Addition to Figure 6-7.

## Acknowledgements

Zuerst möchte ich meinem Doktorvater Herrn Prof. Dr. Frank F. Bier dafür danken, dass ich als externe Doktorandin die Möglichkeit hatte, bei ihm zu promovieren. Herzlichen Dank für Ihre freundliche Betreuung, Diskussionsbereitschaft und stetige Unterstützung während der Promotion. Für ihre Zeit und Mühe bei der Begutachtung meiner Arbeit danke ich Prof. Dr. Ilko Bald und apl. Prof. Dr. Wolfgang Fritzsche.

A very special thank you goes to my supervisor and mentor Dr. David M Smith. Thank you very much for giving me the opportunity to work on such versatile and interesting topics and for demanding a high quality of work. I thank you for encouraging me to present my research at conferences, for supporting me to attend several seminars and workshops and for entrusting me more and more responsibilities in the lab as well as in supervising students and conceiving projects. Moreover, I would like to express my gratitude for your constant willingness to discuss and your offer to give advice in all situations. Certainly, I can speak for the whole group when I say that your positivity and zeal are contagious and we enjoy to work in your group!

Ich danke PD Dr. Sebastian Ulbert, der als mir als Mentor im Fraunhofer IZI zur Seite stand und mich geduldig bei Fragen zur Planung und Vorbereitung der Virenprojekte beraten hat.

Ganz herzlich möchte ich mich bei meinen lieben Kollegen Dr. Jessy Freitag, Elisabeth Wenzel, Martin Glaser, Paul Mollenkopf, Dr. Martin Sajfutdinow, Dr. Jörg Schnauß und Christoph Schneider für deren großartige Unterstützung und Hilfe bei praktischen und theoretischen Fragen bedanken. Außerdem danke ich euch dafür, dass ihr immer ein offenes Ohr für mich habt und ich mich auf euch verlassen kann. Vielen Dank für die schöne Zeit mit euch im Institut, auf Konferenzen und in unserer Freizeit. Ich habe euch sehr ins Herz geschlossen.

I would like to thank the members of our group DNA nanodevices, especially my students Bhanu Kiran Pothineni, Nico Grasse, Florian Seier, Basma Altattan, Robel Belay, Catarina Ferraz, Eleonore Roderfeld, Rola Hanifa, Amr Shaffei Mostafa and Charlotte Pezenburg for their support in the lab and our helpful and vivid discussions from which I learned a lot.

Vielen Dank an Dr. Michael Szardenings für die Bereitstellung der Epitope, seine Ideen beim gemeinsamen Troubleshooting, dafür, dass er mir einen Einblick in die Welt der Oberflächenplasmonenresonanzspektroskopie gegeben und so viel (besonders über Antikörper)



beigebracht hat. Ein weiterer Dank gilt Dr. Nicolas Delaroque und Dr. Karolin Kern für ihre wertvollen Tipps und Tricks zur Durchführung des ELISA Verfahrens.

Dr. Jasmin Fertey möchte ich für ihre Unterstützung und die hilfreichen Tipps bei der Durchführung und Umsetzung der Viren- und Bakterienprojekte, besonders für die aufwändige Vorbereitung der Bakterien, einen großen Dank aussprechen. Von dir habe ich sehr viel über die Arbeit mit Pathogenen gelernt und ich freue mich, dass wir so gut zusammenarbeiten.

Für die Planung und Durchführung der Hämagglutinationsinhibitionstests und MST Experimente und dafür, dass sie ihr Wissen über Influenza A Viren mit mir geteilt haben, gilt ein großer Dank Dr. Daniel Lauster und Dr. Walter Stöcklein. Weiterhin danke ich Dr. Henry Memczak und Paul Becker für ihre Arbeiten am Peptid PeB, die mich maßgeblich vorangebracht haben.

I would like to express my gratitude to Leila Issmail and Dr. Thomas Grunwald for sharing their knowledge about RSV with me. I especially thank Leila for pushing the RSV project forward with her ambition, diligence and dedication as well as for conducting the infection inhibition experiments.

Bedanken möchte ich mich ebenfalls bei Dr. Mirko Buchholz, Christian Jäger, Martin Kleinschmidt und Dr. Daniel Ramsbeck für die Entwicklung und Herstellung der RSV Peptidvarianten und die erfolgreiche Zusammenarbeit.

I would like to greatly acknowledge Dr. Vittorio Bordoni for synthesizing the sugar molecules. Furthermore, I thank our project partners Dr. Martina Delbianco and Dr. Felix Löffler for their help in brainstorming innovative ideas and interesting experiments.

Für die wunderbare Zusammenarbeit bei mehreren Projekten möchte ich Dr. Adrian Keller und Dr. Charlotte Kielar herzlich danken. Es hat mir großen Spaß bereitet mit euch im Labor zu arbeiten. Vielen Dank für eure Bereitschaft AFM Messungen für mich durchzuführen, mich mit nützlichen Hinweisen zu versorgen und mich bei zwei Veröffentlichungen zu integrieren.

Zu guter Letzt möchte ich meiner Familie und meinen Freunden, ganz besonders aber meinen Eltern und Billy von Herzen danken. Danke, dass ich mich immer an euch wenden kann und ihr mich seelisch, moralisch und praktisch so lieb unterstützt.

## **Declaration of authorship**

I hereby declare that this thesis has not been submitted to any other institution of higher education and is the product of my own work. All the assistance received in preparing this thesis and the sources used have been acknowledged.

Potsdam, 17.03.2021

Christin Möser

## Patents and publications

### Patents

- D. M. Smith, **C. Möser**, T. Grunwald, L. Issmail, C. Jäger, M. Kleinschmidt, D. Ramsbeck, M. Buchholz, “Biological and synthetic molecules inhibiting respiratory syncytial virus infection,” WO2020212576A1, 2020.
- D. M. Smith, J. S. Lorenz, **C. Möser**, J. Fertey, W. Stöcklein, A. Herrmann, and D. Lauster, “Nanostructure with a nucleic acid scaffold and virus-binding peptide moieties,” WO2018215660A1, 2018.

### Journal Contributions

- Y. Xin, C. Kielar, S. Zhu, C. Sikeler, X. Xu, **C. Möser**, G. Grundmeier, T. Liedl, A. Heuer-Jungemann, D. M. Smith and A. Keller, “Cryopreservation of DNA Origami Nanostructures,” *Small*, vol. 16, no. 13, p. 1905959, Mar. 2020.
- C. Kielar, Y. Xin, X. Xu, S. Zhu, N. Gorin, G. Grundmeier, **C. Möser**, D. M. Smith, and A. Keller, “Effect of Staple Age on DNA Origami Nanostructure Assembly and Stability,” *Molecules*, vol. 24, no. 14, p. 2577, Jul. 2019.
- C. Möser**, J. S. Lorenz, M. Sajfutdinow, and D. M. Smith, “Pinpointed Stimulation of EphA2 Receptors via DNA-Templated Oligovalence,” *Int. J. Mol. Sci.*, vol. 19, no. 11, p. 3482, Nov. 2018.
- J. Schnauß, M. Glaser, J. S. Lorenz, C. Schuldt, **C. Möser**, M. Sajfutdinow, T. Händler, J. A. Käs, and D. M. Smith, “DNA Nanotubes as a Versatile Tool to Study Semiflexible Polymers,” *J. Vis. Exp.*, no. 128, pp. e56056–e56056, Oct. 2017.

### Conference Contributions – Talks

- C. Möser**, “Imaging of Sugar-functionalized DNA Origami structures using FM/3D-AFM”, 8th Bio-AFM summer school at Nano Life Science Institute, Kanazawa University (Kanazawa, Japan), August 24, 2019
- C. Möser**, “DNA nanostructures as Oligovalent carriers for peptides”, PhD Workshop on Bioanalysis (Luckenwalde), November 23, 2018
- C. Möser**, “Using DNA nanostructures to present and potentiate peptides in an oligovalent manner”, Functional DNA Nanotechnology (Rome, Italy), June 7, 2018
- C. Möser**, “DNA nanostructures as Oligovalent carriers for peptides”, DNA Mitteldeutschland

Meeting (Jena), May 24, 2018

**C. Möser**, “DNA Nanostructures as Multivalent Carriers for Peptides”, PhD Workshop on Bioanalysis (Luckenwalde), November 27, 2017

**C. Möser**, “Targeting and Activation of RTK with DNA-based synthetic Antibodies”, DNA Mitteldeutschland Meeting (Jena), May 18, 2017

**C. Möser**, “Binding of DNA based synthetic antibodies to prostate cancer cells”, IntelliCyt User Meeting (Watford, United Kingdom), October 26, 2016

**C. Möser**, “Impeding virus particles with peptide-conjugated DNA Trimers”, DNA Mitteldeutschland Meeting (Jena), May 19, 2016

**C. Möser**, “Activation of EphA2 receptor by multivalent presentation of SWL-12”, DNA Mitteldeutschland Meeting (Dresden), September 24, 2015

### **Conference Contributions – Posters**

**C. Möser**, J. Fertey, J. S. Lorenz, M. Sajfutdinow, V. Bordoni, M. Delbianco, F. Löffler, S. Ulbert, D. M. Smith. “Oligovalent enhancement of biomolecules presented on DNA nanostructures”, Fraunhofer IZI Science Day (Leipzig), June 27, 2019

**C. Möser**, E. Roderfeld, D. Lauster, D. M. Smith. “Trimeric DNA nanostructures as oligovalent carrier for peptides”, Soft Matter Day (Leipzig), July 6, 2018

**C. Möser**, E. Roderfeld, D. Lauster, D. M. Smith. “Trimeric DNA nanostructures as oligovalent carrier for peptides”, DNA-Nanotechnology (Jena), May 25-26, 2018

**C. Möser**, J. S. Lorenz, D. Lauster, W. Stöcklein, H. Memczak, A. Herrmann, F. Bier, D. M. Smith. “DNA nanostructures as multivalent carriers for peptides”, 4. International Symposium of the Collaborative Research Center (SFB) 765 “Multivalent Interactions of Pathogens with Biological Surfaces” (Berlin), October 4-6, 2017

**C. Möser**, J. S. Lorenz, M. Herbig, O. Otto, J. Guck, F. Bier, D. M. Smith, “Multivalent binding achieved by DNA nanostructures”, Soft Matter Day (Leipzig), June 23, 2017

**C. Möser**, J. S. Lorenz, M. Herbig, O. Otto, J. Guck, F. Bier, D. M. Smith. “DNA nanostructures as multivalent carriers for peptides”, Fraunhofer IZI Science Day (Leipzig), June 22, 2017

**C. Möser**, J. S. Lorenz, M. Herbig, O. Otto, J. Guck, F. Bier, D. M. Smith. “DNA nanostructures as multivalent carriers for peptides”, Physics of Cancer (Leipzig), October 4-6, 2016

**C. Möser**, J. S. Lorenz, M. Herbig, O. Otto, J. Guck, F. Bier, D. M. Smith. “DNA nanostructures as multivalent carriers for peptides”, DNA22 (Munich), September 4-8, 2016

- C. Möser** and A. S. Mostafa, J. S. Lorenz, J. Guck, O. Otto, M. Herbig, D. Lauster, W. Stöcklein, H. Memczak, A. Herrmann, F. Bier, D. M. Smith. “DNA nanostructures as multivalent carriers for peptides”, Fraunhofer IZI Science Day (Leipzig), June 16, 2016
- C. Möser**, J. S. Lorenz, M. Herbig, O. Otto, J. Guck, F. Bier, D. M. Smith. “DNA nanostructures as multivalent carriers for peptides”, Soft Matter Day (Leipzig), June 10, 2016
- C. Möser**, J. S. Lorenz, M. Herbig, O. Otto, J. Guck, F. Bier, D. M. Smith. “DNA nanostructures as multivalent carriers for peptides”, DNA-Based Nanotechnology (Jena), May 19-21, 2016
- J. S. Lorenz and **C. Möser**, J. Schnauß, C. Schuldt, I. Neundorf, F. Bier, D. M. Smith. “Functionalization of DNA nanostructures with biomolecules”, World Conference on Regenerative Medicine (Leipzig), October 21-23, 2015
- C. Möser**, J. S. Lorenz, J. Guck, O. Otto, D. Lauster, F. Bier, D. M. Smith. “DNA nanostructures as platform for multivalent ligands”, Physics of Cancer (Leipzig), October 7-9, 2015

#### **Miscellaneous**

- C. Möser**, “Evaluating the Binding of DNA-Based Synthetic Antibodies to Prostate Cancer Cells”, IntelliCyt Webinar, March 9, 2017

## **Curriculum vitae**

Pages 148-149 (curriculum vitae) contain personal information. They are therefore not part of the online publication.